Resonance Formation in Electron Collisions With Pyrimidine-Like Targets

Thesis

UNRESTRICTED

The Open University

Department of Physical Sciences

A thesis submitted for the degree of Doctor of Philosophy

in the discipline of Physics

Resonance formation in electron collisions with pyrimidine-like targets

by

Zdeněk Mašín

Supervisor: Jimena D. Gorfinkiel

Date of Submission: 30 September 2012

Date of Award: 12 February 2013.

Milton Keynes, 8 October, 2012

ProQuest LLC.
789 East Eisenhower Parkway
P.O. Box 1346
Ann Arbor, MI 48106 – 1346

Abstract

In this thesis we apply the R-matrix method to study low-energy (< 15 eV) elastic and inelastic electron collisions with the diazine molecules (pyrazine, pyrimidine and pyridazine), (2 and 4) oxo-pyrimidines and the RNA nucleobase uracil. We use these molecules as models for the pyrimidinic DNA nucleobases. The main goal of this work is to study resonance formation in these targets. We test various standard scattering models (Static Exchange, Static Exchange plus Polarization, Close-Coupling) to identify those that produce the most accurate results; we also study simplified versions of these models that allow us to provide detailed insights into the resonance formation. We compare our elastic (for pyrazine and pyrimidine) and inelastic (for pyrimidine) cross sections with available experimental data and find a good agreement. A methodology based on the time-delay analysis is applied that allowed us to find and characterize in detail many new resonances not previously identified. We find an unexpectedly large number of resonances. Most of the new resonances have core-excited shape character and many of them do not enhance (significantly) the elastic or inelastic cross sections for collisions with the molecule in the ground state. These resonances, however, significantly enhance the elastic cross sections for collisions with molecules in electronic excited states. The discovery of a large number of these resonances and their unusual properties are novel and unexpected results. We find that oxygen substitution of the pyrimidine ring does not lead to significant changes in the resonance formation: the resonances in pyrimidinic molecules are associated with the ring structure. We conclude that the picture of resonance formation in pyrimidines is much more complex than expected. Most of the work presented in this thesis has been published in peer-reviewed journals.

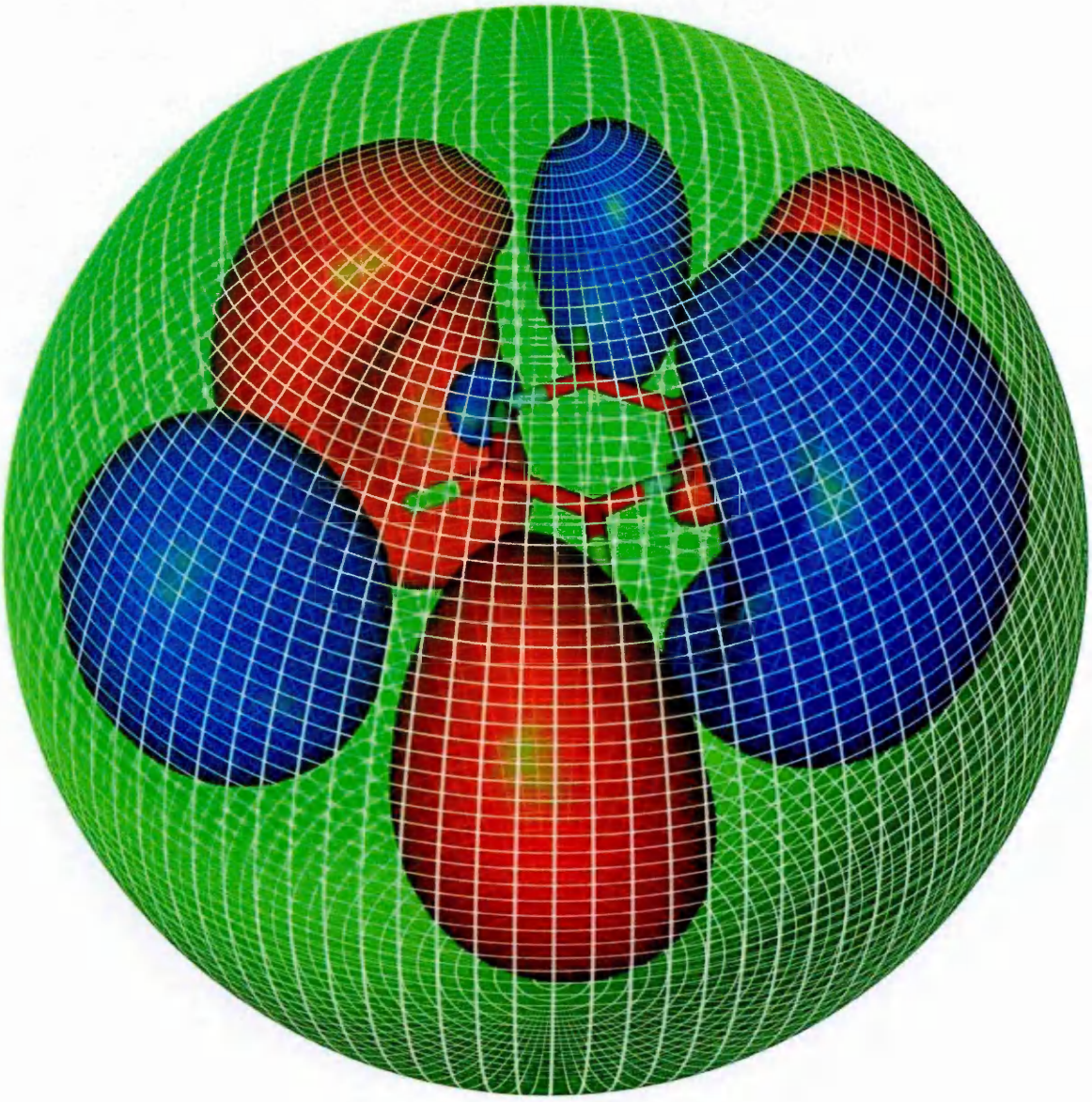

The R-matrix sphere gives name to the R-matrix theory of electron-molecule collisions which plays the central role in this thesis. Above is an illustration of the R-matrix sphere containing molecule of pyrazine together with one of its molecular orbitals.

Contents

Publications and Posters

Publications

- Zdeněk Mašín and Jimena D. Gorfinkiel. Elastic and Inelastic Low-energy Electron Collisions with Pyrazine. The Journal of Chemical Physics 135, no. 14 (October 14, 2011): 144308. doi:10.1063/1.3650236.

- Zdeněk Mašín, Jimena D. Gorfinkiel, Darryl B. Jones, Susan M. Bellm, and Michael J. Brunger. Elastic and Inelastic Cross Sections for Low-energy Electron Collisions with Pyrimidine. The Journal of Chemical Physics 136, no. 14 (April 12, 2012): 144310. doi:10.1063/1.3702629.

- Zdeněk Mašín and Jimena D. Gorfinkiel. Shape and Core Excited Resonances in Electron Collisions with Diazines. The Journal of Chemical Physics 137, no. 20 (November 29, 2012): 204312. doi:10.1063/1.4767345.

- Carr, J. M., P. G. Galiatsatos, J. D. Gorfinkiel, A. G. Harvey, M. A. Lysaght, D. Madden, Z. Mašín, M. Plummer, J. Tennyson, and H. N. Varambhia. UKRmol: a Low-energy Electron- and Positron-molecule Scattering Suite. The European Physical Journal D 66, no. 3 (March 2012): 58. doi:10.1140/epjd/e2011-20653-6.

Posters

- RADAM 2010 (Madrid, Spain): Preliminary calculations on low-energy electron collisions with pyrazine.

- ECAMP 2010 (Salamanca, Spain): Preliminary calculations on low-energy electron collisions with pyrazine.

- ICPEAC 2011 (Belfast, United Kingdom): Low-energy electron collisions with pyrazine.

- POSMOL 2011 (Maynooth, Ireland): Low-energy electron collisions with the azabenzene molecules pyrimidine and pyridazine.

- POSMOL 2011 (Maynooth, Ireland): Low-energy electron collisions with pyrazine.
- EDPML 2011 (Prague, Czech Republic): Exploratory work on the use of mixed B-spline and Gaussian basis sets for scattering calculations.
- EDPML 2011 (Prague, Czech Republic): Low-energy electron collisions with pyrimidine and pyridazine.
- MOLEC 2012 (Oxford, United Kingdom): Describing temporary anion states in diazines.

List of Symbols and Abbreviations

Here we list all abbreviations and the more frequently used mathematical symbols. Atomic units were used throughout this thesis unless otherwise stated.

Abbreviation	Description	Definition
	Mathematical symbols	
H_{N+1}	Non-relativistic Hamiltonian for the electron-molecule scattering problem	page 22
$\mathbf{x}_j$	Spatial and spin coordinates of electron j	page 22
k_i	Momentum of the scattering electron in channel i	page 24
Ψ_k	R-matrix basis function	page 33
a	R-matrix raidus	page 32
$F_i(r)$	Reduced radial wavefunction of the scattering electron for channel i	page 36
$\mathcal{Y}_{l,m}(\Omega)$	Real solid spherical harmonic	page 34
$\mathbf{R}$	R-matrix	page 37
$\mathbf{S}$	S-matrix (scattering matrix)	page 24
$\mathbf{T}$	T-matrix	page 25
$\mathbf{Q}$	Q-matrix (time-delay matrix)	page 43
	Target models and related quantities	
HF	Hartree-Fock approximation	page 44
SA-CASSCF	State-Averaged Complete Active Space approximation	page 46
CAS	Complete Active Space	page 47
μ	Ground state dipole moment	[1]
α	Ground state spherical polarizability	[1]
	Scattering models and related quantities	
SE	Static Exchange approximation	page 50

Abbreviation	Description	Definition
SEP	Static Exchange plus Polarization approximation	page 50
CC	Close-Coupling approximation	page 52
DCS	Elastic Differential Cross Section	page 83
ICS	Integral Elastic Cross Section	page 111
TICS	Total Integral Inelastic Cross Section	page 86
	Resonances	
S	Shape Resonance	page 141
GS	Ground State Resonance	page 141
MCES	Mixed Core-Excited Shape Resonance	page 141
CE*	Core-Excited Resonance	page 141

Acknowledgements

First of all I would like to thank Dr Jimena D. Gorfinkiel for an excellent guidance and support throughout the whole three years. I have learned very much from you and I really could not have asked for a better supervisor!

Dr Elaine A. Moore also helped me a lot by carefully reading this thesis and spotting many typos and several inaccuracies in it. For this I thank you very much.

I thank Dr Darryl B. Jones for useful discussions which helped me to perfect assignments of our calculated pyrimidine electronic states to the experimental ones. Prasanga Palihawadana made me very happy by providing his recently measured elastic differential cross sections for pyrazine which turned out to agree with the models I believed were the most accurate. Only rarely is a theoretician more happy than on occasions when his predictions turn out to agree with nature!

I would like to thank my parents, Marcela and Zdeněk, who taught me the value of education and have supported me in all my efforts. My girlfriend Gemma has been an unconditional source of loving support for me and for that I am very grateful! Last but not least I have found many good friends in England who have made my stay in this wonderful country a very enjoyable experience and I thank you all for that!

Finally, I would like to thank EPSRC and The Open University for providing me with a financial support.

Chapter 1

Introduction

The human body is constantly exposed to radiation, whose main sources are cosmic radiation and radionuclides present in the Earth's soil [2, 3]. Medical imaging and radiotherapy also rely on the use of radiation. It is therefore desirable to have detailed knowledge of the underlying processes taking place in the human body when it is exposed to radiation. DNA (Deoxyribonucleic acid) carries the genetic instructions used in the development and functioning of the body and is present in every living cell. The biological effects of radiation result principally from damage to DNA. Consequently, answering the question of how DNA behaves under radiation is central to studies of radiation damage in living organisms [4].

The molecule of DNA is comprised of phosphate-deoxyribose backbone and four nucleobases: adenine, guanine, cytosine and thymine. The deoxyribose is bound to both the nucleobase and the phosphate group. The basic structure of DNA is represented in Figure 1.1. RNA (Ribonucleic acid) is a molecule closely related to DNA, but in contrast to DNA, it is single-stranded in most of its biological roles, the deoxyribose sugar replaced by ribose and the nucleobase thymine replaced by uracil.

The two DNA nucleobases thymine and cytosine and the RNA nucleobase uracil are pyrimidinic nucleobases, derived from the molecule pyrimidine. The remaining nucleobases adenine and guanine are substituted purine rings (see Figure 1.2).

The particular sources of radiation commonly considered in the studies of radiation induced damage, medical imaging or radiotherapy are: electromagnetic radiation (X-rays and γ-rays), electrons, positrons, protons, α-particles, neutrons and (heavy) charged ions. The first stages of damage to DNA by these sources occur on the time scales of fs to ps [3]. These primary processes can ultimately influence the behaviour and fate of the cell on the time scales ranging from minutes to years [4]. It is therefore no surprise that considerable effort

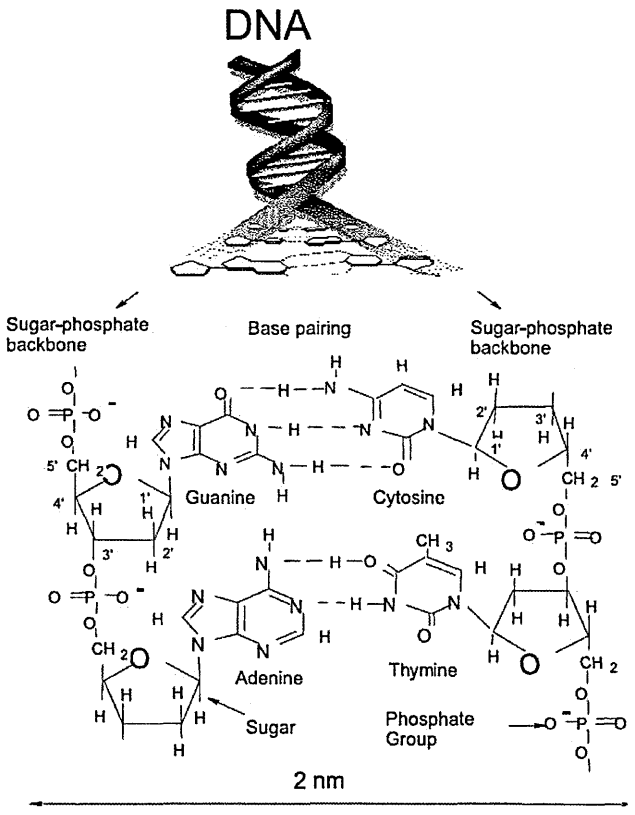

Figure 1.1: Structure of DNA molecule. Taken from [5].

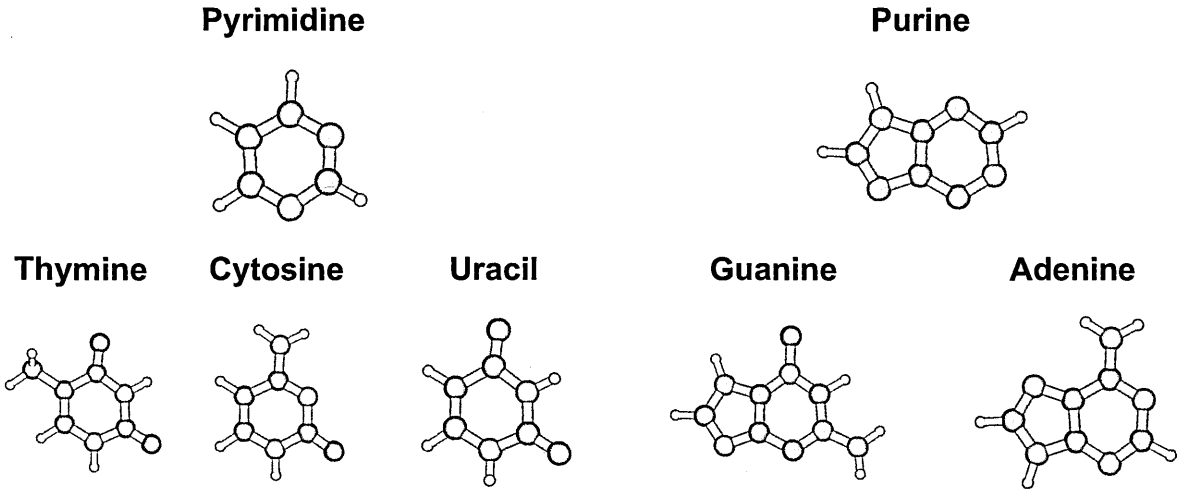

Figure 1.2: DNA bases can be classified as being of purine (guanine, adenine) or pyrimidine character (thymine, cytosine and the RNA base uracil) depending on type of the molecule from which they are derived. In this figure the white balls represent hydrogen, orange - carbon, blue - nitrogen and red - oxygen.

has been put into studies providing insights into these primary processes. The processes that lead to the initial energy deposition within a given volume of tissue are relatively well understood. However, there is still a large gap of knowledge between our understanding of the initial energy deposition and the processes that follow it and that ultimately lead to the slower chemical reactions [5]. Apart from DNA, the cell contains a number of other impor-

tant biomolecules (e.g. proteins, water) and these are also targets for the incoming radiation. However, from now on we will concentrate on DNA and how it can be affected by radiation passing through the cell.

The effects of radiation can be divided into two groups: *direct* and *indirect* [4]. The direct effects are those in which the primary particle ionizes or excites atoms or molecules in DNA initiating the chain of events leading to structural changes. The indirect processes are initiated by interaction of the primary radiation with other atoms or molecules in the cell leading to the production of free radicals and other particles (electrons, protons, etc.) that may subsequently react with DNA and cause damage. It has been estimated that about two thirds of the observed damage to DNA is indirect [4]. The OH radical originating from the radiolysis of water has been deemed to be the main source of this damage.

The research presented in this work focuses on the role of *electrons* in the direct damage of DNA. Electrons are produced in tissue in great amounts by high-energy radiation passing through it. It is estimated that about $\approx 10^4$ electrons are produced per 1 MeV of the primary quantum of radiation [6]. The majority of these electrons have energies below 20 eV. The first confirmation of the significance of the role low-energy electrons play in radiation damage came from the work of Huels et al. [7], who observed resonant induced fragmentation of thymine and cytosine by electrons with subionization energies. However, the main motivation for our work comes from the work of Boudaïffa et al. [8], in 2000, who showed that electrons with energies below 20 eV can *directly* damage DNA. Before this paper, it was thought that only those electrons with energies above ≈ 15 eV could cause direct damage to DNA through the process of ionization of its constituents.

The main result of the work of Boudaïffa et al. on electron collisions with plasmid DNA is shown in Figure 1.3 and clearly proves that low-energy electrons can cause serious damage to DNA, namely single (SSB) and double (DSB) strand breaks. The prominent peaks in the low-energy region responsible for the observed damage have been attributed mainly to processes mediated by *electron resonances* formed somewhere within the DNA [8, 10, 11]. From the biological point of view, well-separated (even multiple) SSB can be repaired easily by the cell using the second strand of DNA as a template. However, if the SSB occur in both strands and are directly opposite or closely-spaced this may lead to DSB in which DNA is split in two pieces and thus to irreparable damage.

Figure 1.4 schematically depicts the process of low-energy electron induced strand break of DNA as we understand it at present. An incoming electron with energy below the ionization threshold of DNA ($\lesssim 10$ eV) [5] attaches to one of its sub-units (thus forming a temporary

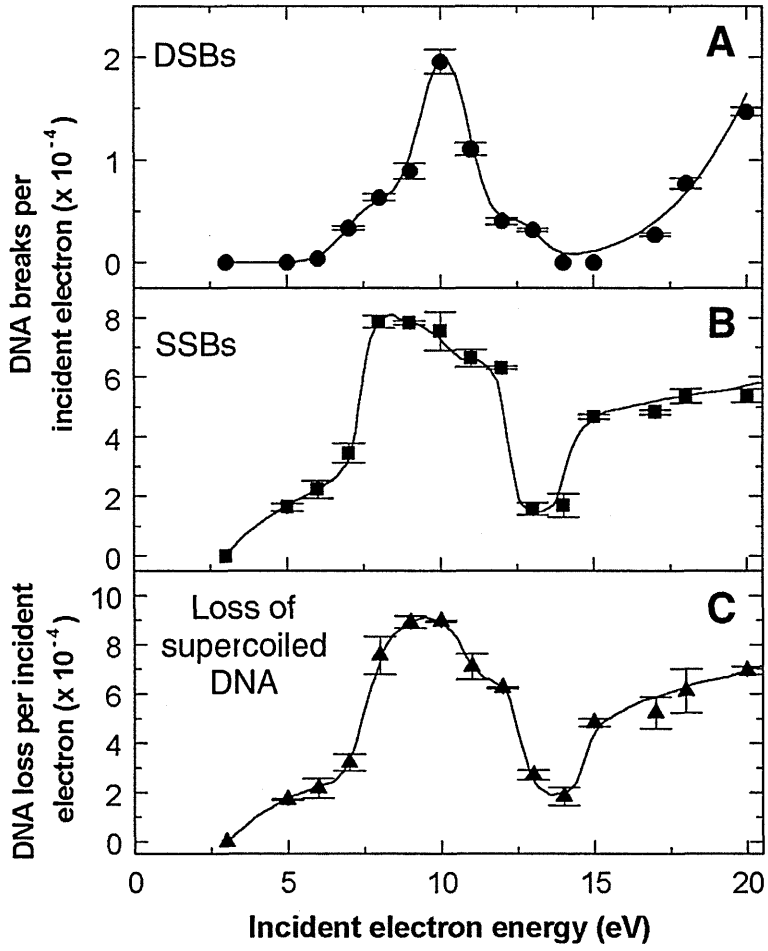

Figure 1.3: Experimental observation of electron induced single and double strand breaks of DNA. Taken from [8]. For SSB yields below 5 eV see [9].

anion state) for a short period of time ($\approx 10^{-15}$ s to 10^{-10} s) and deposits a fraction of its energy in the macromolecule. This process is then followed by a bond dissociation, which ultimately leads to the strand break. The formation of the temporary anion state is caused by the electron attaching to one of the *constituent* molecules of DNA (i.e., nucleobases, deoxyribose or the phosphate group). It is these temporary anion states of the constituents that serve as the "doorway" for the electron-induced DNA damage. Therefore, understanding the formation and types of transient negative ions (also called electron resonances) associated with the constituent molecules of DNA is crucial for understanding the mechanisms behind electron induced SSBs and DSBs.

The research presented in this thesis is set in the broader context of studies of radiation damage to DNA, but focuses on one aspect of the process: the formation of resonances that can lead to the damage of DNA by low-energy electrons. Specifically, the aim of this thesis is to perform calculations, using the R-matrix method [13], of collisions of low-energy electrons ($E \leq 15$ eV) with model molecules of the pyrimidinic DNA bases. The detailed objectives of

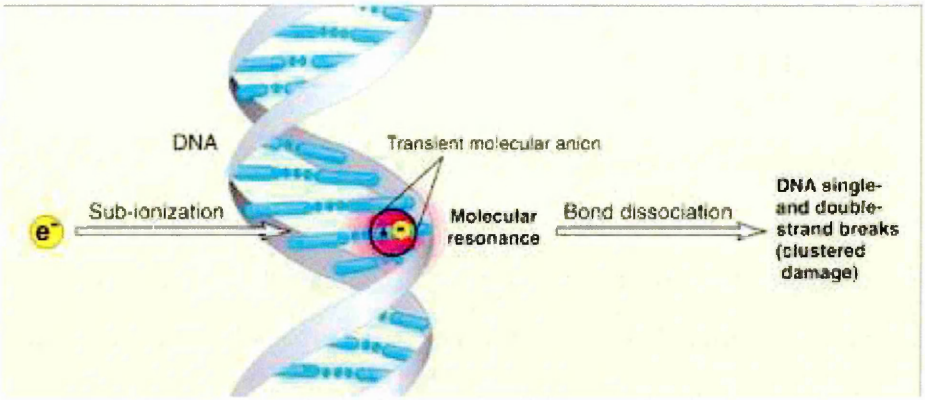

Figure 1.4: Illustration of the mechanism behind the direct electron induced damage of DNA. The image was taken from [12].

this work and the methods used are described in Section 1.4.

Before we proceed with the discussion of the available results on electron resonances in DNA subunits, a phenomenological introduction to the subject of electron-molecule collisions is appropriate.

1.1 Processes induced by low-energy electrons

A low-energy electron, as defined in this work, is defined as one possessing kinetic energy below the ionization threshold of the target molecule, which is typically around 10 eV for the molecules studied here. In this regime a large number of processes involving the target molecule AB can occur [14]:

- Elastic scattering

  $AB + e^- \longrightarrow AB + e^-,$

- Rotational excitation

  $AB(j) + e^- \longrightarrow AB(j') + e^-,$

- Vibrational excitation

  $AB(v) + e^- \longrightarrow AB(v') + e^-,$

- Electronic excitation

  $AB(i) + e^- \longrightarrow AB(i') + e^-,$

- Electron impact dissociation

  $AB + e^- \longrightarrow A + B + e^-,$

- Dissociative electron attachment (DEA)

  $AB + e^- \longrightarrow A + B^-$ (or $A^- + B$).

Elastic scattering does not change the internal state of the target nor the energy of the incoming electron. Electron impact excitation is an inelastic process which causes change in the internal rotational, vibrational and/or electronic state of the target molecule. In electron impact electronic or vibrational excitation the molecule can be left in a dissociative state leading to its fragmentation. During DEA the incoming electron is trapped in a resonant state, cleaves one of the molecular bonds remaining attached to one of the fragments, producing at least one neutral and a negatively charged fragment.

We distinguish between two basic types of collisions: direct and resonant. Direct collisions typically last around 10^{-15} s and their cross sections vary smoothly with energy. In the case of resonant collisions the scattering electron is temporarily trapped in a metastable state. The wavefunction of this state has a large amplitude in the region of space close to the molecule when compared with its amplitude at infinity. This leads to a significant increase in the collision time (by several orders of magnitude) compared with the direct collision. The formation of a metastable state (resonance) occurs only for a particular electron energy. Therefore a resonance is characterized by its energy E and width Γ. The width of the resonance is simply related to its half-life τ:

$$\Gamma \approx \frac{\hbar}{\tau}. \tag{1.1}$$

In principle, an atom or a molecule can possess many different electron resonances. The resonant state can decay via autodetachment (and enhance cross sections for various processes) or lead to molecular break up with the electron remaining attached to one of its fragments (DEA). Therefore the most important property of resonances is that cross sections for all the processes listed above can be significantly affected (enhanced or suppressed). Electronic resonances can be classified [15, 16], depending on whether the target molecule's state changes during their formation:

- Shape resonances

  The incoming electron is temporarily trapped in a potential resulting from a combination of the short-range attractive forces of the target and long-range repulsive forces caused by the angular-momentum barrier of the incoming electron. In practice these resonances are seen as trapping of the incoming electron in one of the unoccupied

orbitals of the target molecule, i.e. they are 1 particle 0 hole states.

- Core-excited resonances

  The resonance is formed by exciting the target molecule to an electronically excited state (called the *parent state*), followed by trapping of the electron into one of the empty spin-orbitals. We distinguish between Type I Core-excited (called *Feshbach*) resonances which lie energetically below the parent (excited) state and Type II Core-excited (also called *Core-excited shape*) resonances, which lie above the trapping parent state. Feshbach resonances have lifetimes much larger than shape or core-excited shape resonances and, consequently, very narrow widths. The configurations of the core-excited resonances are mostly built on single excitations of the target molecule, i.e. they are 2 particle 1 hole states.

- Vibrational Feshbach resonances

  These resonances are mediated by the long-range dipole electron-molecule interaction with the electron trapped in a diffuse (dipole-bound) state. This state is typically weakly bound, i.e. it lies slightly below the ground state of the target. The extra electron attached in a dipole-bound state can excite the nearby vibrational levels of the parent molecule resulting in Vibrational Feshbach resonance. Consequently, these resonances are found just below the thresholds for vibrational excitation for the molecule in its ground state. No centrifugal barrier is needed to support these resonances, i.e. they may form for s-wave electrons.

1.2 Computational methods

While experiments provide us with valuable insights into the resonant processes occurring in electron collisions with biological molecules, it is necessary to complement our understanding of these processes with theoretical calculations, which can ultimately confirm the current interpretation of the experimental findings and/or stimulate further research. In this section we describe, briefly, the main computational methods which have been used for the study of electron-molecule collisions.

At energies above $\approx$ 10 keV the de Broglie wavelength of the scattering electron is much smaller than the internuclear distance and the vibrational and rotational motion of the nuclei is slow compared with the velocity of the incoming electron. Therefore the molecule can be represented as a collection of fixed independent scattering centers [17]. It follows that

the scattering amplitude can be expressed as a coherent sum of amplitudes for scattering from the individual atoms.* As the energy of the scattering electron decreases its de Broglie wavelength becomes larger leading to break down of the independent atom picture of the electron-molecule collision. For electron energies of the order of a few tens of eV the collision process becomes sensitive to details of the molecular structure. Electron resonances may form and effects associated with couplings of various channels (elastic scattering, electronic excitation and ionization) and electron exchange also play an important role. Finally, for even lower electron energies (below the ionization potential of the molecule) complicated effects of target polarization and electron correlation dominate the scattering. Therefore at sub-ionization energies accurate calculations of the electron-molecule collision are most difficult and many-electron *ab-initio* methods are best suited for this task.

Ideally, for very low electron energies or for energies close to a resonance, calculations should take into account the coupling of electrons to the nuclear motion of the target [19]. However, this imposes large demands on the computational resources and therefore all scattering calculations on molecules relevant for this work reported in the literature and in this work itself have been carried out in the so-called *fixed-nuclei* approximation. In this approximation the nuclei of the molecules are not coupled to the electron motion (i.e. their positions are fixed during the scattering calculation). Therefore these calculations focus only on an accurate description of the electron dynamics.

Ab-initio methods can be divided into two basic categories:

- calculations based on purely quantum-chemistry methods like the Density functional methods, e.g: [20, 21],
- scattering calculations.

While purely quantum chemical calculations certainly have value, particularly for very large moities (nucleotides, etc.), when the effects of solvation are taken into account, or for detailed surveys of potential surfaces in the presence of many nuclear degrees of freedom, they suffer from the fundamental problem of using, in principle incorrect, bound-state instead of scattering boundary conditions. Consequently, these methods are not capable of producing scattering cross sections and resonance widths which can be compared with experimental results and are therefore very limited in their use and applicability. These facts make it necessary for accurate scattering calculations to be performed, in order to critically assess the

*For energies down to $\approx$ 100 eV the scattering electron can be described as a plane wave and the Born approximation can be used to calculate the amplitudes for scattering from the individual atoms [18].

predictions based on simplified models and to provide information on scattering phenomena which cannot be described by the quantum chemistry methods.

Several many-electron *ab-initio* methods have been developed for calculations of low-energy electron-molecule collisions:

- The R-matrix method [13, 14],
- The Schwinger Multichannel (SMC) method [22, 23],
- The Kohn variational method [24].

Apart from these high-level methods, approaches based on the use of local effective potentials for the approximation of the exchange and correlation/polarization effects exist. These are:

- The symmetry-adapted single-centre expansion (SA-SCE) approach [25],
- The R-matrix finite element method with effective potentials (FERM3D) [26].

Modelling of the electron-molecule interaction is significantly more difficult than calculations of the electronic structure of the isolated molecule. In addition to the problem of the accurate representation of the target molecule's electrons, electron-molecule studies have to address the following issues:

- The wavefunction of the scattering electron extends over *all space* and has to be described accurately, at a similar level of quality to the wavefunction describing the bound electrons of the target, when this electron is close to the molecule.
- Modelling the interaction between the incoming electron and electrons of the target has to take into account additional effects which are not relevant for bound-state calculations of the electronic structure of the isolated molecule. These effects include: polarization of the target molecule by the incoming electron, long-range electron-molecule interaction (Coulomb or dipole) and most importantly the possible formation of metastable states (electron resonances).

Achieving satisfactory results in the description of both bound and continuum electrons and their interactions at all energies of interest imposes large demands on computational resources and the performance of the computer codes compared with quantum chemistry calculations of bound-state solutions of the Schrödinger equation. This is particularly true for electron-rich targets, such as the nucleobases and their analogues.

1.3 Electron resonances in DNA constituents

Various experimental and theoretical techniques have been used to determine the parameters and types of electron resonances in DNA subunits and their analogues, see e.g.: [3, 5, 10, 11, 17, 20, 27, 28, 29]. In this section we briefly summarize the current state of knowledge about these resonances. We will focus mainly on the information available for the nucleobases and their close analogues since in this thesis we are interested in the formation of resonances in collisions with them.

The first measurements of electron attachment energies to the nucleobases in the gas-phase were performed by Aflatooni et al. [30] in 1998 using electron transmission spectroscopy (ETS). Later Scheer et al. [31] used the same method to determine more accurate DEA spectra of uracil (and halouracils). This research led to the assignment of three resonances of π^* symmetry lying below 5 eV in all nucleobases. These resonances are associated with the aromatic character of these molecules as can be seen from the pioneering research of Nenner and Schulz [32] from 1975 on ETS of azabenzene molecules. Nenner and Schulz studied electron collisions with molecules which are obtained from benzene by replacing one to three carbons in the ring with nitrogen atoms. Three electron resonances of π^* symmetry were observed in benzene and in all diazines[†] (pyrazine, pyrimidine and pyridazine). These three molecules are of particular importance for this thesis since, as we will see later, they can be thought of as model molecules for the pyrimidinic nucleobases. The two lowest-lying resonances were interpreted as shape resonances. The third resonance was suggested to have a mixed core-excited shape character, which was later confirmed by the calculations of Winstead and McKoy [33, 34] on electron collisions with pyrazine and pyrimidine using the Schwinger Multichannel method [22]. The π^* orbitals responsible for these resonances can be ultimately linked to the aromatic π^* orbitals of benzene. Recently, Modelli et al [35] performed ETS on pyrimidine and halopyrimidines, providing further information on the π^* resonances and also on higher-lying ($\gtrsim 4.5$ eV) core-excited resonances in pyrimidinic molecules.

It has been observed [36] that the loss of a neutral H atom is the dominant fragmentation channel in all nucleobases at very low energies (below 3 eV). A detailed investigation [37] of this process in thymine and its deuterated forms led to discovery of a remarkable bond and site selectivity in the DEA process leading to the hydrogen loss. Two peaks in the DEA spectrum of thymine were found: the first one around 1 eV and a second (broad) one around 1.8 eV. It has been found that the hydrogen loss corresponding to the higher-lying peak

[†]Diazines are molecules derived from benzene by replacing two carbon atoms with nitrogens.

occurs selectively from the nitrogen located between the two oxygen atoms (see Figure 1.2) and that the lower-lying peak in the DEA spectra corresponds to the loss of hydrogen from the other nitrogen atom.

A possible explanation of the process corresponding to the lower-lying structure in the DEA of thymine and uracil is based on the formation of a Vibrational Feshbach Resonance (VFR) [38, 16]. These resonances are in fact excited vibrational levels of the dipole bound anion state, which then decay to various channels including dissociation of the molecule. According to this theory [39, 40] the electron attaches to a dipole-bound state of the thymine molecule and couples to a low-lying σ^* resonance, which is strongly repulsive along the hydrogen stretch coordinate. This coupling drives the vibrational motion of the H atom, which eventually leads to its tunneling (i.e. dissociation) through the barrier of the dipole-bound state.

The appearance of the second peak (around 1.8 eV) in the thymine DEA spectrum has been explained [39] as arising from vibronic coupling of the second π^* resonance with a repulsive σ^* valence anion state: the electron attaches to the π^* resonance, which evolves by inducing an out of plane vibrational motion of the hydrogen atom attached to the ring of the molecule. It turns out that this motion then allows transfer of the resonant electron to a σ^* orbital which has a repulsive character and triggers loss of this hydrogen atom. This mechanism has also been found to occur in chlorobenzene [41] and also in nonplanar chlorocarbons [42].

The significance of the observed hydrogen loss in thymine and other nucleobases [43] in the context of DNA strand breaks becomes clear if we have a closer look at Figure 1.1. The loss of hydrogen (at energies below 3 eV) from the isolated bases occurs precisely at the positions where the base attaches to the other complementary base and to the deoxyribose ring, suggesting that these bonds might be broken following electron attachment to the nucleobase. Indeed, condensed-phase experiments on thymidine (thymine+sugar+phosphate) [44, 45, 46] showed that low-energy electrons break the C-N base-sugar bonds as well as the C-O phosphate-sugar bonds. A mechanism of the C-O sugar-phosphate bond breaking involving the nucleobases has been proposed [20, 21]. It starts by initial attachment of the electron to the lowest-lying π^* resonant state of the base, followed by a transfer of the electron to a dissociative σ^* state located in the vicinity of the C-O sugar-phosphate bond which then dissociates. However, this mechanism has been explored so far only using bound state quantum chemistry methods incorporating solvation effects, but still lacks the proper scattering boundary conditions.

At higher energies (> 4 eV) a similar selectivity in the hydrogen loss has been observed in the DEA spectra of thymine and its deuterated analogue [43]. In this case however, the mechanisms behind the hydrogen loss are still not clearly understood. The DEA spectra suggest the presence of several overlapping resonances. Electrons with these higher energies are also capable of breaking the strong aromatic bonds, yielding a large number of different fragments, as was shown, for example, by the study of electron attachment to uracil [47].

The processes leading to fragmentation of the isolated sugar moieties (deoxyribose and ribose) appear to be more complicated than in the case of the nucleobases. The studies [48, 49] on isolated deoxyribose and ribose showed that a large number of different fragments already form at electron energies close to the threshold ($\approx$ 0 eV). Unlike the nucleobases, dehydrogenation is not the predominant reaction channel for these molecules. Instead, the DEA process results in formation of one or two water molecules and formaldehyde (CH_2O) [3]. A second structure in the DEA spectra of these molecules appears in the range of 6 eV to 9 eV. The proposed explanations of the low-energy DEA spectra are based on the presence of low-lying σ^* shape resonances and also on the fragmentation mechanism involving VFRs as in the case of the nucleobases. At higher energies core-excited resonances and possible higher-lying shape resonances are expected to facilitate the DEA process [3].

The role of the phosphate group in electron driven DNA damage is not yet clearly understood. This is partly caused by the fact that experimental studies are forced to use various analogues: the phosphate group is not straightforward to study as an isolated compound since phosphoric acid (H_3PO_4) is not easy to transfer to gas-phase. However, a study on dibutylphosphate and triethylphosphate [50], which were used as models for the phosphate group, showed that the C-O sugar-phosphate bond as well as the intra-phosphate P-O bond can be broken by low energy electrons through resonant processes occurring in the energy ranges $2-4$ eV and $7-10$ eV. Both of these processes would lead to single strand breaks in DNA/RNA.

1.3.1 Theoretical results

The purpose of this section is to summarize the results of calculations performed for the molecules relevant for this work. These molecules have a large number of nuclear degrees of freedom[‡], which so far has been one of the reasons preventing the construction of theoretical models that can be used to calculate cross sections for the DEA processes. Models of DEA can in principle be constructed (see e.g. [51]) from fixed-nuclei scattering calculations spanning all

[‡]A non-linear molecule has $3N-6$ vibrational modes, where N is the number of nuclei.

vibrational modes of the molecule. We can see that even though the fixed-nuclei calculations are not capable of describing the DEA process directly, they can be used, in principle, to generate input data for modelling the DEA. The only calculations of DEA cross sections for nucleobases bases are those of Gallup and Fabrikant [52] for uracil (loss of the neutral hydrogen from the aromatic ring), which were based on single (N-H) bond stretch ab-initio scattering calculations and provide results in qualitative agreement with the experimentally observed data.

Other scattering calculations have focused on identifying and characterizing the electron resonances in the subunits of DNA and in uracil. It is these calculations that are the most important for this work and we discuss them below.

Uracil is the nucleobase with the smallest number of electrons and therefore the most studied target in scattering calculations from pyrimidinic bases [53, 54, 55, 56, 57, 58, 59]. Theoretical calculations of electron collisions with uracil by Gianturco et al. [53, 54] using the SA-SCE method and by Winstead and McKoy [56] using the SMC method suggest the presence of at least one higher-lying broad σ^* shape resonance located at energies above 8 eV Consequently it has been proposed [54] that the observed products [47] of the electron-uracil collision can be explained by an interaction between the higher-lying (above 8 eV) dissociative σ^* resonance and lower-lying π^* resonances.

The only inelastic and fully *ab initio* calculations of electron collisions with uracil are those of Winstead and McKoy [56] using the Schwinger Multichannel Method (SMC) and Dora et al. [59] using the R-matrix method. The calculations of Winstead and McKoy found evidence for Feshbach resonances in the electron-uracil system, but did not characterize them, while the subsequent study of Dora et al. report three Feshbach resonances at energies 6.17 eV, 7.62 eV and 8.12 eV.

In addition to the poor characterization of the possible higher-lying resonances in pyrimidinic DNA bases, previous studies have struggled to produce parameters of, especially, the third (highest-lying) π^* resonance in satisfactory agreement with experimental values (see [27] for a summary of experimental and theoretical results). For this reason Winstead and McKoy investigated elastic electron collisions with a model molecule, pyrazine [33, 60]. The high symmetry of this molecule makes the calculations less computationally demanding and has the further advantage of allowing the study of the third π^* resonance in isolation, because it belongs to a different irreducible representation than the other two. By including in the calculation scattering configurations based on triplet excited states of the molecule a significant shift in the calculated position of this resonance towards its experimentally observed position

was achieved. This observation proved (as mentioned already in Section 1.3) the hypothesis of Nenner and Schulz [32], that the third π^* resonance has a partially core-excited character involving the lowest-lying triplet excited states of the molecule.

Electron collisions with the pyrimidinic and purinic DNA bases were studied theoretically first by Winstead and McKoy [61, 17] (SMC) and recently by Dora et al. [62, 63, 29] (R-matrix method) and Wang et al. [64] (SA-SCE). As mentioned above, these studies have confirmed the presence in these molecules of the three low-lying π^* resonances. Additionally, the study of Wang et al. [64] predicts higher-lying σ^* resonances in all DNA bases. Dora et al. report an additional (fourth) π^* resonance in all DNA bases, several higher-lying Feshbach resonances in guanine and adenine and evidence for the presence of a higher-lying σ^* shape resonance in thymine.

Theoretical studies of low-energy electron collisions with the sugar-phosphate backbone have focused mainly on model molecules such as tetrahydrofuran (THF) and phosphoric acid (H_3PO_4), but high-level computational studies of the ribose and deoxyribose rings and their analogues also exist [65, 66, 67]. THF, the simplest model of ribose and deoxyribose ring, was studied mainly at the level of elastic scattering [65, 68, 69]. These studies found indications of the presence of a higher-lying broad shape resonance. Inelastic collisions with THF were studied only by the R-matrix method [70] which did not report any shape resonances[§], but found several higher-lying core-excited resonances. Similarly, the only inelastic study on phosphoric acid uses the R-matrix method and reports higher-lying broad shape resonances and additionally several Feshbach resonances between 7 eV and 8 eV. The powerful time-delay analysis clearly unravelled the presence of 6 overlapping resonances of shape character in ribose and deoxyribose in the $4 - 18$ eV energy region [66].

Finally, Winstead and McKoy studied electron collisions with the nucleosides and nucleotides of DNA [61, 71, 17], albeit excluding the polarization effects. These results showed that there is a close correspondence between the π^* resonances of the nucleosides and nucleotides and that of the bases.

1.4 Objectives of the present research

In this work we focus on extending the current understanding of the formation of resonances in the *pyrimidinic* nucleobases. We pay particular attention to the higher-lying resonances which are much less understood than the lower-lying ones. The most interesting questions regarding

[§]Although shape resonances were later found in simplified calculations.

electron collisions with these molecules are related to resonances: their type, mechanisms of formation and how they manifest themselves in the cross sections. We have seen in the previous section that the nucleobases have been studied already using high-level ab-initio scattering methods. However, most of these questions still remain unanswered. Trying to answer them by performing and analyzing scattering calculations for the nucleobases only is difficult due to the computational requirements. Furthermore, nucleobases are relatively large molecules and therefore we can naturally ask whether it is possible to link some of the resonances formed in these molecules to resonances forming in their precursors.

Indeed, we know for certain that the nucleobases possess at least some resonances (the three π^* shape ones) that can be clearly correlated to equivalent resonances in the diazines and benzene. We hope to achieve a much deeper understanding of the resonances in the nucleobases by correlating them, where possible, with resonances forming in simpler molecules. In particular, we hope to be able to elucidate the role played by some substituents attached to the pyrimidine ring. Studying molecules with fewer electrons and/or higher symmetry has obvious computational advantages: it allows for the construction of better scattering models that may produce more accurate scattering data. It is for these reasons that *we study in this work electron collisions with molecules that can be thought of as models for the pyrimidinic nucleobases.* These are the diazine molecules (pyrazine, pyrimidine and pyridazine), 2-oxo pyrimidine, 4-oxo pyrimidine and uracil, see Figure 1.5.

In order to carry out our calculations we use the R-matrix method for electron-molecule collisions [14] as implemented in the UKRmol suite of codes [72]. The specific objectives of this research can be summarized as follows:

- Perform elastic and inelastic scattering calculations on the diazine molecules pyrazine, pyrimidine and pyridazine.
- Identify the best scattering models for representation of the low-lying π^* shape resonances.
- Establish trends in the scattering data of the three diazine targets, linking it to changes in their dipole moment.
- Analyze in detail the scattering data at higher energies, look for the presence of higher-lying resonances and characterize them.
- Perform scattering calculations on substituted pyrimidine (oxo-pyrimidines) and finally for uracil using a unified approach that will allows us to compare consistently the results

for all the molecules studied.

- Compare the data on electron resonances in all these targets and establish links between them and (where possible) with experimental results.
- Compare the obtained cross sections with experimental results, where available.

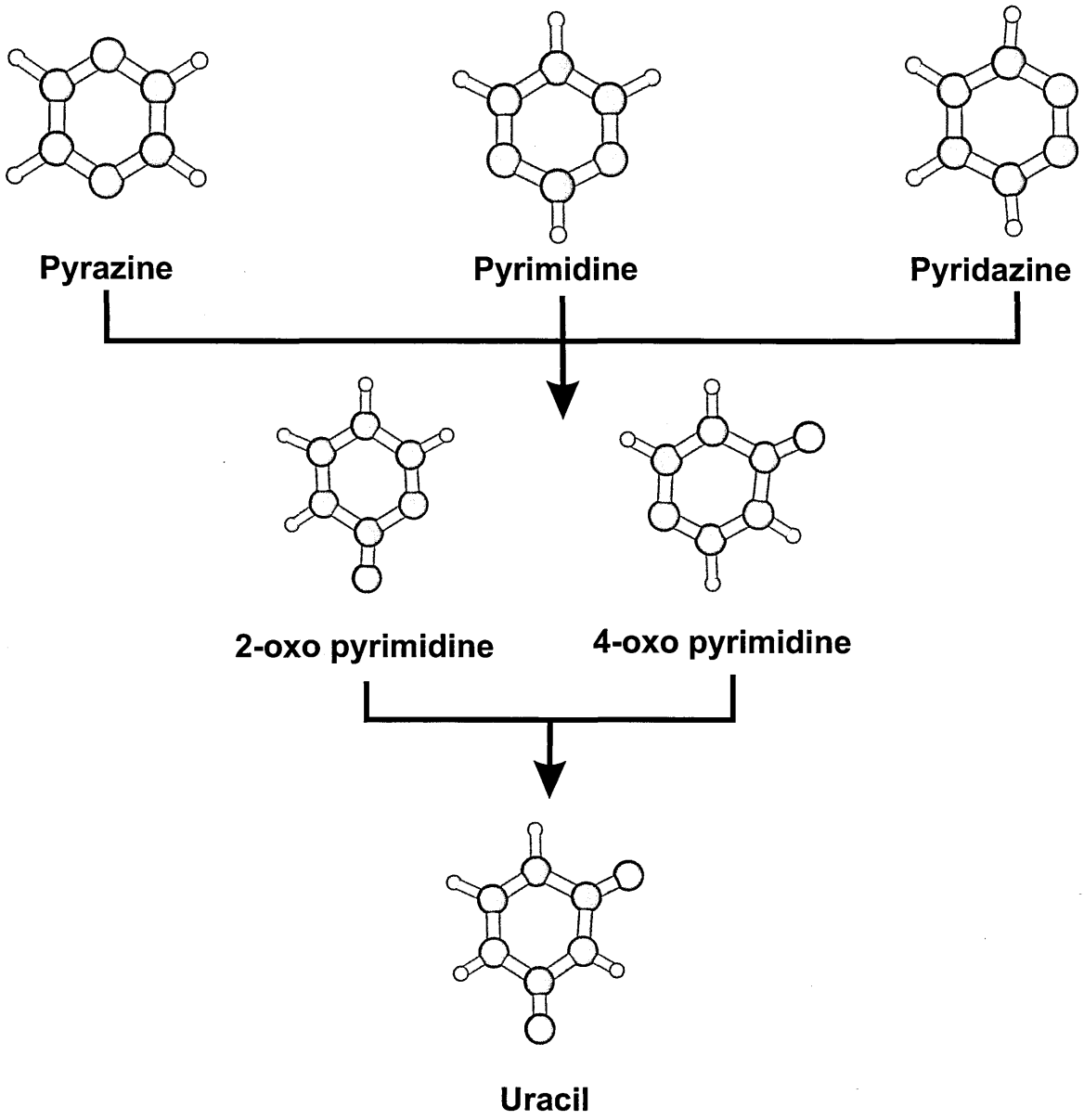

Figure 1.5: Molecules studied in this work: diazines (pyrazine, pyrimidine and pyridazine), 2-oxo pyrimidine, 4-oxo pyrimidine and uracil. The white balls represent hydrogens, orange - carbons, blue - nitrogens and red - oxygens.

1.5 Layout of the thesis

As mentioned above, the scattering calculations in this work were performed using the R-matrix method. Chapter 2 is mainly dedicated to presentation of this powerful theoretical

approach. We also describe the computational tool - the UKRmol suite of codes which were used to carry out all the calculations. In Chapter 3 we present our results on electron collisions with pyrazine, the first molecule studied in this work. The target and scattering models used for the calculations are thoroughly tested and a methodology to be used for the subsequent calculations is developed. In Chapter 4 we complete our studies of electron collisions with diazines by performing calculations on pyrimidine and pyridazine. We present a detailed comparison and analysis of the results obtained for the three molecules. Finally, in Chapter 5 we present our calculations on the oxo-pyrimidines and uracil. In this last chapter we compare all our results (and those available in the literature) on electron resonances in the diazines, the oxo-pyrimidines and uracil and draw general conclusions on the formation of resonances in these molecules. We also discuss how our results help to understand resonance formation in the nucleobases. Our findings and suggestions for future work are summarized in the Conclusions (Chapter 6).

Chapter 2

Theoretical methods

This chapter is devoted to the theoretical methods used in this work. We begin with a general definition of the collision problem to be investigated. The most important theoretical method used in this work is the R-matrix method, whereby we obtain the cross sections and other quantities relevant for analysis of the electron-molecule collision problem. Its description therefore constitutes the main part of this chapter. The fundamental quantity of scattering physics - the **S**-matrix - can be analyzed using different methods in order to obtain insights into processes occurring during the electron-molecule collision. One of these methods - the time-delay analysis - proved very useful for the analysis of the resonances found in this work. The main principles of this approach are presented in Section 2.4. Section 2.5 is dedicated to a short presentation of the standard Hartree-Fock and CASSCF quantum chemistry methods, which are used in our work to obtain the molecular orbitals for subsequent use in the scattering calculations. Finally, in Section 2.7, we describe the UKRmol suite of codes, an implementation of the R-matrix method for electron and positron-molecule collisions, employed to perform all scattering calculations presented in this work.

2.1 General problem

Collisions of low-energy electrons with a molecule can result in various outcomes, which were listed in Section 1.1. In this work we study only the processes involving the electronic degrees of freedom of the (neutral) target molecule (i.e. elastic and electronically inelastic electron scattering) and apply in our calculations the *fixed-nuclei approximation*, in which the molecule's nuclei remain in a fixed configuration during the scattering process.

Therefore the processes studied in this work can be formally represented by the reaction

$$e^- + M_\alpha \rightarrow e^- + M_\beta, \tag{2.1}$$

where M denotes a neutral polyatomic molecule with N electrons, which will be called the *target*. The indices α and β stand for different *electronic* states of the target. For $\alpha = \beta = 1$ we obtain elastic scattering. We can now turn to a formal description of the collision within the framework of quantum scattering theory.

The collision process (2.1) is described by the time-independent Schrödinger equation

$$H_{N+1}\Psi_E^\Gamma(\mathbf{x}_1, \mathbf{x}_2, \ldots, \mathbf{x}_N, \mathbf{x}_{N+1}) = E\Psi_E^\Gamma(\mathbf{x}_1, \mathbf{x}_2, \ldots, \mathbf{x}_N, \mathbf{x}_{N+1}), \tag{2.2}$$

where $\mathbf{x}_i$ denote the three spatial and spin coordinates of i-th electron, Ψ_E^Γ is the total scattering wavefunction for the process, E is total energy of the system and H_{N+1} is the nonrelativistic Hamiltonian describing the electrons and their interactions. In atomic units the Hamiltonian H_{N+1} has the following form

$$H_{N+1} = H_N + H_{int}, \tag{2.3}$$

$$H_N = \sum_{i=1}^{N}\left(-\frac{\nabla_i^2}{2} - \sum_{k=1}^{Nuclei}\frac{Z_k}{\rho_{ki}}\right) + \sum_{i>j}^{N}\frac{1}{r_{ij}} + \sum_{k>l}^{Nuclei}\frac{Z_k Z_l}{R_{kl}}, \tag{2.4}$$

$$H_{int} = -\frac{\nabla_{N+1}^2}{2} - \sum_{k=1}^{Nuclei}\frac{Z_k}{\rho_{k(N+1)}} + \sum_{i=1}^{N}\frac{1}{r_{i(N+1)}}, \tag{2.5}$$

where H_N is the Hamiltonian of the target molecule and H_{int} is the part of the full Hamiltonian describing the scattering electron and its interaction with the target. The charge on the nucleus k is denoted by Z_k and R_{kl} is the distance between the nuclei k and l. The distance between the electron j and the nucleus l is denoted by ρ_{lj} and r_{ij} is the distance between the electrons i and j. The meaning of the coordinates is illustrated in Figure 2.1. In agreement with our fixed-nuclei approximation we have omitted from the Hamiltonian H_N the nuclear kinetic energy terms.

For a general polyatomic molecule, the target Hamiltonian H_N does not commute with the total angular momentum of the molecule and therefore angular momentum eigenvalues cannot be used as good quantum numbers specifying the spatial part of the target wavefunction. However, the Hamiltonian H_N does commute with operators O_R corresponding to the symmetry operations R of the point-group of the molecule. Consequently, the target states can be classified according to their transformational properties given by the irreducible rep-

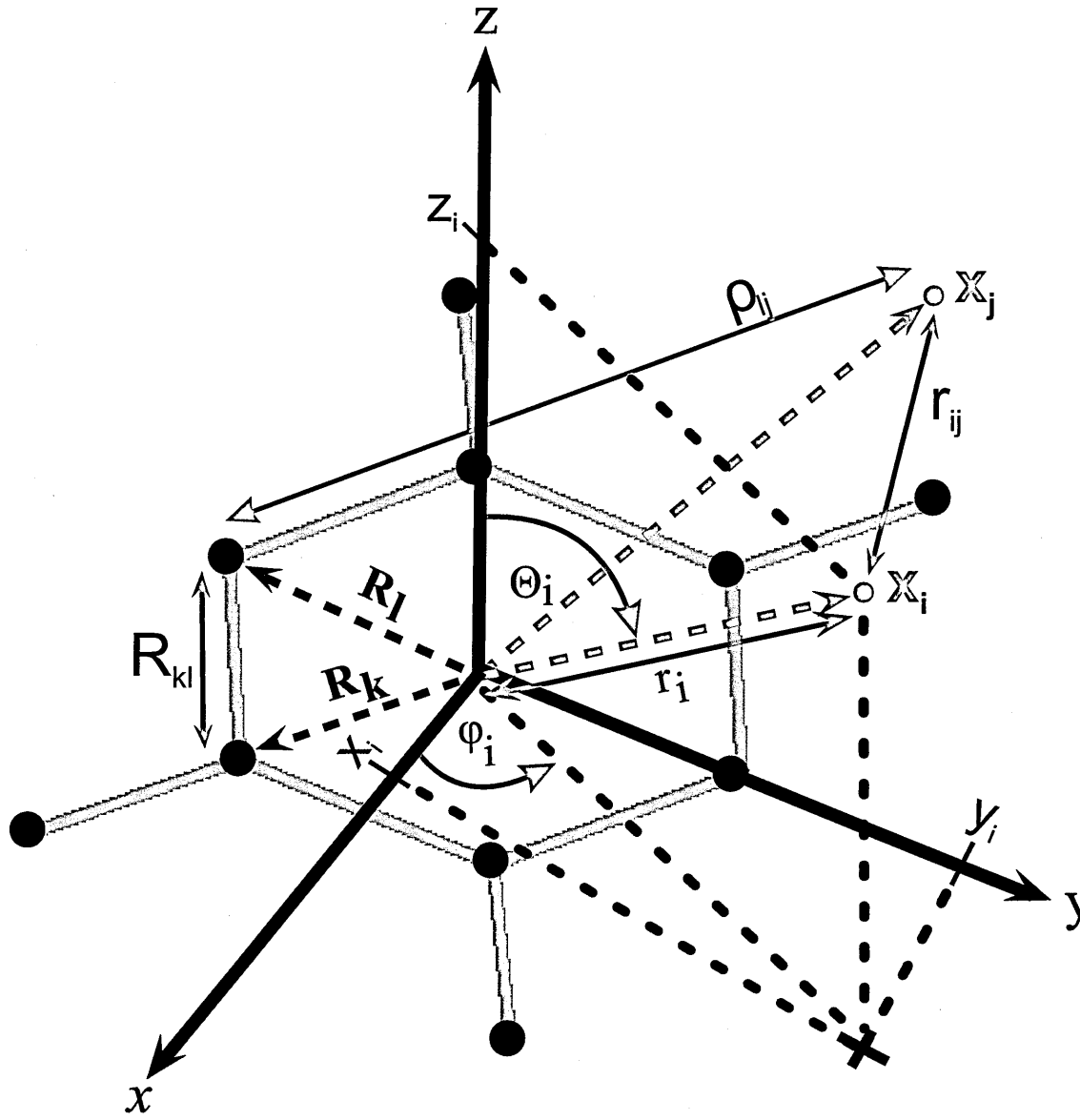

Figure 2.1: Coordinate system for the collision of an electron with a polyatomic molecule. The centre of the coordinate system coincides with the centre of mass (CMS) of the target molecule. The nuclei are represented by black balls, while electrons are red. The dark blue labels indicate the cartesian coordinates $[x_i, y_i, z_i]$ of electron i, while the equivalent spherical coordinates $[r_i, \theta_i, \varphi_i]$ are shown in green. With this choice the spherical coordinates are $[r_i \sin(\theta_i)\cos(\varphi_i), r_i \sin(\theta_i)\sin(\varphi_i), r_i \cos(\theta_i)]$. Also shown are the distance R_{kl} between the nuclei k and l, the distance r_{ij} between the electrons i and j and the distance ρ_{lj} between the nucleus l and the electron j.

resentations of the molecular point-group. The full Hamiltonian H_{N+1} also commutes with the operators corresponding to the symmetry operations of the molecular point-group. In the following we use the label Γ to identify different irreducible representations of the molecular point-group. Therefore the label Γ of the scattering wavefunction Ψ_E^Γ is used to denote that the wavefunction was chosen to be simultaneous eigenfunction of the full Hamiltonian H_{N+1} and the symmetry operators of the point-group of the molecule. The spin part of the wavefunction Ψ_E^Γ is given by the eigenvalue of the operator of the total spin of the system. The full

wavefunction, Ψ_E, describing the scattering process is then obtained as a sum $\Psi_E = \sum_\Gamma \Psi_E^\Gamma$ of the wavefunctions calculated separately for each irreducible representation of the molecular point-group.

The formal description of the scattering problem would not be complete without the specification of the boundary conditions for the scattering wavefunction. Before we address this problem, we need to define the *scattering channels*. When the scattering electron is far from the molecule and their interaction can be neglected, the good quantum numbers characterizing states of the incoming electron are: the orbital angular momentum l, its projection m on the z-axis and the spin s and its projection s_z on the z-axis. Together with a label identifying the electronic states of the target molecule, α_i, the set of numbers $\gamma^\Gamma_{i,l,m} = \{lmS\alpha_i\}$ corresponding to states (target + scattering electron) with appropriate total spin S and transforming according to the irreducible representation Γ define the scattering channels.

All observable information about the collision (2.1) can be extracted from the wavefunction $\Psi^{\gamma^\Gamma_{j,l',m'}}_{\gamma^\Gamma_{i,l,m}}(r)$ that describes the radial behaviour of the scattering electron. This wavefunction can be obtained, for example, using the R-matrix method. Exactly how this is done will be described in the following sections. Asymptotically, $\Psi^{\gamma^\Gamma_{j,l',m'}}_{\gamma^\Gamma_{i,l,m}}(r)$ can be written [73] as a combination of the outgoing (+) and incoming (−) spherical waves $\phi^+_{i,l}(r)$ and $\phi^-_{i,l}(r)$:

$$\Psi^{\gamma^\Gamma_{j,l',m'}}_{\gamma^\Gamma_{i,l,m}}(r) \underset{r\to\infty}{=} \delta_{i,j}\delta_{l,l'}\delta_{m,m'}\phi^-_{i,l}(r) - S^\Gamma_{i,l,m;j,l',m'}\phi^+_{j,l'}(r), \tag{2.6a}$$

$$\phi^+_{i,l}(r) = \sqrt{\frac{2}{\pi k_i}}\exp\left[+\imath(k_i r - l\pi/2)\right], \tag{2.6b}$$

$$\phi^-_{i,l}(r) = \sqrt{\frac{2}{\pi k_i}}\exp\left[-\imath(k_i r - l\pi/2)\right], \tag{2.6c}$$

where $\imath$ stands for the unit imaginary number. These equations are the sought boundary conditions for the Schrödinger equation (2.2) describing the electron-molecule collision. The boundary conditions for the target electrons are included via the terms $\delta_{i,i}$ specifying the target state of the molecule in the incoming channel. The target states are eigenfunctions of the Hamiltonian H_N and we denote their corresponding energies by E_i. The channel momenta $k_i = \sqrt{2(E - E_i)}$ are defined through the energy E_i of the channel target state and the quantities $S^\Gamma_{i,l,m;j,l',m'}$ are the elements of the energy-dependent **S**-matrix. The values of the **S**-matrix elements depend on the details of the collision process described by the Schrödinger equation (2.2) and contain all information about the collision. After the **S**-matrix has been

obtained it can be transformed to the **T**-matrix:

$$\mathbf{T}^{\Gamma} = \mathbf{S}^{\Gamma} - \mathbf{1}, \tag{2.7}$$

to calculate the *cross-sections* $\sigma_{i\to j}(E)$ for transition from state i to state j using the equation:

$$\sigma_{i\to j}(E) = \frac{\pi}{k_i^2} \sum_{\Gamma} \sum_{S} \sum_{l_i,l_j} \sum_{m_i,m_j} \frac{2S+1}{2(2s_i+1)} |T^{\Gamma}_{i,l_i,m_i;j,l_j,m_j}(E)|^2, \tag{2.8}$$

where S is the total spin of the system and s_i is the spin of the target state i.

In practice the quantity of fundamental interest is the **S**-matrix, which in the case of electron-molecule scattering can be obtained by a range of different methods (see Section 1.2).

2.2 The R-matrix approach: one channel potential scattering

The R-matrix method is a particular approach for solving the Schrödinger equation describing the scattering process. In this work we are interested in the scattering solutions of the Schrödinger equation (2.2) specified by the boundary conditions (2.6).

The essential idea of the R-matrix method lies in the partitioning of the configuration space into two parts: the inner region and the outer region. In the outer region the general solution of the differential equation (2.2) is either explicitly known, or can be obtained by methods which are computationally cheaper than in the inner region, where the problem must be treated in its full complexity. On the boundary between these two regions (on the surface of the so-called R-matrix sphere) the R-matrix is constructed and provides the boundary conditions necessary for the solution of the outer region problem once the inner region problem has been solved.

In order to illustrate the basic concepts of the R-matrix method, we first describe its application to the simplest scattering problem: the scattering of a structureless particle by a short-range spherically symmetric central field. The scattering process is described by the time-independent Schrödinger equation

$$H\Psi(r,\theta,\varphi) = E\Psi(r,\theta,\varphi) \quad , \tag{2.9}$$

$$H = -\frac{\nabla^2}{2} + V(r) \quad , \tag{2.10}$$

where $V(r)$ is a short-range potential, which vanishes for $r \geq r_0$:

$$V = 0, \; r \geq r_0, \tag{2.11}$$

$$V = V(r), \; r < r_0. \tag{2.12}$$

We can express the solution of (2.9) in terms of partial waves:

$$\Psi(r,\theta,\varphi) = \sum_{l,m} \Phi_{l,m}(r,\theta,\varphi), \tag{2.13}$$

$$\Phi_{l,m}(r,\theta,\varphi) = \frac{F_l(r)}{r} Y_{l,m}(\theta,\varphi), \tag{2.14}$$

and obtain the following equation for the reduced radial wavefunctions $F_l(r)$:

$$H_r F_l(r) = E F_l(r), \tag{2.15}$$

with

$$H_r = -\frac{1}{2}\frac{d^2}{dr^2} + V(r) + \frac{l(l+1)}{2r^2}. \tag{2.16}$$

This equation can be written in the standard form:

$$\left(-\frac{d^2}{dr^2} + 2V(r) + \frac{l(l+1)}{r^2} - k^2\right) F_l(r) = 0, \tag{2.17}$$

where $k^2 = 2E$. We impose the usual boundary condition [73] at $r = 0$: $F_l(0) = 0$. The solution in the region $r \leq r_0$ is usually obtained using numerical methods. In the region $r \geq r_0$ the solution of equation (2.17) is a linear combination of the Riccati-Bessel $\hat{j}_l(kr)$ and Riccati-Neumann $\hat{n}_l(kr)$ functions

$$F_l(r) \sim \hat{j}_l(kr) + K(E)\hat{n}_l(kr), \tag{2.18}$$

that are the regular ($\hat{j}_l(kr)$) and irregular ($\hat{n}_l(kr)$) solutions of the free radial equation [18]. The energy-dependent constant $K(E)$ can be determined by imposing continuity of the logarithmic derivatives of the solutions at $r = r_0$:

$$\left.\frac{dF_l(r)/dr}{F_l(r)}\right|_{r=r_0} = \left.\frac{d(\hat{j}_l(kr) + K(E)\hat{n}_l(kr))/dr}{\hat{j}_l(kr) + K(E)\hat{n}_l(kr)}\right|_{r=r_0} \tag{2.19}$$

Given the solution $F_l(r)$ for $r \leq r_0$, solving equation (2.19) for $K(E)$ completes the determination of the solution of the equation (2.17) for all r. Asymptotically, the Riccati-Bessel and Riccati-Neumann functions reduce to simple trigonometric functions and equation (2.18) takes the form:

$$F_l(r) \underset{r\to\infty}{\sim} \sin(kr - l\pi/2) + K(E)\cos(kr - l\pi/2) = \sin(kr - l\pi/2) + \\ + \frac{\sin\delta_l(E)}{\cos\delta_l(E)}\cos(kr - l\pi/2) \propto \sin(kr - l\pi/2 + \delta_l(E)). \tag{2.20}$$

We can see that the constant $K(E) = \tan\delta_l(E)$ is directly related to the *phaseshift* $\delta_l(E)$. Asymptotically, the free wave $\hat{j}_l(kr)$ of the incoming electron has the form $\sin(kr - l\pi/2)$ and therefore the phaseshift $\delta_l(E)$ contains the information on the effect of the potential $V(r)$ on the incoming electron. Once $K(E)$ is known, the relevant observables, e.g. partial wave cross sections, can be determined.

In order to obtain the expression (2.19) that allows us to determine $K(E)$ we have taken advantage of the fact that the general solution of equation (2.17) for $r \geq r_0$ is explicitly known. We are now going to solve the scattering problem using the R-matrix method and set the R-matrix radius a conveniently to $a = r_0$, the radius where the short-range potential vanishes. With this choice of the R-matrix radius the inner region corresponds to $r \in \langle 0; a\rangle$ and $r \geq a$ is the outer region. Clearly, the two regions overlap at $r = a$.

In order to determine $K(E)$ we have to solve the inner region problem (i.e. find $F_l(r)$ for $r \leq a$), for which an analytical solution generally does not exist. In the R-matrix method the function $F_l(r)$ for $r \leq a$ is written in terms of an energy-independent basis $\{u_i(r)\}_{i=1}^{\infty}$ defined in the inner region:

$$F_l(r) = \sum_{i=1}^{\infty} A_i^E u_i(r), \; r \in \langle 0; a\rangle. \tag{2.21}$$

The problem of finding $F_l(r)$ for each energy then reduces to that of determining the coefficients A_i^E, which contain the energy dependence of the function $F_l(r)$. However, as we will see below, the R-matrix method allows computation of the desired phaseshifts for each energy even without the need to calculate explicitly the coefficients A_i^E. In practical applications the basis set expansion (2.21) is finite and contains n functions $u_i(r)$ sufficient for an accurate description of $F_l(r)$ over a range of scattering energies.

Since the R-matrix method uses a basis set expansion, we need to calculate the matrix elements of the Hamiltonian in this basis, an issue we focus on below.

Matrix elements of Hamiltonian

Consider first an arbitrary real-valued basis set $\{v_i(r)\}_{i=1}^{n}$ defined only in the inner region. The matrix elements H_{ij} of the Hamiltonian H_r defined in equation (2.16) are:

$$\begin{aligned} H_{ij} &= \int_0^a v_i(r)\left(-\frac{1}{2}\frac{d^2}{dr^2} + V(r) + \frac{l(l+1)}{2r^2}\right) v_j(r)dr = \\ &= -\left[\frac{v_i(r)}{2}\frac{dv_j(r)}{dr}\right]_0^a + \left[\frac{dv_i(r)}{dr}\frac{v_j(r)}{2}\right]_0^a + \int_0^a v_j(r)\left(-\frac{1}{2}\frac{d^2}{dr^2} + V(r) + \frac{l(l+1)}{2r^2}\right) v_i(r)dr = \\ &= \int_0^a v_j(r)\left(-\frac{1}{2}\frac{d^2}{dr^2} + V(r) + \frac{l(l+1)}{2r^2}\right) v_i(r)dr \underbrace{-\frac{v_i(a)}{2}\frac{dv_j(r)}{dr}\bigg|_a + \frac{dv_i(r)}{dr}\bigg|_a \frac{v_j(a)}{2}}_{\mathcal{S}} = \\ &= H_{ji} + \mathcal{S}. \end{aligned} \tag{2.22}$$

Integration by parts was carried out twice and the boundary condition $v_i(0) = 0$ was used in the last step. From this expression we see that the Hamiltonian H_r is nonhermitian in the basis set $\{v_i(r)\}_{i=1}^{N}$. The nonhermicity is caused by the surface term $\mathcal{S}$, arising from the matrix elements of the kinetic energy operator. In the R-matrix approach to scattering this problem can be circumvented by two different methods:

- Bloch operator method (see e.g. [14]),
- Boundary condition method (see e.g. [74]).

In the following we will concentrate only on the Bloch operator method, used in the formulation of the R-matrix method for electron-molecule collisions. We only note that the Boundary condition method solves the problem of nonhermicity of the Hamiltonian by imposing specific conditions at $r = a$ on the logarithmic derivatives of the basis functions $v_i(r)$.

The Bloch operator method

In order to remove the nonhermicity of the Hamiltonian matrix calculated in the basis set $\{v_i(r)\}_{i=1}^{N}$, we introduce an additional operator L defined by the following expression

$$L = \frac{1}{2}\delta(r-a)\frac{d}{dr}, \tag{2.23}$$

where $\delta(r-a)$ is the Delta function. With this operator, the Hamiltonian defined as

$$\tilde{H} = H + L \tag{2.24}$$

is now Hermitian. To see that this is so it is sufficient to calculate the matrix element L_{ij} of the L operator and add it to the matrix element H_{ij} of equation (2.22). Calculating L_{ij} is straightforward:

$$L_{ij} = \frac{1}{2}\int_0^a v_i(r)\delta(r-a)\frac{d}{dr}v_j(r)dr = \frac{v_i(a)}{2}\frac{dv_j(r)}{dr}\bigg|_a . \tag{2.25}$$

The matrix $\tilde{H}_{ij} = H_{ij} + L_{ij}$ is Hermitian, since the $-\frac{v_i(a)}{2}\frac{dv_j(r)}{dr}\big|_a$ term causing nonhermicity is now canceled by L_{ij}. The L operator is called the *Bloch operator* [75]. This approach suggests how to select appropriate basis functions $\{u_i(r)\}_{i=1}^n$ to be used in the inner region calculation. First we choose an arbitrary basis $\{v_i(r)\}_{i=1}^n$. Then we construct the matrix $\tilde{H}$. The functions $u_i(r)$ used in the expansion (2.21) are then taken as eigenvectors of the operator $\tilde{H}$:

$$\tilde{H}u_i(r) = E_i u_i(r). \tag{2.26}$$

In other words the basis functions $u_i(r)$, also called the R-matrix basis functions, have the form:

$$u_i(r) = \sum_{j=1}^{n} c_{ij} v_j(r), \tag{2.27}$$

with the c_{ij} coefficients obtained by diagonalization of the matrix corresponding to the Hamiltonian $\tilde{H}$. Since the operator $\tilde{H}$ is Hermitian in the inner region we know that its eigenfunctions $u_i(r)$ span an orthogonal basis on that space and that the eigenvalues E_i are real. This fact allows us to use the basis $\{u_i(r)\}_{i=1}^N$ as an appropriate basis in terms of which we can expand the sought after solution $F_l(r)$ of the Schrödinger equation. Finally, we note that addition of an arbitrary Hermitian operator to the Bloch operator does not change the hermicity of the resulting $\tilde{H}$. A frequent modification of the Bloch operator based on this property has the following form

$$L = \frac{1}{2}\delta(r-a)\frac{d}{dr} - \frac{1}{2}\delta(r-a)\frac{b}{a} = \frac{1}{2}\delta(r-a)\left(\frac{d}{dr} - \frac{b}{a}\right), \tag{2.28}$$

where b is an arbitrary constant. The second term in this equation is obviously Hermitian. From now on the Bloch operator we will use will have the form defined by equation (2.28).

R-matrix method using the Bloch operator

We are now ready to calculate the R-matrix which provides the boundary condition required for the solution of the outer region problem. Using the Bloch operator we can rewrite equation

(2.15) as

$$(H_r + L)F_l(r) = (E + L)F_l(r) \tag{2.29}$$

and formally invert it to obtain the implicit expression for $F_l(r)$ $(r \leq r_0)$:

$$F_l(r) = (H_r + L - E)^{-1} L F_l(r). \tag{2.30}$$

Now we can insert expansion (2.21) on the left hand side of this equation

$$\sum_{i=1}^{\infty} A_i^E u_i(r) = (H_r + L - E)^{-1} L F_l(r), \tag{2.31}$$

multiply the equation from left by the basis function $u_k(r)$ and integrate over the inner region, i.e. project the above equation on the basis function $u_k(r)$. Because of the orthogonality of the basis functions, we get the following expression for the expansion coefficients:

$$A_k^E = \int_0^a u_k(r)(H_r + L - E)^{-1} L F_l(r) dr. \tag{2.32}$$

Since the basis $\{u_j(r)\}_{j=1}^{\infty}$ is a complete set of orthonormal functions in the inner region and the functions $u_j(r)$ satisfy equation (2.26), we can further simplify the last equation by inserting the complete set of states between the operators $(H_r + L - E)^{-1}$ and L. This operation yields

$$A_k^E = \frac{1}{E_k - E} \int_0^a u_k(r) L F_l(r) dr = \frac{1}{2} \frac{1}{E_k - E} \int_0^a u_k(r) \delta(r - a) \left(\frac{d}{dr} - \frac{b}{a} \right) F_l(r) dr, \tag{2.33}$$

where we have used the explicit form of the Bloch operator. The integral on the right-hand side is the analogue of the integral (2.25). Therefore the final result for the expansion coefficients A_k^E is:

$$A_k^E = \frac{1}{2} \frac{u_k(a)}{E_k - E} \left(\frac{d}{dr} F_l(r) \Big|_a - \frac{b}{a} F_l(a) \right). \tag{2.34}$$

We can insert these coefficients back to expression (2.21) and evaluate the scattering wavefunction at $r = a$

$$F_l(a) = \frac{1}{2a} \sum_{i=1}^{\infty} \frac{u_i(a) u_i(a)}{E_i - E} \left(a \frac{d}{dr} F_l(r) \Big|_a - b F_l(a) \right). \tag{2.35}$$

If we define the **R-matrix** as

$$R(E) = \frac{1}{2a} \sum_{i=1}^{\infty} \frac{u_i(a)u_i(a)}{E_i - E}, \tag{2.36}$$

we can rewrite the equation (2.35) and arrive at the formula

$$F_l(a) = R(E) \left(a \frac{d}{dr} F_l(r) \Big|_a - bF_l(a) \right), \tag{2.37}$$

which is the most important equation of this section. It relates the radial scattering wavefunction and its derivative at $r = a$ to the quantity $R(E)$ which is obtained by solving the inner region problem. Because the general solution in the outer region is known - see eq. (2.18), we can match both solutions at $r = a$ using the equation (2.19) and obtain the coefficient $K(E)$:

$$K(E) = \frac{j_l(ka) - aR(E) \frac{dj_l(kr)}{dr}\big|_{r=a}}{aR(E) \frac{dn_l(kr)}{dr}\big|_{r=a} - n_l(ka)}, \tag{2.38}$$

where for simplicity we assumed the use of the Bloch operator with $b = 0$. In the multichannel case $R(E)$ as well as $K(E)$ become matrices, the latter known as the K-matrix.

Finally, we can present a summary for a practical one channel R-matrix calculation within the Bloch operator formulation:

- choose an arbitrary basis $\{v_i(r)\}_{i=1}^{n}$ in the inner region
- obtain the basis functions $u_i(r)$ by diagonalizing $\tilde{H}$: $(u_k|\tilde{H}|u_{k'}) = \delta_{kk'}E_k$
- calculate the R-matrix for each energy: $R(E) = \frac{1}{2a} \sum_{i=1}^{\infty} \frac{u_i(a)u_i(a)}{E_i - E}$
- calculate the "K-matrix" $K(E)$ for each energy and finally the desired phaseshifts $\delta(E) = \arctan K(E)$ and cross sections.

The K-matrix is related to the T-matrix and the S-matrix through the equation:

$$T(E) = \frac{2\imath K(E)}{1 - \imath K(E)} = S(E) - 1. \tag{2.39}$$

The T-matrix can be used to calculate the partial-wave cross section using the formula:

$$\sigma_l(E) = \frac{\pi}{k^2}(2l + 1)|T(E)|^2, \tag{2.40}$$

which is a one-channel analogue of the general formula (2.8).

One significant advantage of the R-matrix method, immediately obvious from equation (2.36), is the fact that the R-matrix can be calculated for any arbitrary energy once the inner region basis functions $u_i(r)$ and the corresponding eigenvalues have been obtained. Therefore the diagonalization implied by (2.26) and (2.27) must be carried out only once. Finally we note that the scattering wavefunction $F_l(r)$ does not need to be calculated for $r < a$ in order to obtain the phaseshifts and cross sections. It is the basis functions $u_i(r)$ which contain and provide, through the R-matrix, all information that is necessary for the determination of these quantities.

2.3 Application to electron-molecule scattering

This section describes the R-matrix theory of electron-molecule collisions as implemented in the UKRmol [72] suite of codes. The generalization of the R-matrix approach to the case of electron-molecule scattering is straightforward. From the formal point of view the additional difficulty of the problem is only reflected in the increased complexity of the resulting equations. Nevertheless, the basic principles and properties of the R-matrix method as discussed in the preceding section remain valid. The R-matrix method for electron-molecule collisions has been reviewed in detail recently [14].

The selection of the appropriate value of the R-matrix radius is a nontrivial step in the calculation and it depends on the spatial extent of the orbitals of the target molecule used in the inner region calculation. In the inner region the full problem of $N + 1$ interacting electrons has to be solved, the most complex step in the calculation. As in the case of the single channel scattering, the outer region calculation is usually much simpler than the inner region one, allowing us to calculate the cross sections and other observables with a very high energy resolution.

Generally, the inner region ($r \leq a$) is characterized by the short-range correlation and polarization caused by the Coulomb and exchange interaction of all electrons including the scattering electron. The latter interaction arises from indistinguishability of electrons.

In the outer region ($r \geq a$) the scattering electron is far away from the target molecule and hence does not penetrate significantly its electron cloud. Therefore the interaction between the molecule and the incoming electron can be described with sufficient precision by a single-centre potential scattering problem, where the potential is expressed as a multipole expansion of the electrostatic interaction between the electron and the molecule.

In the sections below, we describe the formalism in detail.

2.3.1 Inner region calculation

The calculation in this region proceeds in formal agreement with the prescription given at the end of Section 2.2. Namely, we choose a basis for the inner region, in which we diagonalize the Hamiltonian and then we calculate the R-matrix. However, due to the presence of many electrons and scattering channels the problem becomes very complex. Because of that the choice of the basis functions is made to reflect as closely as possible the underlying electronic processes taking place during the collision and their choice is therefore the most important step in the scattering calculation.

R-matrix basis functions

The starting point of the R-matrix theory for electron-molecule collisions is the expansion of the full scattering wavefunction $\Psi_E^\Gamma(\mathbf{x}_1, \mathbf{x}_2, \ldots, \mathbf{x}_N, \mathbf{x}_{N+1})$ in terms of a basis, denoted as $\Psi_k^\Gamma(\mathbf{x}_1, \mathbf{x}_2, \ldots, \mathbf{x}_N, \mathbf{x}_{N+1})$, defined in the inner region:

$$\Psi_E^\Gamma(\mathbf{x}_1, \mathbf{x}_2, \ldots, \mathbf{x}_N, \mathbf{x}_{N+1}) = \sum_k A_k^E \Psi_k^\Gamma(\mathbf{x}_1, \mathbf{x}_2, \ldots, \mathbf{x}_N, \mathbf{x}_{N+1}). \tag{2.41}$$

This equation is the equivalent of (2.21) from the section on single channel potential scattering R-matrix theory. The basis functions $\Psi_k^\Gamma(\mathbf{x}_1, \mathbf{x}_2, \ldots, \mathbf{x}_N, \mathbf{x}_{N+1})$ do not depend on the scattering energy. The energy dependence of the total wavefunction $\Psi_E^\Gamma(\mathbf{x}_1, \mathbf{x}_2, \ldots, \mathbf{x}_N, \mathbf{x}_{N+1})$ is contained only in the coefficients A_k^E. The basis functions for the inner region are written in the so-called *Close-Coupling approximation*:

$$\Psi_k^\Gamma(\mathbf{x}_1, \ldots, \mathbf{x}_{N+1}) = \mathcal{A} \sum_{i=1}^{n_b} \sum_{j=1}^{n_{c,i}} \Phi_i(\mathbf{x}_1, \ldots, \mathbf{x}_N) \gamma_{ij}(\mathbf{x_{N+1}}) a_{ijk} + \sum_{i=1}^{m} \chi_i^\Gamma(\mathbf{x}_1, \ldots, \mathbf{x}_{N+1}) b_{ik}. \tag{2.42}$$

The functions $\Phi_i(\mathbf{x}_1, \ldots, \mathbf{x}_N)$ describe the n_b (bound) electronic states of the molecule included in the calculation. The functions $\chi_i^\Gamma(\mathbf{x}_1, \ldots, \mathbf{x}_{N+1})$ in the second sum are the L^2 integrable functions whose density is fully contained inside the R-matrix sphere. In fact, the maximum spatial extent of the target states and the L^2 functions determines the R-matrix radius a. The functions $\gamma_{ij}(\mathbf{x}_{N+1})$ represent the unbound scattering electron and are the only functions which have a nonzero amplitude on the R-matrix sphere. The exact form of these functions is discussed below. Finally, the operator $\mathcal{A}$ ensures the correct antisymmetrization of the whole wavefunction, assuming that the target states and the L^2 functions are already antisymmetrized.

The superscripts Γ used for the functions $\Psi_k^\Gamma(\mathbf{x}_1,\ldots,\mathbf{x}_{N+1})$ and $\chi_i^\Gamma(\mathbf{x}_1,\ldots,\mathbf{x}_{N+1})$ indicate, that these functions are constructed to transform according to the chosen irreducible representation Γ of the point-group of the molecule and that they have the appropriate total spin. It should be noted that the target states $\Phi_i(\mathbf{x}_1,\ldots,\mathbf{x}_N)$ entering equation (2.42) are coupled only with those continuum orbitals $\gamma_{ij}(\mathbf{x}_{N+1})$ which together form products transforming according to the irreducible representation Γ. Indeed, only one set of continuum functions is generated for use in the calculations. The index i in γ_{ij} denotes that, for the symmetry reasons explained above, only a subset of these functions is coupled with a given target state.

The target states Φ_i and the L^2 functions χ_i^Γ are constructed as linear combinations of antisymmetrized products of the orthogonalized orbitals of the target molecule (Section 2.5 describes how these orbitals are constructed in our calculations). The particular type and number of target states and L^2 functions included in the Close-Coupling expansion (2.42) constitutes a *scattering model.* The functions $\chi_i^\Gamma(\mathbf{x}_1,\ldots,\mathbf{x}_{N+1})$ allow for the description of the short-range correlation and polarization effects as well as that of electron resonances, and their form is therefore one of the most important properties of the scattering model.

The continuum orbitals $\gamma_{ij}(\mathbf{x}_{N+1})$, describing the unbound scattering electron, are constructed from the orbitals of the target molecule and centre of mass centred spherical GTOs (continuum Gaussian-Type Orbitals). The continuum GTOs contain diffuse Gaussian functions, which generally do not vanish on the R-matrix sphere. The continuum orbitals and are then constructed in the following way: the continuum GTOs are first Schmidt orthogonalized to the target molecule's orbitals and then symmetrically orthogonalized among themselves. The orbitals with eigenvalues of the overlap matrix smaller than a specified threshold are deleted. The retained orthogonal orbitals then correspond to the $\gamma_{ij}(\mathbf{x}_{N+1})$ in equation (2.42). Close to the R-matrix sphere ($r \to a$), where the orbitals of the target molecule vanish, the continuum orbitals reduce to:

$$\gamma_{ij}(\mathbf{x}_{N+1}) \underset{r_{N+1}\to a}{=} \frac{F_{l_{ij},m_{ij}}(r_{N+1})}{r_{N+1}} \mathcal{Y}_{l_{ij},m_{ij}}(\Omega_{\mathbf{r_{N+1}}}), \tag{2.43}$$

$$F_{l_{ij},m_{ij}}(r_{N+1}) = \sum_{p_{ij}} c_{j,p_{ij}} \exp\left[-\alpha_{p_{ij}} r_{N+1}^2\right], \tag{2.44}$$

where the functions $\mathcal{Y}_{l_{ij},m_{ij}}(\Omega_{\mathbf{r}})$ are the real solid spherical harmonics [76, p.210] and $\Omega_{\mathbf{r_{N+1}}}$ stands for the angular variables of the vector $\mathbf{r}_{N+1}$. The index p_{ij} in (2.44) runs over all continuum GTO basis functions with the angular dependence given by the angular momentum l_{ij}. As explained above, the indices i,j in (2.43) ensure coupling of the appropriate spherical

harmonics with the target state i to form products transforming according to the irreducible representation Γ. The exponents α_{pl} of the continuum GTOs are optimized for each value of l and for a given R-matrix radius, in order to obtain an accurate representation of the radial wavefunction of the scattering electron inside the whole R-matrix sphere over a range of scattering energies. We can see now that the inclusion of the centre of mass centred continuum GTOs allows us to use a partial-wave expansion for the wavefunction of the scattering electron. As we will see in Section 2.3.2, this representation of the wavefunction will be the basis for the formulation of the outer region scattering problem in the form of coupled equations for the partial-waves of the scattering electron.

The coefficients a_{ijk} and b_{ik} in equation (2.42) are the analogues of the coefficients c_{ij} in equation (2.27) and are determined by the requirement that these functions diagonalize the Hamiltonian $\tilde{H}_{N+1}$ in the inner region*

$$\left(\Psi_{k'}|\tilde{H}_{N+1}|\Psi_k\right) = (\Psi_{k'}|H_{N+1} + L|\Psi_k) = E_k\delta_{k'k}. \tag{2.45}$$

H_{N+1} is now the Hamiltonian (2.3) of the system of $N+1$ interacting electrons:

$$H_{N+1} = \sum_{i=1}^{N+1}\left(-\frac{\nabla_i^2}{2} - \sum_{k=1}^{Nuclei}\frac{Z_k}{\rho_{ki}}\right) + \sum_{i>j}^{N+1}\frac{1}{r_{ij}} + \sum_{k>l}^{Nuclei}\frac{Z_kZ_l}{R_{kl}} \tag{2.46}$$

and the Bloch operator L has the form

$$L = \frac{1}{2}\sum_{i=1}^{N+1}\sum_{j=1}^{n_{ch}}|\Phi_j\mathcal{Y}_{l_j,m_j}(\hat{\mathbf{x}}_i))\delta(r_i - a)\left(\frac{d}{dr_i} - \frac{b-1}{r_i}\right)(\Phi_j\mathcal{Y}_{l_j,m_j}(\hat{\mathbf{x}}_i)|, \tag{2.47}$$

where the index j runs over all n_{ch} scattering channels. The purpose of this operator is the same as in the one channel case, namely to ensure the hermicity of the Hamiltonian $\tilde{H}_{N+1}$. Its form can be justified by noting that the only terms in the wavefunctions (2.42) which cause the nonhermicity of the Hamiltonian (2.46) are the ones containing the continuum functions $\gamma_{ij}(\mathbf{x}_{N+1})$. The purpose of the projectors $|\Phi_j\mathcal{Y}_{l_j,m_j}(\hat{\mathbf{x}}_i))$ is then to isolate the radial parts of (2.43), which are nonzero on the R-matrix sphere and then remove, using the Delta function, the spurious surface terms in a similar way as in the one-channel case discussed in Section 2.2. The sum over i is then required, because of the antisymmetrized form of the wavefunctions $\Psi_k^\Gamma(\mathbf{x}_1,\ldots,\mathbf{x}_{N+1})$.

*We replace the usuall angled brackets by round ones to indicate that the integration implied by these brackets is carried out only over the inner region. Wherever used, the angled brackets retain their standard meaning, i.e. they indicate integration over the whole configuration space.

R-matrix for electron-molecule collisions

Here we derive the expression for the R-matrix for electron-molecule collisions, which provides the link between the radial functions of the scattering electron from the inner region and the outer region. We simplify the notation for the scattering channels and use instead of the full channel index $\gamma_{i,l,m}$ defined in the Section 2.1, only the single index i running over all n_{ch} channels. In this notation the expression for the channels reads: $|\Phi_i \mathcal{Y}_{l_i,m_i}(\hat{\mathbf{x}}_{N+1})\frac{1}{r_{N+1}})$. In the first step we rewrite the Schrödinger equation (2.2) using the Bloch operator (2.47) to obtain

$$(H_{N+1} + L)\,\Psi_E^\Gamma(\mathbf{x}_1, \ldots, \mathbf{x}_{N+1}) = (E + L)\,\Psi_E^\Gamma(\mathbf{x}_1, \ldots, \mathbf{x}_{N+1}). \tag{2.48}$$

We can formally invert this equation and find an implicit expression for $\Psi_E^\Gamma(\mathbf{x}_1, \ldots, \mathbf{x}_{N+1})$:

$$\Psi_E^\Gamma(\mathbf{x}_1, \ldots, \mathbf{x}_{N+1}) = (H_{N+1} + L - E)^{-1}\, L\Psi_E^\Gamma(\mathbf{x}_1, \ldots, \mathbf{x}_{N+1}). \tag{2.49}$$

We insert the complete set of states for the inner region $\sum_{k=1} |\Psi_k^\Gamma)(\Psi_k^\Gamma| = \hat{1}$ between the two operators on the right hand side, project the equation on the channels $|\Phi_i \mathcal{Y}_{l_i,m_i}(\hat{\mathbf{x}}_{N+1})\frac{1}{r_{N+1}})$ and use equation (2.45) to obtain

$$\left(\Phi_i \mathcal{Y}_{l_i,m_i} \frac{1}{r_{N+1}} \middle| \Psi\right) = \sum_k (E_k - E)^{-1} \left(\Phi_i \mathcal{Y}_{l_i,m_i} \frac{1}{r_{N+1}} \middle| \Psi_k\right) (\Psi_k|L|\Psi). \tag{2.50}$$

For simplicity we omit in the formulas the explicit dependence of the wavefunctions on the variables $\mathbf{x}_1, \ldots, \mathbf{x}_{N+1}$. Projection on the channels $|\Phi_i \mathcal{Y}_{l_i,m_i}(\hat{\mathbf{x}}_{N+1})\frac{1}{r_{N+1}})$ guarantees that the function on the left side is a function of r_{N+1} only and that it does not contain the term $\frac{1}{r_{N+1}}$. We want to evaluate this function on the boundary $r = a$, because this is where we will want to start the calculation for the outer region. We now define the reduced radial wavefunctions

$$F_i(a) = \left(\Phi_i \mathcal{Y}_{l_i,m_i} \frac{1}{r_{N+1}} \middle| \Psi\right)_{r=a}, \tag{2.51}$$

and the surface amplitudes

$$w_{ik}(a) = \left(\Phi_i \mathcal{Y}_{l_i,m_i} \frac{1}{r_{N+1}} \middle| \Psi_k\right)_{r=a} \tag{2.52}$$

and rewrite equation (2.50) evaluated at $r = a$ using this notation to obtain:

$$F_i(a) = \sum_k \frac{w_{ik}(a)}{E_k - E} (\Psi_k|L|\Psi). \tag{2.53}$$

The last step is the evaluation of the matrix element $(\Psi_k|L|\Psi)$:

$$\begin{aligned}
&\frac{1}{2}\sum_{i=1}^{N+1}\sum_{j=1}^{n_{ch}}(\Psi_k|\Phi_j\mathcal{Y}_{l_j,m_j}(\hat{\mathbf{x}}_i))\delta(r_i-a)\left(\frac{d}{dr_i}-\frac{b-1}{r_i}\right)(\Phi_j\mathcal{Y}_{l_j,m_j}(\hat{\mathbf{x}}_i)|\Psi) = \\
&= \frac{1}{2}\sum_{j=1}^{n_{ch}}\overbrace{(\Psi_k|\Phi_j\mathcal{Y}_{l_j,m_j}(\hat{\mathbf{x}}))}^{w_{jk}(r)r}\delta(r-a)\left(\frac{d}{dr}-\frac{b-1}{r}\right)\overbrace{(\Phi_j\mathcal{Y}_{l_j,m_j}(\hat{\mathbf{x}})|\Psi)}^{\frac{F_j(r)}{r}} = \\
&= \frac{1}{2}\sum_{j=1}^{n_{ch}}w_{jk}(r)r\delta(r-a)\left(\frac{1}{r}\frac{dF_j}{dr}-\frac{1}{r}\frac{F_j}{dr}+\frac{1}{r}\frac{F_j}{dr}-\frac{b}{r}\frac{F_j}{r}\right) = \\
&= \frac{1}{2}\sum_{j=1}^{n_{ch}}w_{jk}(a)\left(\left[\frac{dF_j}{dr}\right]_a-b\frac{F_j(a)}{a}\right) = \frac{1}{2a}\sum_{j=1}^{n_{ch}}w_{jk}(a)\left(a\left[\frac{dF_j}{dr}\right]_a-bF_j(a)\right). \quad (2.54)
\end{aligned}$$

The reason why the sum over i was reduced in the first step to only one particular term, in which we replaced x_i by x is that the wavefunctions Ψ_k are antisymmetric products and a projection of the type $(\Psi_k|\Phi_j\mathcal{Y}_{l_j,m_j}(\hat{\mathbf{x}}_i))$ formally yields a sum of terms, but always only one term from such a sum is nonzero. The only nonzero term is the one in which the order of the variables in Ψ_k terms and in the channel function $|\Phi_j\mathcal{Y}_{l_j,m_j}(\hat{\mathbf{x}}_i))$ are the same.

We insert the result (2.54) back into the equation (2.53) and we get the expression

$$F_i(a) = \frac{1}{2a}\sum_{j=1}^{n_{ch}}\sum_k \frac{w_{ik}(a)w_{jk}(a)}{E_k-E}\left(a\frac{dF_j}{dr}\bigg|_a - bF_j(a)\right) \quad (2.55)$$

which can be written in terms of matrix multiplications, where the elements of the **R**-matrix are defined as

$$R_{ij}(E) = \frac{1}{2a}\sum_k \frac{w_{ik}(a)w_{jk}(a)}{E_k-E}. \quad (2.56)$$

The previous expression for $F_i(a)$ simplifies to

$$F_i(a) = \sum_{j=1}^{n_{ch}} R_{ij}(E)\left(a\frac{dF_j}{dr}\bigg|_a - bF_j(a)\right), \quad (2.57)$$

which explicitly demonstrates the role of the **R**-matrix as the quantity linking the inner and the outer region - also see equation (2.37).

2.3.2 Outer region calculation

The outer region calculation is much simpler than the inner region calculation for two main reasons, stemming from the fact that the scattering electron is located far away from the molecule. The first one is that the exchange interaction arising from the indistinguishability of the N electrons of the target and the scattering electron can be neglected. The second

reason is that we can approximate the interaction of the incoming electron with the target molecule by a generally nonspherical single centre potential. Therefore the full scattering wavefunction in the outer region can be written in the following form:

$$\Psi(\mathbf{x}_1,\ldots,\mathbf{x}_{N+1}) = \sum_{j=1}^{n_{ch}} \Phi_j(\mathbf{x}_1,\ldots,\mathbf{x}_N)\mathcal{Y}_{l_j,m_j}(\hat{\mathbf{x}}_{N+1})\frac{F_j(r_{N+1})}{r_{N+1}}, r_{N+1} \geq a. \tag{2.58}$$

The functions $F_j(r_{N+1})$ at $r_{N+1} = a$ are the reduced radial wavefunctions (2.51) corresponding to radial part of the partial waves of the scattering electron.

The equations determining the radial functions $F_j(r_{N+1})$ for $r_{N+1} > a$ are obtained by projecting the Schrödinger equation $H_{N+1}\Psi = E\Psi$ on the channel functions $|\Phi_i\mathcal{Y}_{l_i,m_i}(\hat{\mathbf{x}}_{N+1})\frac{1}{r_{N+1}}\rangle$:

$$\left(\Phi_i\mathcal{Y}_{l_i,m_i}(\hat{\mathbf{x}}_{N+1})\frac{1}{r_{N+1}}\middle|H_N + H_{int}\middle|\sum_{j=1}^{n_{ch}}\Phi_j(\mathbf{x}_1,\ldots,\mathbf{x}_N)\mathcal{Y}_{l_j,m_j}(\hat{\mathbf{x}}_{N+1})\frac{F_j(r_{N+1})}{r_{N+1}}\right) =$$
$$= E\left(\Phi_i\mathcal{Y}_{l_i,m_i}(\hat{\mathbf{x}}_{N+1})\frac{1}{r_{N+1}}\middle|\sum_{j=1}^{n_{ch}}\Phi_j(\mathbf{x}_1,\ldots,\mathbf{x}_N)\mathcal{Y}_{l_j,m_j}(\hat{\mathbf{x}}_{N+1})\frac{F_j(r_{N+1})}{r_{N+1}}\right), \tag{2.59}$$

where we used the separation (2.3) of the full Hamiltonian into its parts. After some algebra we obtain the equation

$$E_iF_i(r) + \left(-\frac{1}{2}\frac{d^2}{dr^2} + \frac{l_i(l_i+1)}{2r^2}\right)F_i(r) \quad + \quad \sum_{j=1}^{n_{ch}} V_{ij}(r)F_j(r) = EF_i(r), \tag{2.60}$$

where we have dropped the index $N+1$ from the radial coordinate of the scattering electron, because r_{N+1} is the only radial coordinate in the resulting formulae. The coupling potentials $V_{ij}(r)$ have the form:

$$V_{ij}(r) \quad = \quad \left(\Phi_i\mathcal{Y}_{l_i,m_i}(\hat{\mathbf{x}}_{N+1})\middle|\sum_{p=1}^{N}\frac{1}{r_{p(N+1)}} - \sum_{k=1}^{Nuclei}\frac{Z_k}{\rho_{k(N+1)}}\middle|\Phi_j\mathcal{Y}_{l_j,m_j}(\hat{\mathbf{x}}_{N+1})\right). \tag{2.61}$$

It is shown in the Appendix A that these potentials can be written using the single-centre expansion of the Coulomb interaction in the form:

$$V_{ij}(r) = \sum_{\lambda=0}^{\infty} a_{ij\lambda}r^{-\lambda-1}, \; i,j = 1,\ldots,n_{ch}, \; r \geq a, \tag{2.62}$$

where the coefficients a_{ij}^{λ} are linked to the permanent ($i = j$) and the transition ($i \neq j$) multipole moments of the target electronic states. In most R-matrix calculations, multipole moments higher than the quadrupole ($\lambda = 2$) are not used. We can now insert the expansion

(2.62) back into (2.60) and obtain the final form of the single-centre no-exchange close-coupling equations:

$$\left(\frac{d^2}{dr^2} - \frac{l_i(l_i+1)}{r^2} + k_i^2\right) F_i(r) = 2\sum_{j=1}^{n_{ch}} \sum_{\lambda=0} a_{ij\lambda} r^{-\lambda-1} F_j(r), \tag{2.63}$$

where $k_i = \sqrt{2(E-E_i)}$ are, as before, the channel momenta. This set of coupled equations allows us to solve for $F_i(r)$ in the outer region for each energy E using the boundary conditions at $r = a$ (2.57) provided by the R-matrix (2.56). These equations represent a multichannel radial scattering problem and can be thought of as a straightforward generalization of the single-channel radial scattering problem discussed in Section 2.2. In principle, the **K**-matrix and its complex equivalent, the **S**-matrix, can be obtained by matching the obtained solutions $F_i(r)$ in the asymptotic region $r \to \infty$ to the scattering boundary conditions in each channel. In practice however, this direct procedure leading to the calculation of the **K**-matrix has been replaced by the techniques of the R-matrix propagation and asymptotic expansion, which together greatly reduce the computational cost and increase the numerical stability of the outer region calculation. Therefore, in the following sections we briefly explain the main principles of the R-matrix propagation and asymptotic expansion.

R-matrix propagation

Standard numerical techniques of, for example, the Numerov type which can be used to solve the coupled equations (2.63), suffer from well known instabilities resulting from the unphysical exponentially increasing solution of the Schrödinger equation. The R-matrix propagation technique [77] circumvents this problem.

The advantage of the R-matrix propagation is that the solution of the equations (2.63) can be obtained utilizing matrix diagonalization. Suppose that for a given energy E we want to obtain the functions $F_i(r)$ for $r = a_m$, $a_m \gg a$. Following the R-matrix approach we select a basis set in each channel i (Legendre polynomials are used in the implementation, as described in [77]) and diagonalize the Hamiltonian corresponding to the problem (2.63) in this basis. Obviously the Hamiltonian needs to be complemented by the appropriate Bloch operator[†] in order to retain the hermicity of the resulting operator. The eigenfunctions and eigenvalues of this matrix can then be used to construct the R-matrix at $r = a_m$. In fact a relation can be obtained [77] directly linking the R-matrices at $r = a$ and $r = a_m$ through

[†]In this case the Bloch operator removes the spurious surface terms from both end points of the radial interval and therefore has, in each channel, the following form: $L = \frac{1}{2}\left(\delta(r-a_m)\frac{d}{dr} - \delta(r-a)\frac{d}{dr}\right)$.

auxiliary matrices constructed from the eigenvectors of the Hamiltonian. Obtaining the R-matrix at $r > a$ using the R-matrix at $r = a$ is called the R-matrix propagation.

In order to reduce the computational cost (the dimension of the Hamiltonian matrix to be diagonalized), the interval $r \in \langle a; a_m \rangle$ is divided into a number of subintervals with endpoints $a_1 < a_2, \ldots, a_{m-1} < a_m$, along which the R-matrix is propagated up to the end point of the last interval: $r = a_m$. The R-matrix at $r = a_m$ is then used in the final step of the calculation, which is the asymptotic expansion.

Asymptotic expansion and the boundary conditions

In order to reduce the computational cost of the outer region calculation, the R-matrix propagation described in the preceding section is carried out only up to a radius $a_m \gg a$, large enough to allow for use of the asymptotic expansion of the radial wavefunctions $F_i(r)$. These functions are solutions of the system of n_{ch} coupled equations (2.63):

$$\left(\frac{d^2}{dr^2} - \frac{l_i(l_i+1)}{r^2} + k_i^2\right) F_i(r) = 2\sum_{j=1}^{n_{ch}} \sum_{\lambda=0} a_{ij\lambda} r^{-\lambda-1} F_j(r),$$

and are complemented by the boundary conditions (2.57), which couple the logarithmic derivatives of these functions at $r = a$. For open channels (i.e. those with real channel momenta), each radial wavefunction $F_i(r)$ solution of (2.63) can be written in the asymptotic region as a linear combination of the following linearly independent functions:

$$R_i^s(r) = \frac{1}{\sqrt{k_i}} \sin(k_i r - l_i\pi/2 + \eta \ln 2k_i r + \sigma_{l_i}), \tag{2.64}$$

$$R_i^c(r) = \frac{1}{\sqrt{k_i}} \cos(k_i r - l_i\pi/2 + \eta \ln 2k_i r + \sigma_{l_i}). \tag{2.65}$$

These functions can be interpreted as the free, R_i^s, and the scattered, R_i^c, radial waves. The last two terms in the arguments of the trigonometric functions only apply in the case of target molecules with a nonzero charge Z and correspond to the Coulomb parameter $\eta = \frac{Z}{k_i}$ and the Coulomb phase $\sigma_{l_i} = \Gamma(l_i + 1 - \imath\eta)$. For closed channels the physically acceptable solution of (2.63) is exponentially decreasing. In practice we set the radial functions in these channels to zero.

The index i in equation (2.63) runs over all open channels at energy E and is, as mentioned in Section 2.3.2, a simplified notation for the full channel index $\gamma^{\Gamma}_{i,l_i,m_i}$ defined in Section 2.1. In equation (2.66) the index i will stand only for the index of the electronic state of the target molecule. The individual channels will be denoted using the full index $\gamma^{\Gamma}_{i,l_i,m_i}$ including

the angular momentum quantum numbers of the scattering electron. The two independent functions (2.64) and (2.65) allow us then to express the general solutions $F^{\gamma^\Gamma_{j,l_j,m_j}}_{\gamma^\Gamma_{i,l_i,m_i}}(r)$ of (2.63) in the asymptotic region as their linear combination

$$F^{\gamma^\Gamma_{j,l_j,m_j}}_{\gamma^\Gamma_{i,l_i,m_i}}(r) = \delta_{i,j}\delta_{l_i,l_j}\delta_{m_i,m_j}R^-_{i,l_i}(r) + K^\Gamma_{i,l_i,m_i;j,l_j,m_j}R^+_{j,l_j}(r),\ r \to \infty. \tag{2.66}$$

The quantities $K^\Gamma_{i,l_i,m_i;j,l_j,m_j}$ are the elements of the real-valued **K**-matrix. The indices of the radial wavefunction $F^{\gamma^\Gamma_{j,l_j,m_j}}_{\gamma^\Gamma_{i,l_i,m_i}}(r)$ denote a solution corresponding to the electron incoming in channel $\gamma^\Gamma_{i,l_i,m_i}$ and outgoing in channel $\gamma^\Gamma_{j,l_j,m_j}$. An important quantity used in the analysis of the calculated data is the *eigenphase sum*, $\delta^\Gamma_{sum}(E)$, obtained from the diagonalized **K**-matrix $\mathbf{K}^\Gamma_D$:

$$\delta^\Gamma_{sum}(E) = \sum_{i=1}^{n_{ch}} \arctan\left[(K^\Gamma_D)_{ii}(E)\right]. \tag{2.67}$$

In Section 2.1 - equation (2.6a) - we specified the boundary conditions using the complex functions $\phi^\pm_i(r)$ and the **S**-matrix as is customary in quantum scattering theory. Since solutions of the Schrödinger equation can always be chosen as real, the basis of real solutions $R^\pm_i(r)$ used in our formulation of the R-matrix theory is completely equivalent to the complex basis. These bases can be obtained from each other using a unitary transformation [73]. Also, the **S**-matrix and the **T**-matrix can be obtained directly from the **K**-matrix using the equations:

$$\mathbf{S}^\Gamma = (\mathbf{1} + \imath\mathbf{K}^\Gamma)(\mathbf{1} - \imath\mathbf{K}^\Gamma)^{-1}, \tag{2.68}$$

$$\mathbf{T}^\Gamma = 2\imath\mathbf{K}^\Gamma(\mathbf{1} - \imath\mathbf{K}^\Gamma)^{-1}. \tag{2.69}$$

The asymptotic expansion allows us to find analytic forms of the solutions $F^{\gamma^\Gamma_{j,l_j,m_j}}_{\gamma^\Gamma_{i,l_i,m_i}}(r)$ for large r, which are in the limit $r \to \infty$ equal to their asymptotic form (2.66). Thanks to this method the **K**-matrix can be obtained using the R-matrix propagated only to a region much smaller than asymptotic. The asymptotic expansion used in the UKRmol suite of codes is that of Gailitis [78] and has the following form:

$$F_i(r) = \frac{1}{\sqrt{k_i}}\left(f(\theta)\sum_{\mu=0} C^\mu_i r^{-\mu} + g(\theta)\sum_{\mu=0} B^\mu_i r^{-\mu}\right), \tag{2.70}$$

with

$$\theta = k_i r - l_i\pi/2 + \eta\ln 2k_i r + \sigma_{l_i}, \tag{2.71}$$

where $f(\theta)$ and $g(\theta)$ are the regular and irregular solutions of the Schrödinger equation with the Coulomb field (see e.g. [73]). We can see that the functions (2.64) and (2.65) can be obtained by setting

$$R_i^s(r) = F_i(r),\ r \to \infty, C_i^0 = 1, B_i^\mu = 0, \tag{2.72}$$

$$R_i^c(r) = F_i(r),\ r \to \infty, C_\mu^i = 0, B_i^0 = 1 \tag{2.73}$$

proving that (2.70) is indeed a valid asymptotic expansion for the radial wavefunctions $F_i(r)$. The exact procedure for determining the coefficients B_i^μ and C_i^μ can be found in [78]. Once these coefficients have been determined, they are used to calculate the **K**-matrix, thus completing the outer region calculation.

2.4 Time-delay analysis

This work places a special emphasis on identification and characterization of electron resonances. It was shown by Hazi [79] in 1979 that an isolated resonance in electron-molecule collisions manifests itself in the eigenphase sum (2.67) as a characteristic jump by π radians, whose shape is described by the Breit-Wigner formula:

$$\delta_{sum}(E) = \delta_r + \delta_{bg} = -\arctan\frac{\Gamma/2}{E - E_r} + \delta_{bg}, \tag{2.74}$$

where E_r and Γ are respectively the position and width of the resonance and δ_{bg} is the background non-resonant contribution, usually weakly dependent on energy. Nevertheless, the analysis of the eigenphase sums is not the only method which can be used for finding resonances in calculated scattering data. Another method is the analysis of the *time-delay*. As we will see throughout this work, the time-delay method proved an essential tool for finding most of the resonances we report. We therefore briefly discuss its main principles here.

The advantages of the time-delay analysis over the conventional analysis of the eigenphase sums have been highlighted already, see e.g.: [80, 81]. The most important is that the time-delay analysis allows for unambiguous identification of resonances even in cases in which the eigenphase sum does not display the typical resonant behaviour, or when its behaviour seems to be completely "non-resonant". This is because the time-delay analysis allows for a complete separation of resonances from the background and also from each other (see Section 4.8.1 for a particular example).

We use the definition of the time-delay as formulated by F.T.Smith [82], which is appropriate for description of the collision process in terms of the time-independent scattering wavefunction. In this formulation the lifetime or time-delay is defined in terms of the excess number of particles (charge density) present near the scattering centre obtained after subtracting the number that would have been present in the absence of the interaction. The time-delay is then obtained by dividing the excess number of particles by the total incoming flux through a closed surface at large distance from the scattering centre.

In practice the time-delay analysis is performed using the **Q**-matrix (the time-delay matrix), which is calculated, for a given energy, directly from the S-matrix [82] using the formula

$$\mathbf{Q}(E) = i\hbar \mathbf{S} \frac{d\mathbf{S}}{dE} \tag{2.75}$$

and can be shown [82, 81] to have several useful properties relating it to the eigenphase sum:

$$Tr\left[\mathbf{Q}(E)\right] = 2\hbar \frac{d}{dE} \delta_{sum}(E), \tag{2.76}$$

$$Tr\left[\mathbf{Q}(E)\right] = \sum_{\alpha=1}^{N_{res}} \underbrace{\frac{\hbar\Gamma_\alpha}{(E-E_\alpha)^2 + (\Gamma_\alpha/2)^2}}_{L_\alpha(E)} + 2\hbar \frac{d\delta_{bg}}{dE}. \tag{2.77}$$

The summation in equation (2.77) goes over all N_{res} resonances present in the system. The values E_α and Γ_α are respectively the position and width of the resonance α.

When searching for resonances, the most important information is gained from the analysis of the positive eigenvalues and the associated eigenvectors of the **Q**-matrix for each scattering energy E. Time-delays (positive eigenvalues of the **Q**-matrix) much larger than $\hbar/E$ can be interpreted as arising from resonant processes and have the shape of the Lorentzian functions $L_\alpha(E)$. The eigenvectors of the **Q**-matrix corresponding to the Lorentzian peaks (resonances) also contain valuable information. The square $|c_j|^2$ of the j-th coefficient of the eigenvector corresponding to a resonance is equal to the branching ratio, i.e. probability of decay of the metastable state into the j-th channel and therefore can be used to determine the parent states of the resonance.[‡]

The negative eigenvalues of the **Q**-matrix correspond to a time-advance, in which case the incoming electron is either accelerated by passing through a strongly attractive interaction region or is reflected by a strongly repulsive interaction. If the initial channel corresponds to an excited state of the target molecule, the electron can obtain extra energy by deexciting

[‡]For Feshbach resonance this approach cannot be applied since its parent state corresponds to a closed channel, i.e. channel not available for decay.

the molecule, a process that may also lead to time-advance.

Further information about the collision process can be gained by analyzing the diagonal element Q_{ii} of the **Q**-matrix, which correspond to the average time-delay experienced by the electron incoming in channel i:

$$Q_{ii} = \sum_j \Delta t_{ij} |S_{ij}|^2. \tag{2.78}$$

The sum runs over all channels open at a particular electron energy and Δt_{ij} is the time-delay (or time-advance) associated with a collision starting in channel i and ending in channel j; the quantity $|S_{ij}|^2$ is equal to the probability of this collision taking place. Finally, the time-delays Δt_{ij} can be calculated using the formula:

$$\Delta t_{ij} = \mathrm{Re}\left[-\imath\hbar (S_{ij})^{-1} \frac{dS_{ij}}{dE}\right], \tag{2.79}$$

where Re stands for the real part of the term in brackets.

2.5 Hartree-Fock and CASSCF methods

The expansion of the R-matrix basis functions (equation (2.42)) contains one or more target electronic wavefunction $\Phi_i(\mathbf{x_1}, \ldots, \mathbf{x_N})$, whose accurate representation is an important factor determining the overall quality of the computed scattering data. This section describes the methods used in this work for the determination of the target states' wavefunctions.

Once the geometry of the molecule has been fixed, the main problem in determining the wavefunctions $\Phi_i(\mathbf{x_1}, \ldots, \mathbf{x_N})$ is the accurate representation of the effects of the Coulomb interaction, also called the *electron correlation*. We use a wavefunction-based approach, in which the target states are represented using a set of $2n_o$ orthogonal spin-orbitals $\omega_1, \bar{\omega}_1, \omega_2, \bar{\omega}_2, \ldots, \omega_{n_o}, \bar{\omega}_{n_o}$. In our work ω_i and $\bar{\omega}_i$ have the same spatial part, but opposite spins. Using these spin-orbitals the ground state of a closed-shell molecule can be written in the following way:

$$\Phi_0(x_1, \ldots, x_N) = \| \, \omega_1 \bar{\omega}_1 \omega_2 \bar{\omega}_2 \ldots \omega_{N/2} \bar{\omega}_{N/2} \, \|, \tag{2.80}$$

that is, the ground state of the molecule is described by the N lowest-energy spin-orbitals, where N is the number of electrons in the molecule. The double vertical lines $\| \cdots \|$ stand for the antisymmetrization (Slater determinant) of the wavefunction, hence forming a wavefunction respecting the Pauli principle.

The orbitals are usually expanded in a selected basis set of Gaussian-type orbitals (GTOs)

centred on each nuclei of the molecule. We can therefore write[§] ω_i:

$$\omega_i(x_i, y_i, z_i) = \sum_{k=1}^{n_o} c_{ik} g_k(x_i, y_i, z_i),\ i = 1, \ldots, n_o. \tag{2.81}$$

The coefficients c_{ik} are determined in different ways depending on the method used and the orbitals ω_i are thus fully specified. As can be seen from equation (2.81) the Gaussian basis set $\{g_k\}_{k=1}^{n_o}$ consists of n_o basis functions. It can be shown that this leads to a set of n_o electron orbitals ω_i, $i = 1, \ldots, n_o$.

In the Restricted Hartree-Fock Self Consistent Field (HF) approximation the orbitals ω_i are determined (see e.g. [83]) by requiring that the wavefunction of the ground state (2.80) minimizes the energy functional of the form:

$$E_{HF} = \langle \Phi_0 | H_N | \Phi_0 \rangle. \tag{2.82}$$

The formulation of the HF method using orthogonal molecular orbitals leads to the set of Roothan equations:

$$\mathbf{FC} = \mathbf{C}\epsilon, \tag{2.83}$$

which are solved for $\mathbf{C}$ by diagonalization of the Fock operator $\mathbf{F}$. The i-th column of the matrix $\mathbf{C}$ then contains the expansion coefficients c_{ik} for orbital ω_i from equation (2.81). We call the resulting orbitals the HF orbitals. The matrix ϵ is a diagonal matrix containing the energies ϵ_i of the orbitals ω_i. The orbitals unoccupied in the HF ground state are called virtual orbitals. The HF orbitals are, in our scattering calculations, used only in conjunction with less sophisticated scattering models, which include only the HF ground state in the expansion (2.42) and are thus capable of describing elastic scattering only.

The Hartree-Fock method accounts for electron correlation only in an average way, because in this approximation each electron is thought to move independently in an effective potential produced by all other electrons and determined in a self consistent way. In order to improve on the description of the ground state and to calculate the excited states, more elaborate methods are needed. One of them, the SA-CASSCF method, is described below.

[§]In practice the basis functions used in expansions (2.81) are not directly GTOs, but rather their linear combinations that produce symmetry-adapted functions which exploit the spatial symmetry of the molecule and reduce considerably the computational effort of the whole calculation.

Configuration interaction and SA-CASSCF methods

The State-Averaged Complete Active Space Self Consistent Field (SA-CASSCF) method was developed by B. O. Roos especially for the accurate representation of electronic excited states (for reviews of the method see e.g. [84, 85]). In this approach the target electronic states are represented using multiple Configuration State Functions (CSFs). A single CSF (also called configuration) has the form of equation (2.80) with one or more orbitals replaced by the virtual orbitals.

If we want to describe at a higher, more accurate level a given electronic state Φ (ground or excited), the most straightforward option we have is the Configuration Interaction (CI) method in which the electronic state is expressed as a linear combination of the following type:

$$\Phi = C_0\Phi_0 + \sum_{a,p} C_a^p \Phi_a^p + \sum_{\substack{a<b \\ p<q}} C_{ab}^{pq} \Phi_{ab}^{pq} + \sum_{\substack{a<b<c \\ p<q<r}} C_{abc}^{pqr} \Phi_{abc}^{pqr} + \dots . \tag{2.84}$$

Here the first term is the ground state configuration of the HF type and the first sum stands for all single-excitation configurations, i.e. one electron moved from an initially occupied orbital a to a virtual orbital p. The second sum corresponds to all possible double excitations, the third one to all triple excitations, etc. The number and type of all these excitations is usually chosen depending on the nature of the excited state we wish to describe and the size of the calculation we can handle. The key principle of the CI method is that the orbitals are determined first, using for example the HF method, and the coefficients C are determined by diagonalization of the molecular Hamiltonian matrix.

Since in practical calculations we are limited only to a finite Gaussian basis set, we have only n_o spatial orbitals ω_i to work with. A CI calculation using all possible (single, double, triple, etc.) excitations with n_o spatial orbitals available is called a *full CI* calculation. Due to the large number of CSFs generated, calculations of this type are usually possible only for relatively simple systems with a small number of electrons.

Unlike the CI method, the CASSCF method determines (optimizes) both the CI coefficients C and the expansion coefficients c_{ik} of equation (2.81) concurrently, i.e. it determines at the same time the importance of the excitations in (2.84) (i.e. how much they contribute) and also the shape of the orbitals $\omega_i(x_i, y_i, z_i)$. By virtue of the method the resulting orbitals $\omega_i(x_i, y_i, z_i)$ are all orthogonal.

A CASSCF calculation can be carried out in two modes:

- state-specific mode,

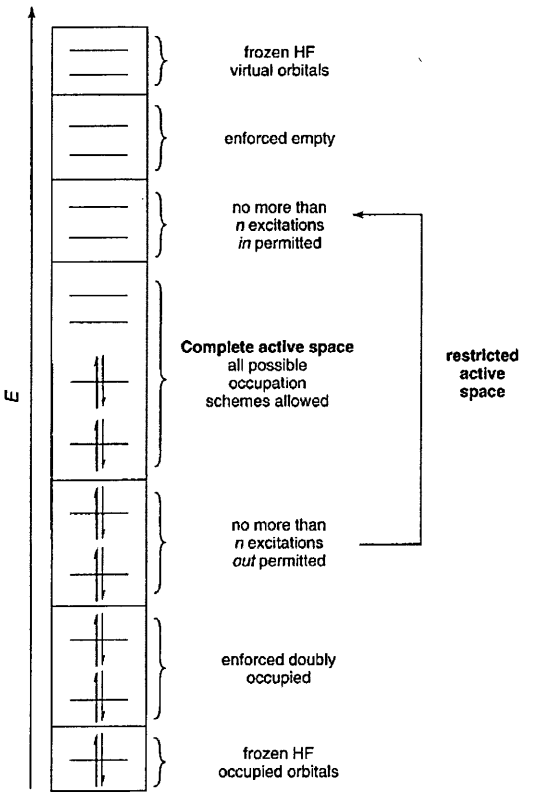

Figure 2.2: Scheme showing the active, frozen and doubly occupied orbitals in the CASSCF method. The optional restricted active space is shown as well. The electrons with spins "up" and "down" are represented by arrows pointing in the corresponding directions. The active electrons are distributed in all possible ways among the active space orbitals. The doubly occupied and active orbitals are optimized whereas the frozen ones are not. From [86].

- state-averaged mode.

Both of these modes have the main idea in common, which is performing the full CI calculation on a *small sub-set* of chosen orbitals. A general scheme of the CASSCF method is shown in Figure 2.2.

Prior to the CASSCF calculation a HF calculation on the ground state of the molecule is performed. This yields a set of orbitals which are used as a starting guess for the procedure. Then the orbitals to be kept *frozen* (i.e. not optimized) are chosen. Most importantly a set of *active orbitals* (also called *the complete active space*) is chosen among which the full CI calculation will be performed. Optionally, a restricted active space can be chosen. The restricted active space contains specific excitations to orbitals which are not included in the active space. Finally *doubly occupied orbitals* consisting of orbitals which are optimized, but are always doubly occupied and no excitations out of them are allowed, are selected.

A particular choice of all these orbital subsets constitutes the *CAS model.* In the literature, CAS models are usually denoted by (n, m), where n stands for the number of electrons being distributed among the m active orbitals. The other $N - n$ electrons occupy the frozen or

doubly occupied orbitals.

Once all orbitals have been divided among frozen, doubly occupied and active, the CASSCF optimization can proceed. The wavefunction to be optimized is written as a unitary transformation of the initial wavefunction [85]:

$$|\Phi_{CASSCF}\rangle = \exp(\gamma)\exp(\delta)|\Phi_c\rangle, \tag{2.85}$$

where $|\Phi_c\rangle$ stands for the initial wavefunction generated from the CAS configurations. The matrices γ and δ are antihermitian and their upper triangles therefore constitute the parameters to be optimized: the orbital coefficients c_{ik} and the CI coefficients C. The CASSCF energy of the target state $|\Psi_{CASSCF}\rangle$ is given by the equation:

$$E_{CASSCF} = \langle\Phi_{CASSCF}|H_N|\Phi_{CASSCF}\rangle. \tag{2.86}$$

The working equations of the CASSCF method are obtained by expanding the commutators to second order and from the requirement of stationarity of the resulting functional. The resulting equations are solved iteratively until a converged set of orbitals and CI coefficients is obtained. In the state-specific calculation the optimization proceeds by minimizing the energy of one chosen electronically excited state. The resulting orbitals are orthogonal, but describe best only this one chosen state.

Alternatively, the state-averaged calculation minimizes a weighted average of energies of several chosen states. We can choose weights for these states arbitrarily (although they must be positive), but it is usual to assign the largest weight to the ground state. The advantage of this method over the state-specific one is that it produces a set of orbitals (that are also orthogonal) describing in the best way possible (for a fixed set of the weights) all chosen electronic states.

A drawback of the state-averaged method is that usually the quality of the description of a larger number of electronic states using one common set of orbitals is poorer than the description of one given state using orbitals optimized only for this state as performed in a state-specific calculation. On the other hand the state-averaged CASSCF calculation is intrinsically more stable than the state-specific calculation, because it avoids the so called root-flipping problem [86]. The state-averaged method is always used in this work to obtain the CASSCF orbitals, because it suits best our need to describe in an optimal way many target electronic states using one set of orthogonal orbitals.

2.6 Scattering models

This section is devoted to a detailed presentation of the scattering models used throughout this work and their properties. These models as described here are standard scattering models used in numerous calculations employing the molecular R-matrix method. In Section 2.3.1 we introduced the R-matrix basis functions (2.42):

$$\Psi_k^\Gamma(\mathbf{x}_1,\ldots,\mathbf{x}_{N+1}) = \mathcal{A}\sum_{i=1}^{n_b}\sum_{j=1}^{n_{c,i}}\Phi_i(\mathbf{x}_1,\ldots,\mathbf{x}_N)\gamma_{ij}(\mathbf{x}_{N+1})a_{ijk} + \sum_{i=1}^{m}\chi_i^\Gamma(\mathbf{x}_1,\ldots,\mathbf{x}_{N+1})b_{ik}, \tag{2.87}$$

and stated that the particular type and number of target states and L^2 functions included in this Close-Coupling expansion define the scattering model *for molecular R-matrix calculations.*

More generally a scattering model can be defined as including specific type(s) of electron-molecule interaction (e.g. exchange interaction, polarization of the target molecule and/or effects associated with coupling of target electronic states during the collision). Therefore, one should be able to compare the results of calculations using different computational methods (see Section 1.2). However, the way the electron-molecule interaction is modelled differs (very much in some cases) depending on the computational method used. As a consequence comparing the results of calculations using scattering models of the same type, but different computational methods is not straightforward. For the same reason the properties of the scattering models described below are strictly-speaking valid only within the molecular R-matrix method.

Among other parameters which enter the specification of an R-matrix scattering calculation are the continuum basis set (or more generally: the number of continuum partial waves included) and the R-matrix radius. However, in this section we do not discuss the choice of these parameters (nor the choice of the atomic basis set) and focus only on the description of the scattering models, i.e. we describe the different levels of approximation at which the electron-molecule interaction can be described.

The choice of an appropriate scattering model for a given target molecule depends first of all on the energy range of the incoming electron. For energies above the ionization threshold it is necessary to also include in the calculation the channels corresponding to the ionized target molecule (in order to represent the second electron in the continuum). In this work we focus only on electron energies lying below the ionization threshold of the molecule. For

reasons explained below, the scattering models described here are capable of the accurate modelling of the electron-molecule interaction only below the ionization threshold.

2.6.1 Static Exchange approximation

The simplest scattering model we employ is the Static Exchange (SE) model in which only one target wavefunction (describing the ground state of the molecule), represented at the Hartree-Fock level, is included in expansion (2.87). The L^2 functions χ_i^Γ also take a simple form, which reflects the nature of the SE approximation in which the target molecule is not allowed to relax (polarize) in the presence of the incoming electron. We can write these L^2 functions in the following way:

$$\chi_i^{SE} : (\text{ground state})^N(\text{virtual})^1, \tag{2.88}$$

which represents the N electrons of the target molecule occupying the ground state configuration (HF) orbitals, while the scattering electron enters one of a selected number of virtual orbitals. The SE approximation is capable of describing only shape electron resonances, but these appear too high in energy due to an incomplete modelling of the interaction between the target and the scattering electron. The SE model can also be defined as the one in which the scattering electron moves in the static potential of the molecule and which includes the exchange interaction between the scattering electron and the electrons of the target molecule [87, p.522]. This makes the SE model well defined and therefore it can be used, in principle, to compare different approaches for solving the electron-molecule scattering problem. The advantage of the multiconfigurational representation (2.87) of the electron-molecule interaction as opposed to effective potential methods (see Section 1.2) is the exact inclusion of the exchange interaction in all scattering models. The number and symmetries of the virtual orbitals included in the SE model (equation (2.88)) depends on the number and symmetries of the shape resonances present in the system. Since each shape resonance can be understood as capturing the scattering electron in a unique virtual orbital, inclusion of each of these virtual orbitals in the SE model is essential for the shape resonances to appear in the calculated scattering data.

2.6.2 Static Exchange plus Polarization approximation

At the level of the Static Exchange plus Polarization (SEP) approximation, we still include only the ground state wavefunction in expansion (2.87), but the molecule is now allowed to be

polarized by the incoming electron, which is reflected in the choice of the L^2 configurations. In addition to those described by (2.88), we include configurations of the type:

$$\chi_i^{SEP} : (\text{core})^{N_c}(\text{valence})^{N-N_c-1}(\text{virtual})^{1+1}, \tag{2.89}$$

where the core orbitals of the molecule are always doubly occupied by N_c electrons and the molecule is allowed to polarize by promoting one electron from the valence space to a selected number of virtual orbitals, which are also available for the scattering electron. The presence of the frozen core in the model is optional and depends on the overall size of the scattering calculation, i.e. in smaller systems it might be possible or even desirable to allow excitations from the core orbitals. The SEP approximation as described can also reveal core-excited resonances associated with single excitations of the target molecule.

However, the R-matrix SEP models suffer from the appearance of so called pseudoresonances and we will see examples of these in the following chapters. These are structures in the eigenphase sums, time-delays and cross sections which have the shape characteristic of resonances and usually appear at higher energies (at least above the first excitation threshold). The pseudoresonances are unphysical and are the result of the multiconfigurational description of the correlation/polarization by means of the L^2 functions (2.89). The polarization of the molecule is modelled, as explained above, by single-excitations of the target molecule from the valence space to the virtual space. Some configurations of this type are associated with the main configurations of the excited states of the molecule, i.e. they have the form of one target electron excited to one of the virtual orbitals and the scattering electron also occupying a virtual orbital. Therefore some of the configurations (2.89) can couple the ground state with the excited states. In this case the target electronic states coupled with the ground state have the form of single-configurations built on single excitation from the valence space to one virtual orbital. As a result, the outgoing probability flux should be allowed to flow also to the channels corresponding to these electronic states of the molecule. However, these channels are not included in the SEP calculations in the outer region: it is their absence which leads to the appearance of the pseudoresonances. It can be impossible to differentiate between pseudoresonances and real physical structures in the eigenphase sums and/or cross sections, making it difficult to identify core-excited resonances from the results of the SEP calculations.

2.6.3 Close-Coupling approximation

The most sophisticated model we use is the Close-Coupling approximation (CC) in which the eigenfunctions Ψ_k^Γ have the full form (2.87) with a number of target electronic excited states included. The term Close-Coupling stands for the fact that from a formally infinite number of states needed for the exact representation of the $N+1$ wavefunction [18], we include in the expansion (2.87) only the electronic states which are energetically closely-coupled. One of the most important aspects of scattering calculations based on the CC expansion is that of balance. This means that the description of the N-electron target electronic states Φ_i should be of the same quality as description of the $N+1$ electronic basis functions Ψ_k^Γ of the electron-molecule collision problem. This requirement is reflected in a particular choice of the target configuration interaction (CI) model and the L^2 functions to be included in (2.87). The problem of balance is highly non-trivial as the target states Φ_i and the basis functions Ψ_k^Γ are in fact solutions of different Schrödinger equations. It is very difficult to find models which lead to solutions of the same "quality" without imposing unrealistic demands on the computational resources[¶]. In our calculations, we choose to base our target models around the complete active space (CAS) CI representation of the target wavefunction. This model has been found to produce satisfactorily balanced results for small targets [88] when a simple set of L^2 functions suffices. These L^2 configurations have the form of the target CAS configurations, but with one extra electron (the scattering electron) entering the CAS:

$$\chi_i^{CC} : (\text{core})^{N_d}(\text{CAS})^{N-N_d+1}, \tag{2.90}$$

where N_d is the number of electrons frozen in doubly occupied target orbitals and CAS represents the orbitals of the active space. Similarly to the case of the SEP L^2 functions (2.89), the frozen "core" is optional (for sufficiently small molecules it might be possible to allow excitations from these orbitals).

For molecules with larger polarizabilities (as is the case for the molecules studied in this work - see Section 2.6.4) it is necessary to expand this scattering model in order to achieve a good description of the resonances. Consequently, balance is harder to achieve. Dora et al. [59] in their study on uracil introduced CC models in which the L^2 functions have the

[¶]Exactly balanced models are those, for example, based on the full CI method. For practical reasons the use of this method for molecules of our size (i.e. number of electrons) is not possible at present.

following form:

$$\chi_i^{CC} : \begin{cases} (\text{core})^{N_d}(\text{CAS})^{N-N_d+1}, \\ (\text{core})^{N_d}(\text{CAS})^{N-N_d}(\text{virtual})^1, \end{cases} \tag{2.91}$$

where the first set of configurations is the same as in (2.90). The second set of configurations can be constructed in two different ways leading to two different CC models:

A: In this model the L^2 configurations are "contracted" with the target CI wavefunctions, so that the occupation of each virtual orbital of the appropriate symmetry (dictated by the symmetry of each of the target states) only contributes one (generalized) CSF. Consequently, these configurations are of the same type as the ones involving the orbitals of the continuum, see (2.87).

B: No contraction of the L^2 functions with the target CI wavefunctions is performed and all configurations satisfying only the symmetry constraints of the $N+1$ wavefunction are generated.

We call the models A and B, respectively, *contracted* and *uncontracted* CC models. Since no contraction is imposed on the L^2 configurations of model B, this model typically generates a much larger number of CSFs than model A. In principle, more complicated CC models (in terms of the number of the CSFs generated) can be constructed by allowing excitations from the CAS, i.e. it is possible to construct CC models using additional configurations of the type:

$$\chi_i^{CC} : (\text{core})^{N_d}(\text{CAS})^{N-N_d-1}(\text{virtual})^2. \tag{2.92}$$

This model is called C in the work of Dora et al. Another way of looking at these configurations is to think of them as single excitations of the target molecule's electrons from the CAS to a subset of the virtual orbitals, which are also available for the scattering electron. Excitations of the target molecule's electrons outside of the CAS can significantly contribute to the description of the target electronic wavefunctions. However, these configurations are not included in the CI wavefunctions of the target electronic states $\Phi_i(\mathbf{x}_1, \ldots, \mathbf{x}_N)$. Consequently, this CC model can suffer from severe balance problems and we do not use it in this work.

Dora et al. compared the results of the CC calculations on uracil which used models A and B and found, as expected, that the model A does not recover a sufficient amount of

polarization/correlation effects required for a good description of the resonances. Model B was found to be a good compromise between the size of the calculation, balance and the quality of description of the electron-molecule interaction. Model B was used in our work for all CC calculations.

CC models can also suffer from the presence of the pseudoresonances. We can avoid this by including in the expansion (2.87) all electronic states whose energies lie in the scattering energy range of interest. In the CC models used in this work, we do not include in (2.87) the electronic wavefunctions representing the ionized target molecule. Inclusion of these states is crucial for accurate modelling of collisions for electron energies straddling the ionization potential of the molecule. Therefore our calculations are intrinsically less accurate in this energy region. The R-matrix with pseudostates method [89] is one of the methods which can be used to model the effects associated with electron impact ionization. This fully ab-initio method is based on the inclusion of discretized continuum states representing the ionized target in the Close-Coupling expansion (2.87). These states are obtained from target orbitals and so-called pseudocontinuum orbitals which are used to represent the ionized electron. The exact procedure leading to generation of the pseudostates and further details of the method can be found in [89].

2.6.4 General remarks

The precise choice of the number and type of the orbitals chosen for calculations describing different target molecules will be detailed later. It is important to mention that the SEP and the CC models as described above do not exhibit "convergence" of the resonance positions as the number of virtual orbitals included in the model is increased. This property of our scattering models is directly related to the issue of balance as explained above. We note that the size (i.e. the number of the L^2 functions generated) of an optimal scattering model is closely related to the behaviour of the target molecule under the presence of a static electric field. The response of the target molecule to a static electric field can be expressed in the lowest order of perturbation theory in terms of the polarizability of the molecule [1]. Accurate representation of the polarizability and perhaps also other higher-order terms from the perturbation expansion is therefore important for the scattering model to give accurate values for observables. The polarizability generally increases with the size of the molecule. The calculated values of polarizabilities of the diazine molecules (see also Table 3.2 in Chapter 3) lie in the range $40 - 60\ a_0^3$ (depending on the computational method) [90].

For comparison, the polarizability of water is $4 - 9\ a_0^3$ [90]. Therefore it is the relatively large polarizabilities of the molecules studied in this work together with the large number of interacting electrons which are the main factors responsible for the complexity and size of our scattering models and in turn their large computational cost.

Finally we note, that despite the fact that the properties of the models introduced in this section are strictly speaking valid only for molecular R-matrix calculations, some of their features prevail also in other computational methods (see Section 1.2). For example the appearance of pseudoresonances in the SEP models (and potentially also in the CC models) is common to all methods relying on the multiconfigurational description of the electron-molecule interaction, which is also used in the Schwinger and the Kohn variational methods. On the other hand pseudoresonances do not appear in the current implementations of the methods using effective potentials (SA-SCE and FERM3D methods - see Section 1.2). These methods are one-electron methods in which only the motion of the scattering electron is modelled (using effective potentials). In the current implementations of these methods no coupling of channels corresponding to different electronic states is taken into account and therefore no pseudoresonances appear in these calculations.

2.7 UKRmol suite of codes

The UKRmol suite of codes [72] is an implementation of the R-matrix method for electron molecule collisions as described in the preceding sections and was used to perform all scattering calculations.

The flow of the R-matrix scattering calculation can be divided into three steps:

- Target calculation
- Inner region calculation
- Outer region calculation.

In the target calculation we obtain the target wavefunctions Φ_i which enter the R-matrix basis functions (2.42) and their energies E_i and the transition moments needed to build the outer region potential. In the inner region calculation the inner region Hamiltonian is diagonalized obtaining the coefficients a_{ijk}, b_{ik} and the energies E_k of the R-matrix basis functions (2.63). In the outer region calculation the R-matrix is constructed and propagated, obtaining the **K**-matrices for selected energies. Various other quantities can also be calculated once the **K**-matrices have been obtained. We now describe the individual steps of the calculation.

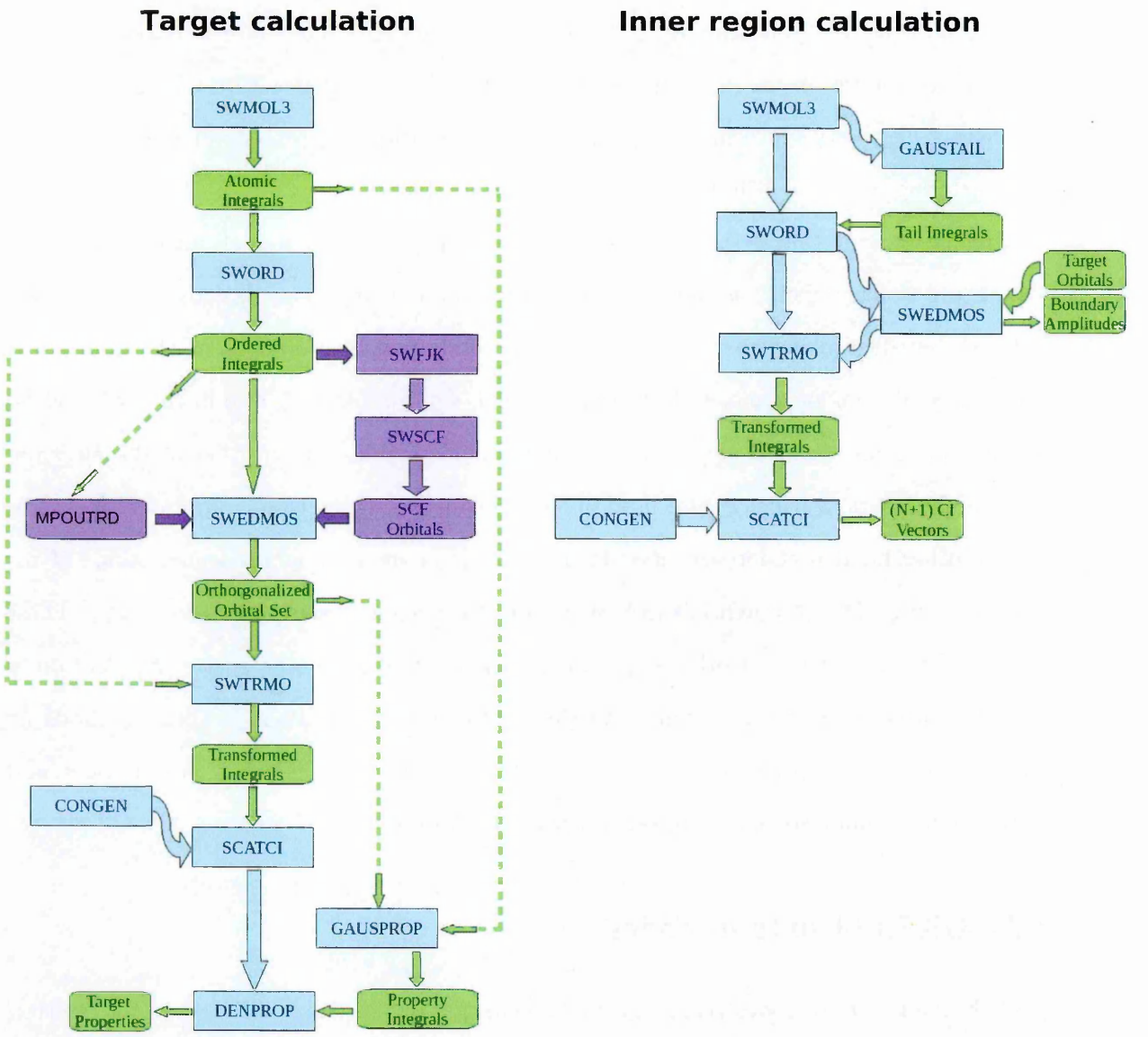

Figure 2.3: The sequence of programs called in the target and inner region calculations. The individual programs are shown in blue boxes and the calculated quantities in green boxes. Purple boxes show optional steps. Adapted from [72].

The flow of the target calculation is shown on the left side of Figure 2.3. The geometry of the molecule and the GTO target basis set are specified first and used as an input for the SWMOL3 program, which calculates the molecular integrals. The calculated integrals are then ordered by SWORD. If HF target orbitals are used, these can be obtained using the SWFJK and SWSCF programs (in this work, however, we always use orbitals obtained from MOLPRO, even in the case of HF orbitals). If orbitals generated by another suite are used, these need to be preprocessed before. The program MPOUTRD was developed during this work to interface between the MOLPRO orbitals (HF or SA-CASSCF) and the UKRmol suite. This program generates input for the SWEDMOS program, which orthogonalizes the orbitals and saves them in a format appropriate for use by the other modules. The

SWTRMO program transforms the integrals over the elementary atomic GTOs into integrals over the target molecular orbitals. The basis of the CSFs is then specified on input to the CONGEN program, which generates these configurations. The CSFs are then used together with the transformed integrals as input for the SCATCI program, which builds and diagonalizes the target molecule's Hamiltonian to obtain the target states and their energies. Finally, the target properties (i.e. dipole and quadrupole permanent and transition moments) are calculated. This is performed using the DENPROP program, which is fed output from the SCATCI and GAUSPROP programs; the latter calculates the property integrals for the atomic GTO basis functions.

The inner region calculation uses many of the same programs as the target calculation and its flowchart is shown on the right hand side of Figure 2.3. In this case however we have to introduce, on input to SWMOL3, the extra continuum GTO basis set describing the scattering electron. The set of optimized continuum GTOs is produced separately using the NUMCBAS and GTOBAS modules as described in [91]. Continuum GTOs (partial waves of the scattering electron) with $l \leq 4$ or $l \leq 5$ are used routinely in the R-matrix calculations. First, the molecular integrals over all space including the ones involving the continuum GTOs are calculated by the SWMOL3 program. The GAUSTAIL program then calculates the tails of the integrals (i.e. the integrals between the R-matrix boundary and infinity) involving the continuum GTOs in order to obtain integrals over the inner region only. These tail integrals are then subtracted from the molecular integrals using the SWORD program which also orders all integrals. The continuum orbitals are obtained using the SWEDMOS program: the continuum GTOs are first Schmidt orthogonalized to a selected subset of the target molecule's orbitals and then symmetrically orthogonalized among themselves. The final set of continuum orbitals is obtained by deleting those continuum orbitals with eigenvalues of the overlap matrix smaller than a selected (deletion) threshold. The boundary amplitudes corresponding to the amplitudes of the radial parts (2.44) of the continuum orbitals on the R-matrix sphere are calculated. These quantities are needed for subsequent use in the outer region calculation. Similarly to the target calculation, SWEDMOS is then followed by the SWTRMO program, which transforms the integrals over the primitive GTOs into integrals over the target and the continuum orbitals. The CONGEN program is then used to generate the basis of CSFs for the R-matrix basis functions (2.42). The set of orbitals from which the CSFs are constructed now contains also the continuum orbitals. Finally, the inner region Hamiltonian is diagonalized using the SCATCI program, obtaining the coefficients a_{ijk}, b_{ik} and the energies E_k of the R-matrix basis functions.

The flowchart for the outer region calculation is shown on Figure 2.4. The calculation starts by calling the SWINTERF program, which gathers all the required information from the target and inner region calculations, i.e. the target properties, the boundary amplitudes and the CI vectors of the R-matrix basis functions. On output SWINTERF produces channel data, the coefficients of the coupling potentials and the surface amplitudes required for the construction of the R-matrix. The program BOUND can be used to calculate the energies of bound states of the $N + 1$ electron system. The main workhorse of the outer region calculation is the module RSOLVE, which constructs and propagates the R-matrix, performs the asymptotic expansion and calculates the **K**-matrices. In a standard R-matrix calculation, the **K**-matrices are then processed by the EIGENP program to calculate the eigenphase sums and by the TMATRX and IXSEC modules to obtain the **T**-matrices and from them the integral elastic (and inelastic) cross sections. Accurate resonance parameters, i.e. the position and the width, can be obtained by processing the eigenphase sum and the **K**-matrices using the RESON and the TIMEDEL programs respectively. In the vicinity of a resonance the RESON program fits the eigenphase sum to the Breit-Wigner formula (2.74) and the TIMEDEL program fits the time-delay spectrum corresponding to the largest eigenvalue of the **Q**-matrix to the Lorentzian function $L(E)$ - see equation (2.77). Both of these programs call the RSOLVE module repeatedly to obtain a finer energy resolution of the eigenphase sum or the time-delay spectrum as needed by the fitting algorithm. Finally, the POLYDCS program [92] developed by N.Sanna and F. Gianturco, external to the UKRmol suite of codes, can be used to obtain the elastic differential cross sections (DCS) for selected electron energies. This program is capable of including the Born correction [18] for the elastic DCS to account approximately for the higher partial waves not included in the ab-initio calculation. The BORNCROS program, utilizing the approach of Chu and Dalgarno [93], can be used to calculate the Born correction for the inelastic cross sections.

2.7.1 Programs developed as a part of this work

During the course of this work several programs were developed for use with the UKRmol suite of codes. These are: MPOUTRD, RADDEN and TD. The first of them, the MPOUTRD program, takes on input the textual output from MOLPRO containing the molecular orbitals and processes it for use in the R-matrix codes. The orbital coefficients are sorted and normalized according to the conventions adopted in the R-matrix codes and output in a text file, which is then used as an input for the SWEDMOS program. The MPOUTRD program

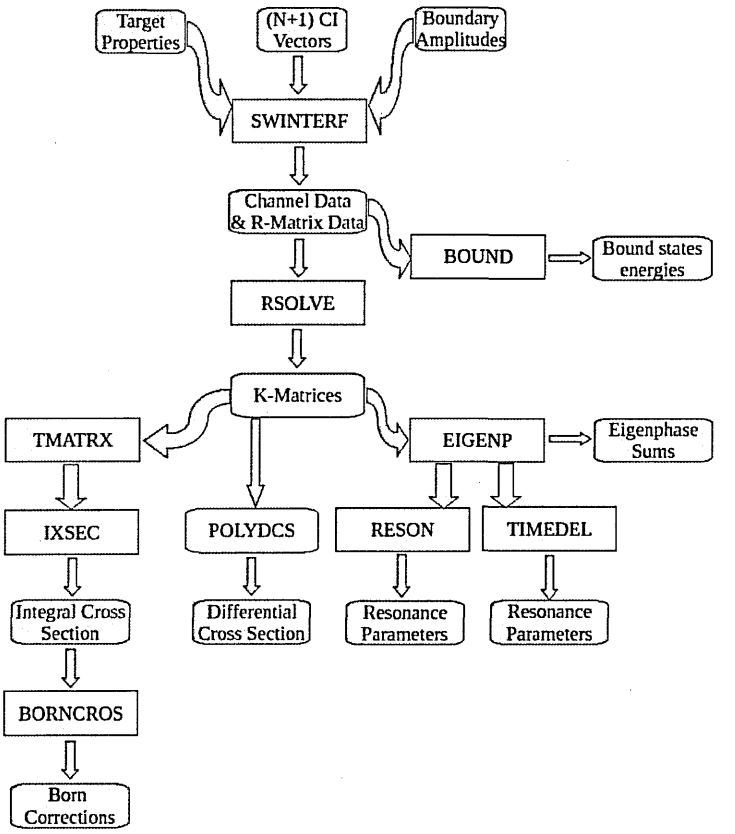

Figure 2.4: The programs used in the outer region calculation. The individual programs are shown in blue boxes and the calculated quantities in green boxes. The POLYDCS program, which is not part of the UKRmol suite, is shown in yellow. From [72].

also calculates the density matrices of the target orbitals for optional use in the RADDEN program. Density matrices corresponding to the target electronic states can be obtained as well, if present in the MOLPRO output file.

The RADDEN program calculates the radial charge densities of the target orbitals (or the target electronic states), which can be used to estimate the appropriate value of the R-matrix radius. Input for this program is provided either by the MPOUTRD program as described above or using a file written in the MOLDEN format [94], containing the target GTO basis set, the molecular geometry and the target orbitals. The calculation of the radial charge densities is performed utilizing adaptive numerical integration over the angular variables θ and ϕ of the charge density $\rho(r, \theta, \phi)$, obtained from the density matrices of the orbitals (or the electronic states) and the atomic GTO basis functions.

In order to access the information available in the **Q**-matrix the TD program was developed, which transforms the **K**-matrices calculated by the RSOLVE program into **S**-matrices and then calculates the **Q**-matrices using the equation (2.75). The TIMEDEL program did not work with the current version of the outer region code and does not provide the same functionality as the TD program: TIMEDEL outputs only the largest eigenvalue of the **Q**-

matrix (and the corresponding branching ratios) for each scattering energy. The TD program allows the user to select how many eigenvalues to output for each energy. The program also calculates, for energies of interest, the diagonal elements of the **Q**-matrix, the branching ratios corresponding to selected eigenvectors and the time-delays Δt_{ij} (see Section 2.4). This extra functionality of the TD program is especially useful for analysis of overlapping resonances and for an additional analysis of the eigenphase sums described later. However, TIMEDEL performs automatic fitting of the time-delay spectra to obtain the positions and widths of the Lorentzian functions (see equation (2.77)), whereas the time-delay spectra obtained from the TD program need to be fitted using an external program.

Chapter 3

Electron collisions with pyrazine: setting up the models

The calculations of electron collisions with pyrazine form the core of this work. We used this molecule to test and establish the scattering models for use on the rest of the targets. In this chapter we discuss in detail the properties of these models and the methodology chosen for the analysis of the results. A significant part of this chapter has been published [95, 96].

Structurally, pyrazine differs from the other two diazines (see Figure 3.1) by its (high) D_{2h} symmetry (the other diazines possess C_{2v} symmetry) which implies a zero ground state dipole moment. As we will see later, the high symmetry and the non-dipolar ground state make pyrazine especially suited for theoretical calculations.

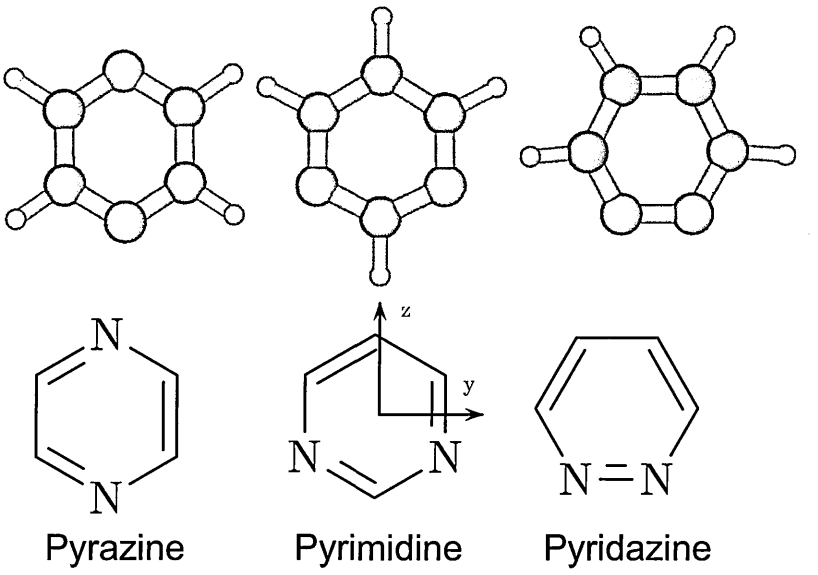

Figure 3.1: Balls and sticks models of diazines and their chemical structures (bottom). Nitrogens are blue, carbons orange and hydrogens white. Also shown is the choice of the coordinate axes for our calculations.

In this chapter we review first the literature available on electron collisions with diazines and then, in Section 3.2, we discuss the literature concerning electronic states of pyrazine. We review the literature for the three diazines together because due to their similarity, these molecules are often studied together which is indeed the case also for this work. In Section 3.3 we describe in detail our target calculations. The choice of the scattering models and the effect they have on the positions of the low-lying π^* resonances in pyrazine is described in Section 3.4. The calculated elastic and inelastic cross sections for various models are compared in Section 3.5. Finally, we discuss in detail the resonances we found in pyrazine. This is done in Section 3.6, where we first describe the methods used for their analysis and then we discuss all resonances in detail. We conclude with a summary of the main results of this chapter.

3.1 Low-energy electron collisions with diazines

The main results of scattering calculations on the constituents of DNA were presented in Section 1.3.1. Here we focus on the results available for the diazine molecules: pyrazine, pyrimidine and pyridazine. Low-energy electron collisions with diazines were first studied by Nenner and Schulz [32] in 1975 using electron transmission spectroscopy (ETS). This study provided information on the low-lying electron resonances of all azabenzene molecules*. The authors also used polarography to measure the electron affinities of these molecules. The electron affinities were found to be positive which means that diazines support bound electronic states of the negative ion. All diazines were found to possess three low-lying (< 4.3 eV) π^* resonances. Table 3.1 summarizes the information on the low-lying resonances in diazines from the work of Nenner and Schulz.

The lowest-lying π^* resonance was interpreted by Nenner and Schulz to arise from trapping of the scattering electron into the lowest-lying unfilled π^* orbital. This trapping leads to the formation of a bound negative ion. The ground vibrational state of this negative ion appears below that of the ground vibrational state of the neutral molecule. Consequently, the observed vibrational progressions in the transmission spectra for this resonance were associated with excited vibrational states of the ground state of the negative ion. The second π^* resonance arises from trapping of the electron into the second unfilled π^* orbital and can be thought of as the first excited state of the negative ion. The third π^* resonance has a slightly different character than the lower-lying ones. Because of its position (above 4 eV, that is, above some

*Azabenzene molecules are substituted benzene rings with one to four carbons replaced by nitrogen atoms.

Resonance	π_1^*	π_2^*	π_3^*
Pyrazine			
Symmetry	$^2B_{3u}$	^2A_u	$^2B_{2g}$
Experiment[32]	$0.065 - 0.8$	$0.87 - 1.2$	≈ 4.10
Pyrimidine			
Symmetry	$^2A_2$	$^2B_1$	$^2B_1$
Experiment[32]	$0.25 - 0.7$	$0.77 - 1.6$	≈ 4.24
Experiment[35]	0.39	0.82	4.26
Pyridazine			
Symmetry	$^2A_2$	$^2B_1$	$^2A_2$
Experiment[32]	$0.317 - 0.65$	$0.73 - 1.5$	≈ 4.05

Table 3.1: The positions (in eV) and symmetries of the π^* resonances in diazines as determined from the experiment of Nenner and Schulz [32]. The symmetries of the resonances coincide with the symmetries of the orbitals in which the electron is trapped.

of the excited states of the diazines) this resonance was suggested to have a *mixed* core-excited shape character. While this resonance can be interpreted as arising from trapping of the electron into the third unfilled π^* orbital, it was suggested by Nenner and Schulz that the scattering wavefunction also contains significant admixtures of configurations based on the lowest-lying triplet excited states. Nenner and Schulz also observed a higher-lying structure above the third one in the transmission spectra, but did not interpret it.

ETS was also applied by Modelli et al. [35] to electron collisions with pyrimidine. A higher-lying structure above the third one in the transmission spectra was interpreted as a core-excited resonance lying around 5.5 eV. It is therefore possible that the higher-lying structure observed by Nenner and Schulz in the other diazines also corresponds to a core-excited resonance.

Experimental cross sections for electron collisions with diazines are not available at present with the exception of pyrimidine. The absolute elastic differential cross sections [97] in the $(50 - 300$ eV) energy range, and absolute differential and integral elastic cross sections in the $3 - 50$ eV range [34] have been measured. The differential cross sections for electron impact electronic excitation of pyrimidine and benzene were measured by Jones et al. [98] for 15 eV and 30 eV. Later, Jones et al. focused on pyrimidine [99] and measured the differential cross sections for electron impact electronic excitation for electron energies in the range $15 - 50$ eV. Measurements have also been performed for condensed pyrimidine [100], for which vibrational and electronic excitation cross sections were determined.

Calculations for electron collisions with a diazine molecule were first performed for pyrazine by Winstead and McKoy [33, 60] using the SMC method (see Section 1.2). Their study on pyrazine was motivated by the large discrepancies between the calculated [53, 54, 55, 56, 58,

	Pyrazine	Pyrimidine	Pyridazine
Ground state energy [H]	−263.394	−263.402	−263.365
μ [D]	-	2.334	4.22
α [a_0^3]	≈ 59	≈ 58	≈ 58

Table 3.2: Ground state energies [104, 105, 106], experimental dipole moments (μ) [107, 108] and isotropic polarizabilities (α) of the diazine molecules. The values of the isotropic polarizabilites were taken from the CCCBDB database [90]: they were calculated using the Density Functional Theory (DFT), B3LYP functional and the 6-311+G(3df,2p) basis set.

71, 101] and the measured positions of the third π^* resonance in the pyrimidinic nucleobases. In order to provide insights into this discrepancy they included in their SEP calculations configurations based on the configurations of the lowest-lying triplet excited states of pyrazine and observed a significant lowering of the position of the third π^* resonance towards its experimentally determined position. This and their later study on pyrimidine [34] confirmed the earlier hypothesis of Nenner Schulz that the third π^* resonance in diazines has mixed core-excited shape character. The mixed character of the resonance means that the resonance is described not only by configurations characteristic of a shape resonance (i.e. electron trapped by the potential of the ground state in an empty virtual orbital), but also by configurations based on (in this case) the configurations of the low-lying triplet excited states. Calculations on electron collisions with pyrimidine were also performed using the Independent Atom Model [102] to determine total and elastic integral cross sections up to 10 keV (integral elastic cross sections for positron collisions for energies up to 45 eV have also been calculated with this method). No scattering calculations incorporating electronically inelastic channels were available prior to this work. As mentioned in Section 1.4, one of the goals of this work was to perform inelastic scattering calculations to close this knowledge gap and to provide more insights into the formation of resonances at higher energies (> 5 eV).

3.2 Electronic structure of diazines

As mentioned earlier, diazines can be thought of as simple models for the pyrimidinic nucleobases. However, all diazines are prevalent in herbicides and pharmaceutical drugs [103] and therefore have also been studied in a different context. This has stimulated theoretical and experimental research into their electronic structure. This is especially true for pyrazine and pyrimidine, whose electronic spectra have been investigated in a number of studies. The availability of this detailed information has been very useful for our work.

Table 3.2 summarizes the basic properties of the diazine molecules (ground state energies, dipole moments and polarizabilities). These molecules possess 42 electrons, have totally

symmetric ground state wavefunctions and positive electron affinities [32]. Pyrazine is a non-polar molecule (D_{2h} symmetry), whereas pyrimidine and pyridazine (C_{2v} symmetry) have ground state dipole moments, whose values are listed in Table 3.2.

As our work places emphasis on the inelastic calculations, accurate information on the electronic excited states of the studied molecules is important. The literature on the electronic states of azabenzenes up to 1988 was reviewed by Innes et al. [109]. The experimental and theoretical work of Walker and Palmer from the early 90s concentrated specifically on electronic states of the azabenzene molecules. They used the vacuum UV (VUV) and the electron energy loss techniques complemented by multireference CI calculations to investigate the electronic spectra of these molecules. For our purposes, their work on diazines (pyrazine [104], pyrimidine [105] and pyridazine [106]) is the most useful. Their results include spectral assignments of a number of valence excited states of singlet and triplet character and also several Rydberg states. Several studies [110, 111, 112] focused specifically on the Rydberg states of diazines. The most comprehensive experimental information on electronic excited states available today is for pyrazine and pyrimidine from the recent studies of da Silva et al. [113] and Stener et al. [114]. The study of Stener et al. also used the Time-Dependent DFT (TDDFT) method to aid the spectral assignment of the excited states of the two molecules. The excited states of pyrimidine were also studied by Fischer et al. [115]. The experimentally determined vertical ionization energies of pyrazine, pyrimidine and pyridazine are [116, 117, 116]: 9.63 eV, 9.730 ± 0.030 eV and 9.310 eV respectively. Because these values are relatively low, the Rydberg and valence excited states tend to overlap [113].

Since in our calculations we describe the target electronic states using the CASSCF method, results of studies utilizing this approach are especially important for our work. For the molecules of interest for this work, the CASSCF method was first applied to benzene [118] and then by Fülscher et al. [119] to the azabenzene molecules. The excited states of pyrazine were studied extensively in the work of Weber and Reimers [120] using a range of different methods, including the CASSCF. Other theoretical studies using the CASSCF method for calculations on diazines are those of Schreiber et al. [121] and Woywod et al. [122]. The latter study focused on singlet Rydberg excited states of pyrazine and their description using the CASSCF method. Li et al. [123] studied benzene and selected azabenzenes using the symmetry adapted cluster-configuration interaction method.

3.2.1 CAS models used in this work

In this work we use the CAS models devised by Fülscher et al. [119] and Weber and Reimers [120]. From the range of the CAS models studied by these authors, we choose the CAS(10,8) model in which 10 electrons are distributed among 8 valence orbitals: 6 orbitals of the π type and two orbitals of the n type (of σ symmetry). The latter orbitals correspond to the lone-pair orbitals on the two nitrogen atoms and their inclusion in the active space is necessary for the description of the $n \rightarrow \pi^*$ excited states which arise in the diazine molecules. The CAS(10,8) model is the smallest one tested by Weber and Reimers, but was found to describe the valence excited states to a similar level of quality as the larger active spaces: CAS(12,11) and CAS(12,14). We apply this CAS model to the target calculations of all diazines. The larger active spaces are appropriate for calculations aiming at the accurate description of the higher-lying valence states, Rydberg excited states or for different molecular geometries. The CAS(10,8) model does not include any Rydberg orbitals in the active space. Inclusion of all orbitals [114] necessary for an accurate description of these states would render our subsequent scattering calculations too large to handle. It is for this reason that we have chosen to use the smallest realistic active space. As we will see in the following chapters the choice of the small active space results in a poor description of the Rydberg and higher-lying valence excited states of diazines in our calculations, as expected.

3.3 Target description

We used the geometry as determined from experiment [109]. The ground state configuration of pyrazine is: $1a_g^2\ 1b_{1u}^2\ 2a_g^2\ 1b_{2u}^2\ 2b_{1u}^2\ 1b_{3g}^2\ 3a_g^2\ 3b_{1u}^2\ 2b_{2u}^2\ 4a_g^2\ 2b_{3g}^2\ 5a_g^2\ 3b_{2u}^2\ 4b_{1u}^2\ 4b_{2u}^2\ 1b_{3u}^2\ 3b_{3g}^2$ $5b_{1u}^2\ 1b_{2g}^2\ 6a_g^2\ 1b_{1g}^2$.

In order to obtain optimal target orbitals for the description of the scattering process, several basis sets were tested. We have found our scattering results for low electron energies ($\lessapprox$ 4 eV) particularly sensitive to the quality of the target orbital description and we therefore extended the analysis of basis set choice carried out by Dora et al. [59]. The study of Dora et al. on uracil was chosen as a starting point for our models because of the similarity of uracil to the molecules studied in this work. Specifically, Dora et al. used the basis set cc-pVDZ, while for their calculations on pyrazine Winstead and McKoy [33] used a larger 6-311++G** basis set, containing diffuse functions on all atoms; we tested these and another three similar basis sets (aug cc-pVDZ, cc-pVTZ and 6-311+G**). We used the Hartree-Fock SCF and the state-averaged CASSCF (SA-CASSCF) methods to generate the target orbitals;

the calculations were performed using MOLPRO 2009.1 [124]. The use of Modified Virtual Orbitals (MVO) [125] in SE scattering models of our type (see Section 2.6 below) had already been tested [59] and no significant differences found in the scattering results when compared with calculations using the HF orbitals. We therefore choose not to use this type of orbitals.

Since the number of configurations included in our scattering calculations based around the CAS model scales rapidly with the size of the active space, we chose to use the smallest realistic active space (10, 8) [120] (see Section 3.2.1) for our SA-CASSCF calculations. This active space comprises 10 electrons distributed among the 6 valence π orbitals and the two lone-pair σ orbitals located on the two nitrogen atoms. Consequently the frozen core in pyrazine comprises the orbitals 1-5 a_g, 1-4 b_{2u}, 1-4 b_{1u} and 1-3 b_{3g}. In the case of uracil, Dora et al. used the full π valence space augmented only by the lone-pair orbitals located on the two oxygen atoms.

We tested several averaging schemes (different number of states and/or weights) in the SA-CASSCF calculations, but found only small differences between the calculated vertical excitation energies of the electronic states. We also attempted an automatic optimization of the weights used in the averaging scheme. This optimization was performed by minimizing the root mean square error (RMSE) calculated from the differences between the observed and the calculated vertical excitation energies of the electronic states. The RMSE is a function of all weights used in the averaging. The RMSE was minimized using the Simplex and gradient BFGS methods available in MOLPRO. However, this approach did not produce RMSEs which were significantly better than the ones obtained from the calculations using equal weights. Therefore our preferred averaging scheme involves equal weights and includes the two lowest-lying excited states of each spatial and spin symmetry (singlet and triplet) and the ground state, i.e. $32 + 1$ states. Table 3.3 demonstrates clearly the insensitivity of the calculated excitation energies to the averaging scheme chosen: comparison with the results of Weber and Reimers [120], who used the same active space and the *state-specific* mode of the CASSCF calculations, in which each of the calculated excited states (and their target orbitals) were optimized individually, shows small differences. In our CC scattering calculations we used the orbitals obtained with the SA-CASSCF method to generate all electronic excited states with excitation energies lying below $\approx$ 10 eV. Table 3.3 lists excitation thresholds for additional states not included in the averaging procedure: these states correspond to the third excited state of some spin-space symmetries with excitation energy below $\approx$ 10 eV (with the exception of the $3\,^1A_g$ state which was included in the averaging scheme). Our calculated values for the vertical excitation energies differ only marginally ($\pm$0.15 eV) between the basis sets cc-pVDZ

No	cc-pVDZ	6-311+G**	Observed[a]	[120]	[122]	Symmetry
1	3.90	3.86	4.0	4.00	-	$1\,^3B_{1u}$
2	4.18	4.16	3.42	4.23	-	$1\,^3B_{3u}$
3_V	4.84	4.80	3.97	4.86	4.87	$1\,^1B_{3u}$
4	4.89	4.81	4.5	4.81	-	$1\,^3B_{2u}$
5_V	4.95	4.88	4.81	5.05	4.96	$1\,^1B_{2u}$
6	5.15	5.10	5.7	5.32	-	$2\,^3B_{1u}$
7	5.34	5.28	4.59	5.33	-	$1\,^3B_{2g}$
8_V	5.91	5.84	5.19	5.91	5.87	$1\,^1B_{2g}$
9	5.93	5.95	4.2	5.86	-	$1\,^3A_u$
10_V	5.98	6.00	4.72[c]	5.92	6.01	$1\,^1A_u$
11	7.13	7.09	-	-	-	$1\,^3B_{1g}$
12_V	7.27	7.24	6.10	7.20	7.23	$1\,^1B_{1g}$
13	7.34	7.27	-	-	-	$1\,^3A_g$
14	7.46	7.40	-	-	-	$1\,^3B_{3g}$
15	8.20	8.15	-	-	-	$2\,^3B_{2u}$
16_V	8.34	8.25	-	-	8.39	$2\,^1A_g$
17_V	8.35	8.28	-	-	8.30	$1\,^1B_{3g}$
18_V	8.46	8.36	-	-	11.66	$3\,^1A_g$
19	8.65	8.56	-	-	-	$3\,^3B_{1u}$
20_V	8.67	8.59	6.51	8.56	8.35	$1\,^1B_{1u}$
21	8.82	8.77	-	-	-	$2\,^3B_{2g}$
22_V	9.03	8.99	-	-	9.12	$2\,^1B_{2g}$
23	9.05	9.00	-	-	-	$3\,^3B_{2g}$
24	9.84	9.77	-	-	-	$2\,^3B_{3u}$
25	10.01	9.92	-	-	-	$3\,^3B_{3u}$
26_V	10.03	9.94	7.67	10.03	9.83	$3\,^1B_{2u}$
27_R	10.04	9.96	-	-	7.28	$2\,^1B_{3u}$
28	10.10	10.08	-	-	-	$2\,^3B_{3g}$
29	10.41	10.29	-	-	-	$2\,^3B_{1g}$
30_R	10.55	10.42	7.13[b]	-	7.37	$2\,^1B_{1g}$
31_V	10.60	10.46	7.67	10.53	10.21	$2\,^1B_{1u}$
32	11.06	10.92	-	-	-	$2\,^3A_u$
33_R	11.33	11.17	-	-	7.45	$2\,^1A_u$
34_V	11.70	11.69	-	-	11.19	$2\,^1B_{3g}$
35	12.51	12.38	-	-	-	$2\,^3A_g$

[a] Weber and Reimers [120] if a different reference is not given.
[b] Oku et al. [110].
[c] Li et al. [123].

Table 3.3: Vertical excitation energies, in eV, for the electronic excited states of pyrazine calculated in this work. For the singlet states, their character (valence or Rydberg) as determined in the work of Woywod et al. [122] is given as a subscript to the number of each state. The first two columns present results of our SA-CASSCF calculations using the active space $(10, 8)$ and the basis sets cc-pVDZ and 6-311+G**. The CASSCF calculations of Weber and Reimers [120] used the state-specific optimization, cc-pVDZ basis set and the active space $(10, 8)$. Woywod et al. [122] used aug cc-pVTZ basis functions on heavy atoms, cc-pVTZ basis functions on hydrogen atoms and the active spaces $(10, 8)$ for the valence excited states and $(10, 9)$ for the Rydberg states.

and 6-311+G**. The symmetry assignment of the experimentally measured electronic states was taken from Weber and Reimers [120].

Table 3.4 summarizes the results for the SA-CASSCF orbitals and all tested basis sets. We can see that although the energy of the orbitals in the active space does not differ significantly, that of the virtual orbitals, i.e. the orbitals not included in the doubly occupied

	Basis set	cc-pVDZ	aug cc-pVDZ	cc-pVTZ	6-311+G**	6-311++G**
	Hartree-Fock energy	−262.69726	−262.70930	−262.76069	−262.73551	−262.73558
	SA-CASSCF(10,8) energy	−262.77481	−262.78472	−262.83669	−262.81221	−262.81227
	Number of GTOs	104	174	236	156	160
Active space orbs.	$1b_{3u}$ (π)	−14.814	−14.950	−14.895	−14.970	−14.969
	$5b_{1u}$ (σ)	−11.897	−12.033	−11.952	−12.058	−12.057
	$1b_{2g}$ (π)	−11.347	−11.506	−11.446	−11.540	−11.539
	$6a_g$ (σ)	−9.515	−9.675	−9.619	−9.719	−9.718
	$1b_{1g}$ (π)	−8.406	−8.484	−8.438	−8.538	−8.537
	$2b_{3u}$ (π)	−0.542	−0.794	−0.700	−0.848	−0.847
	$1a_u$ (π)	1.955	1.770	1.860	1.734	1.735
	$2b_{2g}$ (π)	8.260	8.123	8.191	8.046	8.047
Virtual orbs.	$7a_g$ (σ)	5.380	0.967	4.256	1.770	1.163
	$5b_{2u}$ (σ)	5.804	1.145	4.547	2.101	1.291
	$6b_{1u}$ (σ)	6.469	1.290	5.204	2.210	1.596
	$4b_{3g}$ (σ)	6.640	1.573	5.295	2.686	1.798
	$3b_{3u}$ (π)	17.943	2.843	11.414	3.075	3.076
	$3b_{2g}$ (π)	20.023	3.283	13.142	3.680	3.681
	$2b_{1g}$ (π)	19.337	3.706	12.580	3.956	3.956
	$2a_u$ (π)	21.605	4.701	14.898	5.190	5.190

Table 3.4: Ground state energies of pyrazine (in Hartree) calculated using the Hartree-Fock and SA-CASSCF methods and energies (in eV) of the orbitals used in the active space together with the first SA-CASSCF virtual orbital of each irreducible representation. The virtual orbitals are ordered according to their energies as calculated using the 6-311+G** basis set. Details of the SA-CASSCF calculations are given in the text.

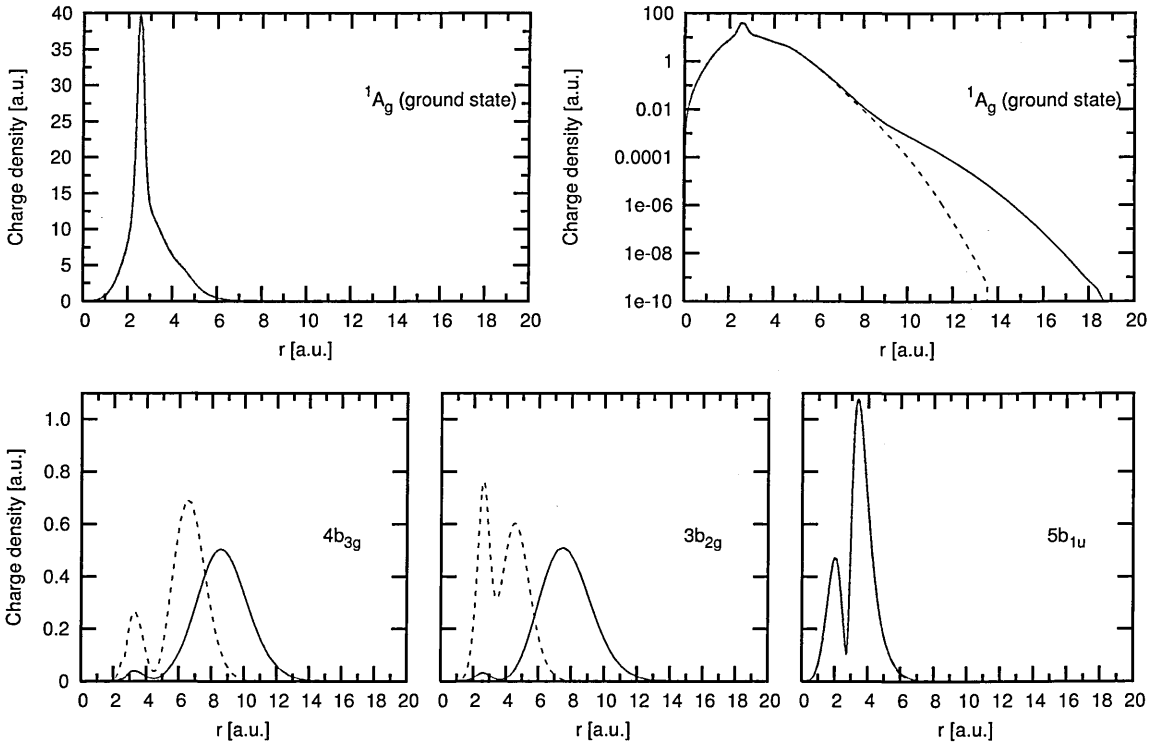

Figure 3.2: The upper panels show the radial charge densities of the ground electronic state of pyrazine (^1A_g) calculated at SA-CASSCF level in the basis sets cc-pVDZ (dashed blue) and 6-311+G** (solid red): the density on the left panel is plotted on a linear scale, while the same density is plotted on the right hand side panel on a logarithmic scale. The bottom panels show radial charge densities of SA-CASSCF orbitals $4b_{3g}$, $3b_{2g}$ and $5b_{1u}$ as calculated in both basis sets. All densities were calculated using the RADDEN module developed as a part of this work.

core or in the active space, differs significantly when calculated using compact basis sets, i.e. those not containing diffuse functions. Figure 3.2 shows the radial charge densities of orbitals $4b_{3g}$ and $3b_{2g}$, and illustrates the significant differences in the shape of the virtual orbitals when calculated in the basis sets cc-pVDZ and 6-311+G**. Similar differences are observed for all the other virtual orbitals calculated in these two basis sets. The orbitals of the active space do not differ much, as is exemplified by the radial charge density of the orbital $5b_{1u}$ (Figure 3.2). The similarity of the active space orbitals calculated in both basis sets is reflected, as expected, in similar shapes of the radial charge densities of the electronic states. The upper panels in Figure 3.2 show the radial charge density of the ground state. The panel on the right hand side shows that the ground state of the molecule is indeed more diffuse in the calculations using the diffuse basis set, but the absolute differences between the densities calculated in both basis sets are negligible. We have observed that the radial charge densities of all electronic states have very similar shapes in both basis sets. As we will see from the results of our scattering calculations, virtual orbitals play a key role in modelling correlation between the molecular and the scattering electrons: cross sections, especially at lower energies, are significantly different depending on whether a compact or diffuse basis sets are used. On this basis we suggest that the selection of an optimal basis set for scattering calculations on large molecules, when using the models presented below, should not be based solely on the comparison of "integral" values (e.g. the ground state energies and dipole moment, if the molecule possesses one) but also on an assessment of the quality of the virtual orbitals. The basis sets for scattering calculations should describe the occupied and virtual orbitals to a similar level of quality.

Taking these considerations into account we should choose (when using SA-CASSCF orbitals) as the optimal basis set one of the diffuse ones (aug cc-pVDZ, 6-311+G** or 6-311++G**), which give significantly lower energies for the virtual orbitals. The last two not correlation-consistent diffuse basis sets give lower values of the ground state energies compared with the aug cc-pVDZ (see Table 3.4). Use of the 6-311++G** basis set would require larger R-matrix radii than is currently possible (see later). Therefore we choose as optimal the 6-311+G** basis set, which presents an excellent compromise between size, diffuseness and the quality of the target description.

Nonetheless, we have also used the cc-pVDZ basis set in our scattering calculations for pyrazine in order to ascertain the effect on the collisional data of using a compact basis set and for a qualitative comparison with the results obtained by Dora et al. for uracil. As we show below the orbitals resulting from the target calculations using the compact basis set

are adequate for the description of all electron resonances present in pyrazine and all other systems studied in this thesis. This property of the compact basis set is very important since our calculations using it are less computationally demanding than those using the diffuse basis set. For these reasons we used only the compact basis set for our calculations on the substituted pyrimidines, which are the largest molecules studied in this work.

3.4 Scattering calculations

In the scattering calculations we used both the Hartree-Fock and the CASSCF target orbitals generated by the averaging procedure described above. The orbitals describing the continuum are obtained using the following procedure (for the flow of the programs see Section 2.7). The continuum Gaussian-type orbitals (GTOs) centred on the centre of mass of the molecule are Schmidt orthogonalized to the target (orthogonal) orbitals. The retained continuum orbitals are then symmetric-orthogonalized among themselves. In order to avoid linear dependence problems, only those continuum orbitals of each symmetry whose eigenvalue is higher than some specified threshold, are retained in the calculation. (The precise selection of those deletion thresholds is described later.)

The main parameters that affect the scattering part of our calculations are the R-matrix radius a and the choice of the continuum GTOs. The latter have to be optimized for each specific radius. The GTOs we used contained functions up to g-wave ($l \leq 4$). In order to check that the assumption of negligible amplitude of target electron density on the R-matrix sphere is satisfied, we performed tests with R-matrix radii (and the corresponding basis sets) of $13a_0$, $15a_0$, $16a_0$ and $18a_0$. (The basis set for radius $a = 13a_0$ was optimized by Faure et al. [91], the one for $a = 15a_0$ was optimized by Bouchiha et al. [126] and the basis set for radius $a = 18a_0$ is due to Tarana [127]. The basis set for $a = 16a_0$ was optimized by us using the NUMCBAS and GTOBAS modules.) Note that the need to perform the calculations for different R-matrix radii has become redundant as we are now able to calculate the radial charge densities of the target orbitals using the RADDEN program, thus allowing us to estimate directly the appropriate R-matrix radius (see below).

We can now turn to the description of our scattering models and results. From now on we will refer to the basis set 6-311+G** as "diffuse" and the cc-pVDZ basis set as "compact". As explained in Section 2.6.4, our scattering calculations do not exhibit convergence of the positions of resonant structures with respect to the number of virtual orbitals included; a behaviour also observed by Dora [59] for uracil. Therefore the optimal number of virtual

orbitals used was chosen to give, within a specific model (SEP or CC), positions of the three π^* resonances as close to the experimental ones as possible without overcorrelating any of them. Consequently a scattering calculation will be called overcorrelated if one of these resonances appears in our calculations at lower energy than its experimentally determined position.

3.4.1 SE and SEP calculations

On these levels of approximation only the elastic channel is open; the response of the target to the incoming electron is taken into account only in the SEP approximation as described in Section 2.6. For both types of calculations the SA-CASSCF orbitals performed marginally worse than the HF orbitals and therefore for the SE and SEP calculations, we present results using the HF orbitals only.

Pyrazine is a relatively large molecule for R-matrix ab-initio scattering calculations using the current UKRmol suite and as such causes some specific practical problems related to the quality of representation of the scattering electron (continuum). The SE calculations proved a useful tool for assessing the quality of this representation and for demonstrating some specific effects associated with it which prevail even in the more sophisticated SEP and CC calculations.

The quality of description of the radial wavefunction of the scattering electron in the inner region is strongly related to the deletion thresholds used in the orthogonalization step for the continuum orbitals. For the calculations using R-matrix radii up to $a = 15a_0$ the deletion thresholds were for all symmetries set to the value 1×10^{-7}. This is the value used most often in R-matrix scattering calculations employing radii $a \approx 10$ a.u. A smaller value would retain more continuum functions, but could cause linear dependence problems. Conversely, a value larger than $\approx 10^{-7}$ usually causes deletion of too many continuum functions which results in an insufficient quality of description of the continuum.

For the calculations using the diffuse basis set and the largest R-matrix radius $a = 18a_0$, the deletion thresholds had to be decreased, as expected [128], in some symmetries to prevent removing too many continuum functions and give a satisfactory description of the continuum. The optimization of the deletion thresholds was done at the level of the SEP calculations, which will be described below. The deletion thresholds so obtained are listed in Table 3.5. We choose the SEP calculations for the optimization step for reasons associated with the diagonalization of the Hamiltonian matrix performed in the inner region calculation. Larger

A_g	B_{3u}	B_{2u}	B_{1g}	B_{1u}	B_{2g}	B_{3g}	A_u
10^{-9}	10^{-7}	10^{-7}	10^{-9}	10^{-7}	10^{-7}	6.10^{-7}	10^{-10}

Table 3.5: Deletion thresholds for the continuum functions used in the calculations with the 6-311+G** basis set and $a = 18a_0$.

matrices imply the need for higher numerical precision of the matrix elements in order to guarantee that the matrix diagonalization is numerically stable. If some of the continuum orbitals are almost linearly dependent with the target orbitals then, due to numerical reasons, the Hamiltonian diagonalization might lead to the appearance of R-matrix poles lying too low or too high in energy, i.e. to linear dependency problems. For small models (e.g. SE models where the dimension of the Hamiltonian is usually of the order of hundreds) this problem may not appear, but may become very severe for large calculations (e.g. CC calculations). From this point of view the SEP calculations are an excellent compromise, allowing for step-by-step optimization of the deletion thresholds, while being of an intermediate size where the problems associated with linear dependency are usually revealed.

We included the 25 lowest-lying virtual orbitals in the SE calculations using both target basis sets. This is a high enough number to guarantee that all shape resonances present in pyrazine will appear in the scattering data (see Section 2.6). Figure 3.3 shows the resulting eigenphase sums for all symmetries. For the compact basis set the results show clearly the presence of the three π^* resonances and some structure in the eigenphase sums above 10 eV. An R-matrix radius as small as $a = 13a_0$ gives SE results nearly identical to the ones obtained using radius $a = 15a_0$ (not shown). Also, no linear dependence problems were observed in any of the calculations using this basis set.

The eigenphase sums have more structure in the case of the calculations using the diffuse basis set. These calculations were initially performed with $a = 15a_0$, but this proved to be too small to contain all the target electronic density. In particular, the structure around 3 eV in the B_{3g} symmetry is unphysical, because it disappears completely when $a = 18a_0$ is used. The unphysical origin of this "step" was also confirmed by our calculations of the radial charge densities of the target orbitals, which indeed showed that the B_{3g} symmetry contains the most diffuse orbitals with some of these having an amplitude $\approx 10^{-3}$ for $r = 15a_0$. For this reason $a = 18a_0$, a value for which the amplitudes of all molecular orbitals is $\ll 10^{-3}$, was used in all later calculations with the diffuse basis set.

In order to further asses the stability of the eigenphase sums calculated using the diffuse basis set and $a = 18a_0$, we performed SE calculations using a different continuum basis set,

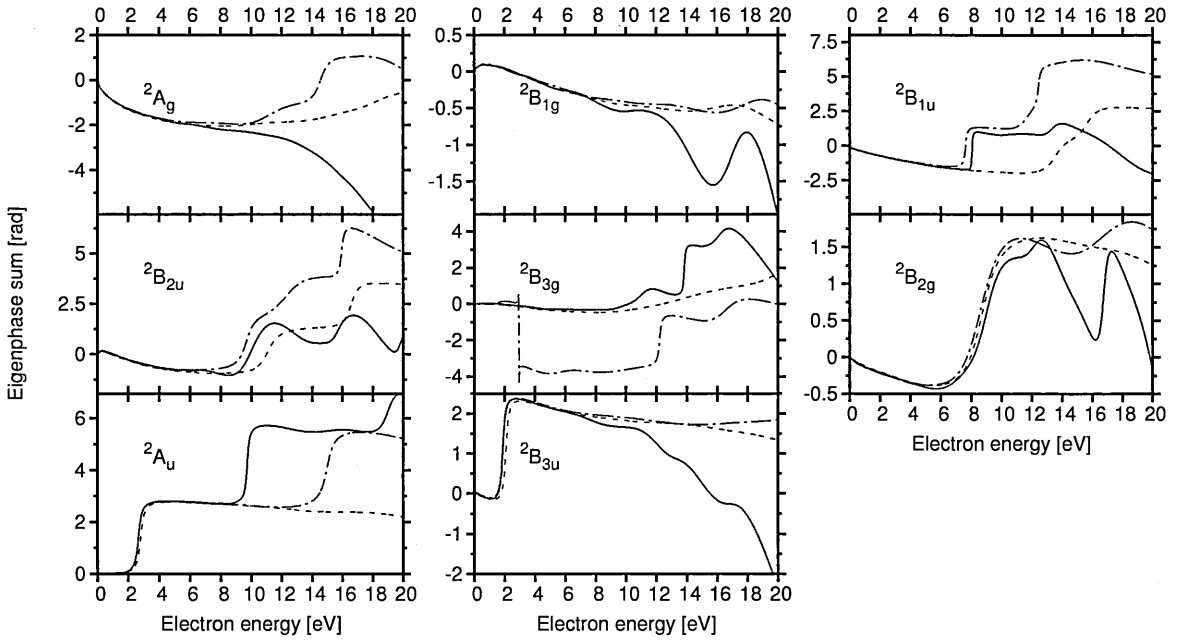

Figure 3.3: Eigenphase sums for the scattering symmetries of pyrazine indicated in the panels at the Static Exchange level. Solid red: calculations performed using the basis set 6-311+G** and an R-matrix radius $a = 18a_0$. Dash-dotted black: basis set 6-311+G** and $a = 15a_0$. Short dashed blue: basis set cc-pVDZ and $a = 13a_0$.

obtained by rescaling the original one by multiplying all the exponents by the factor $\left(\frac{18}{16}\right)^2$; this allowed us to use a slightly higher number of continuum functions in some symmetries, while keeping the deletion thresholds the same as those shown in Table 3.5. Any residual linear dependence present in our calculations will lead to the appearance of non-physical R-matrix poles, which in turn may lead to spurious structures in eigenphase sums and cross sections. Changes in the continuum description are reflected in a change of the values of the R-matrix poles. We then expect any unphysical structures to change their position or appearance significantly, while physical structures should remain the same provided that the quality of the description of the continuum is sufficient. We can see in Figure 3.3 that the second "step" in the A_u symmetry changes its position considerably when the R-matrix radius (and the continuum basis set) are changed from $a = 18a_0$ to $a = 15a_0$, suggesting that this feature might be unphysical. In the SE calculations using the rescaled continuum basis set and the radius $a = 18a_0$ this structure moves to very high energies (around 17 eV) proving again its instability: hence we regard it as unphysical. All other structures remain virtually unchanged.

We note that use of the diffuse basis set, which gives target orbitals of a better quality, results in the shift of some of the structures in the eigenphase sums, e.g. in the B_{1u} symmetry, to considerably lower energies when compared with the calculations using the compact basis

set, stressing the importance of choosing a basis set that represents virtual orbitals sufficiently well. We also note that some of the apparent structure in the higher energy range for the calculation with $a = 18a_0$ are likely to be due to a poor representation of the continuum.

A useful measure of quality of representation of the continuum is given by the comparison of the magnitude of eigenphase sums between calculations using different continuum bases: the eigenphase sum (being variational) approaches its exact value from below and therefore the larger the eigenphase the better the representation of the continuum. It is important to point out that such a comparison is meaningful only within one particular scattering model.

The quality of representation of the continuum can be estimated also by solving the free potential radial scattering problem whose exact solution is, of course, zero phaseshift. Using the continuum GTOs as the R-matrix basis we can solve this scattering problem numerically using the R-matrix formalism (see Section 2.2) and obtain the phaseshifts for scattering in each partial wave. It can be seen [127] that the precision of representation of the exact solution, i.e. zero phaseshift, as a function of the scattering energy generally decreases. At higher energies the calculated phaseshifts develop characteristic oscillations. These oscillations are manifestations of the deteriorating quality of representation of the continuum wavefunction. Oscillations similar to these can be seen for example in the eigenphase sums for $^2B_{1g}$ scattering symmetry calculated using the diffuse basis set (see Figure 3.3). (Similar oscillations also develop in the cross sections.) Based on this criterion we can estimate that the continuum is represented accurately in the calculations using the diffuse basis set and $a = 18a_0$ up to the energy of $\approx 6-8$ eV depending on the scattering symmetry. Features in the eigenphase sums appearing at higher energies have to be analyzed carefully using, for example, the stability tests described above.

SEP calculations

For the SEP calculations we used the L^2 functions (2.88) and (2.89) with the number of virtual orbitals included dependent on the basis set employed. We always include all singlet and triplet-coupled single excitations from the valence space of 15 orbitals of pyrazine to the selected space of virtual orbitals. For the compact basis set, use of the 25 lowest-lying virtual orbitals was found to give the best results, while for the diffuse basis set using 40 lowest-lying virtual orbitals was found to be optimal. Cross sections for SEP calculations are shown in Figure 3.4: the rich structure visible in the energy range above 5 eV is inherent to the approximation of this type and corresponds to pseudoresonances (see Section 2.6.2).

The cross sections in the upper and lower panels correspond to calculations which included

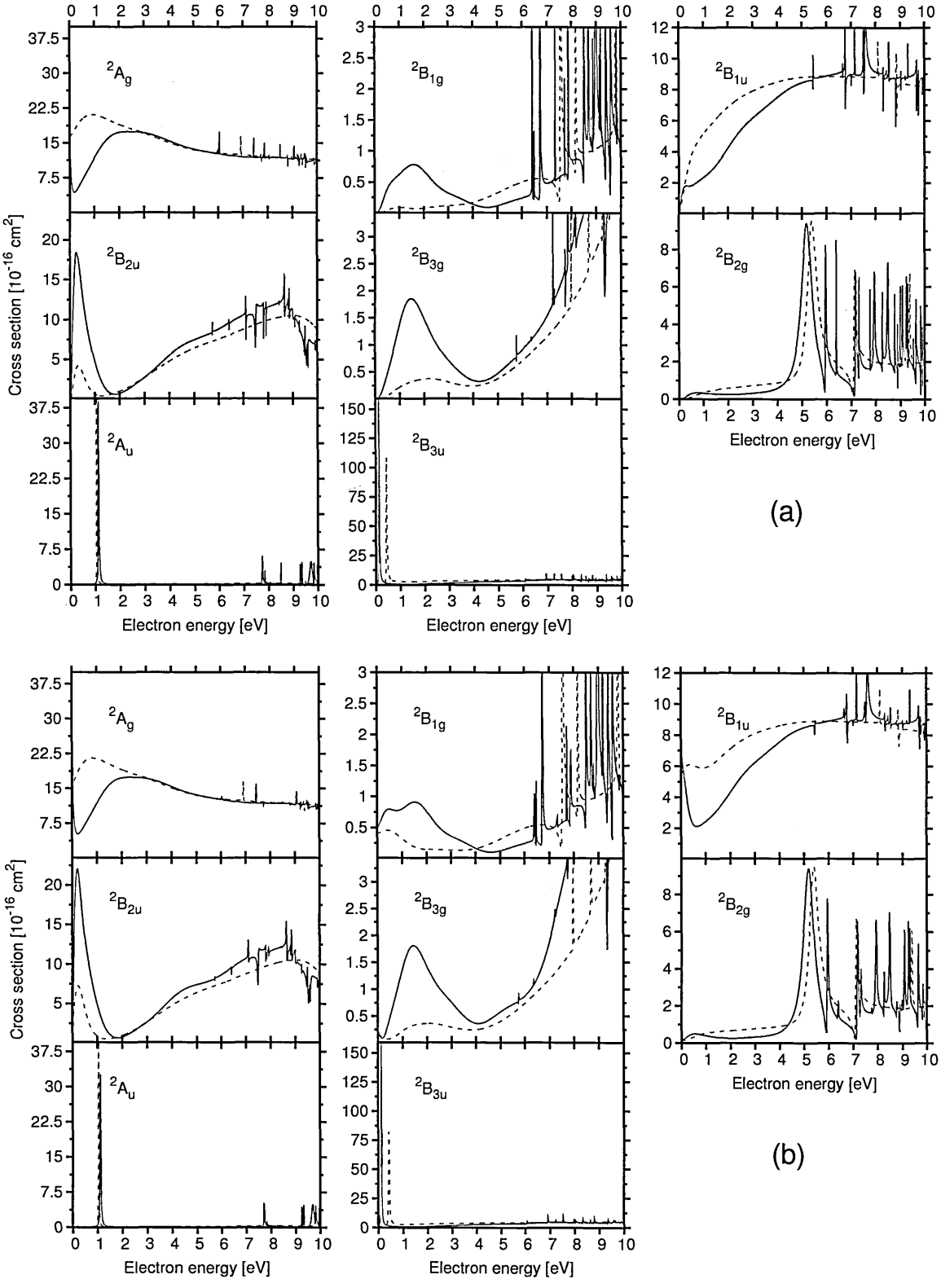

Figure 3.4: Contributions to the elastic cross section from all scattering symmetries at the Static Exchange plus Polarization level. Solid red: calculations performed using the basis set 6-311+G** (40 virtuals) and R-matrix radius $a = 18a_0$. Short dashed blue: basis set cc-pVDZ (25 virtuals) and $a = 13a_0$. The cross sections in the panels (a) were calculated taking into account coupling potentials with $\lambda = 1$ only, whereas the cross sections in the panels (b) were obtained including the potentials up to $\lambda = 2$.

Symmetry	$^2B_{3u}$		^2A_u		$^2B_{2g}$	
Resonance parameters	E	Γ	E	Γ	E	Γ
cc-pVDZ (25 virt.)	0.44	0.032	1.05	0.018	5.38	0.451
cc-pVDZ (35 virt.)	< 0	-	0.79	0.007	4.93	0.453
6-311+G** (40 virt.)	0.14	0.015	1.12	0.030	5.19	0.527
6-311+G** (50 virt.)	< 0	-	0.70	0.006	4.87	0.389
Winstead and McKoy [33]	0.2		1.3		4.4	
Nenner and Schulz [32]	0.065 $0.065 - 0.8$		0.87 $0.87 - 1.2$		4.10 $3.8 - 4.4$	

Table 3.6: Positions, E, and widths ,Γ, (in eV) of the π^* resonances in pyrazine calculated in this work at the SEP level and determined by RESON (see Section 2.7). Also listed are the positions of the resonances calculated by Winstead and McKoy (estimated by us from their graphs) and the experimental results of Nenner and Schulz, quoted by listing the centre of the resonance and the range of its vibrational broadening. The range of the $^2B_{2g}$ resonance was estimated by us from the graph of the measured derivative of the transmitted current.

coupling potentials of different order in the outer region calculation. The panel (a) shows cross sections calculated including the coupling potentials with $\lambda = 1$ only (see equation (2.63)). These potentials are normally linked with the permanent dipole moment of the HF ground state. However as pyrazine does not possess a dipole moment, this choice implies that these calculations regard the electron as free in the outer region. The panel (b) shows cross sections obtained including the coupling potentials with $\lambda = 2$. These are linked with the permanent quadrupole moment of the HF ground state. Comparing the two sets of cross sections we can see that the inclusion of the quadrupole potentials affects most of the cross sections only negligibly. However, small differences arise in the $^2B_{1g}$ symmetry and most importantly in the $^2B_{1u}$ symmetry, where the character of the cross section below ≈ 2 eV changes significantly. Including the quadrupole coupling potentials seems to have a completely negligible effect on the three π^* resonances. We can conclude that for electron energies below ≈ 2 eV the quadrupole coupling potentials significantly influence only the non-resonant part of the cross sections.

Table 3.6 presents our calculated positions and widths for the three π^* resonances together with the results of the SEP calculations of Winstead and McKoy, who however do not determine the widths of any of these resonances. We can see from this Table that the calculation using the diffuse basis set gives results in better agreement with experiment. This calculation also reveals the Ramsauer-Townsend minimum in the A_g symmetry lying below 0.5 eV as reported earlier by Winstead and McKoy. The largest discrepancy with experimental results occurs for the mixed core-excited shape resonance in B_{2g} symmetry. This discrepancy is not caused by the lack of L^2 functions built on the triplet excited configurations, which Winstead

and McKoy found essential for obtaining a good position of this resonance, but we ascribe it to the treatment of polarization in our calculations. Increasing the number of virtual orbitals used in the scattering calculations lowers the positions of all resonances. If we increase the number of virtual orbitals to 35 in the calculation using the compact basis set, the $^2B_{3u}$ resonance becomes bound, while the ^2A_u and $^2B_{2g}$ resonances drop by about 0.25 and 0.5 eV in energy respectively. A similar effect is noticed when the number of virtual orbitals is increased in the calculations with the diffuse basis set (see Table 3.6 and Figure 3.5); however, the Ramsauer-Townsend minimum remains absent from the calculation with the compact basis set. The calculation using the diffuse basis set continues to provide better agreement with experiment.

The reason for the need to include a higher number of virtual orbitals in the SEP calculation using the 6-311+G** basis set lies in their diffuse character: it would seem that the lower HF virtual orbitals do not describe as much correlation as the ones calculated in the compact basis set. As the energy of the scattering electron increases, modelling of the correlation between it and the molecule becomes more difficult. We can also see from our calculations of the vertical excitation energies of the electronic excited states of pyrazine (see Table 3.3), that the discrepancy between the measured and calculated values generally increases as the states become more excited. Achieving a good description of the higher-lying resonances in pyrazine (or in other many electron systems) seems to require the inclusion of higher-lying virtual orbitals as these are needed to sufficiently describe correlation.

A test of convergence of the partial wave expansion was performed by including continuum basis functions with $l = 5$ in the calculation using the cc-pVDZ basis set. We noticed only minor differences in the symmetries B_{3u}, B_{2u}, B_{1u} and A_u with negligible effects on the resonant structures; the effects on the other symmetries (including B_{2g}) could not be tested, because the $l = 5$ continuum functions do not contribute to scattering in these symmetries.

As noted in Section 2.6.2 the pseudoresonances in the eigenphase sums and cross sections for the SEP model prevent us from finding possible higher-lying resonances. Therefore an analysis of the cross sections and eigenphase sums at higher energies was done only at the Close-Coupling level.

3.4.2 Close-Coupling calculations

From the excited states listed in the Table 3.3 we included in our calculations only those with vertical excitation energies up to 10.03 eV (10.08 eV) for the calculations using the compact

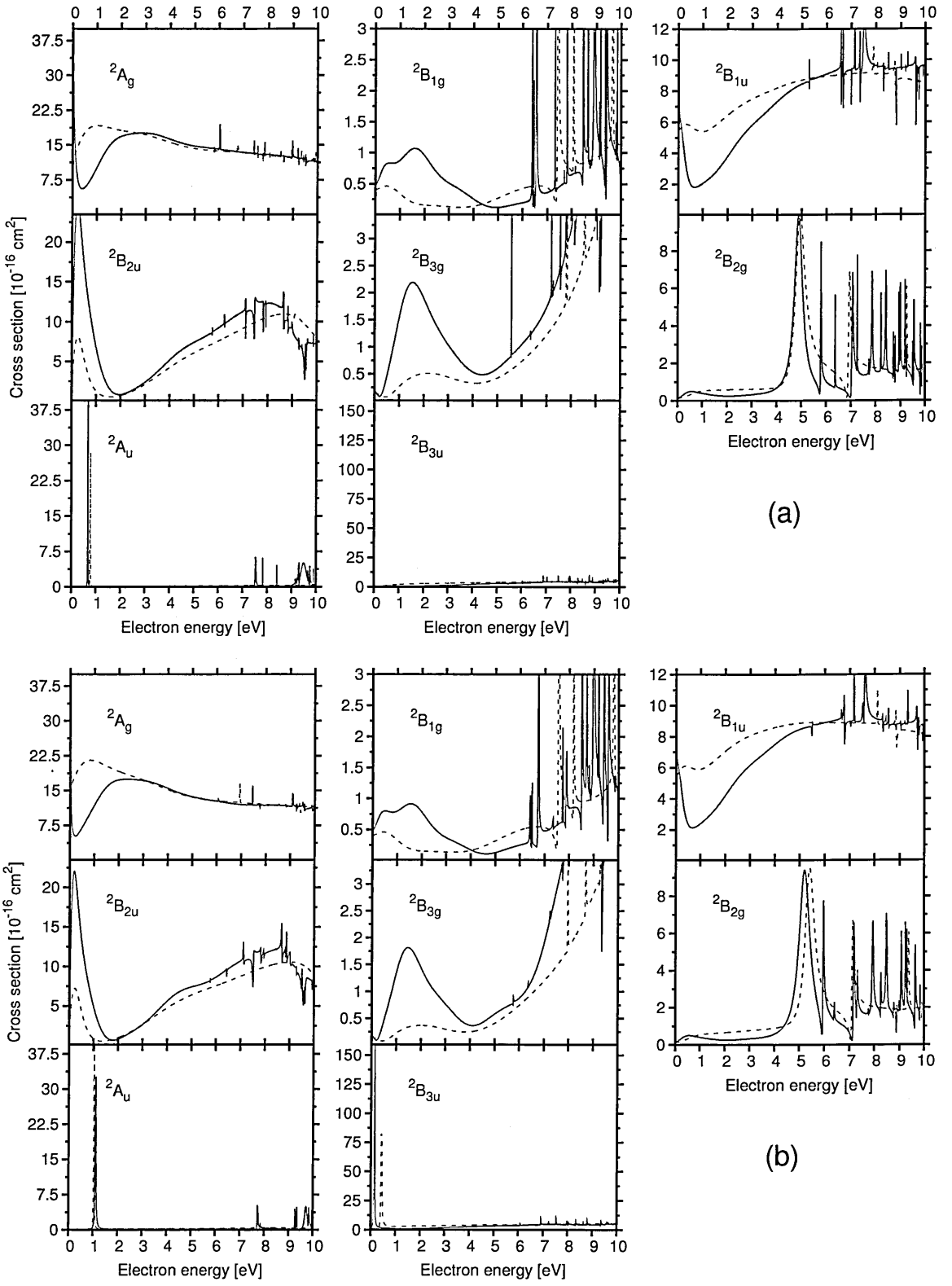

Figure 3.5: Contributions to the elastic cross section from all scattering symmetries at the Static Exchange plus Polarization level. Solid red: calculations performed using the basis set 6-311+G** and R-matrix radius $a = 18a_0$. Short dashed blue: basis set cc-pVDZ and $a = 13a_0$. The cross sections in panels (a) were calculated using 50/30 virtuals for the calculation using the diffuse/compact basis set. For comparison panel (b) is equivalent to panel (b) of Figure 3.4 and shows the cross sections calculated using 40/25 virtuals and the diffuse/compact basis set.

(diffuse) basis set and also the $2\ ^1B_{1u}$ state, which has been experimentally observed to lie below the 10 eV threshold. For the compact, cc-pVDZ, basis set a total of 27 electronic excited states were included in the Close-Coupling calculations. In the case of the diffuse basis set, 6-311+G**, a total of 29 electronic excited states were included. Calculations using the compact basis set employed 40 virtual orbitals, while the ones using the diffuse basis set used 70.

In order to achieve a good description of the continuum when the diffuse basis set is used (and $a = 18a_0$ is needed), we are forced to work at the limit of linear dependence. To ascertain whether unphysical R-matrix poles caused by any residual linear dependence between the continuum and the target orbitals are present, we increased the deletion thresholds for the orthogonalization of the continuum functions (up to 4 orders of magnitude for some symmetries). This increase leads to a decrease in the quality of the representation of the continuum that can be observed in the eigenphase sums, but should cause non-physical features due to linear dependence to disappear or at the very least move significantly. The only unstable structure found was the second step in the ^2A_u symmetry, which has been already identified as unphysical in the SE calculations described in the previous section.

The upper panels in Figure 3.6 show eigenphase sums for our best (with respect to the positions of the three π^* resonances) Close-Coupling calculations using the compact and the diffuse basis sets. We can see that the eigenphase sums are very structured with many of the features present in the calculations using both basis sets. It is apparent from Figure 3.6 that use of the diffuse basis set leads to better defined structures in the eigenphase sums and in some symmetries ($^2B_{1u}$ and $^2B_{2u}$) to the appearance of additional structures.

The corresponding total cross sections are shown in the bottom panels of Figure 3.6. We also tested the use of the scaled continuum basis set described in Section 3.4.1, while retaining the values of the deletion thresholds. The stability of the eigenphase sums was observed again. The results of our Close-Coupling calculations for symmetries $^2B_{3g}$ and $^2B_{2u}$ shown in Figure 3.6 were actually generated using the scaled continuum basis set. It is also worth mentioning that the structures seen in our eigenphase sums moved smoothly towards lower energies as the number of the virtual orbitals included was being increased up to 40 or 70 respectively. The eigenphase sums and cross sections obtained in CC models using the diffuse basis set and a different number of virtuals are shown in Figure 3.7. In this case the calculations for the diffuse basis set used the unscaled continuum basis set. For comparison the figures also contain the results obtained using the CC model with the compact basis set. It is clear from these figures that the structures in the eigenphase sums and cross sections

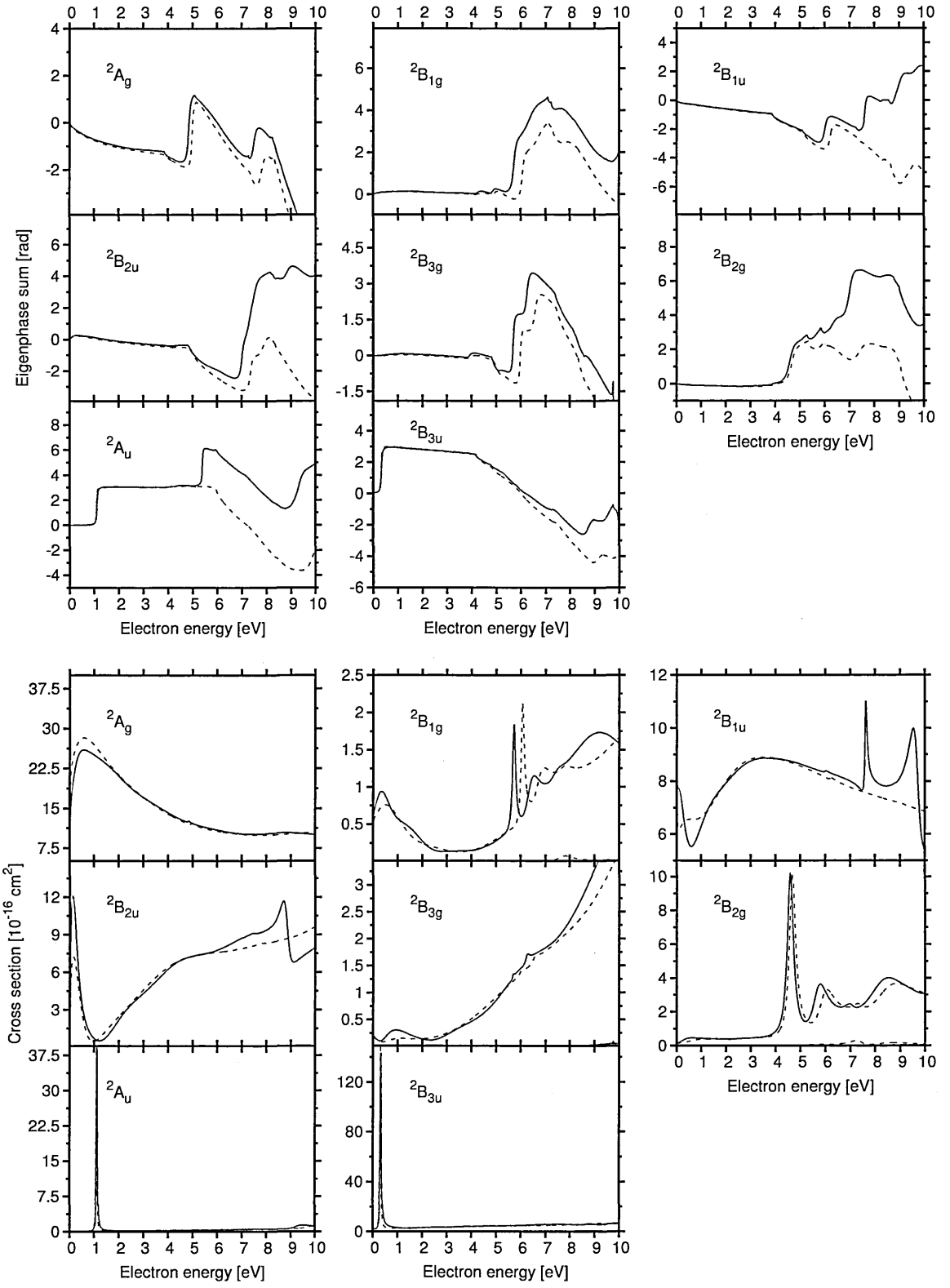

Figure 3.6: Eigenphase sums (upper panels) and contributions to the total cross section from all scattering symmetries (bottom panel) at the Close-Coupling level. Solid red: calculations performed using the basis set 6-311+G**, $a = 18a_0$ and 70 virtual orbitals. Dashed blue: basis set cc-pVDZ, $a = 13a_0$ and 40 virtual orbitals.

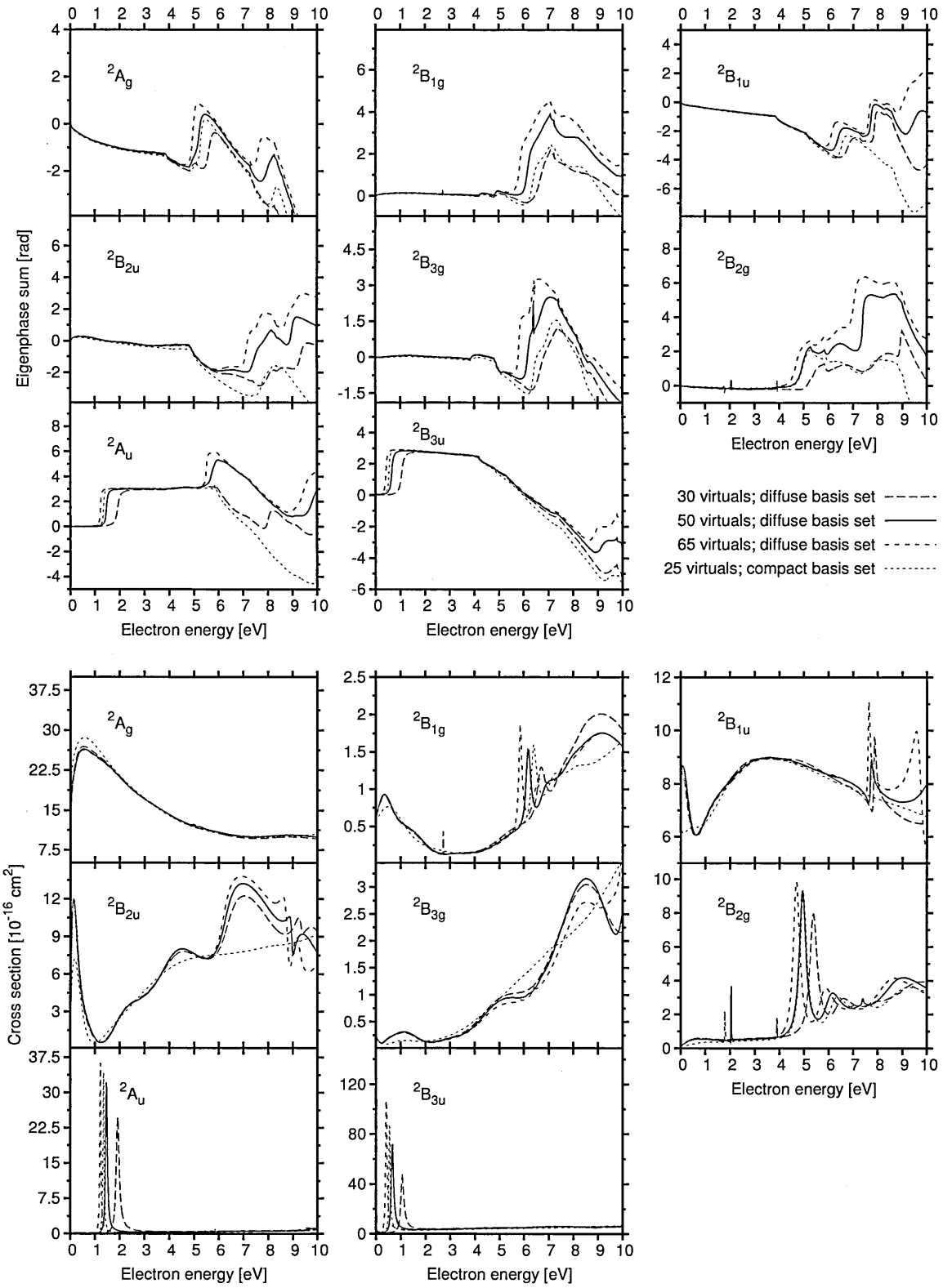

Figure 3.7: Eigenphase sums (upper panels) and contributions to the total cross section from all scattering symmetries at the Close-Coupling level. Solid lines: calculations performed using the diffuse basis set and R-matrix radius $a = 18a_0$. Dashed line: compact basis set, $a = 13a_0$. The number of virtual orbitals is indicated in the Figure.

become more pronounced as the number of virtual orbitals is increased. In symmetry ^2A_u we have identified again (just like on the SE level) an unphysical structure which is unstable with respect to the number of virtual orbitals included. Similar unphysical sharp features are also present in the eigenphase sums and cross sections for scattering in symmetries $^2B_{2g}$, $^2B_{1g}$ (below 4 eV) and $^2B_{3g}$ (around 6.5 eV).

Our scattering codes allow us to individually shift the energies of the target electronic states included in the expansion (2.63). We applied shifts to the vertical excitation energies of those states in Table 3.3 for which experimental values are available. We did not observe any significant changes in the positions of the resonant structures present in the calculations.

3.5 Cross sections

In the sections above we presented our final elastic and total cross sections for the SEP and CC models (see Figures 3.4 and 3.6). Here we present the elastic differential cross sections (DCS) (Figure 3.8), the total summed integral cross sections (Figure 3.9), the cross sections for electron impact electronic excitation of selected states (upper panels of Figure 3.10) and the total (summed over all excited states) inelastic cross sections (bottom panels of Figure 3.10).

Elastic differential cross sections for selected energies are shown in Figure 3.8 for both the SEP and CC models and both basis sets. Also shown on the figure are the recent experimental results of Palihawadana [129]. We first compare our DCS calculated using the SEP model and both basis sets: we can see that the calculations show significant differences below $\approx$ 3 eV. As explained above, we choose the number of virtual orbitals included in our SEP models based on the positions of the three π^* resonances. Looking at Table 3.6 we see that the models using the compact and the diffuse basis set produce resonance positions which are roughly similar. However, the integral elastic cross sections (see Figure 3.4) display significant differences below $\approx$ 3 eV. Naturally, these differences are translated into significant differences in the DCS calculated for energies below $\approx$ 3 eV. The most significant difference occurs for the DCS for 0.1 eV, where the SEP calculation using the diffuse basis set gives DCS with a strong forward-peaking character, while the SEP calculation using the compact basis set gives DCS with almost isotropic behaviour. This difference can be probably traced to the absence of the Ramsauer-Townsend minimum in the ^2A_g symmetry in the calculations using the compact basis set, which is the most significant difference between the elastic cross sections calculated using both basis sets. As discussed above, the difference in the calculated cross sections at very low energies is caused by the different shape of the orbitals which are used to construct

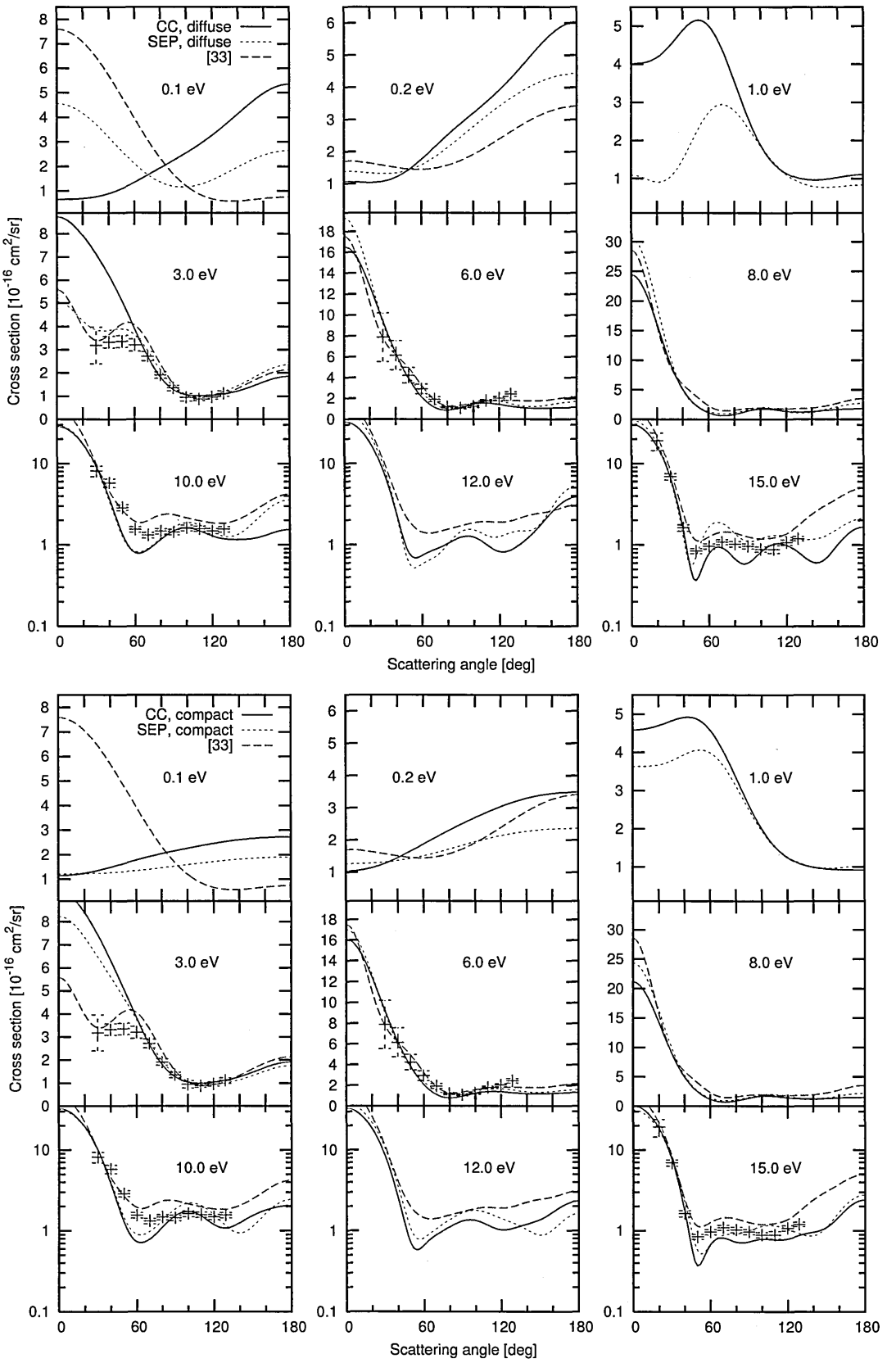

Figure 3.8: Differential cross sections calculated using the final SEP (dashed black) and CC (solid red) models with the diffuse (upper panel) and the compact (bottom panel) basis sets for the energies indicated in the panels. The experimental results of Palihawadana [129] are plotted using blue bars. The results of the SMC calculations of Winstead and McKoy [33] are also included. The ranges on the vertical axes have been kept the same for both basis sets in order to aid visual comparison of the results.

the L^2 functions.

The CC calculations using the compact and the diffuse basis set also produce different DCS for 0.1 eV. In this case, however, both DCS have the same backward-peaking character, but differ in the absolute magnitude. This shape of the DCS is compatible with the absence of the Ramsauer-Townsend minimum in the CC calculations (see Figure 3.6). We can therefore conclude that the presence of the Ramsauer-Townsend minimum in the cross sections is reflected in a strong forward-peaking DCS at energies close to the threshold.

It is worth pointing out that our calculations were carried out in the fixed-nuclei approximation, which is generally not accurate for very low electron energies. Therefore, it is possible that the actual shape of the DCS for very low electron energies (e.g. for 0.1 eV) as measured in an experiment would be significantly affected by nuclear motion.

Winstead and McKoy calculated DCS for pyrazine on the SEP level for electron energies in the range $0.1 - 20$ eV. Although their DCS show some differences in magnitude compared to ours, the overall shape of the cross sections is very similar to the one calculated using the SEP model and the diffuse basis set (see Figure 3.8).

The experimental DCS of Palihawadana generally agree well with our calculations. However, it is clear from the DCS for 3 eV that at low energies the necessary condition for obtaining a good agreement with the experiment is the use of the diffuse basis set. This finding is in an agreement with our previous discussion, where we argued that the use of the diffuse basis set may lead to a better description of the short-range correlation/polarization effects. For energies 15 eV and above it is the CC calculation using the compact basis set which compares better with the experiment. This is probably due to the poorer quality of representation of the continuum for higher energies in the calculations using the diffuse basis set.

The integral total cross sections, calculated on the CC level, summed over contributions from all irreducible representations, shown in Figure 3.9, display peaks corresponding to the three low-lying shape resonances. The small peak below 6 eV is also caused by a resonance, which will be discussed in detail in the next section. Resonant peaks are also visible in the total inelastic cross sections, shown in the bottom panel of Figure 3.10. These latter cross sections were obtained summing the cross sections for electron impact excitation of all electronic states included in the CC calculation. The cross sections for the calculation using the diffuse basis set show peaks which are not visible in the calculations using the compact basis set. These peaks are caused by additional resonances found only in the calculations using the diffuse basis set and are discussed in the next section.

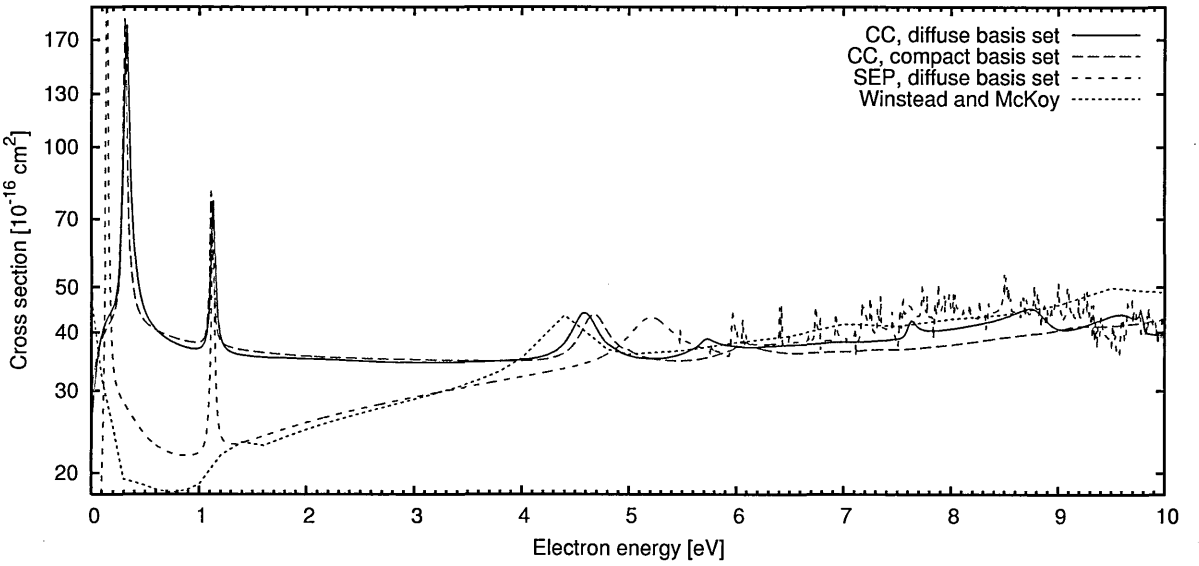

Figure 3.9: Integral total (elastic + inelastic) cross section for electron collisions with pyrazine calculated at the Close-Coupling level. The calculation employing the compact/diffuse basis set used 40/70 virtual orbitals. Also shown are our SEP (elastic) cross sections using the diffuse basis set and the results of Winstead and McKoy [33].

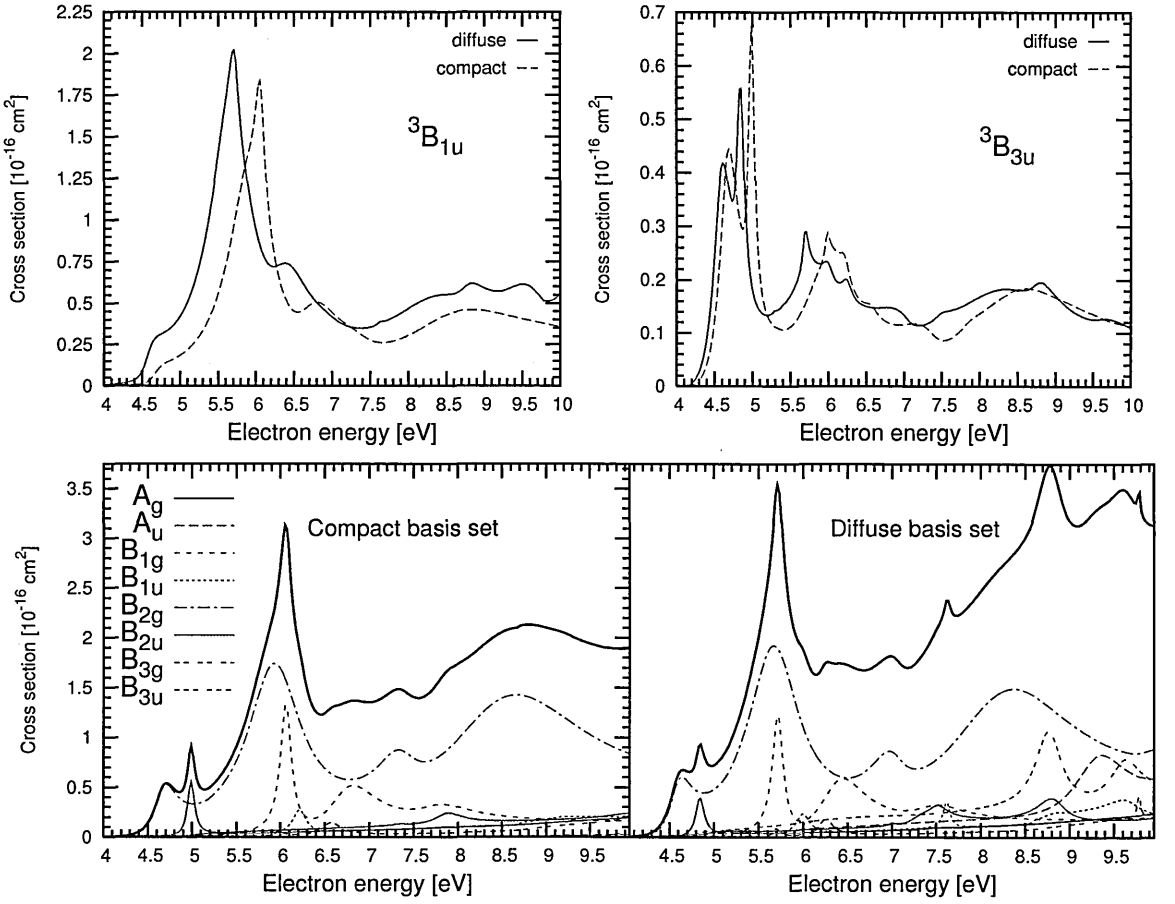

Figure 3.10: Upper panels: integral cross sections for scattering into the two lowest-lying electronic excited states: $1\ ^3B_{1u}$ - upper left panel and $1\ ^3B_{3u}$ - upper right hand panel. Bottom panel: total (summed over all excited states) integral inelastic cross sections for pyrazine and contributions from all scattering symmetries calculated using the compact (left panel) and the diffuse basis set (right hand panel). The total (summed over all excited states) integral inelastic cross section (TICS) is plotted using the thick black line.

The cross sections calculated for energies close to the elastic threshold are finite and converged with respect to the number of the continuum partial waves included in the calculation. Therefore no Born correction is needed in calculations of these cross sections.

3.6 Assignment of the resonant structures

The three π^* resonances of $^2B_{3u}$, ^2A_u and $^2B_{2g}$ symmetries are clearly visible in all our calculations. The main aim of this section is to interpret the rest of the structures present in our Close-Coupling results. We can see from Figure 3.3 that the eigenphase sums for the SE calculations in symmetries ^2A_g, $^2B_{1g}$, $^2B_{2u}$ and $^2B_{3g}$ are essentially flat in the region below 10 eV, while our Close-Coupling calculations show numerous resonant-like structures in these symmetries. Somewhat surprisingly these structures are not significantly visible in the corresponding cross sections shown in Figure 3.6 (with exception of the peaks in $^2B_{1g}$ symmetry). However, most structures in the eigenphase sum have proved to be very stable, as detailed above and therefore we regard them as resonances.

As explained in Section 2.4, an isolated resonance should appear as a characteristic step in the eigenphase sum. Therefore the eigenphase sum has become a standard tool for identification of resonances in theoretical studies of electron-molecule collisions. Resonances usually significantly affect the shape of the cross sections as well. As mentioned above, many of the resonances appearing at higher energies in pyrazine do not affect significantly the elastic scattering cross section. However, as we will see later, some of them are clearly visible in the inelastic cross sections. On the other hand, we found peaks in our inelastic cross sections for particular scattering energies that we could not link to significant steps in the eigenphase sums. We found this behaviour puzzling as peaks in inelastic cross sections might be interpreted as arising from formation of resonances. Initially, we performed an analysis of the R-matrix poles (see below), which can provide us with the most important configurations of the resonances, but this did not lead to a complete explanation of the phenomena described above.

Later on we investigated electron collisions with pyrimidine (see Chapter 4) and found that the cross sections and eigenphase sums possess behaviour qualitatively similar to the one described for pyrazine. Namely, we found peaks in the inelastic cross sections that could not be linked to steps in the eigenphase sum. In order to investigate this phenomenon further we started looking for another observable (apart from the cross sections) that could provide us with a deeper insight into the nature of the processes behind the formation of the peaks in

the inelastic cross sections. We calculated the *time-delay* spectra for pyrimidine and found that this quantity provides us with an explanation of the puzzling behaviour of the cross sections and eigenphase sums. Most importantly, we found that resonances which are not visible in the eigenphase sum are clearly visible as Lorentzian peaks in the time-delay (see Section 2.4). These peaks in the time-delay appear at positions corresponding to the (more or less pronounced) peaks in the elastic and inelastic cross sections. This allowed us to confirm that the peaks in the inelastic cross sections arise from formation of resonances. In Chapter 4 we explain in detail why the resonances are not always visible in the eigenphase sum, but that they are in the time-delay.

Based on our time-delay calculations for pyrimidine, we retraced our steps and performed these and additional calculations for pyrazine. Since we have used pyrazine to establish our models and methodology for analysis of the results, in order to investigate the resonances in detail and postulate their parent state(s), we performed the following additional calculations:

1. Close-Coupling calculations using a Simplified model (see below) followed by an analysis of the R-matrix poles,

2. Calculations of the time-delay spectra,

3. Calculation of elastic cross sections $\sigma_{i\to i}(E)$ for the excited states ($i > 1$).

The following sections describe these calculations in detail. A combined analysis of the results obtained led to the assignment of the resonances (see Section 3.6.4). A summary of the resonances found, their parameters, main configurations and proposed parent states is presented in Table 3.7.

The assignment of resonances based on the analysis of the R-matrix poles was found similar, but not identical to the one obtained using the cross sections and the time-delay method. The assignments of the parent states based on the last two methods are more accurate and therefore the assignments showed in Table 3.7 correspond to the ones made using these methods. However, the method of the R-matrix poles might still be useful, because in some cases it allows us to determine which orbitals play a role in the trapping of the scattering electron (see below). Therefore this method can be used to complement our understanding of the resonance formation based on the results of the time-delay analysis.

Many of the resonances we find possess more than one parent state; however, in Table 3.7 we choose to report only the dominant one(s). We do not characterize resonances which lie close to the ionization threshold ($\approx$ 10 eV), where our calculations become less accurate (see

Section 2.6). The calculations using the diffuse basis set found additional resonances not present in the calculations using the compact basis set and we choose not to characterize them in terms of configurations and parent states. These additional resonances are listed but not numbered in Table 3.7.

Resonance	E	Γ	Main configuration(s)	Most likely parent state(s)
$1\ ^2A_g$	4.99 (4.84)	0.15 (0.16)	$6a_g^\alpha \otimes 2b_{3u}^2$	$1\ ^3B_{3u}$, $1\ ^3B_{2u}$, $1\ ^1B_{2u}$
$2\ ^2A_g$	7.80 (7.49)	0.28 (0.24)	-	$1\ ^3A_u$, $1\ ^1A_u$, $1\ ^3B_{2g}$
$1\ ^2B_{3u}$	0.31 (0.32)	0.07 (0.03)	$2b_{3u}^1$	g.s.
$1\ ^2B_{2u}$	7.35 (7.01)	0.19 (0.17)	$5b_{1u}^1 \otimes 2b_{3u}^1 \otimes 1a_u^1$	$1\ ^3B_{2g}$, $1\ ^1A_u$
$2\ ^2B_{2u}$	7.87 (7.31)	0.37 (0.33)	-	$1\ ^1B_{2g}$, $1\ ^3B_{1g}$
$^2B_{2u}$	(7.50)	(0.29)	-	-
$3\ ^2B_{2u}$	(8.83)	(0.38)	-	-
$1\ ^2B_{1g}$	6.06 (5.72)	0.18 (0.18)	$1b_{2g}^1 \otimes 2b_{3u}^1 \otimes 1a_u^1$ $1b_{1g}^\alpha \otimes 1a_u^2$, $1b_{1g}^\alpha \otimes 2b_{3u}^2$ $1b_{3u}^1 \otimes 1a_u^1 \otimes 2b_{2g}^1$ $1b_{2g}^1 \otimes 2b_{3u}^1 \otimes 1a_u^\alpha$	g.s., $1\ ^1B_{2u}$, $1\ ^3B_{1u}$
$2\ ^2B_{1g}$	6.73 (6.37)	0.67 (0.64)	-	$1\ ^3B_{2u}$, $1\ ^3B_{1u}$
$3\ ^2B_{1g}$	7.75 (7.46)	0.73 (0.69)	-	$2\ ^3B_{1u}$
$1\ ^2B_{1u}$	6.22 (6.00)	0.21 (0.21)	$5b_{1u}^\alpha \otimes 2b_{3u}^2$ $6a_g^1 \otimes 2b_{3u}^1 \otimes 2b_{2g}^1$	$1\ ^3B_{2g}$, $1\ ^3B_{3u}$, $1\ ^1B_{3u}$
$^2B_{1u}$	(7.62)	(0.15)	-	-
$2\ ^2B_{1u}$	9.20 (8.83)	0.35 (0.30)	-	$1\ ^1B_{1g}$, $1\ ^3A_g$
$3\ ^2B_{1u}$	9.49 (9.05)	0.38 (0.31)	-	$1\ ^1B_{3u}$
$1\ ^2B_{2g}$	4.66 (4.58)	0.32 (0.31)	$2b_{2g}^\alpha$ +...see text	g.s., $1\ ^3B_{3u}$, $1\ ^3B_{1u}$
$2\ ^2B_{2g}$	5.93 (5.66)	0.77 (0.72)	-	g.s., $1\ ^3B_{1u}$
$^2B_{2g}$	(6.34)	(≈ 0.6)	-	-
$3\ ^2B_{2g}$	7.36 (6.99)	0.56 (0.31)	-	$1\ ^1B_{2u}$, $2\ ^3B_{1u}$
$4\ ^2B_{2g}$	8.41 (8.21)	1.97 (1.80)	-	g.s., $1\ ^3B_{2u}$
$1\ ^2B_{3g}$	5.98 (5.69)	0.15 (0.15)	$6a_g^1 \otimes 2b_{3u}^1 \otimes 1a_u^1$ $5b_{1u}^1 \otimes 1b_{2g}^1 \otimes 2b_{3u}^2 \otimes 1a_u^1$	$1\ ^3B_{3u}$
$2\ ^2B_{3g}$	6.57 (6.25)	0.26 (0.20)	-	$1\ ^3A_u$, $1\ ^1B_{3u}$
$1\ ^2A_u$	1.11 (1.12)	0.07 (0.09)	$1a_u^1$	g.s.

Table 3.7: Positions and widths (in eV), along with the main configurations and proposed parent states of the electron resonances in pyrazine from the results of our Close-Coupling calculations using the compact basis set, $a = 13a_0$ and 40 virtual orbitals. The parameters and parent states of the resonances were determined from the results of the time-delay calculations. The values in brackets correspond to the positions obtained from the calculations using the 6-311+G** basis set, $a = 18a_0$ and 70 virtual orbitals. The resonances without a number in the first column correspond to those found only in the calculations using the diffuse basis set. Configurations obtained from the R-matrix pole analysis are given in terms of direct products of singly occupied orbitals of the reference HF ground state (g.s.) configuration $(1-6a_g)^{12}1b_{3u}^2(1-4b_{2u})^8 1b_{1g}^2(1-5b_{1u})^{10}1b_{2g}^2 3b_{3g}^6$ and singly or doubly occupied orbitals of the active space. Orbitals in each direct product are grouped from left to right according to their increasing SA-CASSCF energy. Electron spin (up or down) is denoted by α and β and has been replaced by the occupation number 1 in the configurations in which both the singlet and triplet spin symmetries contribute to the given spatial configuration.

3.6.1 Analysis of the R-matrix poles

This analysis was performed using the Close-Coupling model with the first set of L^2 configurations in (2.91) completely removed from our model, i.e., without the L^2 configurations involving the virtual orbitals. From now on this model will be called the *Simplified* model. Depending on the symmetry, the number of L^2 functions generated in this model ranged between 120 and 132 only. (This is to be compared with the number of configurations generated in the full CC model: $\approx$ 14000 and $\approx$ 28000 for the calculations using the compact and the diffuse basis set respectively.) We analyzed the most important L^2 configurations contributing to the R-matrix pole closest in energy to an observed resonant structure: we found that the CI coefficients for the main contributing L^2 configurations describing the resonance differed slightly (± 0.15) between the calculations using the diffuse and the compact basis sets, but their relative magnitude was similar, allowing us to classify consistently the configurations according to their importance. We first analyzed the three π^* resonances, whose character is well established [32, 33] in order to confirm the validity of this approach and then turned to the new structures appearing in our calculations. The assignment of the parent states was done on the basis of correlating the most important L^2 configurations for each resonance with the main configurations responsible for the singlet and triplet excited states of the molecule as determined from the CI vectors for these states resulting from our SA-CASSCF calculations described above. An attempt to perform the same analysis for the full CC model proved unfeasible, due to the large number of configurations in the CI expansion.

From all the structures observed in our standard calculations, only the first for each spatial symmetry were visible in the eigenphase sums calculated using the Simplified model. The exception is the $^2B_{2g}$ symmetry, where the second structure was visible as well. The first structure in $^2B_{2u}$ symmetry was only visible in the Simplified model calculations using the diffuse basis set. The magnitude of the "step" in the eigenphase sum associated with the observed structures was smaller in the Simplified model and the structures were shifted roughly by 1 eV towards higher energies. Whether the steps in the eigenphase sums are visible or not can be explained using the time-delay analysis, as we will see below. In principle the analysis of the R-matrix poles could be performed for all the resonances found in the corresponding time-delay spectra: the information on the exact position of the resonance can be extracted from there and then used to search for the corresponding R-matrix pole. However, we performed the analysis of the configurations only for the resonances which were

visible in the eigenphase sums. As we will see in Section 3.6.2, all resonances which appear in our calculations employing the full CC model appear already on the level of the Simplified model. This result implies two important conclusions:

- the Simplified model is appropriate for finding all resonances while being computationally much cheaper.
- the much smaller number of configurations included in the Simplified model already contains the most important configurations responsible for the description of these resonances.

Finally, analysis of the L^2 configurations from the results of the calculation using shifted states gave the same assignment of the resonant structures, with the R-matrix poles describing the resonant structures hardly moving (at most by ≈ 0.19 eV).

3.6.2 Time-delay analysis

The time-delay spectrum of pyrazine, shown in Figure 3.11, was calculated at the Close-Coupling level using the full and Simplified models and the compact basis set. The results using the full model and both basis sets are shown on Figure 3.12. Resonances appear in the time-delay spectrum as Lorentzian peaks (see Section 2.4). All the prominent peaks in both Figures have shapes that can be accurately fitted by a Lorentzian function. The clarity of the time-delay plots for the full model (Figure 3.12) is to be compared with the eigenphase sums (see Figure 3.6), where the steps characteristic of resonances are often very small and in some cases even invisible (e.g. the resonance $3\ ^2B_{1g}$ lying around ≈ 8 eV). As we saw before the features in the eigenphase sums for the Simplified model become more pronounced only when a large number of virtual orbitals is added. On the other hand the resonances appear clearly (albeit at higher energies) in the time-delay spectrum calculated for the Simplified model. For these reasons the time-delay method will be used from now on for finding resonances in our calculations.

The time-delay method allows us not only to find all resonances, but also to characterize them in terms of their parent state(s). In order to do that we need to look for signatures of the resonances in particular scattering channels. This can be done analyzing the diagonal elements of the **Q**-matrix and the branching ratios. Figure 3.13 shows these quantities calculated for the 1^2B_{3g} resonance (i.e. at 5.99 eV) using the compact basis set and the full model. The horizontal axis corresponds to the channel index i which stands for the set of

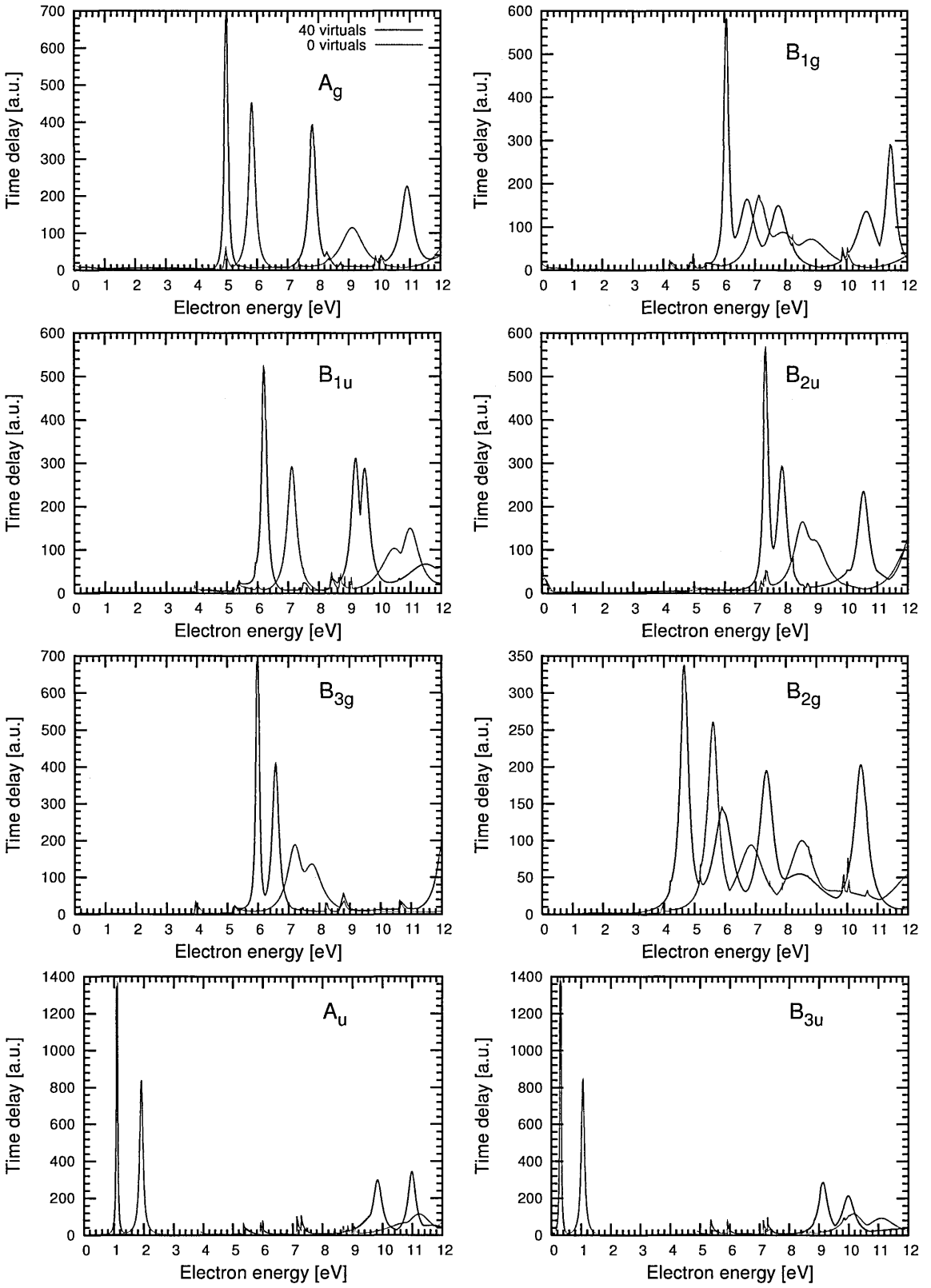

Figure 3.11: The largest eigenvalue of the **Q**-matrix (time-delay) as a function of electron energy. The calculations were performed at the Close-Coupling level using the compact basis set and the full (red line) and Simplified (green line) models.

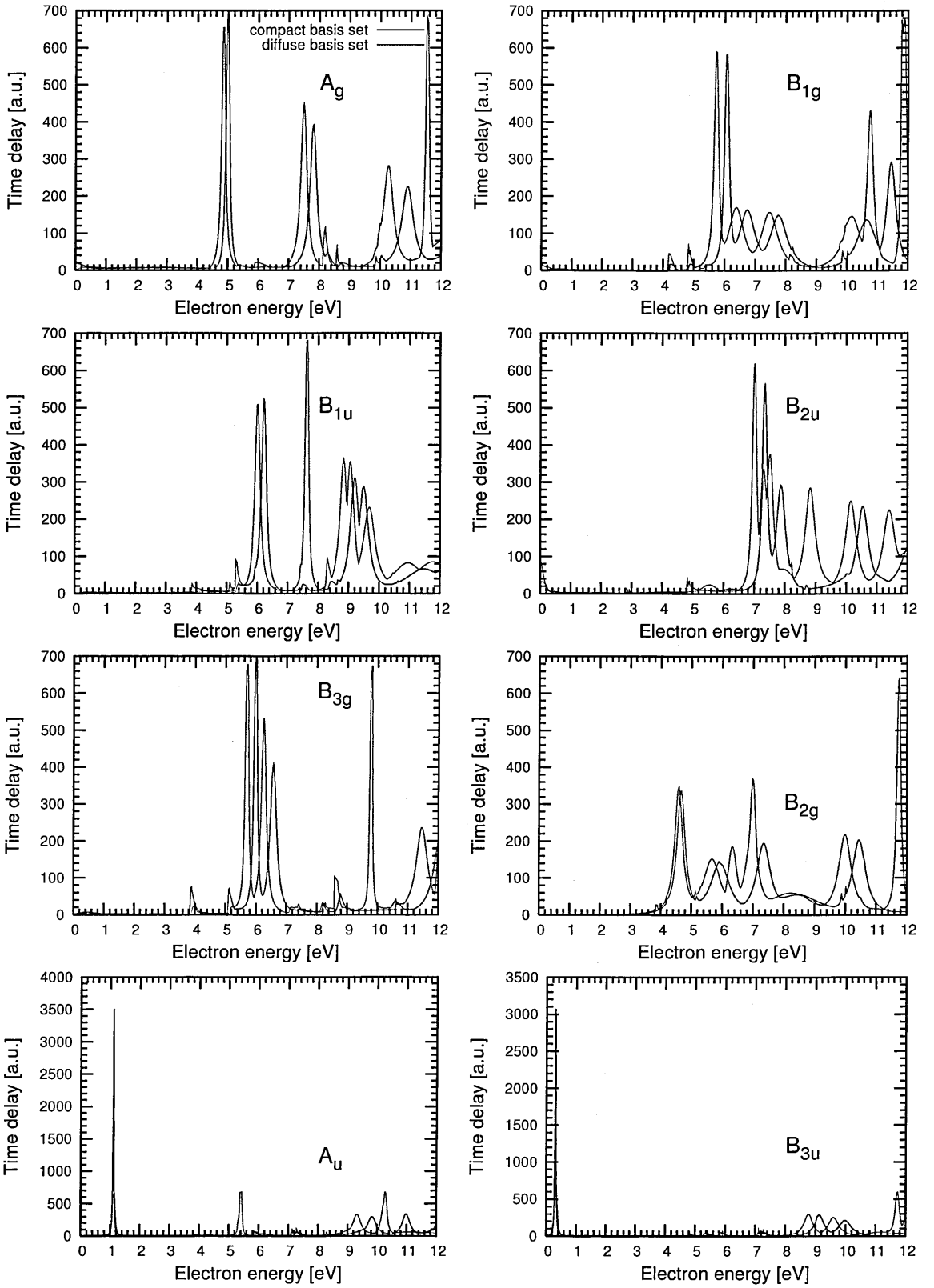

Figure 3.12: The largest eigenvalue of the **Q**-matrix (time-delay) as a function of electron energy. The calculations were performed at the Close-Coupling level using the full models and the compact (40 virtuals) - red line and the diffuse basis sets (70 virtuals) - blue line.

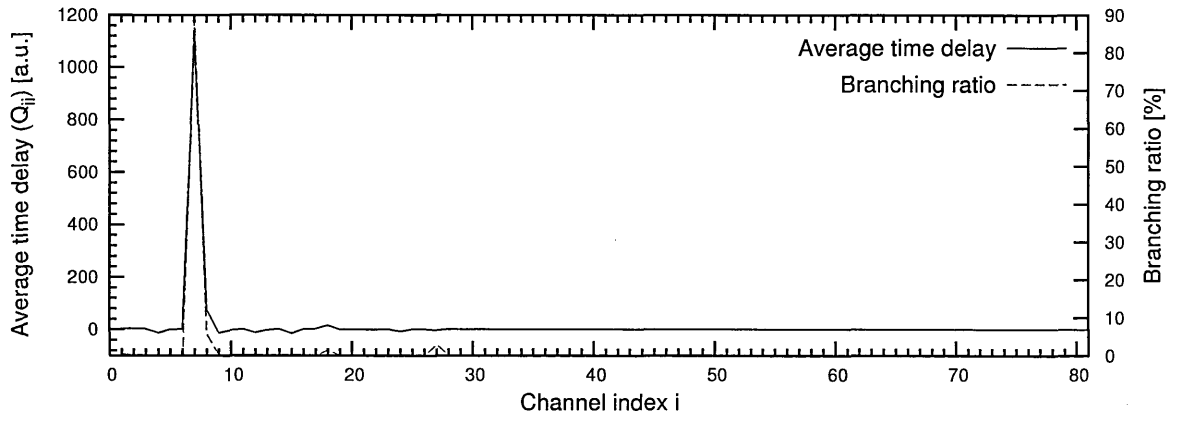

Figure 3.13: The average time-delay and the branching ratio for the 1^2B_{3g} resonance calculated at the Close-Coupling level using the compact basis set and the full model.

values $\gamma^{\Gamma}_{i,l_i,m_i}$ unambiguously defining the initial state (for the average time-delay) or the final state (for the branching ratio) of the scattering system (see Section 2.1). We can see that the positions of the peaks in both curves are strongly correlated. This is indeed the case for all the resonances found in this work. The average time-delay or branching ratio can then be used to determine the parent state of the resonance. This is done by correlating the channel index corresponding to the largest peak in the time-delay and/or branching ratio with the corresponding target state. This procedure is similar to the one described in Section 3.6.3, which uses the excited state elastic cross sections instead. In fact, both approaches lead to identical assignments of the parent states, proving consistency between both methods.

The average time-delays can also be used to explain why some of the resonances do not appear as significant steps in the eigenphase sums. The analysis of the diagonal elements of the **Q**-matrix reveals that the processes which correspond to significant time-delays (i.e. resonances) in some entrance channels, are effectively masked by processes incoming in different, *inelastic*, channels, which lead to a significant time-advance. Since the derivative of the eigenphase sum is related through equations (2.76) and (2.77) to the sum of the diagonal elements of the **Q**-matrix, it becomes clear now why the eigenphase sum does not show a sharp variation in the vicinity of some of the higher-lying resonances. This phenomenon will be illustrated and further discussed in Section 4.8.1.

3.6.3 Cross sections for the excited states

The elastic cross section $\sigma_{i\to i}$ for the i-th excited state (ESE cross section) corresponds to the process in which the molecule is initially and after the collision in the excited state i (see also the equation (2.8)). We found that the analysis of these and the total cross sections for the excited states can provide additional information about resonances lying at energies above the vertical excitation energy of the first excited state. These ESE cross sections were calculated for all excited states included in our calculation using the full CC model (40 virtuals) and the compact basis set. Figure 3.14 shows the total and elastic cross sections for scattering from the state 1^3B_{3u} which has the second lowest vertical excitation energy (see Table 3.3) in our calculations. We illustrate with these cross sections our approach for the analysis of all calculated ESE cross sections. As we will see below, the choice of this particular ESE cross section will also allow us to demonstrate some properties of the third mixed core-excited shape π^* resonance. The excited state total cross section is a sum over all cross sections for transitions from the i-th initial state to all open electronic states. Consequently, this cross section also contains contributions from the deexcitation of the molecule, i.e. transitions to a final state lower in energy than the initial one.

For the cross sections showed before, which correspond to the ground initial state (see e.g. Figure 3.6), the horizontal axis corresponds to the electron energy. In Figure 3.14, the energy on the horizontal axis is $E + \mathrm{VE}(1^3B_{3u})$, where $\mathrm{VE}(1^3B_{3u})$ is the VE energy of the 1^3B_{3u} state (4.18 eV). We make this choice to ease the comparison with the cross sections and eigenphase sums shown in Figure 3.6. In the following when referring to positions of resonances in Figure 3.6, we always refer to the calculations using the compact basis set.

We can see from Figure 3.14 that while the cross sections for scattering in the $^2B_{3u}$ and $^2B_{1g}$ symmetries are generally featureless, all the other cross sections possess one or more peaks. In fact, as we will see later, most of these peaks are associated with resonances. Out of all these peaks the highest ones occur in the ^2A_g and $^2B_{3g}$ symmetries at 4.99 eV and 5.98 eV respectively. The positions of these peaks coincide exactly with the positions of the steps in the eigenphase sums in Figure 3.6 and with peaks in the time-delay in Figure 3.12. We do not observe corresponding peaks in the total (ground state) cross sections, shown in Figure 3.6. On the other hand, the resonance in the ^2A_g symmetry is visible in the TICS (see Figure 3.10), but the $^2B_{3g}$ resonance is barely visible in the $^2B_{3g}$ contribution to the TICS only.

When assigning parent states of resonances we are looking for signatures of resonances in

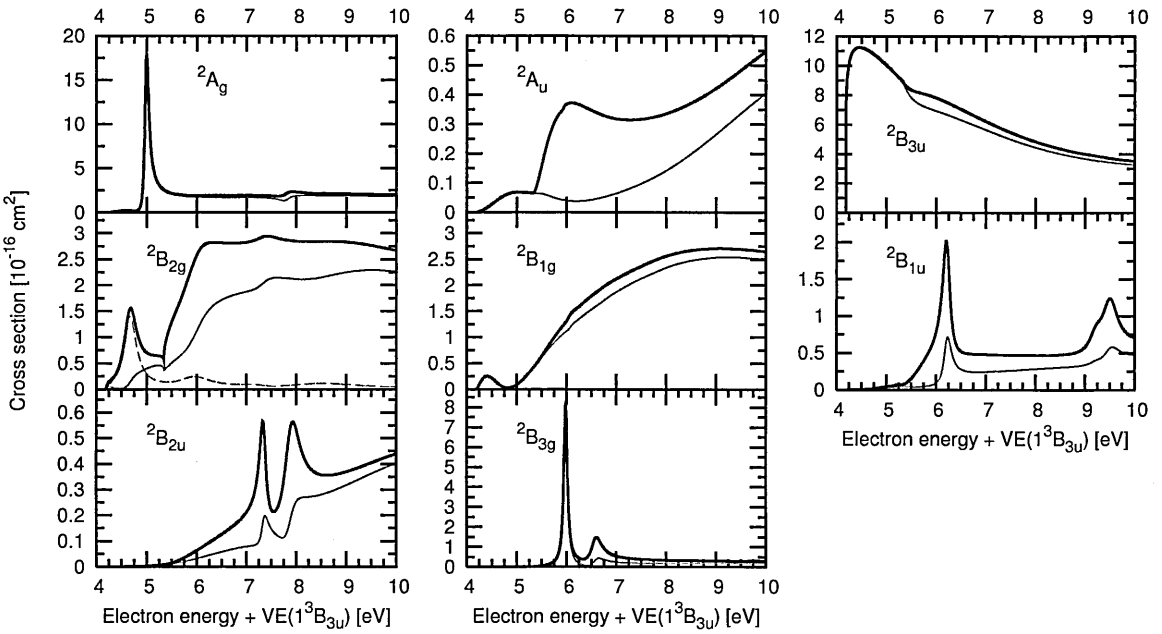

Figure 3.14: Contributions to the total and elastic cross sections for collisions in which the molecule is initially in the excited state 1^3B_{3u} from all scattering symmetries calculated at the Close-Coupling level. The energy on the horizontal axis is that of the scattering electron plus the VE energy of the 1^3B_{3u} state (4.18 eV). The calculations were performed using the compact basis set and 40 virtual orbitals. The black line corresponds to the total cross section for the 1^3B_{3u} excited state and the red line is the elastic cross section for the same state. The green line in the panel for the $^2B_{2g}$ symmetry shows the cross section for transition from the 1^3B_{3u} excited state to the ground state (see text).

particular scattering channels. In this respect, looking at the ESE cross sections for different excited states is similar to using the average time-delay method described in the preceding section. We found that none of the other ESE cross sections possess peaks of a similar magnitude for electron energies corresponding to the resonances at 4.99 eV and 5.98 eV. Based on these observations we are led to the assignment of the 1^3B_{3u} excited state as the main parent state for the resonances 1^2A_g and 1^2B_{3g}.

Analyzing the total and elastic cross sections for excited states allows us to provide more insight into the character of the resonances. We can demonstrate this approach on the third mixed core-excited shape resonance. This resonance is clearly visible in the elastic cross sections calculated on all levels of approximation (see Figures 3.4 and 3.6). Therefore this resonance has shape character and its main parent state is the ground state. The cross section for electron impact electronic excitation of the ground state to the 1^3B_{3u} excited state also displays a peak at the position of the third mixed core-excited shape resonance (see upper right hand panel of Figure 3.10).

Looking again at Figure 3.14, showing cross sections for the initial 1^3B_{3u} excited state, we see that the total cross section for scattering in the $^2B_{2g}$ symmetry clearly shows a peak

centered at the position ($\approx$ 4.66 eV) of this resonance. However, there is no peak in the corresponding ESE cross section at this energy. This property of the resonance is however fully compatible with its mixed core-excited shape character: we found that the peak in the total cross section is 90% from the cross section for transition from the initial state 1^3B_{3u} to the ground state. This cross section is plotted using a green line in Figure 3.14. The large magnitude of the cross section for transition from the 1^3B_{3u} excited state to the ground state is an evidence for a strong coupling of the channels corresponding to the 1^3B_{3u} excited state and the ground state. Therefore the resonance is predominantly associated with the ground state, but is also *mixed* with the 1^3B_{3u} excited state. Based on these observations we can assign the 1^3B_{3u} excited state as one of the parent states of this resonance (the main one being the ground state).

However, a resonance can have more than two parent states. Therefore, we need to investigate whether the mixed core-excited shape resonance is mixed also with other electronic excited states. The only other ESE cross section that displays a very small peak at the position of this resonance is the ESE for the 1^3B_{1u} state. We can therefore assign the 1^3B_{3u} and 1^3B_{1u} excited states as the parent states of this resonance with the first one being more important. Assignment of triplet excited states as parent states for this resonance is in agreement with earlier studies by Winstead and McKoy [33, 60].

An analysis similar to the one described above can be carried out for all the other ESE cross sections, thus obtaining the main parent states of all resonances. For example the other sharp peaks, e.g. in $^2B_{1u}$ and $^2B_{2u}$ symmetries, (albeit small in comparison with the peaks in the ^2A_g and $^2B_{3g}$ symmetries) in Figure 3.14 are indicative of partial involvement of the 1^3B_{3u} excited state in the formation of resonances at these energies. We have to point out however that this approach identifies resonances and their parent states by combining information on the positions of the resonances from the eigenphase sums with the observation of peaks in the (excited state) cross sections. Interpreting peaks in cross sections as resonances is generally not rigorous, especially in situations where the eigenphase sums are not convincing. For example the broad peak in the total cross section centered around 6 eV in the ^2A_u symmetry in Figure 3.14 appears to be nonresonant, mainly because the width of the peak is not compatible with widths of any of the resonances we found around 6 eV. In fact this peak consists mainly of the contribution of the cross section for transition from the 1^3B_{3u} state to the 1^3B_{2g} state. Therefore care must be taken in analyzing resonances *only* in terms of cross sections. However, peaks in the ESE cross sections are further evidence for the possible presence of resonances. For example the structures present above 5 eV in the eigenphase sums

in Figure 3.6 for scattering in $^2B_{2g}$ symmetry are difficult to interpret in terms of resonances, because the steps in the eigenphase sums are much smaller than the steps of π characteristic for a resonance. On the other hand very prominent peaks centered around the energy of the features in the eigenphase sums appear in some of the ESE cross sections. Some of the resonances also appear as non-negligible peaks in the inelastic cross sections for the ground state as explained above. It is the time-delay method that is capable of revealing the presence of resonances unambiguously.

A more detailed comparison of the ESE and the elastic cross sections for the ground state provides us with further examples of how a given resonance influences different cross sections very differently. One of these is the small kink around 8 eV in the ^2A_g symmetry in Figure 3.14. The resonance responsible for this structure is the 2^2A_g resonance at 7.80 eV. However small the footprint of this resonance is in the elastic cross section for the 1^3B_{3u} excited state, it appears as a very prominent peak in the elastic cross section for the 1^3A_u excited state. Another example is the 1^2A_g resonance at 4.99 eV which appears only as a kink of negligible magnitude in the total cross section, but as we can see from Figure 3.14, the peak corresponding to this resonance is the dominant feature of the elastic cross section for the 1^3B_{3u} excited state. Examples similar to these can be found in the total and elastic cross sections for the ground state. All these kinks have the same characteristics: a trough appearing in the elastic cross section for the ground state centered at the position of the resonance and a peak shifted to slightly higher energies appearing in the total cross section.

3.6.4 Resonances

In this section we restrict ourselves to a phenomenological description of the resonances found in our calculations for pyrazine. Further discussion of the resonances and a comparison with the other diazines and experiment will be presented in the next chapter.

$1\ ^2B_{3u}$ resonance

This π^* resonance can be identified unambiguously as the scattering electron being trapped in the $2b_{3u}$ orbital without exciting the molecule from the ground state (g.s.) HF configuration, hence as a pure shape resonance. The CI coefficient for this configuration (in the expansion of the wavefunction of the R-matrix pole which is closest in energy) has a magnitude of ≈ 0.8.

$1\ ^2A_u$ resonance

In this resonance the electron is trapped in the $1a_u$ orbital, while leaving the molecule in its ground state. Therefore this resonance is also purely shape as expected, without any other L^2 configurations significantly contributing. The CI coefficient for the ground state configuration has the value ≈ 0.6 with the rest of the L^2 configurations having negligible CI coefficients.(The second structure visible in the eigenphase sum of this symmetry - see Figure 3.6 - is unphysical: it disappears when the deletion thresholds are increased).

$^2B_{2g}$ resonances

$1\ ^2B_{2g}$ resonance	
Main configuration(s):	$2b^{\alpha}_{2g}$
	$1b^{\alpha}_{1g} \otimes 2b^{\beta}_{3u} \otimes 1a^{\alpha}_{u}$
	$1b^{1}_{3u} \otimes 1b^{1}_{1g} \otimes 2b^{2}_{3u} \otimes 1a^{\alpha}_{u}$
	$1b^{\beta}_{2g} \otimes 2b^{2}_{3u}, 1b^{\beta}_{2g} \otimes 1a^{2}_{u}$

Table 3.8: The main configurations of the $1\ ^2B_{2g}$ resonance as determined from the results of the Simplified model and the R-matrix pole analysis.

Out of all resonances found in this symmetry, we discuss in greatest detail the $1\ ^2B_{2g}$ resonance. This resonance is the mixed core-excited shape π^* resonance. We can fully confirm the character of this resonance as demonstrated previously by Winstead and McKoy. However, as we will see below, identification of its parent states using the method of the R-matrix poles and the time-delay was not entirely consistent.

The most important configurations of this resonance in the Simplified model are showed in Table 3.8. Unlike the previous two resonances, the main, shape-like, configuration (HF g.s.)$^{42}\otimes$ $2b^{1}_{2g}$ has now CI coefficient of only ≈ 0.4 with the other configurations listed in Table 3.8 having CI coefficients ranging from ≈ 0.3 to ≈ 0.1. These properties prove the mixed core-excited shape character of this resonance. The time-delay analysis of the results of the Simplified model shows that the parent states of this resonance are (in the order of importance): ground state, $2\ ^3B_{1u}$, $1\ ^3B_{1u}$ and $1\ ^3B_{3u}$. This is consistent with the time-delay analysis of the full model.

Although we do not find the main configuration ($6a^{\alpha}_{g} \otimes 2b^{\alpha}_{3u}$) of the state $1\ ^3B_{3u}$ among the ones in Table 3.8, the configurations listed are compatible with the main parent states of this resonance being the ground state and the $2\ ^3B_{1u}$, $1\ ^3B_{1u}$ excited states. This discrepancy between the results of the time-delay and the R-matrix pole analysis is acceptable: the latter

method is generally less accurate than the time-delay analysis. This is caused mainly by the fact that the time-delay provides us with quantitative information (time-delays for each scattering channel) about the collision for a given electron energy, which allows us to link straightforwardly the electronic states with resonant processes occurring in the corresponding channels.

Interestingly, the state 1 $^3B_{3u}$ was identified as the main parent state in the time-delay/cross section analysis of the results of the *full* scattering model; naturally we deem this result to be more accurate than the results of the Simplified model. We can see that the time-delay analysis lists in both models the 1 $^3B_{3u}$ excited state as one of the parent states. On the other hand, the analysis of the R-matrix poles does not, in this case, agree fully with the time-delay analysis. Therefore in order to assign parent states to this resonance, we use the results of the time-delay analysis, because (as explained in the paragraph above) it is more reliable than the R-matrix pole analysis.

Generally if, for any resonance, a discrepancy between the results of the time-delay analysis and the R-matrix poles analysis is found, we choose not to consider the results of the latter reliable and consequently we do not provide configuration(s) of the resonance. It is for this reason that we do not list the core-excited configurations of the 1 $^2B_{2g}$ resonance in Table 3.7.

Intriguingly, the third L^2 configuration contributing to the description of the 1 $^2B_{2g}$ resonance as identified by us is based on double excitation of the target molecule, which is a configuration not present in the calculations of Winstead and McKoy. Accounting for this type of configuration in their models could perhaps shift the resonance even closer towards its experimental position.

The 1 $^2B_{2g}$ resonance is responsible for the shoulders seen in the upper panels of Figure 3.10 around 4.6 eV in the cross sections for excitation of the ground state of the molecule into the 1 $^3B_{1u}$ and 1 $^3B_{3u}$ excited states respectively.

The peaks around 5.7 eV in the inelastic cross sections (Figure 3.10) are caused by a significant contribution of the 2 $^2B_{2g}$ resonance. However, this resonance is barely visible in the eigenphase sum of the Simplified model and we have not attempted to interpret it in terms of configurations. The main parent states of this resonance are the ground state and the lowest-lying (triplet) excited state; we discuss this resonance further in Section 3.6.5. The peak corresponding to this resonance is also visible in the total cross section (Figure 3.9).

The 3 $^2B_{2g}$ resonance is core-excited and a peak corresponding to it is visible in the total inelastic cross sections shown in Figure 3.10.

The highest-lying (broad) resonance of this symmetry is visible in the total and inelastic cross sections (Figures 3.9 and 3.10). One of the parent states of this resonance is the ground state and we discuss further properties of this resonance in Section 3.6.5.

The calculations using the diffuse basis set show the presence of an additional resonance around 6.34 eV (see Figure 3.12). It remains to be determined whether this structure is physical or caused by linear dependence problems.

^2A_g resonances

Figure 3.6 shows the presence of two structures in this symmetry although the SE results from Figure 3.3 using the compact basis set do not show any resonances in the whole energy region studied. A detailed analysis of the scattering data using the three methods described before reveals that the most likely parent state responsible for the first, core-excited, resonance in this symmetry is the $1\ ^3B_{3u}$ state. This assignment together with the position of this resonance agree very well with the largest peak in the upper right hand panel of Figure 3.10 for inelastic scattering into the $1\ ^3B_{3u}$ excited state. The $1\ ^2A_g$ resonance manifests itself only as a small kink in the corresponding total ^2A_g cross section. The second structure in the eigenphase sum becomes apparent only when a higher number of virtual orbitals is included in the Close-Coupling model (see Figure 3.7), but it does not show up in the total or inelastic cross section at all.

$^2B_{1g}$ resonances

The absence of structures in the SE results suggest that these resonances are of core-excited character. However, the $1\ ^2B_{1g}$ resonance has several parent states and causes a significant time-delay in collisions with the target in its ground state. Therefore we assign the ground state as one of the parent states of this resonance. The resonance is clearly visible as a peak in the total cross sections showed in Figure 3.6. A small peak corresponding to this resonance is also visible in the summed integral total cross section in Figure 3.9. We can see that the properties of this resonance are similar to the properties of the $2\ ^2B_{2g}$ and $4\ ^2B_{2g}$ resonances and we discuss all these resonances further in Section 3.6.5.

The $1\ ^2B_{1g}$ resonance along with the $2\ ^2B_{2g}$ resonance (that provides the main contribution) are responsible for the largest peak in the cross section for inelastic scattering $1\ ^1A_g \rightarrow 1\ ^3B_{1u}$. The second and the third resonances in this symmetry have core-excited character and the peaks in the TICS corresponding to these resonances are visible in the bottom panel of Figure 3.10.

$^2B_{1u}$ resonances

The eigenphase sums in Figure 3.6 suggest the presence of up to three resonances in this symmetry. In fact the time-delay results then reveal that the calculations using the diffuse basis set support an additional resonance at 7.62 eV. We do not attempt to interpret the resonance seen around 9.5 eV using the diffuse basis set (see Figures 3.12 and 3.6), because our calculations may become unreliable at these energies. Analysis of the $1\ ^2B_{1u}$ resonance shows the most significant contribution to be from the excitation responsible for the $1\ ^3B_{2g}$ excited state.

Our SE calculations performed with the diffuse basis set show a significant step around 8 eV and we argue that it corresponds to the resonance at 7.62 eV seen in this symmetry in the Close-Coupling calculations (using the diffuse basis set). The similarity of the positions of the two resonances in the SE and the Close-Coupling models is unexpected and might suggest problems with linear-dependency at this energy, but we are not able to resolve this at present.

Close-Coupling calculations using both basis sets show a structure in the eigenphase sum below 10 eV which actually corresponds to two resonances as apparent from the time-delay results shown on Figure 3.12. Our analysis of the time-delay and excited state cross sections shows that the resonances in this symmetry do not have the ground state as one of the parent states. Therefore we suggest that in this case the steps in the eigenphase sums visible in the SE calculations (see Figure 3.3) describe, at least partially, an effective electrostatic potential which is responsible for trapping of the electron in the Close-Coupling model, where we cannot confirm the shape character of this resonance. The resonances $1-3\ ^2B_{1u}$ are not visible in the total cross sections (see Figure 3.6).

$^2B_{2u}$ resonances

The value of the corresponding CI coefficient for the main configuration of the $1\ ^2B_{1u}$ resonance is relatively small (≈ 0.2) and this excitation can correspond to three different parent states: $1\ ^3B_{2g}$, $1\ ^1B_{1g}$ and $1\ ^3B_{1g}$. By combining this information with the one obtained using the time-delay/cross section analysis, we find that the parent state is the $1\ ^3B_{2g}$. The second resonance in this symmetry is core-excited, but our SE results show it and suggest that it might be associated with one of the higher lying virtual orbitals in this symmetry. However, we argue, as in the case of the higher-lying $^2B_{1u}$ resonances, that in this case the SE calculations are probably not describing a resonance of shape character. The $3\ ^2B_{2u}$

resonance might not be physical and the oscillatory behaviour of the eigenphase sum seen above 8 eV may be due to a poor description of the continuum at higher energies in this symmetry. Nonetheless a third structure was also observed above 10 eV in calculations using the compact basis set, where the description of the continuum is generally much better.

$^2B_{3g}$ resonances

The two resonances in this symmetry are core-excited and are visible in the total cross sections (see Figure 3.6) only as small kinks. These peaks in fact originate in the corresponding small peaks in the TICS shown in the bottom panel of Figure 3.10. Additionally a very sharp structure, which we do not interpret, appears around 10 eV in the time-delay and eigenphase sums for the calculation using the diffuse basis set.

3.6.5 Characteristics of selected resonances

In the preceding section we described the properties of all resonances we found in pyrazine. However, the properties of some of them merit a deeper discussion, to which we turn here. The resonances, which are discussed here are the 2 $^2B_{2g}$, 4 $^2B_{2g}$ and 1 $^2B_{1g}$ resonances (see Table 3.7).

These three resonances were not found in pyrazine before and they differ from the other new resonances we find in that they are clearly visible in the elastic cross sections. Our time-delay analysis also shows that these resonances are the source of a significant delay in collisions corresponding to the ground initial state of the molecule. These two properties are similar to those of the third π^* mixed core-excited shape resonance and make these resonances significantly different to the other new resonances we found. We might be tempted to assign a mixed core-excited shape character to them as well, but the following reasons prevent us from doing so with confidence. A mixed core-excited shape resonance (like the third π^* resonance) usually appears at the level of the SE calculations. However, our SE calculations (see Figure 3.3) are inconclusive: those using the diffuse basis set display some structure at higher energies (above the third π^* resonance), whereas those using the compact basis set do not show any structure that could correspond to the 2 $^2B_{2g}$, 4 $^2B_{2g}$ and 1 $^2B_{1g}$ resonances. (It is actually more likely that the structure appearing in the calculations using the diffuse basis set is unphysical and is caused by a poor representation of the continuum). Another feature which makes these resonances different from the third π^* resonance is the fact that the third π^* resonance possesses a much smaller time-delay associated with channels corresponding to

the excited states compared with the time-delay corresponding to the ground state, which is the dominant one. The 2 $^2B_{2g}$, 4 $^2B_{2g}$ and 1 $^2B_{1g}$ resonances, on the other hand, possess time-delays associated with the excited states of a magnitude that is similar to the time-delay associated with the ground state. Therefore, while these resonances clearly have some similarities with the π^* mixed core-excited shape resonance, they also have properties that make them appear rather differently in the scattering data. Consequently, we cannot ascertain whether these resonances possess a mixed core-excited shape character.

The label "shape" is used to designate those resonances which are formed by trapping of the incoming electron by a combination of short-range attractive forces of the ground state of the target and long-range repulsive forces caused by the angular-momentum barrier of the incoming electron (see Section 1.1). The SE calculations, which do not show the presence of the 2 $^2B_{2g}$, 4 $^2B_{2g}$ and 1 $^2B_{1g}$ resonances, do not include the polarization effects of the ground state electronic density caused by the incoming electron. Polarization of the charge density of the target molecule has an attractive effect on the incoming electron and hence can play a role in the formation of a shape resonance. The potential associated with this interaction is approximately given by the formula

$$V_{pol}(r) = -\frac{\alpha}{2r^4}, \tag{3.1}$$

where α is the spherical polarizability of the molecule and r is the distance of the scattering electron from the center of mass of the molecule. The above formula is actually valid only asymptotically and neglects anisotropy of the polarization interaction, but we can use it to support the following qualitative arguments. Given the fact that the 2 $^2B_{2g}$, 4 $^2B_{2g}$ and 1 $^2B_{1g}$ resonances have, as shown above, some characteristics of a shape resonance and the large polarizability of pyrazine (see Table 3.2), we are led to speculate that the polarization interaction itself might be causing the formation of these resonances and that therefore these resonances actually have a shape character.

If this is the case then these resonances should appear at the SEP level, which incorporates polarization. However, due to the presence of pseudoresonances at higher energies in our SEP calculations, we cannot draw conclusions from analyzing the eigenphase sums or cross sections at these energies. The CC calculations, which do not display pseudoresonances are not helpful in answering the question of the character of these resonances, because we cannot easily determine whether their formation is caused by polarization of the ground state of the molecule followed by trapping of the scattering electron in a virtual orbital or if they are

formed through coupling to excited states, i.e. the resonances are core-excited.

Therefore it remains to be seen what is the exact character of these resonances (mixed core-excited shape or pure core-excited shape). Consequently, the fact that the ground state is listed as one of the parent states of these three resonances in Table 3.7 has to be understood only as a mere statement of the fact that they cause a significant time-delay in collisions corresponding to the ground initial state of the target molecule.

3.7 Summary

In this Chapter we established scattering models for calculations with the diazine molecules. Pyrazine was used as a model example. Calculations using two basis sets (a compact one and a diffuse one) were performed and compared. We found that the calculated cross sections (integral and differential) display differences for energies below $\approx$ 3 eV. We link this phenomenon to the different shape of the target virtual molecular orbitals in both basis sets which are used to construct the L^2 functions describing the polarization/correlation. Based on this observation (and because pyrazine possesses a number of Rydberg excited states), we suggest that the diffuse atomic basis set is more appropriate than the compact one for scattering calculations on diazines. However, calculations using the compact basis set are computationally cheaper and preserve almost all resonances found in the calculation using the diffuse basis set (some of the additional resonances found in the calculation employing the diffuse basis set might not be physical).

We compared the positions of the low-lying π^* shape resonances with the experimental data of Nenner and Schulz and with the calculations of Winstead and McKoy and obtained good agreement for the first two resonances. The third π^* resonance lies too high in energy in all our models. The SEP calculations of Winstead and McKoy place this resonance closer to the experimental position than our calculations. We ascribe this difference between their and our SEP results to the use, in their calculations, of modified HF target molecular orbitals and to a different choice of the L^2 functions used to construct their models. The elastic cross sections (integral and differential) calculated at SEP level using the diffuse basis set have shapes and magnitude similar to those of Winstead and McKoy. Comparison of the calculated DCS with experiment confirms that the use of the diffuse basis set and the SEP models leads to more accurate results for low electron energies. For higher energies (above $\approx$ 6 eV) it is the CC calculations using the compact basis set which give a better agreement with the experiment.

We have demonstrated the indispensability of the time-delay method for finding and characterizing resonances. This method can be complemented by examining the R-matrix poles of the Simplified model and cross sections corresponding to the molecule initially in an excited state to obtain a more detailed picture of the resonances. The assignment of the parent states of the resonances in pyrazine performed by analyzing the R-matrix poles of the Simplified model is consistent with, in most cases, but less accurate than, the assignments based on the time-delay method. This result supports the validity of both approaches. We used these methods to confirm the properties of the well-known low-lying π^* shape resonances. Additionally, we find a number of resonances lying above the third π^* resonance. Some of these resonances are visible in the calculated total and elastic cross sections (corresponding to the molecule being initially in its ground state). A number of resonances were found which do not show up significantly in the total and elastic cross sections, but which manifest themselves strongly in collisions with the molecule initially in an excited state. The resonances and their properties were found to be the same in calculations employing both basis sets. An important property of the resonances is that all of them are already visible in the calculations using the Simplified model which includes only 8 active orbitals. Therefore we propose that this computationally cheap model followed by the time-delay analysis can be used to search for presence of resonances in similar biomolecules.

In the next chapter all resonances we found in pyrazine will be compared with the ones found in the other diazines and with experimental data available for pyrimidine.

Chapter 4

Electron collisions with diazines

This chapter describes in detail the calculations performed for pyrimidine and pyridazine and presents a comparison of our results for all diazines. First, we describe the results of our scattering calculations on pyrimidine and compare them with available experimental data. These include the differential and integral cross sections as well as the electron impact electronic excitation cross sections. The results of this work have been published [130]. In the second part of this chapter we describe our scattering calculations on pyridazine, the last diazine studied in this work. Finally, calculated cross sections and electron resonances found in the three diazines are compared and discussed in detail. This work has also been published [96].

4.1 Pyrimidine

Pyrimidine is the precursor of the pyrimidinic nucleobases and as such has received the greatest experimental and theoretical attention compared with the other diazines. However, up to date only a few calculations of electron collisions with this molecule have been reported (see Section 3.1 for a detailed literature review). The only *ab-initio* calculations which were available prior this study were those of Winstead and McKoy [34] employing the SEP model, i.e. elastic calculations. And unlike the other two diazine targets, elastic experimental cross sections were available for comparison. The experimental elastic differential and integral cross sections have been published recently [34]. The comparison of our integral inelastic cross sections (i.e. cross sections for electron impact electronic excitation) with experimental data was carried out in collaboration with the group of Professor Michael Brunger (Flinders University, Australia), where the measurements were performed (see Section 4.2.2 for details of the experimental technique).

	cc-pVDZ	6-311+G**	Acc. value
HF [H]	−262.71	−262.75	−263.4019
SA-CASSCF [H]	−262.79	−262.83	
μ_{HF} [D]	2.31	2.53	2.334 ± 0.010
$\mu_{SA-CASSCF}$ [D]	2.36	2.53	

Table 4.1: Energy, in Hartree, and dipole moment, in Debye, of pyrimidine in its ground electronic state calculated at the HF-SCF and SA-CASSCF levels, using the basis sets cc-pVDZ and 6-311+G**. Also shown is the experimental value [107] of the ground state dipole moment and accurate value [105] of the ground state energy of the molecule calculated using the multi-reference CI method and the TZVP basis set.

4.1.1 Target description

The calculations used the geometry of pyrimidine [121] optimized at the level of the second-order Møller-Plesset perturbation theory (MP2). The ground state configuration of pyrimidine is: $1a_1^2\ 1b_2^2\ 2a_1^2\ 3a_1^2\ 2b_2^2\ 4a_1^2\ 5a_1^2\ 3b_2^2\ 6a_1^2\ 4b_2^2\ 7a_1^2\ 8a_1^2\ 5b_2^2\ 9a_1^2\ 6b_2^2\ 10a_1^2\ 1b_1^2\ 11a_1^2\ 1a_2^2\ 7b_2^2\ 2b_1^2$. For our target calculations we followed our work on pyrazine and used two different basis sets: a compact basis set, cc-pVDZ, and a diffuse one, 6-311+G**. For the SEP calculations presented below, we generated Hartree-Fock SCF orbitals. For the CC ones, we performed state-averaged CASSCF calculations using MOLPRO [124]. The averaging scheme was selected following tests performed for pyrazine (see Section 3.3), namely the ground state and the two lowest-lying states of each spatial and spin symmetry, i.e. 17 states were used in the averaging. We did not perform further tests concerning the avergaging scheme. For our CASSCF calculations, we chose the active space $(10, 8)$. Just like the pyrazine active space, this one comprises 10 electrons distributed among the 6 valence π orbitals and the two lone-pair σ orbitals located on the two nitrogen atoms. The doubly occupied core in our calculations is therefore (1-10 a_1)^{20} (1-6 b_2)^{12}. Further details about the active space used can be found in Section 3.2.1.

Table 4.1 shows our results for the ground state properties (energy and dipole moment) of pyrimidine. The energy at both HF and CASSCF levels, with both basis sets, is only in fair agreement with more accurate calculations. The dipole moments are within 10% of the experimental data, with the compact basis set providing results within 1%, which can be considered a very good agreement. Table 4.2 shows our calculated vertical excitation energies along with an assignment of the states to the measured electron energy loss features (for details of this assignment, see section 4.2.3). We also report the data of Ferreira da Silva et al. [113] used to classify the experimental cross sections (see Section 4.2.3) as well as results from the measurements of Fischer et al. [115] and the TDDFT calculations of Stener et al. [114]. These latter calculations, geared specifically towards providing an accurate

	VE energy [eV]						Energy loss Spectra	
	This work		Fischer	Ferreira da	Stener			
State No.	cc-pVDZ	6-311+G**	et al. [115]	Silva et al. [113]	et al. [114]	Symmetry	Label	Energy [eV]
1	4.00	3.97	4.0	–	4.45	$1\,^3A_1$	I	4.3
2	4.54	4.54	3.8	–	3.05	$1\,^3B_1$	I	4.3
3	4.99	4.97	4.3	4.183	3.44	$1\,^1B_1$	I	4.3
4	5.12	5.08	4.8		4.50	$1\,^3B_2$	I	4.3
5	5.13	5.09	5.3	5.22(5)	5.44	$1\,^1B_2$	II	5.2
6	5.24	5.29	4.4		3.46	$1\,^3A_2$	I	4.3
7	5.27	5.23	5.1		–	$2\,^3A_1$	II	5.2
8	5.63	5.63	4.8		3.67	$1\,^1A_2$	I	4.3
9	6.45	6.43	5.4		4.20	$2\,^3A_2$	II	5.2
10	6.71	6.67	5.9		4.65	$2\,^1A_2$	III	5.9
11	7.07	7.05	5.7		4.60	$2\,^3B_1$	III	5.9
12	7.23	7.21	6.1	~ 6.0	4.89	$2\,^1B_1$	III	5.9
13	7.42	7.37	–		–	$2\,^3B_2$	IV	6.7
14	7.54	7.50	–		–	$3\,^3A_1$	IV	6.7
15	8.07	8.02	–		–	$3\,^3B_2$	IV	6.7
16	8.34	8.27	6.8	6.69(1)	6.35	$2\,^1A_1$	IV	6.7
17	8.53	8.46	–		6.55	$2\,^1B_2$	IV	6.7
18	8.84	8.76	–		7.40	$3\,^1A_1$	V	7.5
19	9.04	9.03	–		–	$3\,^3A_2$	VI	8.3 and 9.2
20	9.20	9.18	–		–	$3\,^1A_2$	VI	8.3 and 9.2
21	9.37	9.33	–		–	$3\,^3B_1$	VI	8.3 and 9.2
22	10.18	10.10	7.6	7.478	7.19	$4\,^1A_1$	V	7.5
23	10.26	10.21	–		–	$4\,^3A_2$	VI	8.3 and 9.2
24	10.26	10.22	–		–	$4\,^3B_1$	VI	8.3 and 9.2
25	10.29	10.22	7.6	7.478	7.42	$3\,^1B_2$	V	7.5
26	10.31	10.30	–		–	$4\,^3B_2$	VI	8.3 and 9.2
27	10.46	10.41	–		7.42	$3\,^1B_1$	V	7.5
28	10.51	10.48	–		7.50	$4\,^1B_2$	V	7.5

Table 4.2: Vertical excitation energies, calculated at SA-CASSCF level with the indicated basis sets, for the electronic states of pyrimidine included in the CC calculation. Also listed are the experimental results of Fischer et al. [115] and Ferreira da Silva et al. [113] and values from TDDFT calculations by Stener et al. [114]. The experimental energy loss features (see Figure 4.4) and spectral assignments are also presented.

description of the excited states, report many more singlet states in the $0-10$ eV range than we find in our calculations. Some of these are of Rydberg/partial Rydberg character, that is poorly represented by our models, and therefore probably appear at much higher energies in our calculations. The limited active space we use accounts for the absence of some higher-lying valence states (see Section 3.2.1). It is clear at first sight that both our calculations overestimate the excitation thresholds. Comparing with the results of Fischer et al. [115], the difference is smaller than 0.75 eV for states below 5 eV but increases to more than 1 eV above that energy. The relatively poor match is not surprising and is due to the fairly 'simple' nature of our target calculations (see Section 4.5).

4.2 Pyrimidine: scattering calculations and comparison with experiment

The scattering models employed for pyrimidine were of the same type as the ones used for pyrazine, i.e. we performed the SEP and CC calculations (see Section 2.6) to generate the cross sections. We chose to use 35/40 virtual orbitals when using the cc-pVDZ basis set and 40/70 virtual orbitals when using the 6-311+G** one, for the SEP/CC calculations respectively. Details of how the number of virtuals was chosen and how it affects resonances will be described in Section 4.7. For our CC calculations we set the threshold for inclusion of the electronically excited states to 10.51 eV.

Pyrimidine is a polar molecule, a property that causes some specific problems in our calculations. Most importantly, for a polar target molecule our ab-initio calculations need to be complemented with the use of the Born-correction in order to obtain cross sections suitable for comparison with experiment. The specific properties of scattering from a polar target molecule and the use of the Born-correction in our calculations are described in detail in Appendix B.

In order to ensure that the electronic density of both the target states and L^2 functions included in the CC expansion is contained inside the R-matrix sphere we have employed a radius $a = 13\ a_0$ when using the cc-pVDZ basis set and $a = 18\ a_0$ when using the 6-311+G** basis set (this is the same choice as for pyrazine). For the calculations using the compact basis set we included partial waves with $l \leq 5$ and for the diffuse basis set we included those with $l \leq 4$. For pyrazine we obtained cross sections converged with respect to the partial wave expansion when using continuum functions with $l \leq 4$ only. The use of the partial waves with $l \leq 5$ for pyrimidine is required due to the dipolar character of the target (see Appendix B). The reason behind the smaller number of partial waves included in the calculations using the diffuse basis set lies mainly in difficulties associated with the orthogonalization of a large number of continuum functions to some of the *diffuse* target orbitals (see Appendix B.2). The corresponding optimized continuum basis sets for these R-matrix radii were the same as the ones used for pyrazine (see Section 3.4). The deletion thresholds used in the orthogonalization step (see Section 2.7) were set to the standard value 10^{-7} for the calculations using the compact basis set. For the calculations using the diffuse basis set, they were set to values which were mainly larger (up to $\approx 10^{-6}$): this choice is different to the one made for pyrazine. These values correspond to a conservative choice: we decrease the quality of representation of the continuum in favour of avoiding potential linear

dependence problems.

4.2.1 Elastic cross sections

Figure 4.1 compares our calculated elastic differential cross sections (DCS) for several scattering energies. We present the SEP and CC results calculated using both basis sets with the Born correction included and also the results of the SEP calculations using the compact basis set without the Born correction. The figure also includes the experimental results of Palihawadana et al. [34]. However, comparison with the experiment will be discussed in detail later and in the following we concentrate only on the calculated results. We can see that all DCS for low electron energies (3 eV and 4 eV) and also for the energy 8 eV are very similar. At 6 eV, however, the CC calculation using the diffuse basis set has a much more pronounced backward scattering character compared with the other results shown. This difference can be most probably attributed to a worsening of the quality of the description of the continuum above $\approx$ 5 eV in the calculations using the diffuse basis set. At 8 eV the magnitudes of the cross sections calculated in both basis sets are more similar than at 6 eV. However, at 8 eV, the agreement between the CC calculations using the compact and the diffuse basis sets is rather fortuitous: as we will see later, the *integral* cross section calculated at the CC level using the diffuse basis set develops an irregular structure above $\approx$ 5 eV which can be explained by the fact that for some electron energies the representation of the continuum is accidentally better than for the other ones (see Section 3.4.1 for more details on this phenomenon).

We now turn to a comparison of our calculated DCS with the experimental data. The agreement with the experiment is very good for all four energies for which experimental results [34] are available. At 15 eV, the SEP model provides cross sections in better agreement with experiment, particularly in the 50-130° range. The oscillatory behaviour of the CC DCS using the diffuse basis set is probably due to the fact that, in calculating the DCS, we are neglecting the majority of open channels (see Appendix B.2.1) and a worse quality of representation of the continuum; the CC results are very good for 10 eV, but at 12 eV (not shown) they already exhibit this behaviour. Oscillations, albeit of a smaller magnitude, can be seen also in the cross sections for 10 eV and 15 eV calculated using the compact basis set. These are probably due to the Born closure method used to calculate the contributions of the partial waves with large angular momentum (see Section B.2.1). Nonetheless, the magnitude of the cross section is similar with both methods at all energies. The calculated cross sections show the typical feature of dipolar scattering which is the divergence of the cross sections for scattering in the

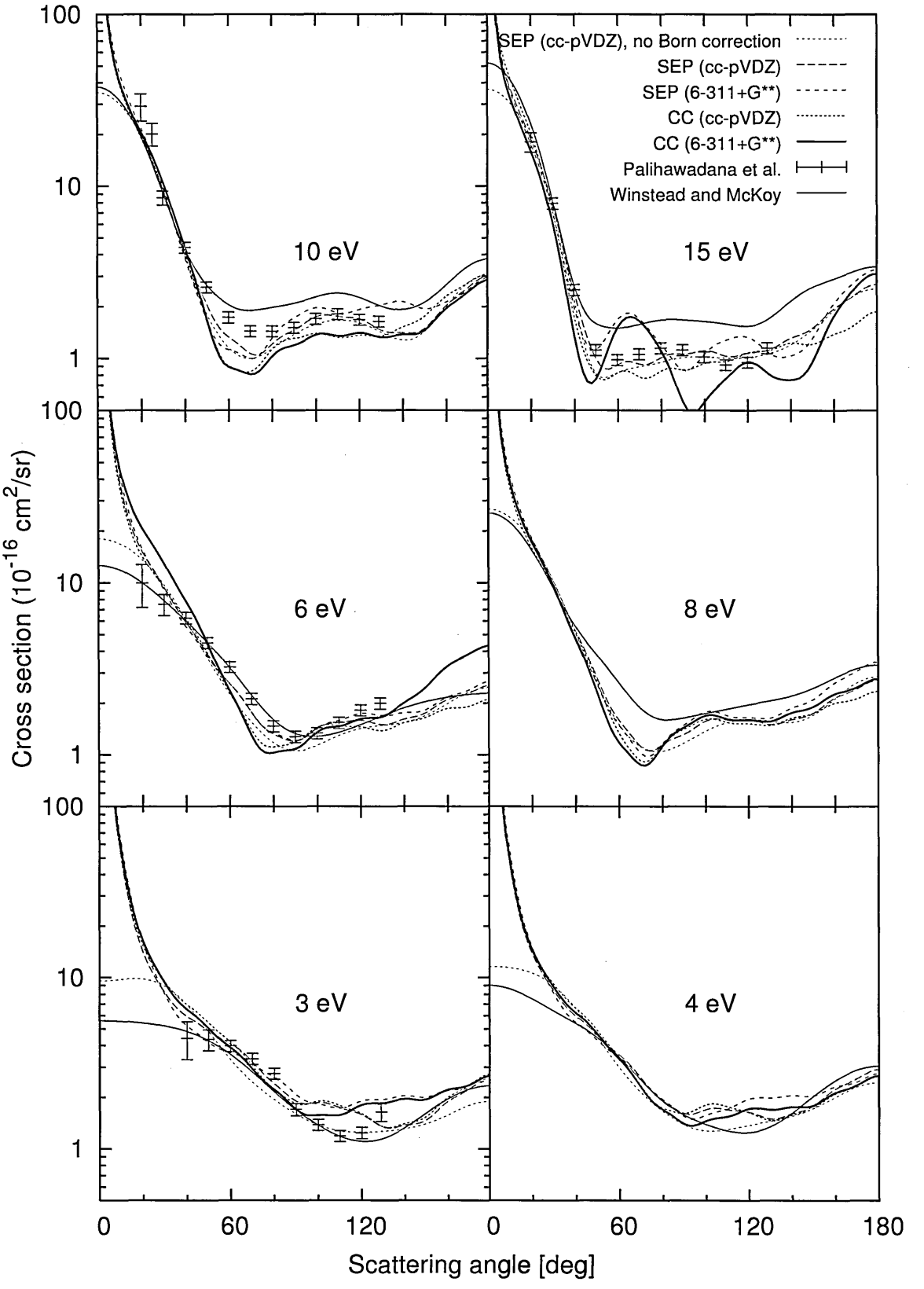

Figure 4.1: Elastic differential cross sections for pyrimidine for the scattering energies indicated in the panels, at both the SEP and CC levels of approximation and using the compact and the diffuse basis sets. Born-corrected results are presented with exception of the results of the calculation indicated on the upper panel. Also shown are the experimental results of Palihawadana et al. [34] and the results of the SMC calculations of Winstead and McKoy (ibid.).

forward direction (see Appendix B).

Figure 4.2 shows the comparison between experiment and calculation for the integral elastic cross section (ICS). We present the Born-corrected cross section, appropriate for comparison with the experiment, as well as the (uncorrected) cross sections resulting from the R-matrix calculations at SEP and CC levels, all calculated with the compact basis set. The cross section displays divergence at low energies, which is a manifestation of dipolar scattering. The very narrow peaks visible in the SEP cross section above 7 eV correspond mostly to non-physical resonances, a normal feature of SEP calculations that use a multi-configuration description for the $N + 1$ wavefunction (see Section 2.6.2 for details). The peaks below this energy (and those visible in the CC cross section) correspond to physical resonances [32, 34, 96]. Except for the change in the position of these physical resonances, the SEP and CC approximations produce similar results. In the SEP model, the resonance positions are in reasonable agreement with earlier data [32, 34, 96]. The small peak below 7 eV visible in the results of the CC calculations using the compact basis set can also be attributed to resonances. (We postpone a detailed discussion of the resonances until Section 4.8). We can see from the Born corrected curves that the previously mentioned disagreement between the DCS at 6 eV calculated using both basis sets correlates well with similar differences in the ICS at the same energy. The irregular character of the ICS calculated using the diffuse basis set (caused by a poor representation of the continuum) is clearly visible as well.

Despite the excellent agreement of the DCS, the calculated ICS (including the Born correction) is larger than the experimental one for the whole energy range presented. The Born-corrected theoretical ICS corresponds to integrating the Born-corrected DCS in the whole 0-180° angular range; in order to obtain the experimental ICS, the results need to be extrapolated before they are integrated. It is this extrapolation that leads to the apparent differences in the ICS. When both experimental and calculated DCS are integrated only in the angular range for which there are measurements (20-130° for 6 eV and above and 40-130° below 6 eV) the agreement between theory (Born-corrected) and experiment is, as expected, very good. The comparison for these 'partially integrated' results is shown in Figure 4.3: notice that now both the CC and SEP Born-corrected results fall (with exception of the 10 eV one) within the error bars of the experiment. The apparent jump in magnitude of the partially integrated cross sections between 5 eV and 6 eV is caused by the different angular range of integration for the lower and the higher energies.

The good agreement between the uncorrected ICS and the experimental results integrated over all angles is no coincidence: as can be seen in Figure 4.1, the uncorrected R-matrix

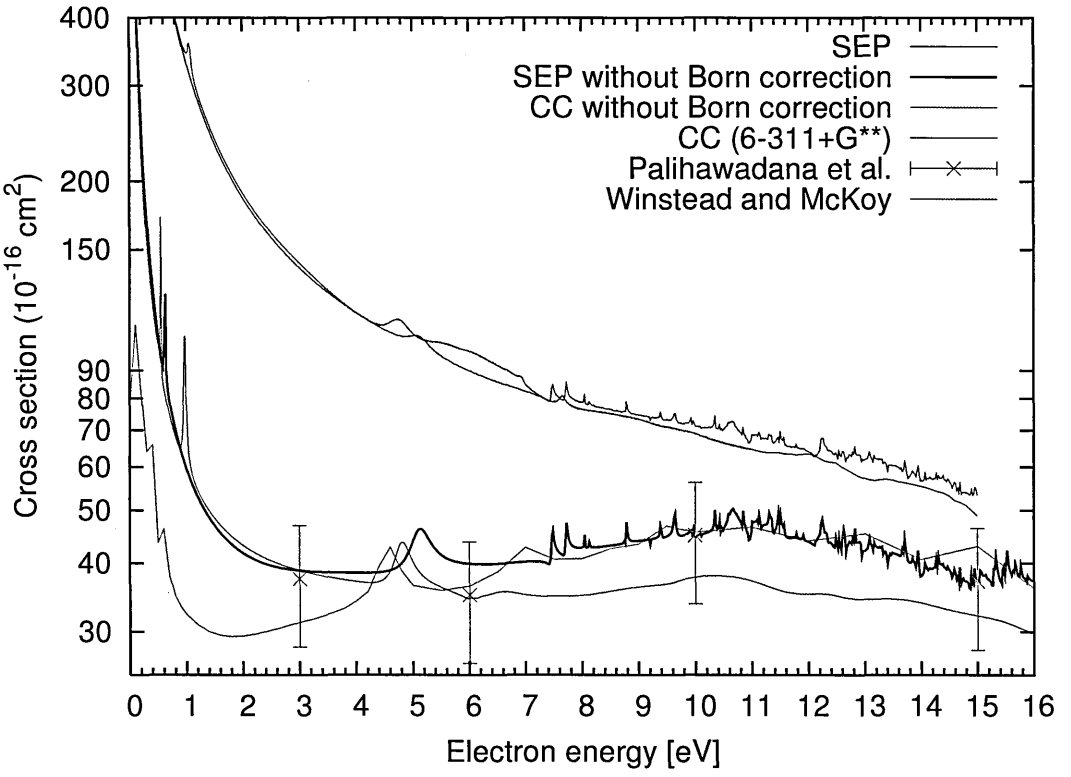

Figure 4.2: Elastic integral cross sections for pyrimidine at the SEP and CC levels with and without a Born-type correction (the cc-pVDZ basis set was used unless otherwise stated), are compared to the experimental results of Palihawadana et al. [34] and to the results of the SMC calculations of Winstead and McKoy (ibid.).

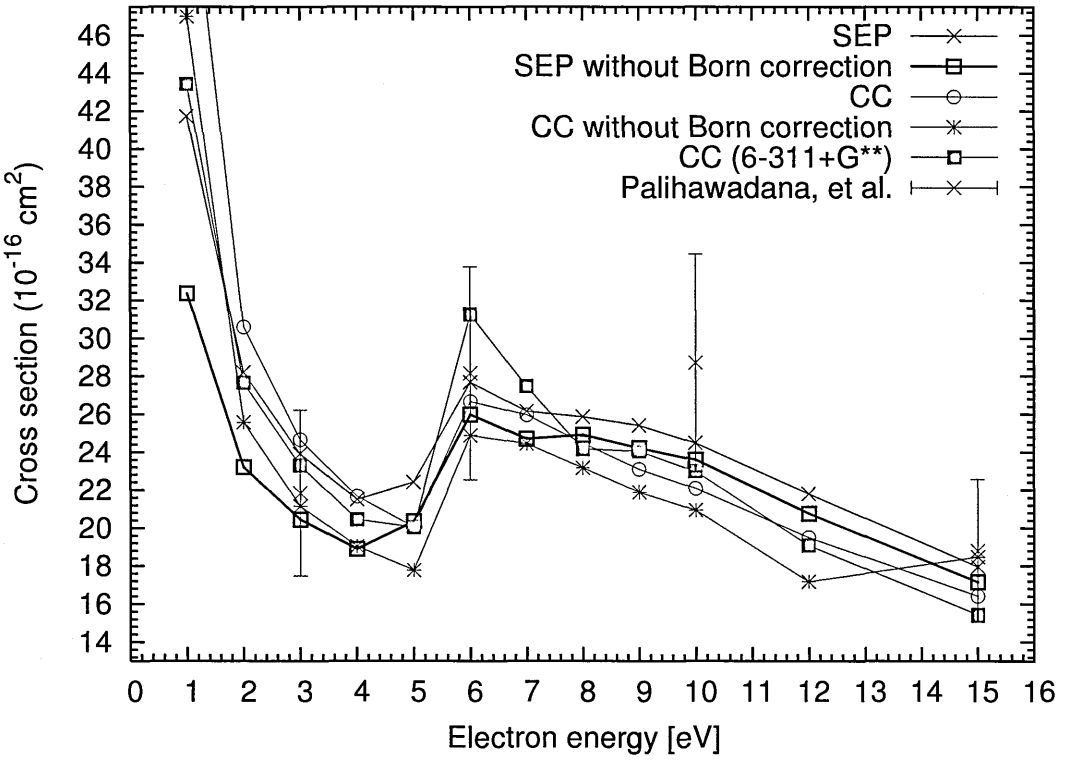

Figure 4.3: Elastic integral cross sections for pyrimidine at the SEP and CC levels with and without a Born-type correction (the cc-pVDZ basis set was used unless otherwise stated), are compared to the experimental results of Palihawadana et al.[34]. The cross sections were obtained by integrating over a restricted angular range (see text for details).

calculation significantly underestimates the DCS below 10-20°, a range for which the extrapolation of experimental results is probably also underestimating the DCS. Nonetheless, a more consistent comparison is given by the partial angular integration described above. If this partial integration is performed for the (uncorrected) R-matrix DCS, the results (shown on Figure 4.3) are in slightly poorer agreement with experiment than the corrected ones.

4.2.2 Experimental technique and the measured scattering data

As mentioned above, the experimental data were obtained by the group of Professor Michael Brunger. *The author of this work did not participate in acquiring or processing of this data.* In this section we provide (for completeness) a simplified description of the principles of the experimental procedure and data processing used to obtain this data. A full description of the experimental technique can be found in [130].

The experimental technique used was based on measurements of the electron energy loss spectra (the difference between the energy of the incoming and scattered electrons). In the implementation of this technique employed in the group of Professor Brunger a beam of monochromatic electrons with energies $15 - 50$ eV was incident on an orthogonal beam of pyrimidine molecules. The intersection of these beams defined a collision volume where the electrons interacted with the pyrimidine molecules. Electrons that collided with the molecules in the beam scattered into the θ-direction (scattering angle) were energy analyzed before being detected with a channel electron multiplier. Energy loss spectra were accumulated at each scattering angle and incident electron energy by recording the number of scattering electrons detected at each energy loss value.

The respective energy loss spectra were next deconvolved into contributions arising from each individual or unresolved combination of electronic states. Examples of the deconvolution at two different scattering conditions are shown in Figure 4.4. Here either 1 or 2 Gaussian functions were employed as fitting functions that approximated the spectral profiles observed over the range of scattering conditions covered in the experiments, for each resolvable inelastic feature and the elastic scattering peak. Note that the respective positions and widths of the Gaussian functions for each inelastic feature were established through consideration of the experimental photo-absorption spectra, previous electron energy loss spectra and calculated electronic excitation energies [105, 114, 115, 131, 132]. The ratio of the area under the fitting function for the i^{th} inelastic scattering feature to that found under the elastic feature determines the intensity ratio $\frac{I_i}{I_0}$ at that incident energy and scattering angle. The absolute

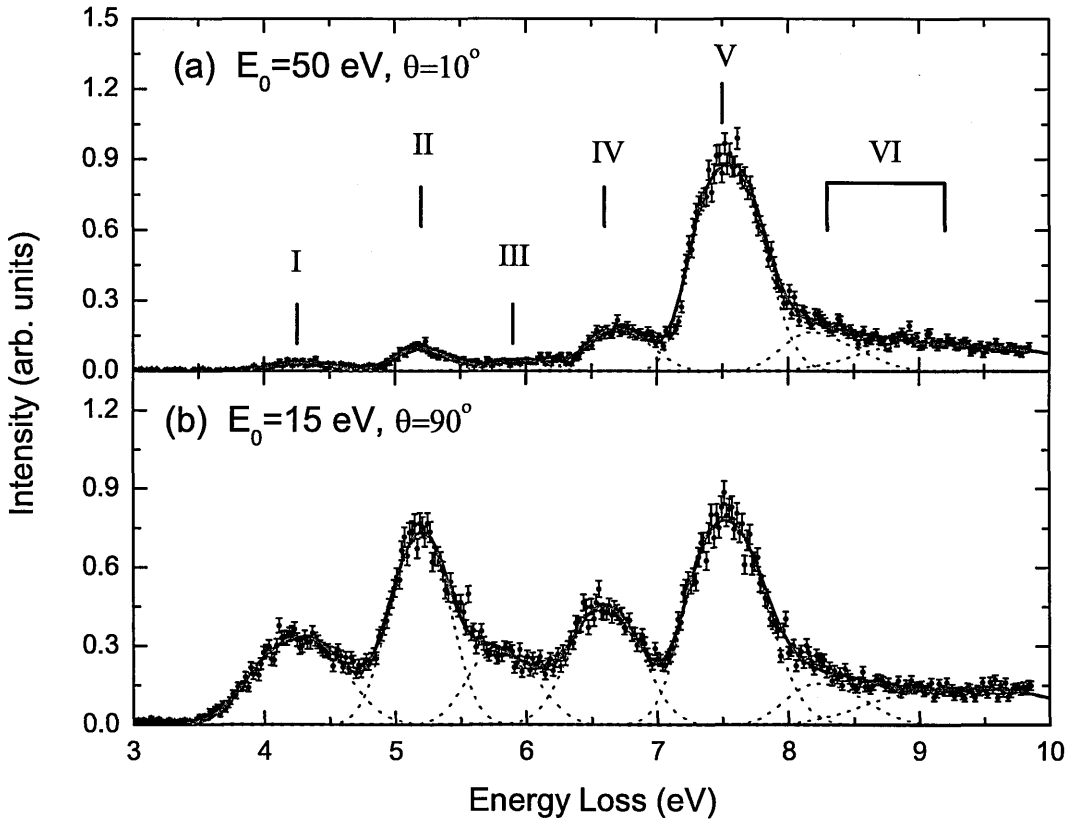

Figure 4.4: Typical electron impact energy loss spectra measured for a) $E_0 = 50$eV and $\theta = 10°$ and b) $E_0 = 15$eV and $\theta = 90°$. For each spectrum the spectral deconvolutions for each feature (dashed lines) and their sum (solid line) are also presented. The spectral assignments for each feature are also given in Table 4.2.

differential cross sections for the inelastic processes contributing to the i^{th} feature, $\frac{d\sigma_{i0}}{d\Omega}(E,\theta)$, can then be determined through:

$$\frac{d\sigma_{i0}}{d\Omega}(E,\theta) = \frac{I_i}{I_0}\eta_{i0}\frac{d\sigma_0}{d\Omega}(E,\theta)\,. \tag{4.1}$$

Here $\frac{d\sigma_0}{d\Omega}(E,\theta)$ are the recently measured DCSs for elastic scattering from pyrimidine [34]. η_{i0} is the relative transmission efficiency of the analyser for inelastically and elastically scattered electrons. The DCS for a scattering process is related to the integral inelastic cross section, $\sigma_{i0}(E)$, for that process through the standard formula [133]:

$$\sigma_{i0}(E) = 2\pi \int_0^{\pi} \frac{d\sigma_{i0}}{d\Omega}(E,\theta)\sin(\theta)\,d\theta. \tag{4.2}$$

In order to convert experimental DCS data, measured at discrete angles that span a finite angular range determined by the physical constraints of the apparatus, to an integral cross section, one must first extrapolate/interpolate the experimental data so that it covers the full angular range (0 to 180°) [134]. Two different methods were used to extrapolate the measured

		E_0 = 15eV		E_0 = 20eV		E_0 = 30eV		E_0 = 50eV	
Label	E_{loss} (eV)	SE	GOS	SE	GOS	SE	GOS	SE	GOS
I	4.3	0.168	0.165	0.09	0.10	0.054	0.057	0.020	0.025
II	5.2	0.24	0.26	0.12	0.13	0.073	0.083	0.031	0.039
III	5.9	0.11	0.106	0.056	0.061	0.042	0.047	0.017	0.019
IV	6.7	0.23	0.24	0.159	0.154	0.136	0.156	0.071	0.084
V	7.5	0.54	0.55	0.57	0.72	0.54	0.67	0.32	0.45
VI	8.3	0.141	0.140	0.165	0.162	0.156	0.161	0.081	0.086
VI	9.2	0.25	0.23	0.27	0.27	0.31	0.31	0.155	0.164
Sum		1.67	1.69	1.43	1.60	1.31	1.49	0.70	0.87

Table 4.3: Measured electron impact excitation ICS (10^{-16} cm^2) for pyrimidine. ICS were calculated using a standard extrapolation (SE) or an extrapolation based on the Generalised Oscillator Strength (GOS) behaviour of dipole-allowed transitions. The uncertainty on the data is of the order of 42-65%.

DCSs to forward and backward angles: a standard extrapolation (SE) and an extrapolation based on the generalized oscillator strength (GOS) behaviour of dipole-allowed transitions. The final integral cross sections obtained using both methods are presented in Table 4.3.

The experiment is unable to determine state-to-state cross sections, i.e. cross section for electron impact excitation of a given electronic state. However, the behaviour of each spectral feature measured in the energy loss spectra with respect to the incident electron energy and scattering angle (see Figure 4.4) provides sensitive information that can assist in assigning the origins of the spectral contributions. This information can be combined with the theoretical calculations described above, sophisticated calculations from the literature and other experimental results [105, 113, 114, 115, 131] to determine the states that contribute to the calculated cross sections at specific energy loss values. The present assignments of our calculated electronic states to the experimental spectral features are shown in Table 4.2 and we discuss them in detail in the next section.

4.2.3 Inelastic cross sections

Figure 4.5 shows the theoretical results for the total electronically inelastic cross section (TICS), that is, the sum of the electron impact electronic excitation cross sections for the 28 excited states included in the CC expansion. We present the cross section determined with both the compact and the diffuse basis sets: the latter is up to 50% bigger above 10 eV. The

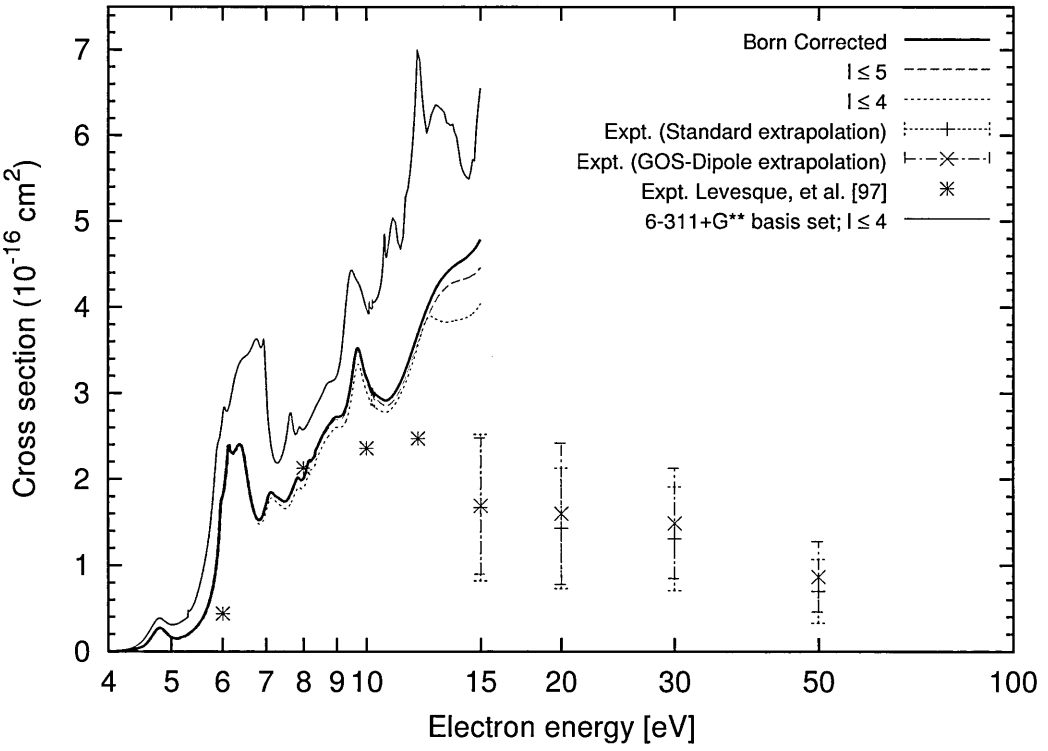

Figure 4.5: Calculated integral inelastic cross sections for pyrimidine presented for various models as indicated in the figure; the cc-pVDZ basis set was used unless otherwise stated. Gas phase experimental results have been determined as described in Section 4.2.2. Also shown are experimental results for collisions from pyrimidine deposited on an argon substrate from Levesque et al. [100].

structure below this energy corresponds mostly to physical resonances for both calculations. The calculated TICS are compared with the gas-phase experimental cross sections, which are listed in Table 4.3. Also included in the figure are the corresponding results from experiments with condensed pyrimidine from Levesque et al. [100].

A Born correction (see Appendix B.2.2) has been added to the TICS calculated with the compact basis set to account for the partial waves not taken into account in the R-matrix calculation (the increase in the TICS calculated with the diffuse basis set would be similar). It is the corrected cross section that should be compared with experiment. We also show, as an indication of convergence, the uncorrected TICS calculated with partial waves up to both $l = 4$ and $l = 5$.

The agreement for the TICS with the experimental data of Levesque et al. is excellent up to 10 eV, even if the experimental results have insufficient data points to detect the resonances visible in the calculated cross section. For the only energy (15 eV) for which the gas phase experimental and theoretical results are available, the calculations overestimate the total electronically inelastic experimental cross section by about a factor of 3 for the compact

basis set and even more for the diffuse one. Given the limitations in both the calculations and experiment, this is probably reasonable agreement. The better agreement with the results of Levesque et al. [100] is possibly due to our calculations being more accurate in this lower energy range.

The panels in Figure 4.6 show the comparison for the inelastic integral cross sections for excitation of states contributing at specific energy loss values. As mentioned above, the experiment (like the one on condensed pyrimidine) is able to determine only cross sections for excitation of groups of states contributing at specific energy loss values. Assignments of the electronic states to these features and the comparisons in Figure 4.6 are now discussed in detail.

For the lower-lying electron energy loss features (at 4.3 eV, 5.2 eV and 5.9 eV, panels (a), (b) and (c) respectively) we find no problems matching our calculated electronic spectrum with the experimental assignments, even though our calculated excitation energies are overestimated. The energy loss feature at 6.7 eV (panel (d) in Figure 4.6) is associated in the experiment to two states ($2\ ^3B_2$ and $2\ ^1A_1$). Our calculations, however, produce two triplet states ($3\ ^3A_1$ and $3\ ^3B_2$) with vertical excitation energies lying between the $2\ ^3B_2$ and $2\ ^1A_1$ states. Therefore, we also assign these two states to this energy loss feature as well as the $2\ ^1B_2$ state; the latter because we include the state $3\ ^1B_2$ in the 7.5 eV energy loss feature (see below).

The most intense energy loss feature in the experimental spectra around 7.5 eV (Figure 4.6(e)) arises from contributions of the $3\ ^1A_1$ and $2\ ^1B_2$ states, which possess a large oscillator strength [114]. We assume that in our calculations these features are associated to those states, among all those included, that have the largest transition moments with the ground state (-1.96 a.u. and 1.94 a.u. respectively): $4\ ^1A_1$ and $3\ ^1B_2$. Our calculations find another $^1B_2$ state lying below the $3\ ^1B_2$, that appears to have a small oscillator strength [114] and probably does not significantly contribute to the experimental spectra; our assignment of the $3\ ^1B_2$ state to this energy loss feature is therefore consistent with the experiment and other calculations. The state of $^1A_1$ symmetry contributing to this energy loss feature was identified by Stener et al. [114] as the second excited state of this symmetry but, as stated above, we select the third excited state ($4\ ^1A_1$) because it has the largest transition moment; this swap of states is probably due to the limitations of our description of the target excited states. Since the second and third $^1A_1$ excited states were found to lie close in energy in the calculations of Stener et al. [114], we choose to assign the $3\ ^1A_1$ state to this energy loss feature as well. In addition, the states $3\ ^1B_1$ and $4\ ^1B_2$ appear in the calculation of

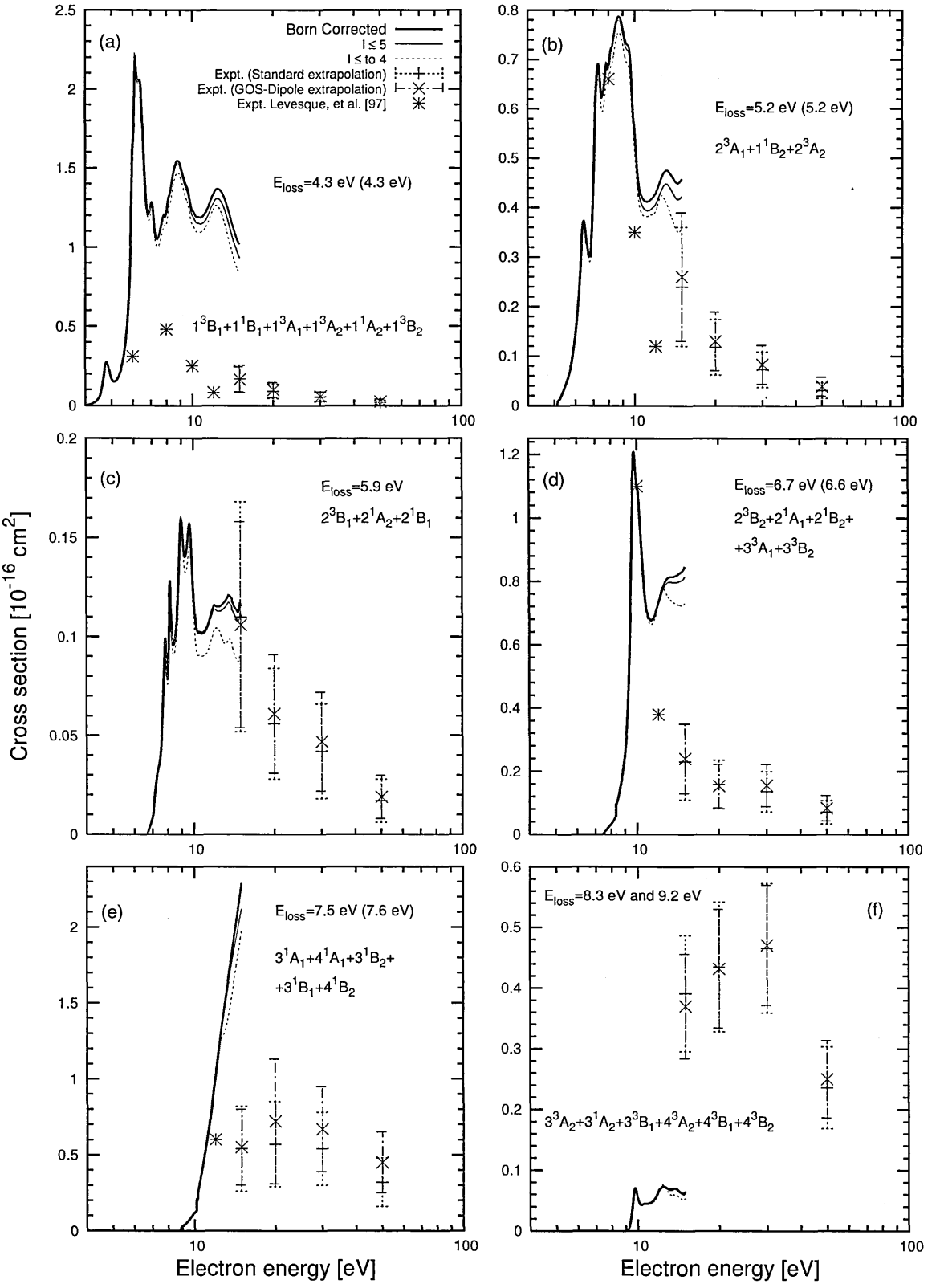

Figure 4.6: Integral inelastic cross sections for pyrimidine for excitation into the states indicated in the panels. The choice of target states 'grouped' together is given by the experiment (see text). The bottom right hand panel shows the calculated cross section for those states included (and energetically open) in our calculation but that are not reported in the literature (Stener et al. [114] study states up to energy 13.15 eV for which the transitions are dipole allowed and, the triplets only up to 5 eV). The values in brackets correspond to the E_{loss} (electron energy loss) in the experiments by Levesque et al. [100].

Stener et al. [114] at 7.42 eV and 7.50 eV, respectively, and we therefore deem them to contribute to the 7.5 eV feature too. In summary, five states contribute to the cross section associated to E_{loss} =7.5 eV, however, the feature is dominated by the contributions from the dipole-allowed transitions to the $4\,^1A_1$ and $3\,^1B_2$ states.

The highest-lying electron energy loss structures at 8.3 eV and 9.2 eV (Figure 4.6(f)) are suggested to arise mainly from contributions of the Rydberg states. We compare these with the sum of the calculated cross sections for all the states we cannot assign to the lower-lying energy loss peaks: these are higher lying states (some of which may possess a partial Rydberg character). It is worth mentioning that Ferreira da Silva et al. [113] reported a $^1A_1$ valence state at 8.800 eV (probably corresponding to the state $7\,^1A_1$ at 8.71 eV in the calculations of Stener et al. [114]). This state might correlate with our $5\,^1A_1$ state, which in our case appears above 10.5 eV, and is not included in our scattering calculations.

Looking at Figure 4.6 we note that the gas and condensed phase experimental results seem to be consistent, with the magnitude of the cross sections being very similar. The calculations produce 'partial sum' cross sections that are always bigger than the experimental ones, as one would expect given that the total inelastic cross section is overestimated by the calculations. The only exception is the cross section interpreted in the experiment as arising from excitation to Rydberg states: where for the other cases, calculations produce results that are as much as 4 times bigger for 15 eV, this cross section is underestimated by a factor of 4. As mentioned above, our calculations do not include the excited state of $^1A_1$ symmetry found in the experiment at 8.8 eV. The calculated [114] oscillator strength of this state is 5.97, suggesting that its contribution to the inelastic cross section might be non-negligible. Omitting this state from the calculations might well be the reason for the calculated cross section being underestimated here.

The biggest 'partial sum' cross section is that for E_{loss} =7.5 eV, for both calculations and measurements; at 15 eV, it contributes 40% to the calculated cross section. It is this and the cross section associated to E_{loss} = 8.3 and 9.2 eV that correspond to excitation of the higher lying states. It is conceivable that a better representation of those states may change the cross section for their excitation and therefore reduce the TICS at higher energies.

It is interesting to note that the agreement with theory both for the TICS and the 'partial sum' cross sections, as measured for condensed pyrimidine [100], is better than that for the gas phase results. In the case of the 'partial sum' cross sections, the states grouped together are somewhat different and so this better agreement may therefore be fortuitous. Since most of the states considered are valence, their thresholds are unlikely to change significantly in

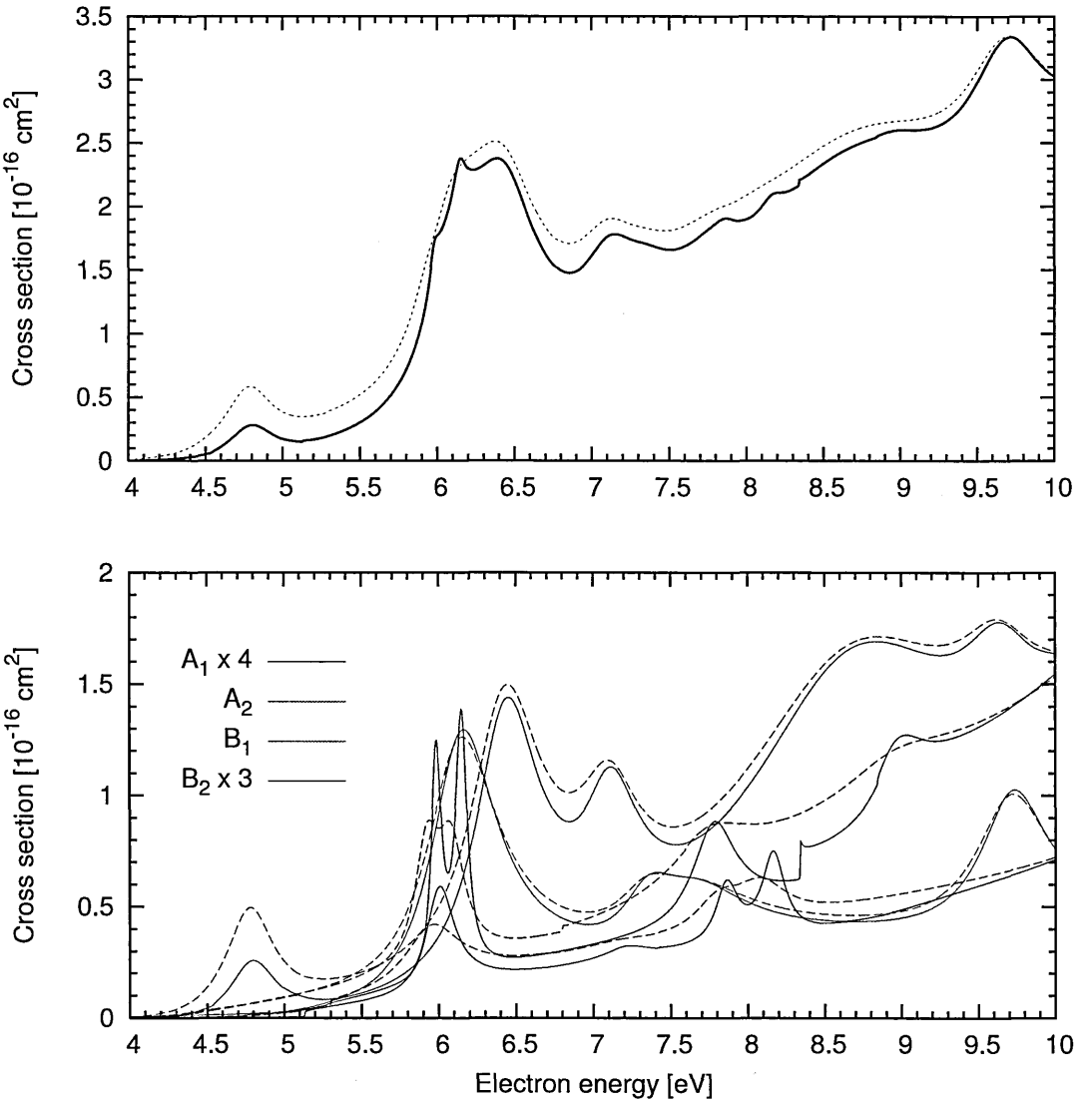

Figure 4.7: Summed integral inelastic cross sections for pyrimidine (upper panel) and the contributions to the TICS from all scattering symmetries (bottom panel). The cross sections calculated using the unshifted thresholds are plotted with full lines, while the ones calculated using the thresholds of Fischer et al. [115] are plotted with dotted lines. The contributions from symmetries A_1 and B_2 are multiplied by 4 and 3 respectively.

going from the gas to condensed phase. Usually, the thresholds are lower in the condensed phase; our calculated excitation thresholds are, in most cases higher than those reported by both experiments and accurate calculations as shown in Table 4.2. We have consequently performed calculations in which we have shifted the excitation thresholds to the values determined by Fischer et al.: we observed only small differences in both the TICS and the 'partial sum' cross sections. This is demonstrated in Figure 4.7, where the TICS (along with the contributions from all scattering symmetries) calculated using the shifted and unshifted thresholds are plotted. The most notable difference between the two TICS is the overall "smoother" shape of the TICS calculated using the shifted thresholds.

4.3 Pyridazine

Pyridazine is the last diazine studied in this work. Unlike pyrimidine, pyridazine is not a ubiquitous precursor of many complex biomolecules. However, studying pyridazine allows us to investigate in greater detail the effects (on electron scattering from diazines) associated with the magnitude of the dipole moment of the target molecule. Pyridazine has dipole moment almost twice as large as that of pyrimidine (see Table 3.2) and close to that of uracil ($\approx$ 4.4 D). Thus we can see that we have, in this work, progressed from investigating a molecule with zero dipole moment (pyrazine) to molecules with increasingly larger dipole moments. However, it is important to mention that studying the effect of the dipole moment on electron scattering cannot be easily separated from the effect of isomerisation: the large dipole moment of pyridazine is caused by the two nitrogen atoms being next to each other unlike the other two diazines.

In setting up our scattering models for pyridazine we follow the choices made for pyrazine and the experience gained for pyrimidine. Therefore we restrict ourselves to only a brief description of the calculations and results on pyridazine and postpone a detailed comparison of the results with the other diazines until Section 4.8.

4.3.1 Target description

The optimized geometry of pyridazine was taken from [121]. The ground state configuration of the molecule is: $1a_1^2\ 1b_2^2\ 2b_2^2\ 2a_1^2\ 3a_1^2\ 3b_2^2\ 4a_1^2\ 4b_2^2\ 5a_1^2\ 5b_2^2\ 6a_1^2\ 7a_1^2\ 8a_1^2\ 6b_2^2\ 7b_2^2\ 9a_1^2\ 1b_1^2\ 10a_1^2\ 8b_2^2\ 2b_1^2\ 1a_2^2$. (Note that since there is no trivial correlation between the orbitals belonging to a specific irreducible representation in pyrimidine and pyridazine the configurations of the ground states of both are not identical or trivially correlated.) The active space for the SA-CASSCF calculations was chosen to contain orbitals $10a_1$,$1-3b_1$,$8b_2$,$1-3a_2$. The averaging scheme was identical to the one used for pyrimidine (see Section 4.1.1), i.e. 17 states were included in the averaging. As apparent from Table 4.4 the values of the dipole moment are again in good agreement with the experiment. In this case the calculations using the diffuse basis set overestimate the experimental value by less than 10%. The electronic spectrum of pyridazine has received less attention compared with the other two diazines, but as expected the VUV and near threshold EEL spectra [106] reveal the presence of a high number of Rydberg states. We set the threshold for inclusion of the electronically excited states to 10.62 eV. Following the approach we used for pyrimidine (see Section 4.2.3), we assign the states of $^1A_1$ and $^1B_2$ symmetries responsible for the most intense feature in the

Basis set	cc-pVDZ	6-311+G**	Acc. value
HF [H]	−262.667	−262.706	−263.365
SA-CASSCF [H]	−262.749	−262.787	
μ_{HF} [D]	4.32	4.62	4.22
$\mu_{SA-CASSCF}$ [D]	4.18	4.42	

Table 4.4: Energy, in Hartree, and dipole moment, in Debye, of pyridazine in its ground electronic state calculated at the HF-SCF and SA-CASSCF levels, using the basis sets cc-pVDZ and 6-311+G**. Also shown is the experimental value [108] of the ground state dipole moment and accurate value [106] of the ground state energy calculated using the multi-reference CI method and the TZVP basis set.

VUV spectra [106] to the states in our calculations possessing the largest transition moments with the ground state: the 5 $^1A_1$ and 3 $^1B_2$ states whose transition moments are 2.04 a.u. and −1.99 a.u. respectively.

The calculated ground state energies of pyridazine, shown in Table 4.4, are not in very good agreement with the accurate values. The agreement of our calculated VE energies, shown in Table 4.5, with experiment is better for the states with observed VE energies up to 5 eV, but deteriorates significantly for the higher-lying states, where the differences reach several electron-volts. The calculations performed with the diffuse basis set lead to VE energies which are mostly slightly lower but do not differ significantly (by up to $\sim$ 0.1 eV) from the ones obtained using the compact basis set. Again, the relatively poor agreement of the calculated VE energies with the accurate values is not surprising due to the limited size of the active space used in our calculations (see Section 4.5).

4.3.2 Scattering calculations

The scattering calculations were performed with both basis sets and at all levels of approximation (SE, SEP and CC). The HF orbitals were used for the SE and SEP calculations, while the SA-CASSCF orbitals were used for the CC calculations. For the SEP calculations we used 25/40 virtual orbitals for the calculations using the compact/diffuse basis set. The CC calculations used 30/70 virtual orbitals for the calculations using the compact/diffuse basis set. The choice of the deletion thresholds for the calculations using the diffuse basis set was a conservative one: in most cases the deletion thresholds were set to larger values (up to $\approx 10^{-6}$). This choice was similar, but not identical, to the choice made for pyrimidine. The calculations using the compact basis set used the standard value 10^{-7} for all symmetries. The R-matrix radii were set to the same values as before, i.e. 13/18 a.u. for the calculations using the compact/diffuse basis sets.

Integral cross sections calculated using the SEP and CC models are shown on Figure 4.8.

No	cc-pVDZ	6-311+G**	[106]	Symmetry
1	3.71	3.71	2.78 [109]	$1\,^3B_1$
2	3.78	3.75	-	$1\,^3B_2$
3	4.47	4.47	3.3 [109]	$1\,^1B_1$
4	4.63	4.63	-	$1\,^3A_2$
5	4.90	4.86	-	$1\,^3A_1$
6	4.95	4.91	5.0	$2\,^1A_1$
7	5.04	5.04	-	$1\,^1A_2$
8	5.11	5.07	-	$2\,^3B_2$
9	6.15	6.14	-	$2\,^3A_2$
10	6.20	6.18	5.3	$2\,^1A_2$
11	6.94	6.93	-	$2\,^3B_1$
12	7.14	7.09	-	$3\,^3B_2$
13	7.14	7.13	5.5-6.0	$2\,^1B_1$
14	7.28	7.23	-	$2\,^3A_1$
15	7.94	7.88	6.5	$1\,^1B_2$
16	8.05	8.00	-	$3\,^3A_1$
17	8.24	8.23	-	$3\,^3B_1$
18	8.44	8.38	-	$3\,^1A_1$
19	8.51	8.50	7.10	$3\,^1B_1$
20	8.85	8.81	-	$3\,^3A_2$
21	8.89	8.84	-	$2\,^1B_2$
22	9.03	9.01	-	$4\,^1A_1$
23	9.16	9.14	-	$4\,^3B_2$
24	9.37	9.34	-	$4\,^3B_1$
25	9.68	9.65	-	$4\,^3A_2$
26	9.79	9.75	-	$3\,^1A_2$
27	9.87	9.81	7.3	$3\,^1B_2$
28	10.14	10.09	-	$5\,^3B_1$
29	10.28	10.19	7.3	$5\,^1A_1$
30	10.31	10.29	-	$5\,^3B_2$
31	10.44	10.40	-	$4\,^1B_1$
32	10.62	10.59	-	$5\,^3A_2$

Table 4.5: Vertical excitation energies, in eV, for the electronic excited states of pyridazine calculated in this work. The first two columns present results of our SA-CASSCF calculations using the active space $(10, 8)$ and the basis sets cc-pVDZ and 6-311+G**. The experimental values of the vertical excitation energies given in the fourth column correspond to those of Palmer and Walker [106] unless a different reference is given.

To the best of our knowledge there are no data to compare our results with. In Section 4.7 we present the DCS for pyridazine and a detailed comparison of the cross sections for all diazines. Here we just note that the total cross sections presented in Figure 4.8 are very similar up to the energy of ≈ 5 eV, where the cross sections using the diffuse basis set (especially the CC ones) develop an irregular structure which is due to a poor representation of the continuum for these larger electron energies.

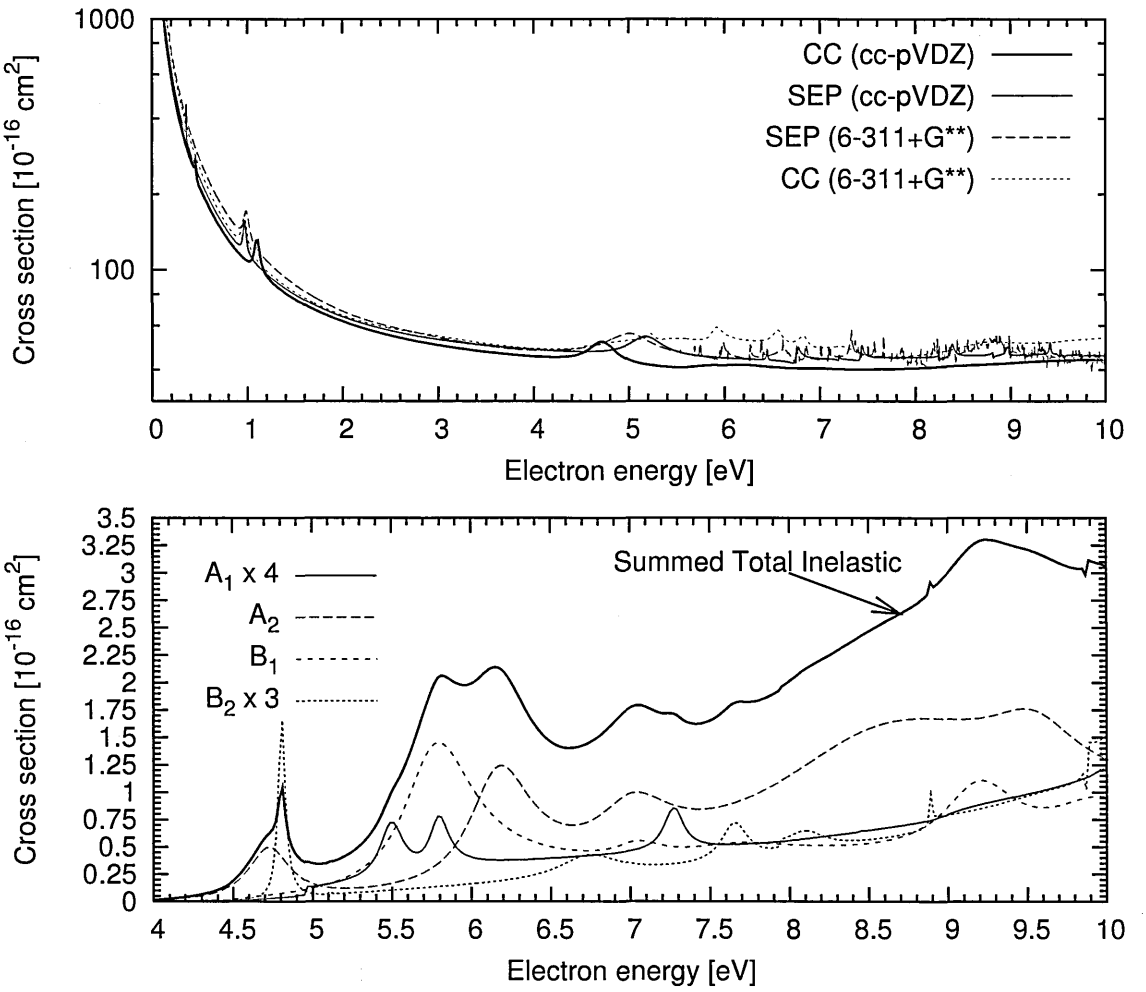

Figure 4.8: Summed total cross sections for pyridazine calculated at the SEP and CC levels using both basis sets (upper panel) and the integral inelastic cross sections and the contributions from all scattering symmetries (bottom panel). The inelastic cross sections were calculated using the CC model and the compact basis set.

4.4 Summary of the results for pyrimidine and pyridazine

We have performed calculations of elastic and inelastic electron scattering from gaseous pyrimidine and compared the resulting cross sections with experimental data. For the only overlapping energy (15 eV), agreement between measured and calculated inelastic cross sections is quite fair, particularly when one allows for the very difficult nature of the calculations and measurements. This comparison has been performed both for the total (summed) inelastic cross section and for 'partial sum' cross sections for excitation into groups of states. For electron energies in the range $6 - 12$ eV we compared our calculated inelastic cross sections with the experimental data on condensed pyrimidine and obtained a good agreement, especially for the total inelastic cross section. The present calculations for various models (basis sets and levels of approximation) also provide integral and differential elastic cross sections in very good agreement with prior experimental results.

	Pyrazine			Pyrimidine			Pyridazine		
Basis set	cc-pVDZ	6-311+G**	Acc. value	cc-pVDZ	6-311+G**	Acc. value	cc-pVDZ	6-311+G**	Acc. value
HF [H]	−262.697	−262.736	−263.394	−262.712	−262.752	−263.402	−262.667	−262.706	−263.365
SA-CASSCF [H]	−262.775	−262.812		−262.787	−262.826		−262.749	−262.787	
μ_{HF} [D]	-	-	-	2.31	2.53	2.334	4.32	4.62	4.22
$\mu_{SA-CASSCF}$ [D]	-	-	-	2.36	2.53		4.18	4.42	
g.s. configuration	$a_g^{12}b_{3u}^2b_{2u}^8b_{1g}^2b_{1u}^{10}b_{2g}^2b_{3g}^6$			$a_1^{22}b_1^4b_2^{14}a_2^2$			$a_1^{20}b_1^4b_2^{16}a_2^2$		
CAS orbitals	$6a_g$,$1-2b_{3u}$,$1b_{1g}$,$5b_{1u}$,$1-2b_{2g}$,$1a_u$			$11a_1$,$1-4b_1$,$7b_2$,$1-2a_2$			$10a_1$,$1-3b_1$,$8b_2$,$1-3a_2$		

Table 4.6: Properties of the ground state of the diazine molecules calculated at the HF-SCF and SA-CASSCF levels, using the basis sets cc-pVDZ and 6-311+G**. The ground state configuration of each molecule and the orbitals forming the active space in the CASSCF calculations (for simplicity, the orbitals are not listed in energy order) are also tabulated. Also shown are the experimental values [107, 108] of the ground state dipole moments of pyrimidine and pyridazine and accurate values [104, 105, 106] of the ground state energies of the three molecules.

Using the experience gained for pyrimidine we applied the SEP and CC scattering models to pyridazine. Summed integral total and inelastic cross sections calculated using the compact and the diffuse basis set were presented. In the following sections we provide a detailed comparison of the calculated target properties, cross sections and resonances found in all diazines.

4.5 Comparison of target data for all diazines

Details of the target models and calculations have been presented in previous chapters, in particular Section 3.3. Table 4.6 summarizes the calculated properties of the diazine molecules and the active spaces used for the CASSCF calculations.

The calculated ground state energies for all three targets, shown in Table 4.6, are not in very good agreement with the accurate values. The ground state energies of the three molecules calculated using the same basis set are very similar. This is also true for the accurate values of the ground state energies. We note that Palmer et al. [104, 105, 106] also used the CASSCF method and the active space $(10, 10)$, to calculate the ground state energies of diazines and obtained values close to ≈ -262.68 H for pyrazine and pyrimidine and ≈ -262.64 H for pyridazine, which are all slightly larger than any of our (even the HF) values. This fact can be probably attributed to a different choice of atomic basis set (double zeta + Rydberg) in their calculations. This basis set, as opposed to ours, does not include polarization functions, possibly the reason why all our energies are lower than those of Palmer et al. On the other hand, the inclusion of the Rydberg basis functions makes the basis used by Palmer et al. appropriate for the description of Rydberg excited states. Our cc-pVDZ basis set does not include any diffuse functions and is therefore not appropriate for

this task. The 6-311+G** basis set includes diffuse functions on the heavy atoms. Whether the inclusion of diffuse functions on the hydrogen atoms is necessary for a good description of the Rydberg states remains to be seen.

In Table 4.7 we compare the calculated vertical excitation energies of the three diazines. We present only the results calculated using the compact basis set, because, for the reasons explained below, this basis set was chosen to obtain the scattering data which will be discussed in the next sections. The assignment of the experimentally observed states to the calculated ones was described in detail earlier. The electronic states of pyrazine have been given the corresponding C_{2v} labels. However, these labels can not be used for a straightforward correlation of the excited states in the three molecules. As mentioned before (see Section 4.3.1), there is no straightforward correlation between orbitals belonging to a specific irreducible representation in the three diazines nor can electronic excited states be correlated based only on their symmetry labels and energy order.

The agreement of our calculated VE energies with experiment is better for the states with observed VE energies up to 5 eV, but deteriorates significantly for the higher-lying states, where the differences reach several electron-volts. The calculations performed with the diffuse basis set (shown in the previous sections) lead to VE energies which are mostly slightly lower but do not differ significantly (by up to ~ 0.2 eV) from the ones obtained using the compact basis set. Clearly, the use of the diffuse basis set is not enough to improve the Rydberg states (see below).

In general our calculated VE energies are not in a very good agreement with the accurate values. This is not surprising given our relatively "simple" description of the target electronic states: studies focusing solely on the accurate description of electronic states routinely include perturbational corrections and a larger CAS in the calculations [121]. It is the absence of these corrections together with the small active space and a small atomic basis set which are responsible for these discrepancies. We did not apply any perturbational corrections to the wavefunctions of the target states, because the equivalent perturbational corrections would have to be applied *consistently* to the $N+1$ R-matrix basis functions (2.87) which is not a straightforward procedure.

As described in the previous chapters, we decided to include in the CC calculations all electronically excited states with vertical excitation energies up to about 10.6 eV. It is apparent that, as we move from pyrazine to pyrimidine and pyridazine, the number of electronic states included in our calculations increases. However, the calculations of Stener et al. [114], geared specifically towards providing an accurate description of the excited states, report a

No	Pyrazine (D_{2h})					Pyrimidine (C_{2v})					Pyridazine (C_{2v})		
	VE energy [eV]			Sym.	Sym.	VE energy [eV]				Sym.	VE energy [eV]		Sym.
	Calc.	[120]	[114]	(D_{2h})	(C_{2v})	Calc.	[115]	[113]	[114]		Calc.	[106]	
1	3.90_V	4.0	4.43	$1\,^3B_{1u}$	$1\,^3A_1$	4.00_V	4.0	–	4.45	$1\,^3A_1$	3.71_V	2.78 [109]	$1\,^3B_1$
2	4.18_V	3.42	2.61	$1\,^3B_{3u}$	$1\,^3B_1$	4.54_V	3.8	–	3.05	$1\,^3B_1$	3.78_V	–	$1\,^3B_2$
3	4.84_V	3.97	3.16	$1\,^1B_{3u}$	$1\,^1B_1$	4.99_V	4.3	4.183	3.44	$1\,^1B_1$	4.47_V	3.3 [109]	$1\,^1B_1$
4	4.89_V	4.5	4.07	$1\,^3B_{2u}$	$1\,^3B_2$	5.12_V	4.8	–	4.50	$1\,^3B_2$	4.63	–	$1\,^3A_2$
5	4.95_V	4.81	5.23	$1\,^1B_{2u}$	$1\,^1B_2$	5.13_V	5.3	5.22(5)	5.44	$1\,^1B_2$	4.90_V	–	$1\,^3A_1$
6	5.15_V	5.7	–	$2\,^3B_{1u}$	$2\,^3A_1$	5.24_V	4.4	–	3.46	$1\,^3A_2$	4.95_V	5.0	$2\,^1A_1$
7	5.34_V	4.59	4.15	$1\,^3B_{2g}$	$2\,^3B_1$	5.27_V	5.1	–	–	$2\,^3A_1$	5.04_V	–	$1\,^1A_2$
8	5.91_V	5.19	4.80	$1\,^1B_{2g}$	$2\,^1B_1$	5.63_V	4.8	–	3.67	$1\,^1A_2$	5.11_V	–	$2\,^3B_2$
9	5.93_V	4.2	3.54	$1\,^3A_u$	$1\,^3A_2$	6.45_V	5.4	–	4.20	$2\,^3A_2$	6.15	–	$2\,^3A_2$
10	5.98_V	4.72 [123]	3.64	$1\,^1A_u$	$1\,^1A_2$	6.71_V	5.9	–	4.65	$2\,^1A_2$	6.20_V	5.3	$2\,^1A_2$
11	7.13	–	–	$1\,^3B_{1g}$	$2\,^3A_2$	7.07_V	5.7	–	4.60	$2\,^3B_1$	6.94	–	$2\,^3B_1$
12	7.27_V	6.10	–	$1\,^1B_{1g}$	$2\,^1A_2$	7.23_V	6.1	~ 6.0	4.89	$2\,^1B_1$	7.14	–	$3\,^3B_2$
13	7.34	–	–	$1\,^3A_g$	$3\,^3A_1$	7.42	–	–	–	$2\,^3B_2$	7.14_V	5.5 – 6.0	$2\,^1B_1$
14	7.46	–	–	$1\,^3B_{3g}$	$2\,^3B_2$	7.54	–	–	–	$3\,^3A_1$	7.28	–	$2\,^3A_1$
15	8.20	–	–	$2\,^3B_{2u}$	$3\,^3B_2$	8.07	–	–	–	$3\,^3B_2$	7.94_V	6.5	$1\,^1B_2$
16	8.34	–	–	$2\,^1A_g$	$2\,^1A_1$	8.34_V	6.8	6.69(1)	6.35	$2\,^1A_1$	8.05	–	$3\,^3A_1$
17	8.35	–	–	$1\,^1B_{3g}$	$2\,^1B_2$	8.53_R	–	–	6.55	$2\,^1B_2$	8.24	–	$3\,^3B_1$
18	8.46	–	–	$3\,^1A_g$	$3\,^1A_1$	8.84_R	–	–	7.40	$3\,^1A_1$	8.44	–	$3\,^1A_1$
19	8.66	–	–	$3\,^3B_{1u}$	$4\,^3A_1$	9.04	–	–	–	$3\,^3A_2$	8.51_R	7.10[109]	$3\,^1B_1$
20	8.67_V	6.51	6.43	$1\,^1B_{1u}$	$4\,^1A_1$	9.20	–	–	–	$3\,^1A_2$	8.85	–	$3\,^3A_2$
21	8.82	–	–	$2\,^3B_{2g}$	$3\,^3B_1$	9.37	–	–	–	$3\,^3B_1$	8.89_R	–	$2\,^1B_2$
22	9.03	–	–	$2\,^1B_{2g}$	$3\,^1B_1$	10.18_V	7.6	7.478	7.19	$4\,^1A_1$	9.03_R	–	$4\,^1A_1$
23	9.05	–	–	$3\,^3B_{2g}$	$4\,^3B_1$	10.26	–	–	–	$4\,^3A_2$	9.16	–	$4\,^3B_2$
24	9.84	–	–	$2\,^3B_{3u}$	$5\,^3B_1$	10.26	–	–	–	$4\,^3B_1$	9.37	–	$4\,^3B_1$
25	10.01	–	–	$3\,^3B_{3u}$	$6\,^3B_1$	10.29_V	7.6	7.478	7.42	$3\,^1B_2$	9.68	–	$4\,^3A_2$
26	10.03_V	7.67	7.67	$2\,^1B_{2u}$	$3\,^1B_2$	10.31	–	–	–	$4\,^3B_2$	9.79	–	$3\,^1A_2$
27	$10.60_{V/R}$	7.67	7.43	$2\,^1B_{1u}$	$5\,^1A_1$	10.46_R	–	–	7.42	$3\,^1B_1$	9.87_V	7.3	$3\,^1B_2$
28						10.51_R	–	–	7.50	$4\,^1B_2$	10.14	–	$5\,^3B_1$
29											10.28_V	7.3	$5\,^1A_1$
30											10.31	–	$5\,^3B_2$
31											10.44	–	$4\,^1B_1$
32											10.62	–	$5\,^3A_2$

Table 4.7: Electronic excited states included in the Close-Coupling calculations together with their vertical excitation (VE) energies. The values labelled 'Calc.' correspond to our SA-CASSCF calculations using the cc-pVDZ basis set. In order to aid the comparison of the electronic states present in all three molecules, the states of pyrazine are also given the corresponding C_{2v} labels. For pyrimidine we list the experimental results of Fischer et al. [115], da Silva et al. [113] and also the values from the work of Stener et al. [114], which were determined from TDDFT calculations. For pyrazine we list the experimental results quoted by Weber and Reimers [120] and the results of calculations by Stener et al. [114] and for pyridazine we list the experimental results of Palmer and Walker [106] and Innes et al. [109]. The character of the states (valence - V, Rydberg - R or mixed valence-Rydberg - V/R) is given, if known, as a subscript to the calculated VE energy; it is taken from Stener et al. [114], Weber and Reimers [120] and Palmer et al. [105] for pyrazine and pyrimidine and from Palmer and Walker [106], Innes et al. [109] for pyridazine.

much higher number still of singlet electronic states of pyrimidine and pyrazine than ours. This is mainly because we made no attempt to represent the plethora of Rydberg states accurately.

Inclusion of all the relevant higher-lying (Rydberg) orbitals [114] in the active space would increase the computational demand of the Close-Coupling scattering calculations beyond our current capabilities. Apart from inclusion of these orbitals in the active space, it would be necessary to use a diffuse atomic basis set (e.g. the 6-311+G**) to obtain a good description of these states. As we discussed previously (see Section 3.4.1), the use of a diffuse basis set causes some specific problems in our scattering calculations. Although in principle more appropriate, we have found that the use of the basis set 6-311+G** does not lead to significantly different conclusions regarding the formation of resonances in diazines.

Our calculated electronic spectra is also missing some of the higher-lying valence states [114], again because their main configurations involve orbitals not included in our active space. Conversely, there are states appearing in our calculations for all three molecules which have not been observed experimentally (see Table 4.7); since we tend to overestimate the VE energy, we believe these states are likely to be present in the electronic spectrum below the ionization threshold. In summary, the states included in our calculations correspond predominantly to valence states with perhaps only a few poorly described Rydberg states. We can see from Table 4.7 that the valence states included in our calculations have experimentally determined VE energies below 8 eV. It is worth noting, that for pyrazine and pyrimidine we compared the main configurations of the electronic states from Table 4.7, as calculated by our SA-CASSCF model using the compact basis set, with the configurations of the states reported by Stener et al. [114]. The valence electronic states of Stener et al. with VE energies up to 7.42 eV have main configurations which are in agreement with our assignments for the same states. From the reasons explained above, the Rydberg states are poorly represented by our models and therefore their configurations do not agree with those of Stener et al.

4.6 Scattering calculations for all diazines

The parameters of our scattering calculations were discussed in detail in the previous chapters. Briefly, the HF target orbitals were used in the SE and SEP calculations, while the SA-CASSCF orbitals were used in the CC calculations. The SE and SEP calculations include only the HF ground state of the molecule in expansion (2.63). In the case of the CC calculations, all states listed in Table 4.7 were included in (2.63). The specific choice of the L^2 configurations

	Pyrazine			Pyrimidine			Pyridazine		
Scattering model	SE	SEP	CC	SE	SEP	CC	SE	SEP	CC
cc-pVDZ (compact)	25	25	40	25	25	40	25	25	30
6-311+G** (diffuse)	25	40	70	25	40	70	25	40	70

Table 4.8: Number of virtual orbitals used for all three models employed in scattering calculations on the diazine molecules.

for all these models was described in detail in Section 2.6 and will not be repeated here.

The scattering calculations using the compact basis set were performed with the R-matrix radius 13 a.u., while the calculations employing the diffuse basis set used $a = 18$ a.u. The precise choice of the corresponding continuum basis sets as well as the deletion thresholds was described in Sections 3.4, 4.2 and 4.3.2.

In Table 4.8 we list the number of virtual orbitals used in the scattering calculations for all three (SE, SEP and CC) models and both target basis sets (cc-pVDZ, 6-311+G**). The number of virtual orbitals used in the SEP and CC models was chosen so that the calculated positions of the two lowest-lying π^* resonances fall roughly in the experimentally determined ranges of Nenner and Schulz [32]. As expected, the values presented in Table 4.8 are very similar for the three targets. The most notable difference is the lower number of virtual orbitals (as compared with the other two diazines) used in the CC calculations on pyridazine with the compact basis set. We ascribe this to the large dipole moment of pyridazine, which seems to affect the way correlation needs to be represented in our calculations. Uracil has a dipole moment of similar magnitude and indeed, the CC calculations of Dora et al. [59] on uracil also found 30 to be the optimal number of virtual orbitals.

We perform the CC calculations using the Simplified model for all diazines, in which we do not include among the L^2 configurations those in which the scattering electron occupies virtual orbitals. This model produces resonance positions that are too high, but its simplicity (i.e. a small number of configurations generated) allows us to investigate and understand some important aspects of resonance formation. In the latter we will denote as *full* a CC scattering model other than the Simplified one. The significance of the Simplified model for characterization of resonances and a comparison with the results of the full model were discussed for pyrazine in Section 3.6.

All calculations were performed using both basis sets, but this did not lead to different conclusions regarding the formation and properties of the resonances. However, we find a few more higher-lying resonance-like structures (see Section 3.6.4) when using the diffuse basis set although it is not clear these are physical (the CC calculations using the diffuse basis set

may suffer from linear dependence problems that can lead to the appearance of unphysical structures). Therefore, in the following, unless otherwise stated, we discuss only the results of the calculations performed using the compact basis set. In Section 3.5 we showed that the shape of the pyrazine elastic cross sections calculated using the diffuse and the compact basis set differ significantly below ≈ 3 eV. However, for the dipolar diazines, the differences between the elastic cross sections calculated in these two basis sets are completely masked by the strong dipolar behaviour of the cross section.

4.7 Cross sections: comparison for all diazines

Figure 4.9 shows the Born-corrected differential (DCS) (left panel) and integral (right hand panel) elastic cross sections for the three diazines. The uncorrected integral cross sections are shown as well. Figure 4.10 shows the total inelastic (TICS) cross sections calculated with the Born correction. All these cross sections were determined using the CC scattering model and the compact target basis set. Cross sections calculated at the SEP level were presented in the previous sections and chapters and we will not discuss them here. The DCS were calculated from the K-matrices using the POLYDCS program [92], which includes a Born correction for the dipolar molecules pyrimidine and pyridazine. The Born correction for the inelastic cross sections was calculated (utilizing the values of the dipole transition moments) using the method described in Appendix B.

The DCS follow the expected behaviour: that for pyridazine, which possesses the largest dipole moment, is larger than the ones for pyrimidine and pyrazine (that does not have a ground state dipole moment). The magnitude of the cross sections for pyrazine and pyrimidine become approximately equal at energies around 6 eV, except below $\sim 20° - 30°$, where their behaviour is, as expected, different. At 10 eV the DCS for pyridazine is still larger than the other two, but the shapes of the cross sections for pyrazine and pyrimidine remain very similar. The oscillatory behaviour of the pyridazine cross sections is an artifact of the Born closure approximation (see Section B.2.1) used to calculate contributions of the partial waves with large angular momentum.

The integral elastic cross sections (right hand panel of Figure 4.9) for pyrimidine and pyridazine show again the typical diverging dipolar behaviour at low energies. Clearly visible in the ab-initio (Born-uncorrected) cross sections are the three low-lying π^* resonances. Another higher-lying (above ≈ 5.5 eV) resonance can be seen in the cross sections for all diazines and we will discuss it later, in Section 4.8.4.

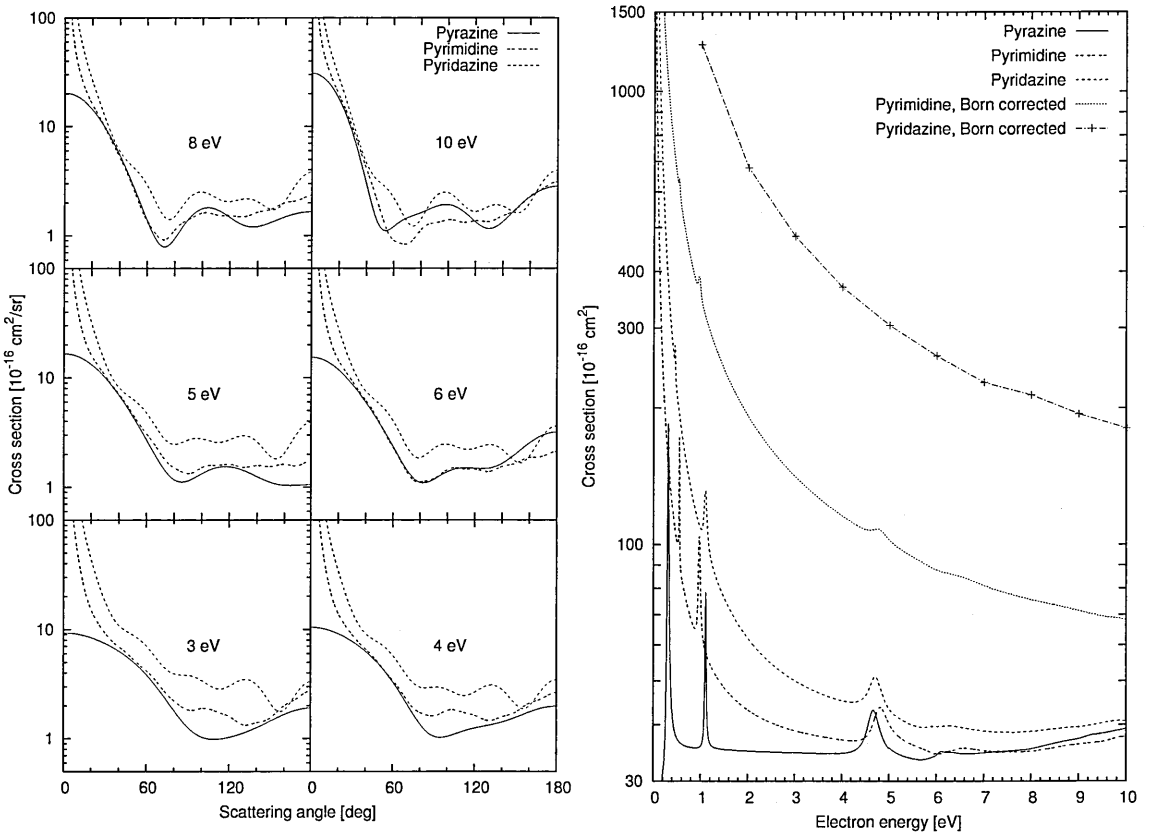

Figure 4.9: Left panel: Elastic differential cross sections for pyrazine, pyrimidine and pyridazine calculated at the CC level using the compact basis set, for the energies indicated in the panel. The cross sections for pyrimidine and pyridazine include the Born correction. Right hand panel: Integral elastic cross sections for diazines calculated at the CC level using the compact basis set. The Born corrected results for the dipolar molecules are plotted as well. Note the logarithmic scale for the y-axis.

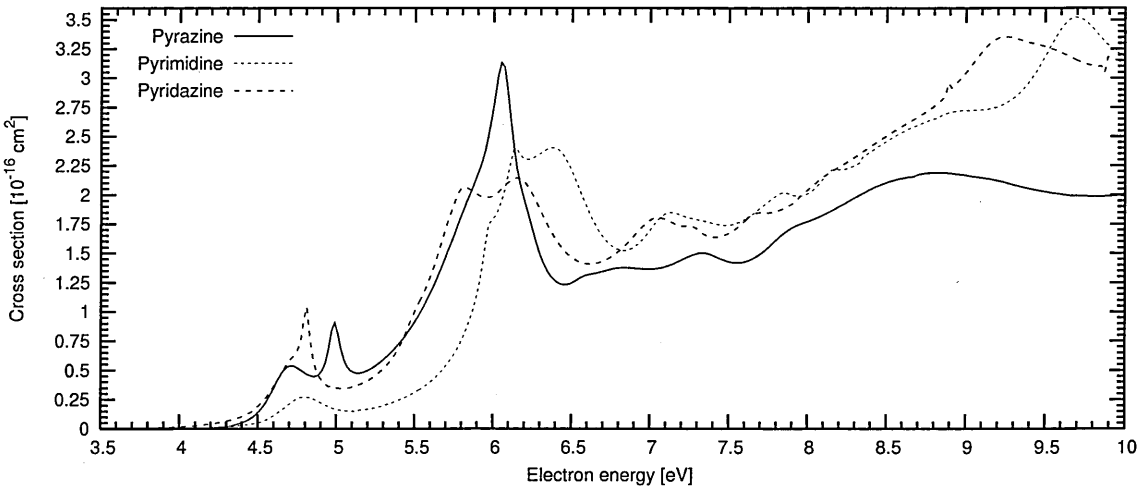

Figure 4.10: Left panel: Total inelastic cross sections for pyrazine, pyrimidine and pyridazine calculated at the CC level using the compact basis set. A Born correction [93] based on dipole transition moments has been added to the cross sections for the dipolar diazines.

The elastic cross section for a dipolar molecule scales approximately as $|\mu|^2$, where μ is the dipole moment of the molecule (see Appendix B). Consequently, the magnitude of the Born corrected integral cross section for pyridazine should be larger by a factor of about 3.15 than the corresponding cross section for pyrimidine. Computing the ratio of the two cross sections shows that in the energy range $0 - 10$ eV the pyridazine cross section is larger by approximately $2.6 - 3.6$, depending on the energy. This fact is in a rough agreement with the estimate above.

The TICS, shown on Figure 4.10, have similar magnitudes for all diazines. Generally, all the peaks in them can be attributed to resonances. The most prominent structure in the TICS are the two resonant peaks around 6 eV. Again, we will discuss the imprints of all resonances in these cross sections later.

4.8 Resonances in diazines

In this section we present a detailed analysis of resonances found in the three diazines. In order to characterize them we use the results of the scattering calculations presented in the previous sections and we supplement these results with calculations of the time-delay spectra. We show that the resonances can be correlated one-to-one across all targets. Additionally, we characterize Feshbach resonances, found only in the dipolar diazines. Finally, we identify structures in the elastic and inelastic cross sections which originate in resonances. We conclude with a discussion in which we correlate some of the resonances in diazines with resonances found previously in other pyrimidinic molecules, particularly in uracil. This analysis will be extended in the next chapter.

4.8.1 Appearance of resonances in eigenphase sums and time-delay spectra

Our calculations reveal a large number of resonances in all three diazines. As we mentioned above and we will see below, the resonances can be correlated one-to-one across all diazines. Therefore it is not surprising that also the individual properties of these resonances (e.g. how they appear in our calculated data) are very similar in all diazines. In the paragraphs below we explain (taking pyrimidine as an example case) how these resonances appear in our calculated eigenphase sums and the time-delay spectra.

It is clear that in order to analyze resonances, it is necessary in the first place to have a method which is capable of identifying them unambiguously. It was stated in Section 3.6.2 that the analysis of the time-delay has proved essential for finding and characterizing reso-

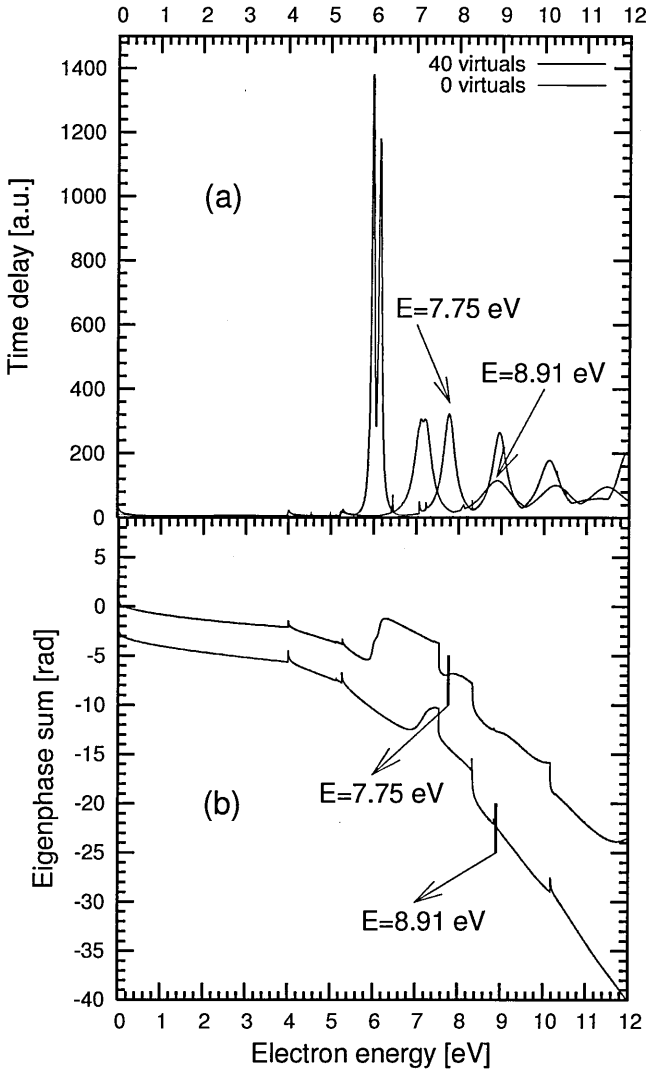

Figure 4.11: Time-delays and eigenphase sums for pyrimidine CC calculations in $^2A_1$ symmetry using the compact basis set. The red lines correspond to the results obtained from the calculations using the full CC model. The black lines are results of the calculations performed using the Simplified CC model. Panel (a): time-delays obtained as the largest eigenvalue of the **Q**-matrix for each electron energy. The resonances discussed in the text are indicated by the blue arrows. Panel (b): calculated eigenphase sums. The vertical bars correspond to the positions of the two resonant structures marked on panel (a).

nances. Figure 4.11 provides clear justification for this claim; it shows the time-delay - panel (a) - and the eigenphase sums - panel (b) - obtained from CC calculations in $^2A_1$ symmetry for pyrimidine using the compact basis set. (The particular molecule and scattering symmetry were picked only as an example to show the behaviour observed for all molecules and most of the resonances studied in this work.) Both the results obtained from the calculations using the full (40 virtuals) and the Simplified model (i.e. 0 virtuals) are presented in the Figure. For clarity, the narrow features corresponding to Feshbach resonances have been removed from the curves shown.

The arrows mark the position of a chosen resonance as calculated in the two scattering models. This resonance appears at 7.75 eV in the full CC model while in the Simplified model it is found at 8.91 eV. We can see that the resonance is clearly visible in the time-delay spectrum, while the eigenphase sums are inconclusive: for the full CC model the eigenphase sum shows only a small change in the derivative in the vicinity of the resonance and for the Simplified model the eigenphase sum does not show any structure at all. We can explain

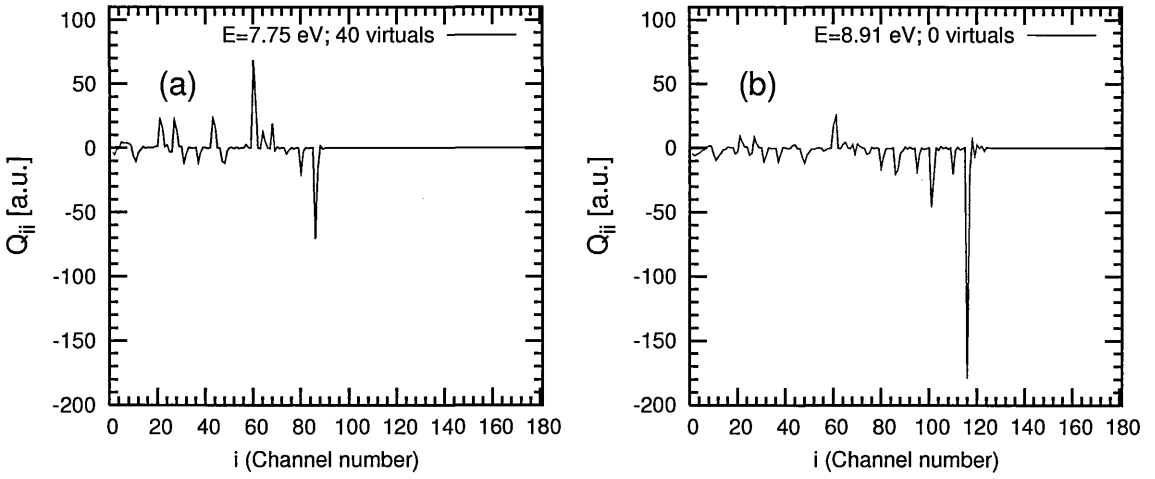

Figure 4.12: Average time-delays (diagonal elements of the **Q**-matrix) calculated for the resonance appearing at 7.75/8.91 eV in pyrimidine CC calculations in $^2A_1$ symmetry using the compact basis set and the full and Simplified model. The red line - panel (a) - corresponds to the results obtained from the calculation using the full CC model. The black line - panel (b) - is the result of the calculation performed using the Simplified CC model. The channel number on the horizontal axis corresponds to a particular combination of the target electronic state and a partial wave of the scattering electron (see Section 2.1). Channel number 9 is the last elastic channel in the $^2A_1$ symmetry.

this effect by the fact that our calculations intrinsically describe also the collisions in which the target molecule is initially in an excited electronic state. The eigenphase sum, therefore, contains information on all collisions in which the molecule is initially in each electronic state included in the CC expansion.

The analysis of the diagonal elements of the **Q**-matrix, shown in Figure 4.12, reveals that the processes which correspond to significant time-delays (i.e. resonances) in some entrance channels, are effectively masked by processes incoming in different, *inelastic* (the last elastic scattering channel has number 9 in Figure 4.12), channels, which lead to a significant time-advance. Since the derivative of the eigenphase sum is related through equations (2.76) and (2.77) to the sum of the diagonal elements of the **Q**-matrix, it becomes clear now why the eigenphase sum does not show a sharp variation in the vicinity of some of the higher-lying resonances. Whether this a general phenomenon which can be observed in a wide range of molecules and/or under which conditions remains to be determined.

An alternative analysis of the resonances can be based on the analysis of the *eigenphases* (i.e. the individual eigenvectors and the associated eigenvalues of the **K**-matrix), because all the resonances are visible in them. However, the eigenphases do not have the property of separating the resonance from the background, which is the case for the eigenvectors of the **Q**-matrix. This causes the resonances to appear in many different eigenphases. Consequently, analysis of the resonances using the eigenphases is very cumbersome as it requires looking

at many eigenvalues of the **K**-matrix and the associated eigenphases. Determining accurate parameters for the resonances (position and width) as well as their parent states from the analysis of the eigenphases is considerably more difficult when compared to the analysis of the time-delay matrix.

4.8.2 Properties and parameters of the resonances

The methods used in this work for the analysis of resonances were described in detail in Section 3.6, where we also described in detail the properties of the resonances found in pyrazine. In this section we focus on the results of a similar analysis carried out for the remaining two diazines. First we discuss the results for the well-established low-lying π^* resonances and then turn to a description of our results on the additional resonances we found.

The positions of the low-lying π^* resonances calculated at the SEP level using both basis sets, along with the experimental positions, are listed in Table 4.9. The agreement for pyrimidine and pyridazine is quantitatively similar to the agreement reached for pyrazine: the positions of the two lowest-lying shape resonances agree very well with the experimental values. The third (mixed core-excited shape) resonance is for all diazines found at energies higher than in the experiment. A detailed discussion of the reasons for this discrepancy and the models better suited to describe this resonance, such as those of Winstead and McKoy, can be found in Section 3.4.1.

The widths of the π^* resonances calculated using the compact and the diffuse basis set are very similar. The narrowest resonance is the first π^* one and the widest is the third π^* resonance. We note that no conclusions should be derived from our results regarding the relative positions of the π^* resonances in the three molecules: a different number of virtual orbitals employed in the scattering models could lead to shifts of the resonance positions such that the relative energy order is modified.

It is worth pointing out that the calculations of Winstead and McKoy [34] predict a different order (with respect to scattering energy) of the two lowest-lying π^* shape resonances: $^2B_1$, $^2A_2$. The order of these resonances inferred from the measurements of Nenner and Schulz is $^2A_2$, $^2B_1$ (see Table 4.9). This apparent disagreement with the experiment can be explained by a closer analysis of the SEP models of Winstead and McKoy. Their SEP models use L^2 configurations which are based on singlet-coupled single excitations of the target molecule from the valence space to a sub-set of virtual orbitals. These models are

Resonance	π_1^*		π_2^*		π_3^*	
Basis set	C	D	C	D	C	D
Pyrazine						
Symmetry	$^2B_{3u}$		^2A_u		$^2B_{2g}$	
Calculation	0.44 (0.032)	0.14 (0.015)	1.05 (0.018)	1.12 (0.030)	5.38 (0.451)	5.19 (0.527)
Experiment [32]	$0.065 - 0.8$		$0.87 - 1.2$		≈ 4.10	
Pyrimidine						
Symmetry	$^2A_2$		$^2B_1$		$^2B_1$	
Calculation	0.68 (0.015)	0.554 (0.016)	1.033 (0.034)	1.068 (0.015)	5.479 (0.468)	5.328 (0.574)
Experiment [32]	$0.25 - 0.7$		$0.77 - 1.6$		≈ 4.24	
Pyridazine						
Symmetry	$^2A_2$		$^2B_1$		$^2A_2$	
Calculation	0.36 (0.004)	0.186 (0.002)	0.971 (0.036)	0.986 (0.064)	5.175 (0.413)	5.018 (0.536)
Experiment [32]	$0.317 - 0.65$		$0.73 - 1.5$		≈ 4.05	

Table 4.9: Positions and widths in brackets (in eV) of the low-lying π^* shape resonances in diazines calculated at the SEP level using the compact (C) and the diffuse (D) basis set. Also listed are the ranges of positions of the π^* resonances as determined from experiment by Nenner and Schulz [32].

sufficient for the description of pure shape resonances. However, the third π^* resonance in pyrimidine (in all diazines in fact) has mixed core-excited shape character. In order to describe the mixed character of this resonance, Winstead and McKoy include *additional* configuration state functions (CSFs) in the calculations for the $^2B_1$ symmetry, where this resonance appears. The additional CSFs are those built on triplet-coupled single excitations of the target molecule. Inclusion of these CSFs in the $^2B_1$ symmetry allows for an accurate description of the core-excited shape resonance, which then appears in their calculations at energy around 4.6 eV close to the experimental one ($\approx$ 4.24 eV). However, there is another resonance of pure shape character appearing in this symmetry at energy approximately 3 eV below. Clearly, inclusion of the additional CSFs in the $^2B_1$ symmetry can be thought of as including more correlation in the $N + 1$ calculation when compared with the other symmetries. Therefore it is not surprising that the first shape resonance in $^2B_1$ symmetry appears lower in energy than the shape resonance in the $^2A_2$ symmetry, because the quality of the calculations for these two symmetries is different. Winstead and McKoy applied the same SEP models earlier for scattering calculations on pyrazine. Due to its higher symmetry, the π^* shape resonances appear in different symmetries, in pyrazine. Not surprisingly, in that case the calculated energy order of the π^* resonances was in agreement with experiment.

Tables 4.10, 4.11 and Figure 4.13 summarize the information on the resonances. In Figure 4.13 we show the time-delays obtained using our highest-level CC scattering models.

		Pyrazine			Pyrimidine			Pyridazine		
Res.	Type	Pos.	Width	Sym.	Pos.	Width	Sym.	Pos.	Width	Sym.
E1	S	1.11	0.07	A_u	0.96	0.14	B_1	1.10	0.14	B_1
E2	MCES	4.66	0.32	B_{2g}	4.78	0.38	B_1	4.72	0.34	A_2
E3	CES	5.93	0.77	B_{2g}	6.37	0.58	B_1	6.14	0.53	A_2
E4	CES	8.41	1.97	B_{2g}	8.47	1.69	B_1	8.34	1.88	A_2
E5	S	0.31	0.07	B_{3u}	0.53	0.17	A_2	0.45	0.19	A_2
E6	CES	6.06	0.18	B_{1g}	6.11	0.51	A_2	5.76	0.54	B_1
I1	CE*	4.99	0.15	A_g	5.96	0.18	A_1	5.48	0.27	A_1
I2	CE*	6.22	0.21	B_{1u}	6.15	0.18	A_1	5.80	0.19	A_1
I3	CE*	7.80	0.28	A_g	7.75	0.35	A_1	7.27	0.18	A_1
I4	CE*	9.20	0.34	B_{1u}	8.94	0.42	A_1	9.03	0.66	A_1
I5	CE*	7.36	0.56	B_{2g}	7.11	0.48	B_1	7.02	0.62	A_2
I6	CE*	5.98	0.15	B_{3g}	5.98	0.24	B_2	4.81	0.14	B_2
I7	CE*	6.57	0.26	B_{3g}	7.19	0.35	B_2	6.73	0.47	B_2
I8	CE*	7.35	0.19	B_{2u}	7.83	0.22	B_2	7.65	0.24	B_2
I9	CE*	7.87	0.37	B_{2u}	8.16	0.22	B_2	8.12	0.35	B_2
I10	CE*	6.73	0.67	B_{1g}	7.33	0.43	A_2	7.04	0.39	B_1
I11	CE*	7.75	0.73	B_{1g}	7.60	0.67	A_2	7.58	0.85	B_1

Table 4.10: Positions and widths (in eV) and symmetries of the shape and core excited resonances found in all three targets determined from our CC scattering calculations using the compact basis set. (The Feshbach resonances are listed in Table 4.11.) We use the following abbreviations for the type of the resonances: shape (S), mixed core-excited shape (MCES), core-excited shape (CES) and 'inelastic' (CE*). The CE* resonances, labelled as 'I', are in the bottom part. All other resonances, designated as 'E' are grouped in the upper part of the table. The resonances E1-E6 and I1-I11 are reported in the energy order in which they appear in pyrimidine for each C_{2v} symmetry.

Pos.	Width	Sym.	Parent
Pyrimidine			
8.336	2×10^{-4}	$^2A_1$	2^1A_1
10.182	6.9×10^{-5}	$^2B_2$	4^1A_1
Pyridazine			
7.275	3×10^{-4}	$^2A_1$	2^3A_1
7.934	3×10^{-4}	$^2B_2$	1^1B_2
8.893	1.7×10^{-3}	$^2B_2$	2^1B_2
9.868	9×10^{-4}	$^2B_2$	3^1B_2
10.266	3.1×10^{-3}	$^2A_1$	5^1A_1

Table 4.11: Positions and widths (in eV) and symmetries of the Feshbach resonances found in our CC scattering calculations using the compact basis set. The Feshbach resonances were found only in the dipolar molecules. Their most likely parent states as well as the resonance symmetry are also listed in the Table.

For clarity, these figures exclude Feshbach resonances found in pyrimidine and pyridazine, but these are listed in Table 4.11. Table 4.10 summarizes the results for shape and core-excited shape resonances obtained in our calculations on the three diazines. We do not list the parameters of some of the resonances lying close to 10 eV as our calculations become inaccurate close to the ionisation threshold and above due to the missing ionisation channels.

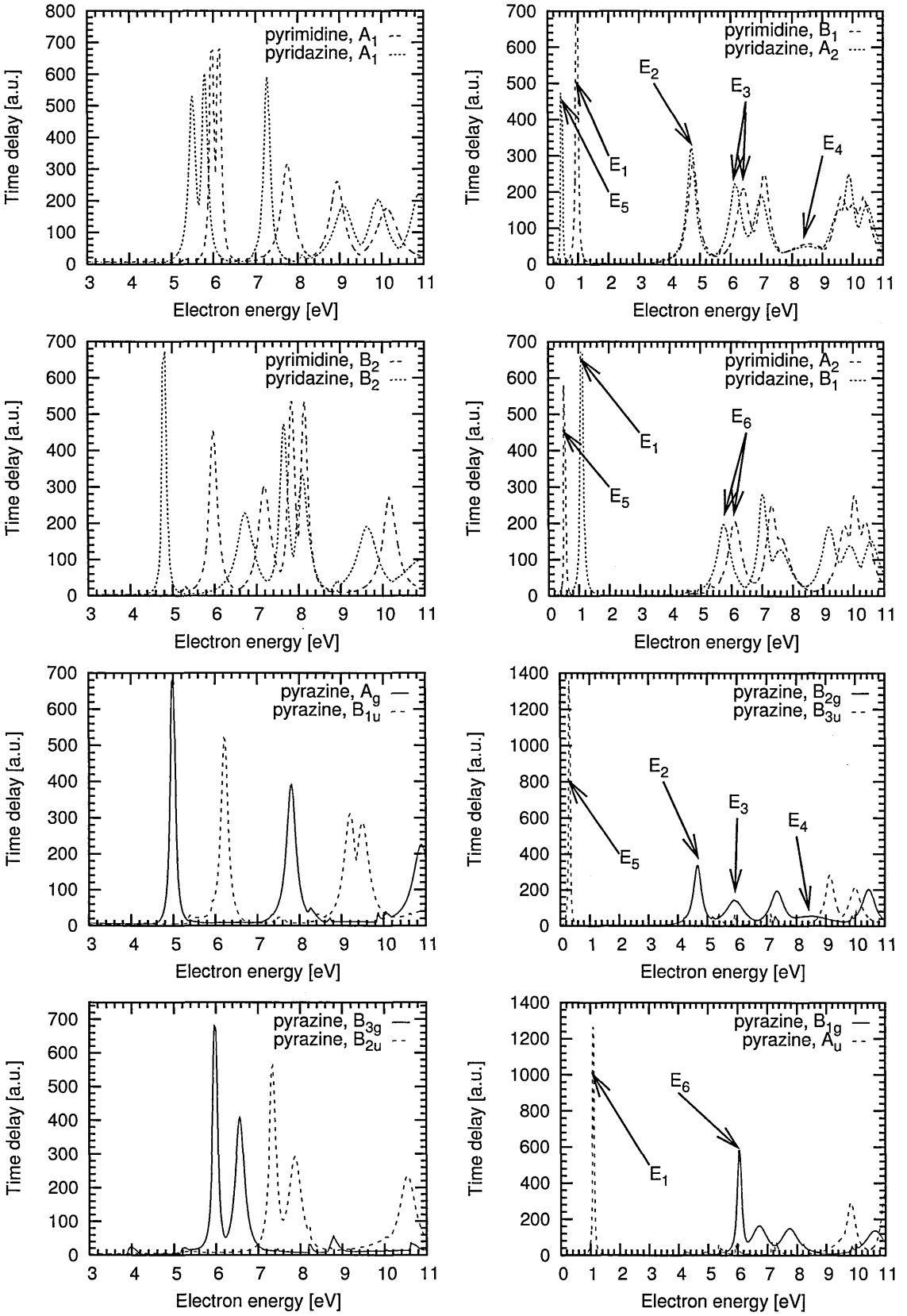

Figure 4.13: The largest eigenvalue of the **Q**-matrix as a function of energy for pyrazine, pyrimidine and pyridazine. The scattering calculations were performed at the CC level using the compact basis set. The symmetries are grouped following Table 4.13. For clarity the Feshbach resonances are omitted from these plots. Note that the panels on the left are plotted for the energy range starting at 3 eV. The positions of the resonances labelled 'E' in Table 4.10 are marked by arrows.

Generally, both experimental and theoretical studies focus on collisions with the target molecule in its ground electronic state and therefore on resonances that form in this process. Our calculations, however, also implicitly model collisions in which the target molecule is initially in an excited electronic state. We discussed already (see Section 3.6.3) that some of the resonances we found in pyrazine significantly enhance the elastic cross section corresponding to these processes, as well as the total electronic excitation cross section for collisions with the molecule in its ground state. Specifically, these resonances enhance the elastic cross section for collisions in which the molecule is initially in an electronic state that is a parent state of the resonance. This is the case also for many of the resonances we found in pyrimidine and pyridazine.

We adopt the abbreviation CE* to denote those resonances that we believe will significantly enhance the elastic scattering from molecules in an excited electronic state. We list in Table 4.10 the positions of these resonances with respect to the target ground state energy but, evidently, these resonances will appear at lower scattering energies in collisions with the molecule in an electronic excited state. Further properties of these resonances are discussed in Section 4.8.6. All other resonances are characterized as shape (S), Feshbach (F), core-excited shape (CES) or mixed core-excited shape (MCES) in the usual manner. We will refer to these resonances collectively as *ground state* (GS) resonances.

The assignment of the character of the resonance (i.e. GS or CE*) was done utilizing the method detailed in Section 3.6.2: a negligible value of the average time-delay for the resonant energy for channels corresponding to the ground state of the molecule indicate the resonance is of CE* type, i.e., it does not manifest itself significantly in collisions with molecules in their ground state. These resonances are labelled 'I' in Table 4.10. An example of the average time-delay spectra for this type of resonance is shown in Figure 4.12. This time-delay spectrum corresponds to the resonance I3 in pyrimidine. We can see that this resonance causes no appreciable average time-delay for collisions starting in the channels associated with the ground state ($i = 1, \ldots, 9$). Conversely, if a significant time-delay is found for channels associated with the ground state of the molecule, then the resonance will be visible in collisions with molecules in the ground state. GS resonances, labelled 'E' in Table 4.10 were further classified as S or CES depending on the magnitude of the average time-delay and/or branching ratio for the channels corresponding to the electronically excited states. The CES resonances possess average time-delays corresponding to the ground and the excited states of a similar magnitude. On the other hand, the mixed core-excited shape resonance E2 possesses a very dominant average time-delay associated with the ground state

of the molecule and much smaller time-delays associated with the excited states. Feshbach resonances were identified on the basis of the observation of a sharp peak in the calculated cross sections or time-delay or a steep increase in the eigenphase sum. A number of very sharp peaks were visible in the time-delay just *above* a specific state and too far in energy from the next state to be deemed to correspond to Feshbach resonances. Finally, the mixed core-excited shape character of the third π^* resonance is well known [33].

The assignment of the character (GS or CE*) of the resonances was confirmed by examining the elastic cross sections for collisions in which the molecule was in its ground and excited electronic states (see Section 3.6.3): GS resonances appeared as a significant peak in the elastic cross section corresponding to the ground state of the molecule and the CE* ones did not (although barely discernible dips in the ground state elastic cross section are normally present at the CE* resonant energies). The parent states of all GS and CE* resonances found in the diazine molecules are shown in Table 4.12 and will be further discussed in Section 4.8.3.

4.8.3 Comparison of resonances in diazines

All the reported resonances (except the Feshbach resonances, found only for the polar molecules) can be correlated one-to-one across the three diazines taking into account the empirical correlation of the symmetries (irreducible representations) indicated in Table 4.13. Note that the symmetries of the two lowest-lying π^* shape resonances do not change when moving from pyrimidine to pyridazine (i.e., the correlation indicated in the Table does not apply). The correlation of the resonances in pyrimidine and pyridazine can be easily derived from a visual comparison of the time-delay plots (see Figure 4.13). Correlating the resonances in pyrazine with the ones in the other diazines is less obvious, because of the higher number of irreducible representations (IRs) in this molecule.

We chose pyrimidine to perform a large number of stability tests (using the compact basis set), in which we varied the following parameters: the number of partial waves included, the values of the dipole transition moments used in the outer region calculations, the thresholds of the electronically excited states (using experimental values), the number of electronically excited states and virtual orbitals included in the CC model. The assignments of the parent states were all stable with respect to these changes. The largest variation was observed when the thresholds of the electronically excited states were shifted (to the values of Fischer et al. - see Table 4.7). Nevertheless, these variations did not lead to different assignments of parent states or character of the resonances, but only to differences in the positions ($\approx$ 0.1 eV

	Pyrazine	Pyrimidine	Pyridazine
Res.	Parent states		
E1	g.s.	g.s.	g.s.
E2	g.s., 1^3B_{3u} (1^3B_1), 1^3B_{1u}, (1^3A_1)	g.s., 1^3A_1, 1^3B_1	g.s., 1^3B_2
E3	g.s., 1^3B_{1u} (1^3A_1)	g.s., 1^3A_1	g.s., 1^3B_2, 2^3B_2
E4	g.s., 1^3B_{2u} (1^3B_2)	g.s., 1^3A_1, 2^3A_1, 1^3B_2	g.s., 1^3B_2, 2^3B_2, 1^3A_1
E5	g.s.	g.s.	g.s.
E6	g.s., 1^1B_{2u} (1^1B_2), 1^3B_{1u} (1^3A_1)	g.s., 1^3A_1, 1^3B_2	g.s., 1^3B_2, 1^3A_1, 1^3B_1
I1	1^3B_{3u} (1^3B_1), 1^3B_{2u} (1^3B_2), 1^1B_{2u} (1^1B_2)	1^3B_1, 1^1B_1	1^3B_1, 1^3A_2, 1^1A_2
I2	1^3B_{2g} (2^3B_1), 1^3B_{3u} (1^3B_1), 1^1B_{3u} (1^1B_1)	1^3A_2, 1^1B_1, 1^3B_1	1^1B_1, 1^3A_2, 1^3B_1
I3	1^3A_u (1^3A_2), 1^1A_u (1^1A_2), 1^3B_{2g} (2^3B_1)	2^3A_2, 2^3B_1, 1^3A_2	2^3A_1, 1^1B_1, 2^3A_2
I4	1^1B_{1g} (2^1A_2), 1^3A_g (3^3A_1)	2^3B_1, 2^1B_1, 2^3A_2	2^3B_1, 2^1B_1, 2^3A_2
I5	1^1B_{2u} (1^1B_2), 2^3B_{1u} (2^3A_1)	1^3A_1, 1^3B_2, 1^1B_2	1^3B_2, 1^3A_1, 2^3B_2
I6	1^3B_{3u} (1^3B_1)	1^3B_1, 1^1B_1	1^3B_1
I7	1^3A_u (1^3A_2), 1^1B_{3u} (1^1B_1)	1^3A_2, 1^1A_2	1^3A_2, 1^3B_1, 1^1A_2
I8	1^3B_{2g} (2^3B_1), 1^1A_u (1^1A_2)	2^3A_2, 1^1A_2, 2^1A_2	2^1A_2, 1^1A_2, 1^1B_1
I9	1^1B_{2g} (2^1B_1), 1^3B_{1g} (2^3A_2)	1^3A_2, 2^3A_2, 2^3B_1	2^3B_1, 2^3A_2, 1^3B_1
I10	1^3B_{2u} (1^3B_2), 1^3B_{1u} (1^3A_1)	2^3A_1, 1^1B_2, 1^3A_1	2^3B_2, 2^1A_1, 1^3A_1
I11	2^3B_{1u} (2^3A_1)	1^3B_2, 1^1B_2, 2^3A_1	1^3A_1, 2^1A_1, 2^3B_2

Table 4.12: Parent states of the resonances found in the CC calculations on diazines employing the full model. The excited states correspond to those listed in Table 4.7. The electronic states of pyrazine have also been given the corresponding C_{2v} label. The order of the states (from left to right) indicates, approximately, the importance of the states as parent states for a given resonance. See text for details on how the parent states were determined.

Pyrazine	Pyrimidine	Pyridazine
$A_1 : A_g + B_{1u}$	A_1	A_1
$B_1 : B_{2g} + B_{3u}$	B_1	A_2
$B_2 : B_{3g} + B_{2u}$	B_2	B_2
$A_2 : B_{1g} + A_u$	A_2	B_1

Table 4.13: Empirical correlation of the C_{2v} symmetry labels of the three diazine molecules derived from the analysis of the resonances. Also included is the resolution of the D_{2h} IRs of pyrazine into the IRs of its subgroup C_{2v}. This correlation does not apply to all states or resonances.

towards lower energies) and widths (more than 50 % larger in some cases) of the higher-lying resonances in some symmetries. We choose to present the parameters of the resonances as obtained from the calculations using the unshifted thresholds. Comparison of the time-delay spectra for pyrimidine calculated using partial waves up to $l = 4$ and the shifted and the unshifted thresholds is shown in Figure 4.14. In light of the stability tests performed, we consider the positions of the higher-lying resonances more stable than the widths, which seem to be more sensitive to the vertical excitation energies.

The results for pyrimidine reported in Tables 4.10, 4.11 and Figure 4.13 were obtained using partial waves up to $l = 5$. The results for the other two diazines were obtained using partial waves with $l \leq 4$ only. As mentioned above, the inclusion of the $l = 5$ partial wave did not change the results significantly. The positions and widths of the resonances were obtained by fitting a Lorentzian function to the individual time-delay peaks in Figure 4.13.

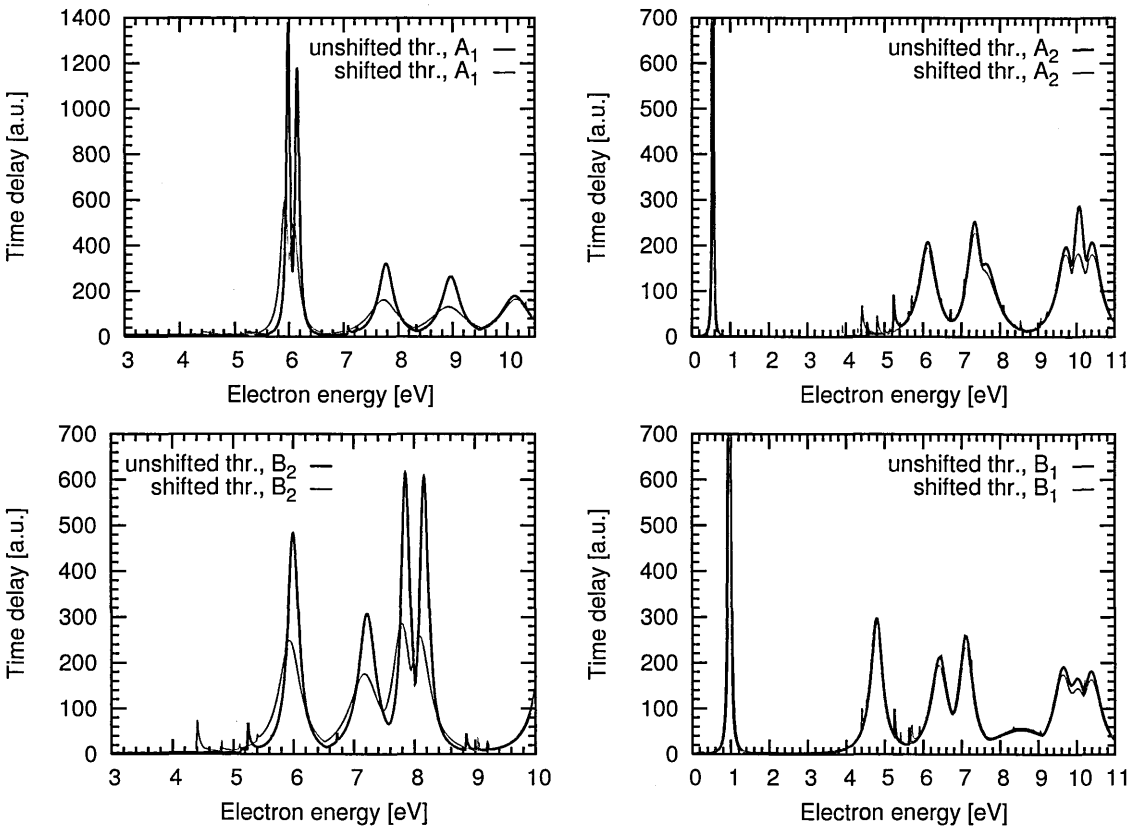

Figure 4.14: The largest eigenvalue of the **Q**-matrix as a function of energy for pyrimidine. The Figure shows comparison between time-delay spectra obtained from the CC scattering calculations using the compact basis set, partial waves up to $l = 4$ and the shifted (to the values of Fischer et al. [115] - see Table 4.7) and unshifted thresholds of the electronic excited states. For clarity the Feshbach resonances are omitted from these plots. Note that the panels on the left are plotted for the energy range starting at 3 eV.

A more sophisticated approach, such as the one using equation (2.77) and genetic algorithms to perform the fitting exists [80] and would probably give slightly more accurate parameters, especially for the partially overlapping resonances. Nevertheless, we are confident that the resonance parameters we report in Table 4.10 would not change significantly. As mentioned in Section 2.7.1 the TIMEDEL program for automatic fitting of the time-delay spectra, which was developed for use with the UKRmol codes, was not compatible with the current version of the codes.

It is apparent from Table 4.10 that the parameters of all resonances in pyrimidine and pyridazine are relatively similar (with the exception of the resonance I6; see below). This is not the case when these resonances are compared with the ones found in pyrazine: the positions of some of them differ by more than 1 eV. This fact can be probably ascribed to the strong dipolar interaction of the scattering electron with the target molecule in collisions with pyrimidine and pyridazine. Nonetheless, resonances E2,E4,E6 and I2,I3,I6 have similar positions and widths in pyrazine in pyrimidine. The resonances that are most similar in these

two systems are the narrow resonance I6 and the widest of all of the resonances, resonance E4.

Further information about the formation of the resonances in diazines can be gained analyzing their parent states. Naturally, one would expect the characteristics of the parent states (i.e. their symmetry, VE energy and other properties) of a given resonance to play a role in its formation. Given the correlation of resonances in Table 4.10 and their parent states (Table 4.12), one can follow how the parent states of these resonances change when going from pyrazine to pyrimidine and pyridazine. It would be expected that the resonances which correlate with each other, in the three diazines, will have as parent states electronic states with the same C_{2v} symmetry label and number. A detailed analysis of the parent states (see Table 4.12) reveals that some resonances (E2, E3, I3, I4, I5, I11) do not have even one common parent state (in the sense of the symmetry labels) in all three molecules. However, this does not necessarily mean that the underlying physical character of these resonances (i.e. their wavefunction) is very different: there is no straightforward correlation of the symmetry labels and numbering of the electronic states in all molecules (see Section 4.5). This means that comparing only the symmetry labels and order of the parent states alone is not sufficient to decide how much the actual parent states of a given resonance change in the three molecules. Consequently, it is not straightforward to derive conclusions on the actual change in the resonant wavefunction when going from pyrazine to pyrimidine and pyridazine. On the other hand, for pyrazine and pyrimidine we always find, for a given resonance, at least one parent state which has the same symmetry label in both molecules. It is entirely possible that wavefunctions of some electronic states with different symmetry labels in pyridazine and the other two diazines are similar. It is also possible that this effect can be at least partially ascribed to the fundamentally different choice of the plane of symmetry in pyridazine (see Figure 3.1), which passes *in between* the atoms of the ring. This is in contrast with pyrazine and pyrimidine, where one plane of symmetry always passes through an atom. We discuss the role of parent states in formation of the resonances further in Section 4.8.6

4.8.4 Imprints of the resonances in the calculated cross sections

In this section we discuss only the cross sections obtained using the full CC model. We do not discuss the results of the SEP calculations (which were presented in the previous Chapters), because the main focus of this chapter is on the identification of resonant structures in the calculated cross sections. Since our SEP cross sections show (unphysical) pseudoresonances

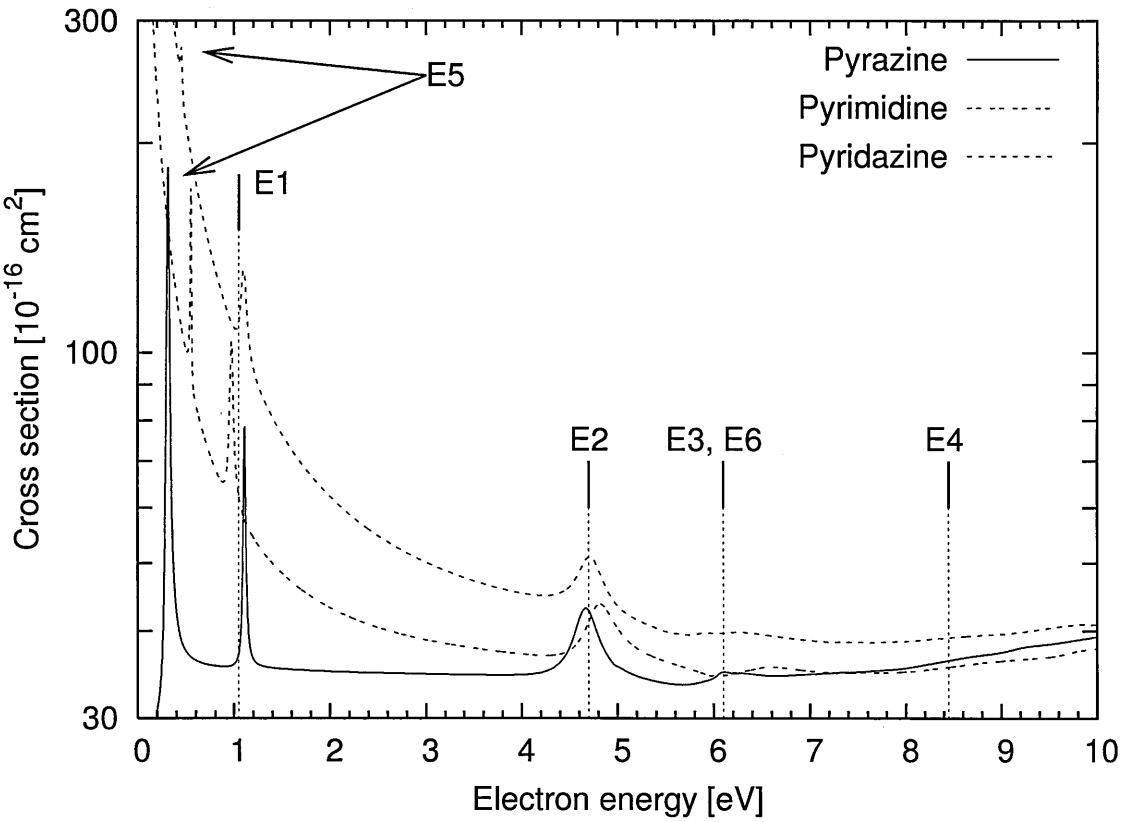

Figure 4.15: Integral elastic cross sections for diazines calculated at the CC level using the compact basis set. The Born correction for the dipolar molecules is not included. (For Born-corrected results see Figure 4.9). The vertical lines indicate approximate positions of the four CES resonances. Note the logarithmic scale for the y-axis.

in the energy region where many of the resonances actually appear, discussion of the SEP cross sections would not be helpful (reliable) for identifying footprints of resonances in them.

Figure 4.15 shows integral elastic cross sections for the three diazines. Figure 4.16 shows the total inelastic (TICS) cross sections calculated with (left panel) and without (right panel) the Born correction as well as the contributions to the TICS from all scattering symmetries. All these cross sections were calculated using the CC scattering model and the compact target basis set. The elastic cross sections do not include the Born correction for the dipolar molecules. The Born correction for the inelastic cross sections was calculated (utilizing the values of the dipole transition moments) using the method detailed in Appendix B.

The integral elastic cross sections (Figure 4.15) for pyrimidine and pyridazine show again the typical diverging dipolar behaviour at low energies. Clearly visible in all cross sections are the three low-lying π^* resonances and the peak around 6 eV corresponding to the two core-excited shape π^* resonances E6 and E3 from Table 4.10. The wide shoulder in the cross sections starting above 8 eV is caused by the core-excited shape π^* resonance E4. The small peak above 9 eV in all diazines is caused by a core-excited shape resonance of B_{3u} symmetry

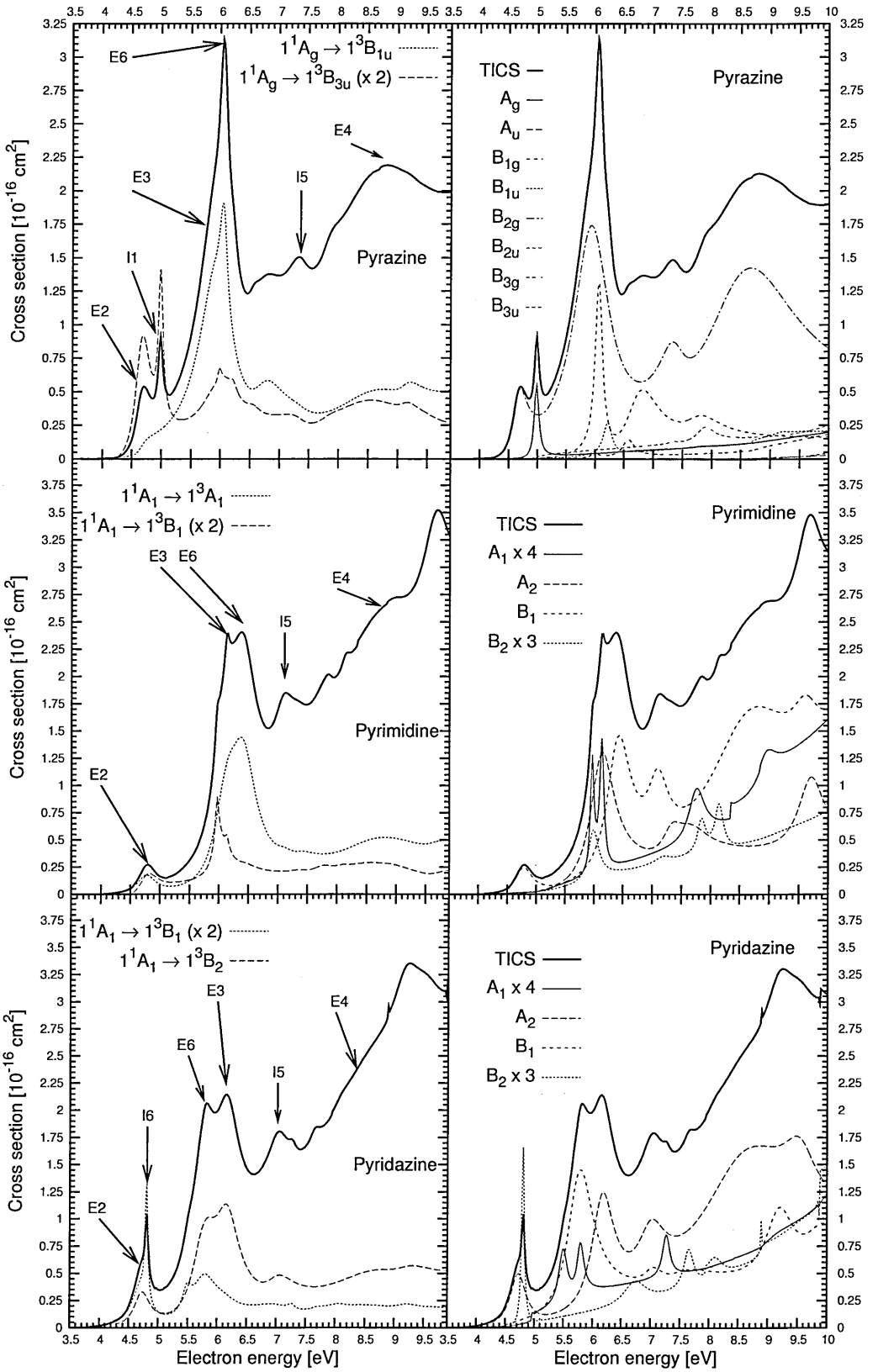

Figure 4.16: Left panel: Total inelastic cross sections for pyrazine, pyrimidine and pyridazine calculated at the CC level using the compact basis set. Also shown are the cross sections for electron impact excitation of the two lowest-lying electronic states for each molecule. A Born correction [93] based on dipole transition moments has been added to the cross sections. Right hand panel: contributions from all scattering symmetries to the total inelastic cross sections for all three diazines. No Born correction has been added in this case. The Feshbach resonances are not visible in any of the panels because of the energy resolution chosen for calculation of these cross sections.

in pyrazine and A_2 symmetry in pyrimidine and pyridazine. However, due to its proximity to the ionisation threshold, where our calculations might become inaccurate, we choose not to include this resonance in Table 4.10.

In pyrimidine and pyridazine we find a high-lying (above 10 eV) σ^* broad shape resonance in the A_1 symmetry, which appears in the elastic cross sections and in the time-delay, but for the reasons stated in the previous paragraph we do not include this resonance in Table 4.10. Our tests for pyrimidine show that this resonance is quite sensitive to the number of partial waves included: it becomes much broader in the calculation using partial waves up to $l = 5$. In pyrazine we find a very similar broad structure around 10 eV in the A_g elastic cross section, but the time-delay spectra do not show a broad peak that could be unambiguously associated with this structure.

Several interesting features can be observed in the TICS (see Figure 4.16). Generally, all the peaks in this cross section can be attributed to resonances. However, their positions are slightly shifted towards higher energies with respect to the center of the resonance as determined from the fits to the peaks in the time-delay. The third π^* resonance (E2 in Table 4.10 and visible in the TICS as a small bump around 4.7 eV) was analyzed in detail in the previous chapter.

The most notable peaks in TICS are the two located around 6 eV, which are seen in all diazines, although in pyrazine they largely overlap. It can be seen from the contributions to the TICS from the individual symmetries (see right hand panel of Figure 4.16) that they arise from the (core-excited shape) resonances E3 and E6 - see Table 4.10. Grandi et al. [55] performed SEP calculations on uracil (that has C_s symmetry), in which the symmetry of the scattered electron was increased to D_{2h}. In these calculations a shape resonance of B_{1g} symmetry was found lying at 9.07 eV. Our calculations show that this resonance in uracil can very probably be traced to the resonance E6 in the diazines (of B_{1g} symmetry in pyrazine), lying about 3 eV lower. Furthermore, this resonance appears clearly as a distinctive peak in the elastic cross sections. It is possible that the calculations of Grandi et al. significantly overestimate the position of this resonance, because they do not include any coupling of the resonance to the excited states. Inclusion of such coupling can influence the position of a resonance significantly [33]. Therefore, the B_{1g} resonance in uracil is likely to lie much lower in energy. We discuss this resonance further in Section 4.8.6.

A sharp peak located around 5 eV in the TICS for pyrazine (resonance I1) is seemingly missing in pyrimidine, but appears in pyridazine slightly below 5 eV. However, the two peaks correspond to different resonances: examining the contributions of the individual scattering

symmetries (see right hand panel of Figure 4.16) shows that resonance I1 (in A_g symmetry in pyrazine and in A_1 symmetry in the other two diazines) is much less pronounced in pyrimidine and pyridazine and is located at higher energies. Resonance I6 (in B_{3g} symmetry in pyrazine and in B_2 symmetry in the other two diazines), on the other hand, contributes much more to the pyridazine TICS and is responsible for the sharp peak around 4.8 eV. Therefore, the peaks around 5 eV in pyrazine and pyridazine are caused by different resonances which seem to be significantly affected by the position of the nitrogen atom in the ring. Interestingly, Table 4.10 implies that the resonance I6 is affected only upon transition from pyrimidine to pyridazine.

The other structure which deserves an explanation is the broad peak in pyrazine with maximum around 8.7 eV. A similar structure with only minimal variations in magnitude, position and width is present in pyrimidine (in symmetry B_1) and pyridazine (in symmetry A_2). We ascribe this broad maximum to the broad core-excited shape resonance E4. The peak around 7.4 eV in pyrazine (around 7 eV in pyrimidine and pyridazine) is caused by the resonance I5, whose parameters are quite stable in all diazines. Above 9 eV, an additional peak appears in pyrimidine and pyridazine, which is seen above 10 eV in pyrazine and we choose not to characterize it.

4.8.5 SE model for scattering from 1^1B_1 excited state of pyrimidine

Throughout this work we have interpreted the CE* resonances as those which strongly enhance cross sections for elastic scattering from those excited states that are their parents. The purpose of the SE calculations described here was to see if these resonances appear also in a very simple scattering model which describes electron collision with a molecule in an excited state (i.e. the channels associated to the ground state are absent). These calculations were performed for pyrimidine for scattering in the $^2A_1$ symmetry, where four resonances appear in the full model with energies below 10 eV (see Table 4.10). Before we describe the SE model we examine first the parent states of these resonances.

Looking at Table 4.12 we see that the resonances I1 and I2 in pyrimidine have two parent states in common: the 1^1B_1 excited state with VE energy 4.99 eV and the 1^3B_1 excited state with VE energy 4.54 eV. In the following, however, we choose to focus on the 1^1B_1 parent state. As one of the parent states of the resonances, the elastic cross section for scattering from the 1^1B_1 excited state, shown on Figure 4.17 - panel (a), displays two prominent peaks at positions corresponding to the two resonances. The resonant origin of these peaks is fully

confirmed by the time-delay spectrum shown on panel (b). A third, smaller, peak below 8 eV is present in the cross section as well and corresponds to the I3 resonance. Indeed, the time-delay analysis shows that the 1^1B_1 excited state is also one of the parent states of this resonance. However, this parent state is much less important for the I3 resonance than are the other ones listed in Table 4.12. Not surprisingly, this fact is then reflected in a much smaller peak (compared with the resonances I1 and I2) in the 1^1B_1 excited state elastic cross corresponding to this resonance. Since the 1^1B_1 excited state is a parent state for three resonances in this symmetry and its elastic cross section is relatively large, it is an ideal candidate for our simple SE calculations, whose aim will be to model electron collisions with pyrimidine in this electronic state. (By choosing the parent state with the largest resonant peaks in the elastic cross section we maximize our chances to see the corresponding resonances in a simpler model). In order to show how the resonances in $^2A_1$ symmetry affect (or not) cross sections for scattering from other excited states, we show in Figure 4.17 several examples of these. In the scattering calculations described below we will attempt to construct a very simple model of electron collision with the 1^1B_1 excited state (for the $^2A_1$ scattering symmetry).

To construct this scattering model we identified the main configuration (as determined from our SA-CASSCF calculations) of the 1^1B_1 excited state: $7b_2^1 \otimes 2a_2^1$ with CI coefficient 0.62 (the remaining electrons doubly occupy the same orbitals as in the ground state configuration). We then used the SA-CASSCF orbitals and constructed the single determinant corresponding to this configuration. This single determinant was then taken as a simple approximation for the wavefunction of the 1^1B_1 excited state. This single configuration description of the 1^1B_1 excited state replaces the HF description of the ground state in our SE scattering model. Following the prescription of the SE model, we constructed the L^2 configurations by coupling the single excited determinant with several (12) virtual orbitals of the b_1 symmetry to produce configurations of $^2A_1$ total symmetry. The cross sections and eigenphase sums calculated using this simple SE model are shown on panels (c) and (d) in Figure 4.17. In panel (d) we choose to present the eigenphase sum rather than the time-delay spectrum, because in the case of the SE model the eigenphase sum and the time-delay spectrum show the resonances equally clearly. We can see immediately from these graphs that the SE model is capable of describing (albeit on a very simple - qualitative - level) all three resonances with the 1^1B_1 excited state as one of their parents. The overall shape of the cross section is similar to the one calculated using the much more sophisticated CC model, with the two lowest-lying resonances appearing closer to each other. The resonances in the SE

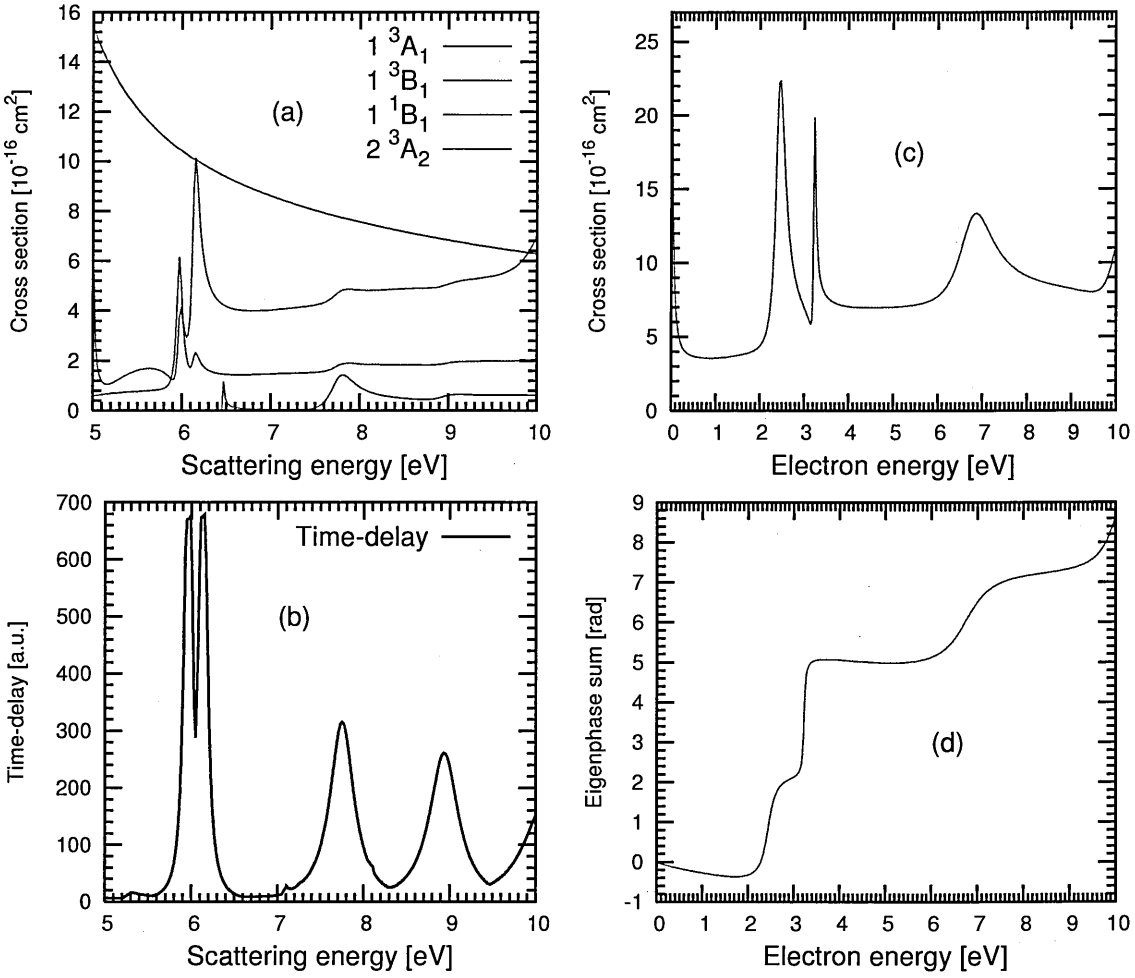

Figure 4.17: Panel (a): elastic cross sections obtained from CC calculations using the full model for scattering in $^2A_1$ symmetry from selected excited states of pyrimidine listed in the panel. Panel (b): time-delay for electron scattering in $^2A_1$ symmetry obtained using the same scattering model. Panels (c, d): cross section for elastic scattering from the 1^1B_1 excited state obtained in the SE approximation and the corresponding eigenphase sum (see text for detail).

model are found at energies roughly twice as large as in the full CC model. The magnitude of the SE cross section is larger than the one calculated using the full model, which is not surprising, because the SE model does not include other electronic channels (and couplings to them), where some probability flux is allowed to flow in the full model. As expected, the highest-lying resonance appears in the SE cross section as a smaller peak than the other two. This is fully compatible with the fact that the 1^1B_1 excited state is not one of the most important parent states for this resonance. It is also clear from the construction of the simple L^2 functions of this model, that the three resonances are associated with three different orbitals of the b_1 symmetry.

The results of this section show clearly that formation of the resonances in $^2A_1$ symmetry of pyrimidine can be understood using a simple qualitative picture. The SE model which we

used for description of the interaction of the scattering electron with the 1^1B_1 excited state includes only two types of the electron-molecule interaction (see Section 2.6.1): exchange interaction of the scattering electron with electrons of the molecule and the interaction of the incoming electron with the static charge distribution of the target electronic state. Even in this simple model we observe the formation of the $^2A_1$ resonances associated with the 1^1B_1 excited state. In fact it would be possible to associate these resonances with the individual orbitals of b_1 symmetry. Consequently, these resonances can be described as "shape resonances" with respect to the parent 1^1B_1 excited state. These calculations therefore confirm that these resonances are core-excited shape. The properties of the CE* $^2A_1$ resonances in pyrimidine (i.e. how they manifest themselves in the calculated scattering data) are not fundamentally different from the properties of the other CE* resonances. Therefore the other CE* resonances are also core-excited shape. A detailed investigation of the role of parent states in formation of the CE* resonances would require further work, which we briefly discuss in the next Section.

4.8.6 Resonance analysis

The formation of the core-excited shape resonances in diazines is not significantly sensitive to the magnitude of the dipole moment of the molecule. However, a dipole moment seems to be a necessary condition for formation of the Feshbach resonances: these are observed only for the polar molecules. Therefore, we deem these resonances to be dipole-supported [135].

The CE* resonances seem unlikely to be observed in experiments measuring the elastic cross sections for target molecules in the ground state because their presence hardly enhances the calculated elastic cross section. The "inelastic character" of the CE* resonances explains why they appear only as small kinks/dips. We also showed that the presence of some (I1, I5, I6), but not all, the CE* resonances is clearly visible in the TICS. We suggest, on the basis of our calculated elastic cross sections corresponding to the excited states (see Figures 3.14 and 4.17 for examples of these) and the average time-delays, that these resonances would manifest themselves significantly in collisions with molecules initially in some of the lowest-lying excited states. Based on the values of the calculated vertical excitation energies of the electronic states (see Table 4.7) and the positions of the CE* resonances (Table 4.10), we predict that these resonances would appear at energies below ≈ 5.5 eV.

Using the time-delay/cross sections analysis (see Section 3.6) we assigned parent states of the CE* resonances. For our calculations on pyrazine, assignment of the parent states

for some of the resonances was also done using the method of R-matrix poles that enabled us to obtain their configurations. However, we found that interpreting the configurations of the higher-lying GS resonances is not straightforward. Consequently, we were not able to identify unambiguously the orbitals responsible for trapping of the scattering electron. As we mentioned earlier (see Section 3.6.2), the time-delay method is completely sufficient for the assignment of the parent states. The time-delay analysis was applied to the results of the full CC model, which provides the most accurate description of the collision. Analyzing the R-matrix poles would be very difficult (if not impossible) for the full CC model containing several tens of thousands of eigenvectors. In contrast, there is no difference in the ease of application of the time-delay analysis between the full and Simplified CC models once the K-matrices have been calculated. The disadvantage of the time-delay analysis is that it does not allow us to establish what orbitals are the most important for trapping the incoming electron, particularly in the case of the Feshbach and the CE* resonances. In this case the analysis of the R-matrix poles might be able to supply this missing information. Alternatively, one can also apply the SE model for calculations of electron collisions with the molecule in an excited states (see Section 4.8.5). This method is also capable of providing information on the target orbitals involved in trapping the incoming electron. We showed, with an example for pyrimidine (see Section 4.8.5), how the configurations of the resonances can be "guessed" analyzing the elastic cross sections for the electronically excited states. Finally, we remark that branching ratios and average time-delays calculated with the full and the Simplified model are fairly similar, showing that the character of the resonances can be estimated from the computationally cheap Simplified model.

It would be very intersting to investigate further the formation of the CE* resonances, which are associated with electronically excited states of the molecule. It would be natural to associate formation of these resonances with certain properties of the electronic states. However, in diazines there are many CE* resonances which have several parent states. Hopefully, an in-depth analysis of how the properties of the parent states influence the formation of these resonances would be simpler in smaller systems possessing fewer CE* resonances with fewer parent states. It is not clear from our results which are the most important properties of the parents responsible for formation of these resonances. Useful information about the formation of some of them can be gained from calculations which include only the channels corresponding to one electronic excited state. The results of these calculations suggest that the presence or not of the couplings between many electronically excited states (as in the full CC calculation) does not influence the formation of these resonances significantly. However,

a confirmation of this hypothesis would require more work (a detailed analysis of the full time-delay matrix might be helpful in this task).

We showed explicitly in our work on pyrazine (see Section 3.6.4) that the most significant configurations for at least some of the resonances included only the orbitals of the active space. In this Chapter we established that in fact *all resonances* we find (excluding the shape ones) have configurations based on an excitation of the HF ground state configuration, with the scattering electron trapped in one of the orbitals of the active space. This follows from the fact that the resonances are present in the Simplified model, which utilizes only the orbitals of the active space.

Correlation of resonances in diazines and resonances in uracil

In a recent study Wang et al. [64] predicted higher-lying σ^* resonances in all DNA bases and Winstead and McKoy discuss [56] the possible presence of a σ^* resonance in uracil around 8.5 eV. These resonances may correlate to the high-lying broad σ^* shape resonances we find in the diazines. We discuss this possibility further in the next chapter in the context of our calculations for substituted pyrimidines. A core-excited resonance in pyrimidine lying around 5.5 eV was recently found by Modelli et al. [35] in their electron transmission spectra. Our calculations suggest that this structure corresponds in fact to two overlapping core-excited shape resonances (E3 and E6 in Table 4.10) in B_1 and A_2 symmetries found by us around 6 eV. The difference in the position is consistent with the discrepancy of a similar magnitude for the third π^* resonance. Resonance E6 is the diazine equivalent of the one found in uracil [55] around 9 eV, although Grandi et al. [55] assign it shape character and we assign it core-excited shape character. We do not deem this resonance shape because we do not observe a resonance in our SE calculations (in the energy range $0-20$ eV) which might correspond to it. However, inclusion of polarization may be necessary for the formation of this resonance (see Section 3.6.5). Unfortunately, our SEP calculations display the presence of a large number of non-physical pseudoresonances that would hide any resonance of this type in the higher energy range. (See Section 2.6.2 for a detailed discussion of the origin of pseudoresonances in our SEP calculations.)

In order to confirm the correspondence between these resonances, we applied our time-delay analysis to CC calculations on uracil using the Simplified model and the compact basis set (following Dora et al. [59] for the choice of all other parameters). The calculations (which are described in detail in Chapter 5) indeed show the presence of a core-excited shape resonance of A″ symmetry around 7 eV, providing further evidence for the proposed

correlation of resonances in diazines and uracil. Dora et al. [62] did not report this resonance, in all likelihood because it is not visible in the eigenphase sum (although we do see a peak in the A″ contribution to the elastic uracil cross section).

The measurements of Modelli et al. were performed for electron energies up to ≈ 6.5 eV and therefore could not reveal the presence of the broad core-excited shape resonance E4, which we predict to lie around $8.3-8.5$ eV in all diazines. Since this resonance is not affected by the dipole moment of the target molecule, we would expect it to appear at similar energies in uracil.

The proposed explanation [39, 40] of the main features of the DEA spectra of uracil involves a low-lying σ^* resonance. Winstead and McKoy find [56] a low-lying ($\approx$ 1.45 eV) σ^* resonance in their scattering calculations on uracil but Dora et al. [59] do not. None of our models for the diazines and for uracil reveal a resonance equivalent to this low-lying σ^* resonance either. This could be explained by the very diffuse character of the resonance [56]: ours and Dora's calculations for uracil use a compact basis set that would not be able to describe it. For the diazines we also used a basis set with diffuse functions on the carbon and nitrogen atoms (6-311+G**), but we did not find a structure that could correspond to the low-lying σ^* resonance. It is possible that our diffuse basis set is not appropriate for the description of this resonance due to the lack of diffuse functions on the hydrogen atoms.

4.9 Summary

In this chapter we have completed our calculations on diazines by performing scattering calculations for pyrimidine and pyridazine. We have used the time-delay method to characterize resonances in these molecules and compared them with those found in pyrazine.

For pyrimidine, we were able to compare the elastic and inelastic cross sections calculated for electron energies $0-15$ eV with experimental data and found a good agreement. The magnitude of the inelastic cross section agrees well with the experimental results, however the experiment has an insufficient number of data points to detect the presence of the structures caused by resonances. Nevertheless, the overall agreement between the calculated and measured cross sections is good, strengthening our confidence in the quality of our scattering models.

For pyridazine, we presented integral total, elastic and inelastic cross sections and the elastic differential cross sections calculated at various levels of approximation. To the best of our knowledge there are no other calculated or experimental data to compare these results

with.

Finally, we performed a detailed analysis of the resonances in all three diazine molecules. We have found that the positions of the three π^* resonances in the three targets are, as expected, similar. The positions of the two lowest-lying π^* resonances agree well with the experimental positions of Nenner and Schulz. However, the third mixed core-excited shape resonance lies in our calculations and for all targets approximately 1 eV above the experimental position.

In addition to characterizing the π^* resonances we analyzed in detail the time-delay spectra of the three molecules resulting from our Close-Coupling calculations and found a large number of core-excited resonances. All these resonances (with exception of the Feshbach resonances found only in the dipolar diazines) can be correlated one-to-one across the three targets. We identified structures in the elastic and inelastic cross sections, which correspond to resonances.

The time-delay analysis has proved easier to apply than an analysis of the eigenphase sum when searching for resonances, providing not only more accurate but also more detailed information on the collisions. We found three higher-lying core-excited shape π^* resonances, not characterized before theoretically, in all diazines. Two of these resonances lie around 6 eV in our calculations, whereas a broader resonance lies around 8.4 eV. We also provide evidence for the possible presence of a core-excited shape resonance of π^* symmetry lying around 9 eV. These resonances are visible in the integral elastic cross sections. However, whether these resonances possess a *mixed* core-excited shape or only a pure core-excited shape character cannot be determined from the results of our calculations. The inelastic cross sections show prominent peaks associated with the (mixed) core-excited shape resonances. We have found that many, but not all, of the resonances characterized in uracil so far can be traced back to equivalent resonances in diazines.

We found a surprisingly large number of resonances likely to play an important role in collisions with the target molecule initially in an excited electronic state. These resonances influence only negligibly the elastic cross section associated with the ground state of the molecule. However, they show up as prominent peaks in elastic cross sections corresponding to collisions with the target in those excited states which are the parent states of the resonance. In order to further elucidate the formation of these resonances we performed an SE calculation for pyrimidine for the $^2A_1$ symmetry, in which the target was represented by a single determinant representing the selected (1^1B_1) excited state. We showed that this simple model allows for the description of the CE* $^2A_1$ resonances which have the 1^1B_1 excited state

as a parent state. This result further confirms that the CE* resonances form predominantly, but not exclusively, in elastic collisions with the target in an excited state.

We note that the calculations of Dora et al. [62, 63] on electron collisions with pyrimidinic and purinic nucleobases report inelastic cross sections containing peaks which, based on our experience, have the footprint typical of the CE* resonances found in diazines. A time-delay analysis similar to the one carried by us should provide more insight into the nature of these structures. Our time-delay analysis of CC calculations for uracil using the Simplified model reveals the presence of resonances of CE* type in this system as well.

Generally, all the resonances we found in our high-level Close-Coupling calculations are present also in the Simplified Close-Coupling model, which utilizes only a relatively small number (8) of active-space orbitals. More work is needed in order to understand why a large number of resonances are formed in these molecules with configurations requiring only a relatively small number of orbitals.

The discovery of the three higher-lying resonances (above the third π^* resonance), which are visible in the elastic cross section associated with the ground state of the molecule, was not so surprising, but is potentially very important. However, the discovery of an even larger number (11) of CE* resonances, which affect significantly only elastic cross sections for the electronically excited states was totally unexpected. At present it seems unlikely that electron scattering experiments with the target molecules in their excited states are feasible. This is due to the short lifetime of the excited states of these molecules, which tend to decay rapidly to the ground electronic state. Therefore confirming, directly, the presence of the CE* resonances using experimental techniques seems very difficult. On the other hand, some of these resonances appear as peaks in the integral cross section for electron impact electronic excitation of the molecules in the ground state. Therefore measuring in detail these inelastic cross sections might be one way of confirming the presence of these resonances in diazines.

A comparison of the CC models for pyridazine and uracil [59] (30 virtuals chosen when using the compact basis set) with the pyrazine one (40 virtuals) leads us to the conclusion that the presence of a strong dipole moment in the target molecule is a significant factor affecting the choice of the optimal number of virtual orbitals for this model. Since the same number of virtuals was used for pyridazine and uracil [59], despite uracil having 16 more electrons corresponding to the extra two oxygen atoms attached to the ring, we expect that the CC models of our type using the compact/diffuse basis set and 30/70 virtual orbitals will be a good choice even for calculations on pyrimidinic molecules for which experimental information on resonances is not available.

However consistent our results for the resonances are, they are limited by the poor description of the target electronic states. More specifically, our calculations suffer from inaccurate values of the VE energies of the electronic states. A straightforward approach to this problem would be to increase the size of the CAS which should, in principle, improve the quality of description of the electronic states. However, for a given CAS model there is a factorial dependence of the number of CSFs generated on the number of active orbitals. Therefore adding even a relatively small number of orbitals into the active space results in a much larger Hamiltonian matrix. For pyrazine, CAS models of different size were tested in the work of Weber and Reimers [120] and it was found that even those as large as (12, 14), i.e. 12 electrons distributed among 14 orbitals, do not lead to better values of the VE energies when compared with smaller CAS models, e.g. the CAS (10, 8) used in our work. It follows that *for large molecules*, like the ones studied in this thesis, an active space that would give an accurate description of the electronic excited states would be of size exceeding the current limits of the best desktop computers. It is going to be necessary to extend the functionality of our codes to be able to run them on large parallel computers (this work is currently under way). Nevertheless, it remains to be seen whether this purely variational approach will be practical and lead to a significant improvement in the description of the electronic states. We are convinced that a computationally much cheaper alternative would be (see [76, p.278]) to use small to moderate-sized CAS models and include *perturbative corrections* in both the target and the $N + 1$ calculations. In quantum chemistry perturbative corrections to the CASSCF wavefunctions have been applied routinely with great success and to a wide range of molecules (see e.g. [120, 121] to compare the accuracy of CASPT2 and CASSCF methods). In order to apply this method in scattering calculations one would have to define the perturbative corrections for the $N + 1$ wavefunctions in a way that would be consistent with the corrections applied to the target wavefunctions. This is a very complicated problem, but it would provide huge benefits if resolved.

We note that the problem of accurate representation of the electronic states is much more complicated for large molecules than for smaller molecules. For smaller targets (the size of water) it may be possible to increase the size of the CAS to obtain an accurate representation of the electronic states, while keeping the calculation within the limits of the current best desktop computers.

We have seen that the diazines possess a large number of Rydberg states. Improving the representation of these states would require not only the use of perturbative corrections, but also the use of a very diffuse atomic basis and a larger CAS including orbitals which are

responsible for the main configurations of these states (see e.g. [114]). The use of a very diffuse basis set leads to the need for a large value of the R-matrix radius and in turn to large demands on the quality of representation of the continuum which our current codes cannot provide. For this reason we have not been able to use very diffuse basis sets in our calculations.

Even though our calculations suffer from the limitations associated with the quality of description of the electronically excited states, we are confident that the main results of this work (characterization of many new resonances in diazines) are valid. This claim is supported by the fact that the observable quantities (elastic and inelastic cross sections for pyrimidine) are in a good agreement with experiment. These facts lead us to the conclusion that the scattering models and methods of analysis of the results presented are robust enough to be considered for use in scattering calculations on different target molecules.

Chapter 5

Electron collisions with oxygen containing substituted pyrimidines

In this chapter we present the results of the calculations for the last set of molecules studied in this work. We study the oxygen containing pyrimidines (see Figure 5.1) 2-oxo pyrimidine, 4-oxo pyrimidine and uracil. The first two molecules (oxo-pyrimidines) contain one oxygen atom in positions 2 and 4 respectively. We can think of them as obtained from pyrimidine by replacing with oxygen one hydrogen atom attached to the ring and attaching one hydrogen to one of the nitrogen atoms. Uracil contains two oxygens in positions 2 and 4 and is the nucleobase which replaces thymine in RNA. It is obvious that uracil has, from the molecules studied in this work, the closest relationship to the DNA nucleobases. We will investigate electron collisions with the oxo-pyrimidines and uracil and compare the results with those

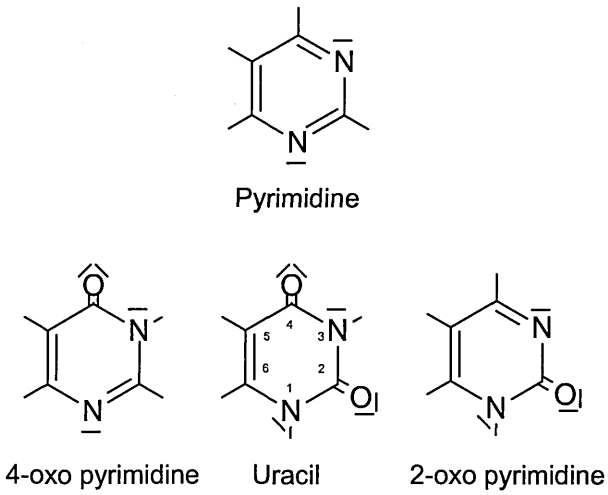

Figure 5.1: Chemical structures of the oxo-pyrimidines, uracil and comparison with pyrimidine. The green lines denote pairs of non-bonding electrons. All oxo-pyrimidines belong to the C_s point group. The numbering of the atoms of the ring is exemplified on uracil.

obtained for pyrimidine: this will allow us to study the effects the oxygen atoms have on the scattering process. However, the aim of the work presented here is not to provide results of the best quality, but to produce results on a level sufficient for comparison of the resonances found in these molecules with those found in diazines. Therefore, the results of this chapter are less accurate and thus more speculative than the ones obtained in the previous chapters.

As mentioned several times throughought this work, Dora et al. [59] already used the R-matrix method to perform SEP and CC (using the *full* model) calculations on uracil. However, the results of these calculations were not analyzed using the powerful time-delay method used by us and not surprisingly, as we will see below, they did not reveal the presence of all resonances in this system. It is for this reason that we performed the scattering calculations for uracil. Additionally, we found that due to the limitations of the UKRmol code, the calculations of Dora et al. for the outer region did not fully take into account the dipole moment of the molecule. This problem seems to lead to the disappearance of some Feshbach resonances which we then found in our calculations.

Based on the experience gained in the previous chapters we perform the target and the scattering calculations for the three molecules using the models of the type used for the diazines. The diazine molecules possess 42 electrons. The two oxo-pyrimidines and uracil have 50 and 58 electrons respectively and possess C_s symmetry. The larger number of electrons in these molecules and the lower (point-group) symmetry significantly increases the computational time of the scattering calculations when compared with the diazine molecules. This is especially true for the Close-Coupling calculations. For this reason, we did not perform the CC calculations using the full model. Instead, we limited the size of the calculation to what can be run on our best desktop computer and we used only the Simplified model (see Section 3.6.1). This model gives resonances that are too high in energy. However, as demonstrated in earlier chapters, it allows us to find all resonances in these systems and elucidate their character. Using these results we were able to compare resonances in the oxo-pyrimidines and uracil with those found in pyrimidine.

The layout of this chapter is as follows. In Section 5.1 we review the literature on uracil and electron-uracil collisions and in Section 5.2 we describe the target models used for the three molecules. To the best of our knowledge there are no studies of electron collisions with the oxo-pyrimidines. Therefore we do not have any data to compare our results with. We have not found any studies discussing electronically excited states of the oxo-pyrimidines either. The parameters of the scattering calculations are described in Section 5.3. The results of our SEP calculations for the three molecules are described in Section 5.3.1. We then continue, in

Section 5.3.2, with the presentation of the results of the Close-Coupling calculations. Finally, in Section 5.4, we compare the resonances found in the oxo-pyrimidines and uracil with those found in pyrimidine. Section 5.6 summarizes our findings.

5.1 Low-energy electron collisions with uracil

Uracil has been studied extensively using a range of experimental and theoretical methods. Here we restrict ourselves to mention only the most important results relevant for our work (see Section 1.3 for a more detailed discussion of the available literature).

The electron attachment energies of uracil were measured first by Aflatooni et al. [30] and revealed the presence of three low-lying π^* resonances at energies 0.23 eV, 1.58 eV and 3.83 eV. The measurements of Scheer et al. [31] using the same technique confirmed these parameters. These resonances are analogues of the three π^* resonances in diazines and originate in the aromatic character of the uracil ring. At higher energies (below $\approx$ 10.5 eV) measurements of the dissociative electron attachment (DEA) spectra [40, 47, 136, 137] suggest the presence of a number of higher-lying resonances responsible for the various detected fragments of the target molecule: the total DEA cross section shows peaks at $5, 6.2, 6.9, 9.5$ eV [40]. For low-electron energies the DEA measurements show peaks in the ion yield at $0.7, 1.01$ eV (associated with Vibrational Feshbach resonances) and at $1.48, 1.72$ eV (associated with the second π^* resonance), see Section 1.3 for details.

Recently, electron impact electronic excitation of the lowest-lying states of uracil were measured by Chernyshova et al. [138]. The measurements revealed features in the excitation spectra at 3.75 eV, 4.76 eV and 6.8 eV, which were interpreted as arising from excitations, respectively, of the electronic states $1^3A'$, $1^3A''$ and $2^1A'$. The first of these features lies close to the third π^* resonance which is therefore assumed to have a significant influence on the corresponding excitation cross section. The study of Chernyshova et al. also compares data on the experimental and calculated lowest-lying vertical excitation energies of uracil and it is therefore our main source for these values.

Electron collisions with uracil were also investigated theoretically. Calculations of elastic electron collisions with this target were performed by Gianturco et al. [53, 54], Grandi et al. [55], Winstead and McKoy [56] and others [58, 101]. All these studies confirm the presence of the three π^* resonances in this system. Grandi et al. also found a higher-lying (around 9.07 eV) shape resonance. Winstead and McKoy reported electron impact electronic excitation cross sections for this molecule. Dora et al. [59] used the R-matrix method to study elastic and

inelastic electron collisions with uracil. In addition to the three π^* resonances, Dora et al. found three narrow resonances of A′ symmetry at energies 6.17 eV, 7.62 eV and 8.12 eV which they interpreted as Feshbach resonances.

5.2 Target description

Although, to the best of our knowledge, there are no studies of the electronic spectrum of the two oxo-pyrimidines, 4-oxo pyrimidine [139, 140, 141, 142] and 2-oxo pyrimidine [143, 144, 145, 146] have been studied in connection with their tautomeric forms. For 4-oxo pyrimidine Sanchez et al. [139] report the experimental and theoretical values for the dipole moment of the molecule. Hydrogen-bonded water-2-oxo pyrimidine clusters [147, 148, 149] have been studied.

Uracil is the only molecule studied in this chapter for which calculations and experiments on the electronic spectrum are available. We compare our values of the vertical excitation energies of uracil with the results of the recent studies of Silva-Junior et al. [150] who used the CASPT2 theory to calculate singlet electronically excited states of uracil and Epifanovsky et al. [151] who used the Equation of Motion Coupled-Cluster method. Fleig et al. [152] studied electronic spectra of all nucleobases using the Coupled-Cluster method. Petke et al. [153] and Lorentzon et al. [154] studied the spectrum of uracil earlier. We also utilize the experimental values of the vertical excitation energies measured by Chernyshova et al. [138]. The experimentally determined ionization energy of uracil is 9.5 eV [117], which is similar to that of the three diazines. Consequently, we expect the two oxo-pyrimidines to possess a similar ionization energy.

For all three molecules we performed target calculations at the HF and the SA-CASSCF levels of approximation. Our target calculations for uracil used exactly the same model (see below) as Dora et al. We also used these models as a template for our target calculations for the two oxo-pyrimidine molecules and therefore the target calculations for all three molecules possess a number of similar characteristics.

We used the cc-pVDZ ("compact") target basis set. This basis set was used by Dora et al. for uracil and was also found sufficient, by us, for the description of all resonances lying below their ionization thresholds in the diazines. Therefore we expect it to perform similarly well for the three molecules studied in this chapter. For uracil we used the (planar) geometry optimized by Schreiber et al. [121]. The geometries of the two oxo-pyrimidines were optimized by us using MOLPRO and the basis set cc-pVDZ at the level of the second-order

	2-oxo pyrimidine		4-oxo pyrimidine		Uracil	
Basis set	Calc.	Acc. value	Calc.	Acc. value	Calc.	Acc. value
HF [H]	−337.587	–	−337.595	−339.570	−412.502	−414.107
SA-CASSCF [H]	−337.655		−337.663		−412.563	
μ_{HF} [D]	6.65	–	2.87	2.22	4.93	4.33
$\mu_{SA-CASSCF}$ [D]	5.46		1.71		4.06	
g.s. configuration	$1-21a'^{42},1-4a''^{8}$		$1-21a'^{42},1-4a''^{8}$		$1-24a'^{48},1-5a''^{10}$	
CAS orbitals	$19-21a',1-7a''$		$19-21a',1-7a''$		$23-24a',1-8a''$	

Table 5.1: Ground state properties of 2-oxo pyrimidine, 4-oxo pyrimidine and uracil calculated at the HF-SCF and SA-CASSCF levels, using the basis set cc-pVDZ. The ground state configuration of each molecule and the orbitals forming the active space in the CASSCF calculations (for simplicity, the orbitals are not listed in energy order) are also tabulated. For 4-oxo pyrimidine we list the experimental value of Sanchez et al. [139] for the ground state dipole moment and an accurate value of the ground state energy obtained using DFT theory (ibid.). For uracil we include the accurate theoretical values of Silva-Junior et al. [150] obtained using the CASPT2 method.

Møller-Plesset perturbation theory (MP2). We forced the planar geometries of both molecules during the optimization step. The geometries so obtained are detailed in Appendix C.

For the SA-CASSCF calculations on uracil, following Dora et al., we used the active space $(14, 10)$, i.e. 14 electrons distributed among 10 orbitals. The active space comprised all 8 π orbitals and the two non-bonding σ orbitals on the oxygen atoms (see Figure 5.1). All π orbitals were of valence character.

The active space for the two oxo-pyrimidines was chosen to have a similar size. It was, for both molecules, of the type $(14, 10)$ including all 7 π orbitals and 3 σ orbitals. The σ orbitals correspond to the highest-lying non-bonding orbitals on the oxygen atom and the two nitrogens. A $(12, 9)$ active space was also tested for 2-oxo pyrimidine; no significant differences were observed in the results.

The averaging scheme used for the SA-CASSCF calculations for all three molecules was very similar to the one used by Dora et al, who included 16 states: 4 states of each spin and space symmetry. In our calculations we choose to include 17 states, i.e. 4 excited states of each spin and space symmetry and the ground state. This averaging scheme is identical to the one used for pyrimidine and pyridazine. For uracil the differences between the VE energies, dipole moment and the ground state energy obtained by our averaging scheme and the values of Dora et al. are completely negligible.

Table 5.1 contains the calculated ground state properties of the three molecules and, where available, comparison with accurate experimental or theoretical values. There is strong evidence from theoretical calculations that uracil possesses a large dipole moment between

4 – 5 D [153, 154, 155]. This value is in accord with our HF and CASSCF calculations which both give dipole moment > 4 D in reasonable agreement with the accurate value 4.33 D. Interestingly, the measurements of the dipole moment inferred from the microwave spectra of uracil report a smaller value: 3.87 D [156]. The dipole moment of 4-oxo pyrimidine is smaller than that of uracil and the value obtained using the CASSCF method is in a fair agreement with the experimental value 2.22 D. We can see that for both molecules, uracil and 4-oxo pyrimidine, the HF values of the dipole moment overestimate and the CASSCF ones underestimate the accurate values. Nevertheless, the CASSCF values are in a better agreement with the accurate ones. To the best of our knowledge an accurate value (either experimental or theoretical) for the dipole moment of 2-oxo pyrimidine has not been determined so far. However, given the fact that for the two previous molecules the accurate value lies within the range delimited by the HF and the CASSCF values, we estimate that the accurate value of the dipole moment for 2-oxo pyrimidine molecule is $\approx$ 6 D.

In Table 5.2 we list the electronic states of all three molecules included in our CC calculations. For uracil we include, as recommended by Dora et al., the 32 lowest-lying electronic states. This means including all states up to the VE energy of 11.17 eV. In the case of the 2-oxo pyrimidine we include all states up to VE energy of 10.42 eV, i.e. 31 states. Finally, for the 4-oxo pyrimidine we include all states up to the VE energy of 11.45 eV, i.e. 40 states. We can see that our calculated VE energies for uracil are in a very good agreement with the available experimental data up to the 8th state. For the higher-lying states the agreement is significantly worse (the differences reach several electronvolts) and is similar to the agreement reached for the diazines (see Table 4.7). Uracil (and probably the two oxo-pyrimidines as well) is known to possess Rydberg states, which we cannot represent accurately using our target model; therefore these states probably lie too high in energy in our calculations. For this reason we do not list in Table 5.2 the value 6.01 eV which in the calculations of Epifanovsky et al. [151] corresponds to $2^1A''$ Rydberg state: we cannot determine which of our A'' states might correspond to this state. In general the quality of representation of the excited states of uracil is similar to the one obtained for the diazine molecules and therefore the same comments as in Section 4.5 can be made in its regard.

It is known that uracil, like the diazines, possesses states (of singlet A′ symmetry) with large oscillator strengths. Silva-Junior et al [150] report the oscillator strengths and found that the three largest correspond, in their calculations, to the states $2^1A'$, $4^1A'$ and $5^1A'$. However, the relative magnitudes of the oscillator strengths of these states differ depending on the basis set used. In our calculations we found 4 states with dipole transition moments

No	Uracil					2-oxo pyrimidine		4-oxo pyrimidine	
	VE energy [eV]				Sym.	VE energy [eV]	Sym.	VE energy [eV]	Sym.
	Calc.	[138]	[151]	[150]		Calc.		Calc.	
1	3.86	3.75	3.87		$1^3A'$	3.14	$1^3A'$	3.40	$1\ ^3A'$
2	4.75	4.76	4.95		$1^3A''$	4.17	$1^3A''$	4.81	$2\ ^3A'$
3	4.92	5.2	5.22	4.91	$1^1A''$	4.44	$1^1A''$	4.84	$1\ ^3A''$
4	5.49				$2^3A'$	4.77	$2^3A'$	5.00	$1\ ^1A''$
5	6.28				$2^3A''$	4.81	$2^1A'$	5.25	$2\ ^1A'$
6	6.35				$3^3A'$	4.84	$2^3A''$	5.59	$2\ ^3A''$
7	6.47	6.54	6.57	6.28	$2^1A''$	5.01	$2^1A''$	5.75	$3\ ^3A'$
8	6.59	5.5	5.58	5.23	$2^1A'$	5.62	$3^3A'$	5.85	$2\ ^1A''$
9	7.01	6.8	6.72	6.15	$3^1A'$	5.93	$3^3A''$	6.20	$3\ ^3A''$
10	7.70				$4^3A'$	6.05	$3^1A''$	6.30	$3\ ^1A''$
11	7.78				$3^3A''$	6.44	$3^1A'$	6.66	$3\ ^1A'$
12	7.89			6.98	$3^1A''$	6.93	$4^3A'$	7.32	$4\ ^3A''$
13	7.94				$4^3A''$	7.30	$4^3A''$	7.35	$4\ ^3A'$
14	7.96				$4^1A''$	7.35	$4^1A''$	7.77	$4\ ^1A''$
15	8.56				$5^3A'$	7.67	$5^3A'$	8.02	$5\ ^3A'$
16	8.76	6.6 [157]		6.74	$4^1A'$	8.04	$4^1A'$	8.12	$6\ ^3A'$
17	9.24				$5^1A'$	8.21	$6^3A'$	8.17	$4\ ^1A'$
18	9.25				$6^3A'$	8.52	$5^1A'$	8.96	$5\ ^1A'$
19	9.35				$7^3A'$	9.08	$5^3A''$	9.34	$5\ ^3A''$
20	9.56	6.9-7.0 [157]		7.42	$6^1A'$	9.11	$6^3A''$	9.38	$6\ ^1A'$
21	10.13				$5^3A''$	9.18	$6^1A'$	9.42	$5\ ^1A''$
22	10.17				$6^3A''$	9.19	$5^1A''$	9.55	$6\ ^3A''$
23	10.21				$5^1A''$	9.41	$7^3A''$	9.79	$7\ ^3A''$
24	10.31				$7^1A'$	9.59	$6^1A''$	9.79	$7\ ^1A'$
25	10.45				$8^3A'$	9.68	$8^3A''$	9.93	$7\ ^3A'$
26	10.48				$7^3A''$	9.78	$7^3A'$	10.01	$6\ ^1A''$
27	10.59				$6^1A''$	9.89	$7^1A'$	10.08	$8\ ^3A''$
28	10.64				$8^3A''$	10.20	$8^3A'$	10.19	$8\ ^3A'$
29	10.76				$8^1A'$	10.39	$8^1A'$	10.31	$9\ ^3A'$
30	10.93				$9^3A'$	10.42	$7^1A''$	10.54	$8\ ^1A'$
31	11.17				$9^3A''$			10.56	$10^3A'$
32								10.67	$11^3A'$
33								10.68	$12^3A'$
34								10.83	$9\ ^1A'$
35								10.85	$9\ ^3A''$
36								10.90	$10^1A'$
37								10.97	$10^3A''$
38								11.15	$7\ ^1A''$
39								11.46	$11^3A''$

Table 5.2: Electronic excited states included in the Close-Coupling calculations for uracil, 2-oxo pyrimidine and 4-oxo pyrimidine together with their vertical excitation (VE) energies. The values labelled 'Calc.' correspond to our SA-CASSCF calculations using the cc-pVDZ basis set. For uracil the experimental results correspond to those of Chernyshova et al. [138] and Clark et al. [157]. We also list the results of the calculations of Epifanovsky et al. [151] and Silva-Junior et al. [150].

with the ground state larger than 2.2 a.u.: $2^1A'$, $4^1A'$, $6^1A'$, $7^1A'$. We assume that three of these states correspond to the three states of Silva-Junior et al. However, the exact mapping between our states and the states of Silva-Junior et al. differs depending on the criterion used for the assignment: the energy order of the states or their oscillator strengths (transition moments). In Table 5.2 the assignment was made using the energy order of the states, but as explained, this assignment is only tentative.

5.3 Scattering calculations

The choice of parameters for the scattering calculations was again based on the work of Dora et al. for uracil. Namely, the R-matrix radius was set to $13a_0$ and the continuum basis set optimized for this radius was used. The R-matrix radius and the continuum basis set were the same as the ones used for the scattering calculations for diazines which used the compact (cc-pVDZ) atomic basis set.

For the SEP calculations we used the HF target orbitals, the CC calculations used the SA-CASSCF target orbitals. As in the previous chapters, the continuum orbitals for each of these calculations were Schmidt orthogonalized to the orbitals of the target (see e.g. Sections 2.7 and 3.4 for details of this process). For all molecules and all calculations the deletion thresholds were set to the value 1.10^{-7}. This is the same choice as for the diazine calculations using the compact atomic basis set.

The SEP scattering model was described in detail in Section 2.6.2. The number of virtual orbitals used in calculations for each of the molecules is specified in the next section. For the reasons explained above, we did not perform the CC calculations using the full CC model (see Section 2.6.3). Instead, we used the Simplified CC model as described in Section 3.6.1. In Section 5.3.2 below, we will describe how we expect our results derived from the Simplified CC model to change when the full CC model is used.

5.3.1 SEP cross sections and the π^* resonances

In this section we focus on the description of the main features of the collisions with oxo-pyrimidines and uracil. For this task we use the results of our SEP calculations, the lowest-level calculations performed for the three molecules studied here.

As we will see below, the SEP calculations reveal again the presence of the three low-lying π^* resonances, which are characteristic for molecules of this type. At higher energies (above the first excitation threshold) these calculations display pseudo-resonances (see Section 2.6.2)

in the cross sections and eigenphase sums which do not allow us to provide reliable information on the physical resonances that appear, as we will see later, in this energy region. This problem is removed in the CC calculations which do not display pseudoresonances in the energy region of our interest (i.e. up to about $\approx$ 10 eV). Nonetheless, the SEP calculations have one important advantage over the CC calculations presented below: in order to keep the computational demands of the CC calculations manageable we choose to use the Simplified CC model which describes the correlation/polarization effects at a lower level than the SEP calculations presented in this section. This leads to the SEP model providing parameters for the low-lying π^* resonances and cross sections which we expect to be in better agreement with experimental data than the results of the Simplified CC model.

The SEP models of our type suffer from the fact that they are not converged with respect to their size, i.e. it is not a priori clear what is the optimal number of virtual orbitals to include in the calculation. In the case of the diazines we were guided in the choice of the number of virtual orbitals by the experimental values of the positions of the low-lying π^* resonances (see Section 4.8.2). For uracil we can utilize the experimental positions of the π^* resonances measured by Aflatooni et al. [30] and therefore we choose the number of virtual orbitals in the SEP model such that the calculated positions of the three π^* resonances are in optimal agreement (as defined in Section 3.4) with the experimental ones. In the case of the oxo-pyrimidines we do not have any experimental data on the resonances to compare with and therefore the choice of the number of virtuals for the SEP model becomes rather arbitrary. However, comparing the experimental values of the positions for the three π^* resonances in pyrimidine and uracil, we can see that these do not differ dramatically. Therefore in order to construct SEP models for the two oxo-pyrimidines we assume the following:

- The positions of the π^* resonances in the oxo-pyrimidines do not change significantly when compared with pyrimidine and uracil, so that these lie approximately within the range determined by Nenner and Schulz [32] for pyrimidine.

- The lowest-lying π^* resonance is indeed a resonant state and not a bound state (see Section 3.1), i.e. it lies in our (fixed-nuclei) calculations above the threshold for elastic scattering.

In constructing the models we also utilize the fact that, the larger the magnitude of the dipole moment of the molecule, the smaller the number of virtual orbitals needed in the SEP model (see Section 4.6). Based on this principle we expect that for 2-oxo pyrimidine

Pyrimidine	2-oxo pyrimidine	4-oxo pyrimidine	Uracil
25	20	25	30

Table 5.3: Number of virtual orbitals used for the SEP calculations employing the compact basis set in scattering calculations on pyrimdine, uracil, 2-oxo pyrimidine and 4-oxo pyrimidine.

the number of virtual orbitals will not be larger than for uracil whose ground state dipole moment is smaller than that of 2-oxo pyrimidine.

The results of the SEP calculations of Dora et al. for uracil show that using $15 - 18$ virtual orbitals per symmetry (i.e. $30 - 36$ virtual orbitals in total) gives positions of the π^* resonances in an acceptable agreement with the experimental data: a larger number of virtuals causes the lowest-lying resonance to disappear below the threshold. We chose to use the 30 lowest-lying virtual orbitals in our SEP calculations. Based on the points made above, we chose 20 virtuals for the SEP calculations for 2-oxo pyrimidine and 25 virtuals for the 4-oxo pyrimidine. Table 5.3 compares the number of virtual orbitals used in the SEP calculations for pyrimidine (using the compact basis set), the oxo-pyrimidines and uracil. As we can see, the number of virtual orbitals in the calculation for 2-oxo pyrimidine is the smallest, in agreement with the principle stated above. (In a test calculation using 25 virtual orbitals, the lowest-lying π^* resonance of 2-oxo pyrimidine disappears below the threshold).

Figure 5.2 shows our calculated elastic cross sections. All sharp structures in the A' and A'' symmetries above ≈ 8 eV and ≈ 6 eV respectively are caused by pseudoresonances. The low-energy cross sections follow the expected behaviour, namely the cross section for 2-oxo pyrimidine (possessing the largest dipole moment) is the largest one, followed by uracil, 4-oxo pyrimidine and finally pyrimidine. All π^* resonances are clearly visible even in the summed integral cross section in the bottom panel except for the lowest-lying π^* resonance of 2-oxo pyrimidine that is largely hidden by the strong dipolar character of the cross section and is therefore barely visible as a small dent in the summed integral cross section.

The cross sections for A' symmetry for uracil and 4-oxo pyrimidine show clearly broad peaks around or just above 7 eV which we might be tempted to assign to resonances. However, we cannot draw definitive conclusions on the presence of higher-lying resonances from the results of the SEP calculations (see Section 2.6.2). Nevertheless, in Section 5.3.2 we investigate in detail a broad resonance lying above 11 eV in the CC results of the full model for pyrimidine and provide strong evidence that the A' resonances in uracil and 4-oxo pyrimidine are very probably equivalents of this pyrimidine resonance which appears to have exclusively shape character. The A' cross section for 2-oxo pyrimidine does not show a clear peak at

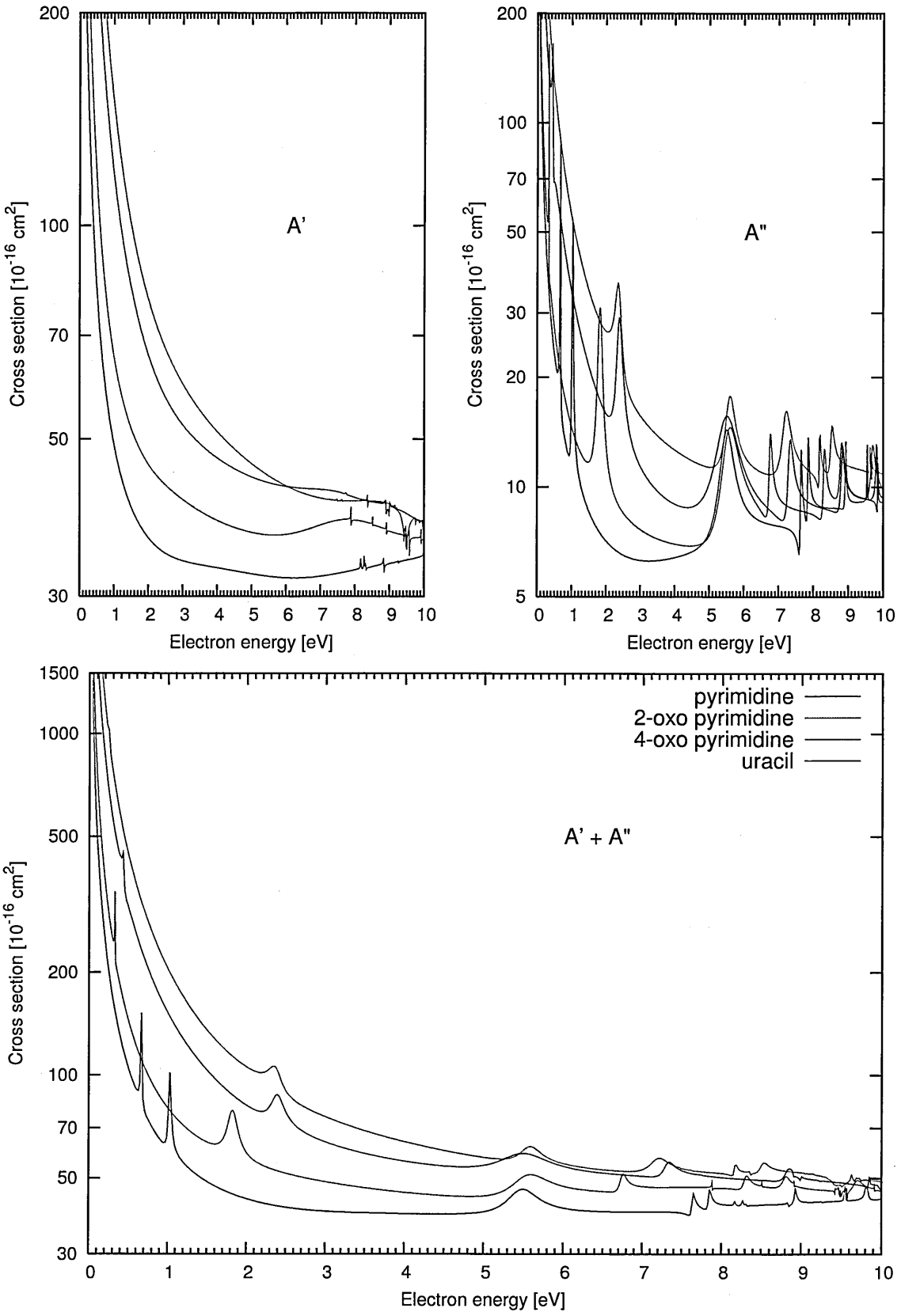

Figure 5.2: Integral elastic cross sections for 2-oxo and 4-oxo pyrimidines, uracil and pyrimidine calculated at the SEP level using the compact basis set. The upper panels show the A′ and the A″ contributions to the cross section. The bottom panel shows the summed integral cross sections. No Born correction has been added to these cross sections.

Resonance	π_1^*	π_2^*	π_3^*
Pyrimidine			
Symmetry	$^2A_2$	$^2B_1$	$^2B_1$
Calculation	0.68	1.033	5.479
	(0.015)	(0.034)	(0.468)
Experiment [32]	$0.25 - 0.7$	$0.77 - 1.6$	≈ 4.24
2-oxo pyrimidine			
Symmetry	$1^2A''$	$2^2A''$	$3^2A''$
Calculation	0.25	2.373	5.571
	(0.005)	(0.208)	(0.333)
4-oxo pyrimidine			
Symmetry	$1^2A''$	$2^2A''$	$3^2A''$
Calculation	0.33	1.822	5.531
	(0.006)	(0.160)	(0.572)
Uracil			
Symmetry	$1^2A''$	$2^2A''$	$3^2A''$
Calculation	0.44	2.384	5.467
	(0.024)	(0.202)	(0.769)
Experiment [30]	0.22	1.58	3.83

Table 5.4: Positions and widths in brackets (in eV) of the low-lying π^* shape resonances in pyrimidine, 2-oxo pyrimidine, 4-oxo pyrimidine and uracil calculated at the SEP level using the compact (cc-pVDZ) basis set. Also listed are experimental positions of the π^* resonances in pyrimidine and uracil as determined by Nenner and Schulz [32] and Aflatooni et al. [30] respectively.

higher energies, but rather a through around 9.5 eV, which might actually be caused by a pseudoresonance. Therefore, we cannot ascertain whether a similar shape resonance appears also in 2-oxo pyrimidine.

As mentioned above we cannot estimate, due to the lack of experimental data for the two oxo-pyrimidines, how close to the accurate values the calculated parameters of the π^* resonances are. Nevertheless, Figure 5.2 suggests that the position of the second lowest-lying resonance in the oxo-pyrimidines and in uracil is affected when compared with pyrimidine and that the third resonance remains at approximately the same position in all molecules. In Table 5.4 we list the positions and the widths of the low-lying π^* resonances in the three molecules and in pyrimidine as determined by the Breit-Wigner fits to the SEP eigenphase sums. Also included in the Table are the available experimental positions of the resonances in pyrimidine and uracil.

Since we cannot ascertain with confidence from the calculated data how the π^* resonances are affected by the presence of the oxygen atoms in the target molecule we turn to the experimental values which might provide the answer. It is not clear from the comparison of the experimental values for pyrimidine and uracil how the positions of the two lowest-lying resonances in these molecules differ: both resonances in uracil fall within the range of the

corresponding resonance in pyrimidine as given by Nenner and Schulz [32]. Nevertheless, the positions of the first and the second uracil resonances are, respectively, on the lower and the upper limit of the first and the second pyrimidine resonance. The calculated positions of the uracil and the oxo-pyrimidine resonances give the same qualitative picture: the lowest-lying resonance in both molecules is lower in energy than the corresponding resonance in pyrimidine and the second resonance is always higher in energy than the second resonance in pyrimidine. Furthermore, we can infer from the Table that if we were to lower (by using more virtual orbitals in the SEP calculation) the position of the second π^* resonance in the three molecules, so that it falls within the range determined for pyrimidine, the first π^* resonance would disappear below the threshold. That is, we would violate the assumption that the first π^* state in the oxo-pyrimidines is a resonant state. It follows that if our assumption is correct then our calculations indicate that the presence of oxygen atoms attached to the ring affects the positions of the two lowest-lying π^* resonances. We can see that despite the fact that our calculations possess significant uncertainty and cannot provide a definitive answer they indicate that the presence of *at least one oxygen atom* attached to the pyrimidine ring might lead to significant perturbations in the parameters of the two lowest-lying π^* resonances.

The third π^* resonance is not significantly affected by the presence of the oxygen atoms in the target molecule, probably because it lies at a higher energy: we can speculate that at these energies the sensitivity of the scattering electron to perturbations of the correlation/polarization effects caused by the oxygen atoms might be smaller than at low energies, where the two lowest-lying resonances are formed. This behaviour would be consistent with the general properties of the short-range electron-molecule interaction effects (see Appendix B).

Perhaps a more direct way of elucidating the differences in the π^* shape resonances in the four molecules lies in comparing the shapes of the virtual orbitals responsible for their formation. These orbitals are shown in Figure 5.3. Since we would like to understand the effects the oxygen atoms attached to the pyrimidine ring have on the formation of resonances, we first focus on the shapes of the π^* orbitals in pyrimidine. We can see that the first π^* orbital is characterized by a density located on four atoms of the ring with a nodal plane passing in between two pairs of atoms. The second orbital is characterized by the density localized largely on the two carbon atoms that are opposite each other. Finally, the third π^* orbital of pyrimidine is rather delocalized over the whole ring of the molecule with nodal planes perpendicular to the bonds of the aromatic ring. For pyrimidine we also calculated the orbital densities of the three π^* orbitals using the diffuse basis set and found that those

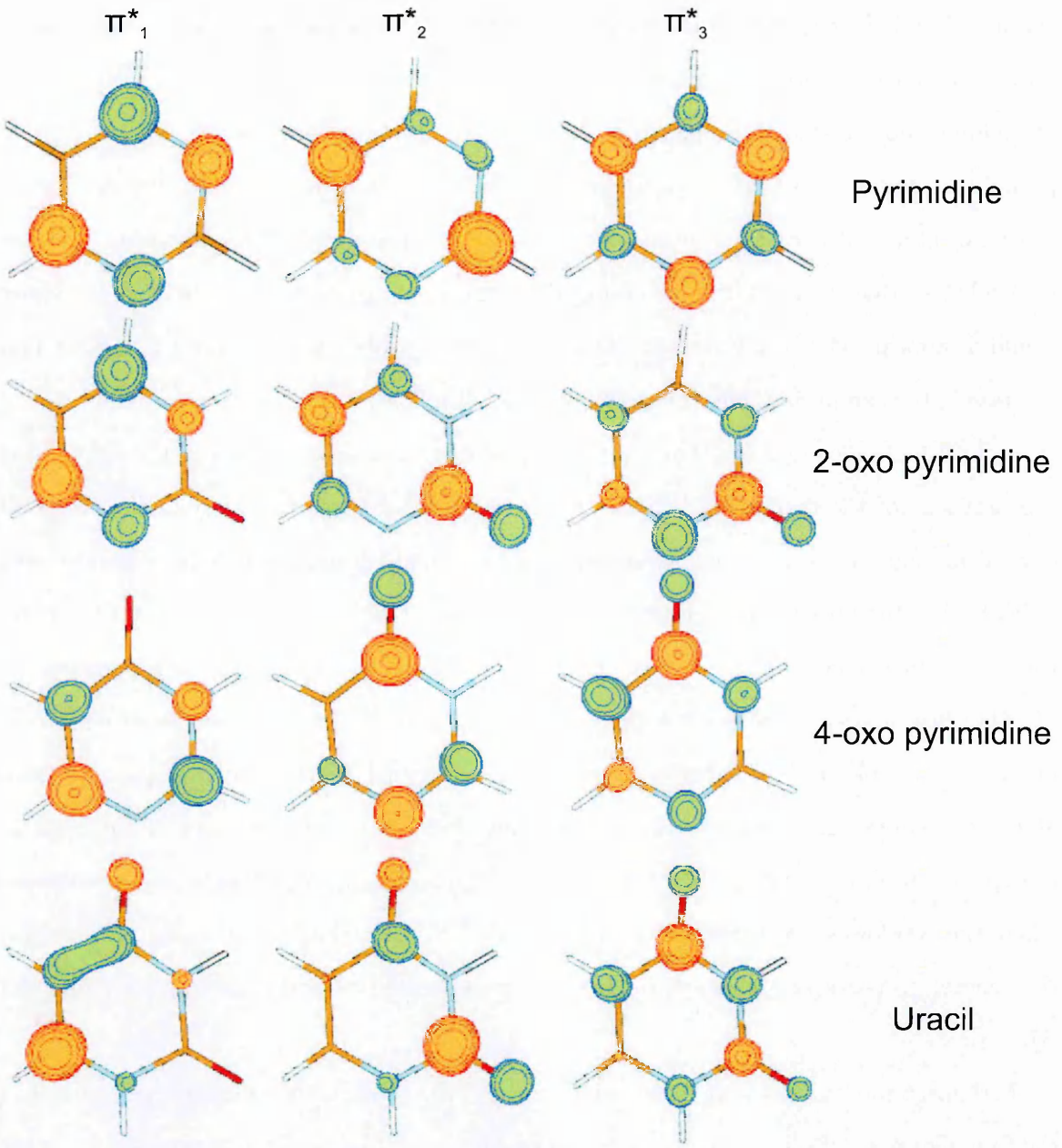

Figure 5.3: The three lowest-lying π^* virtual orbitals of pyrimidine, 2-oxo pyrimidine, 4-oxo pyrimidine and uracil calculated at the HF level responsible for the formation of the three lowest-lying π^* resonances in these targets. The shapes of the orbitals were obtained using MOLDEN [94] by calculating the isosurface of the electron density with contour value 0.1. The wireframe model of the molecules is shown as well: blue - nitrogen atoms, orange - carbons, red - oxygens and white - hydrogen atoms. The positive and the negative values of the charge density are distinguished by the orange and green colours. Note these have only relative meaning since the orbitals are determined uniquely only up to an overall phase factor of -1.

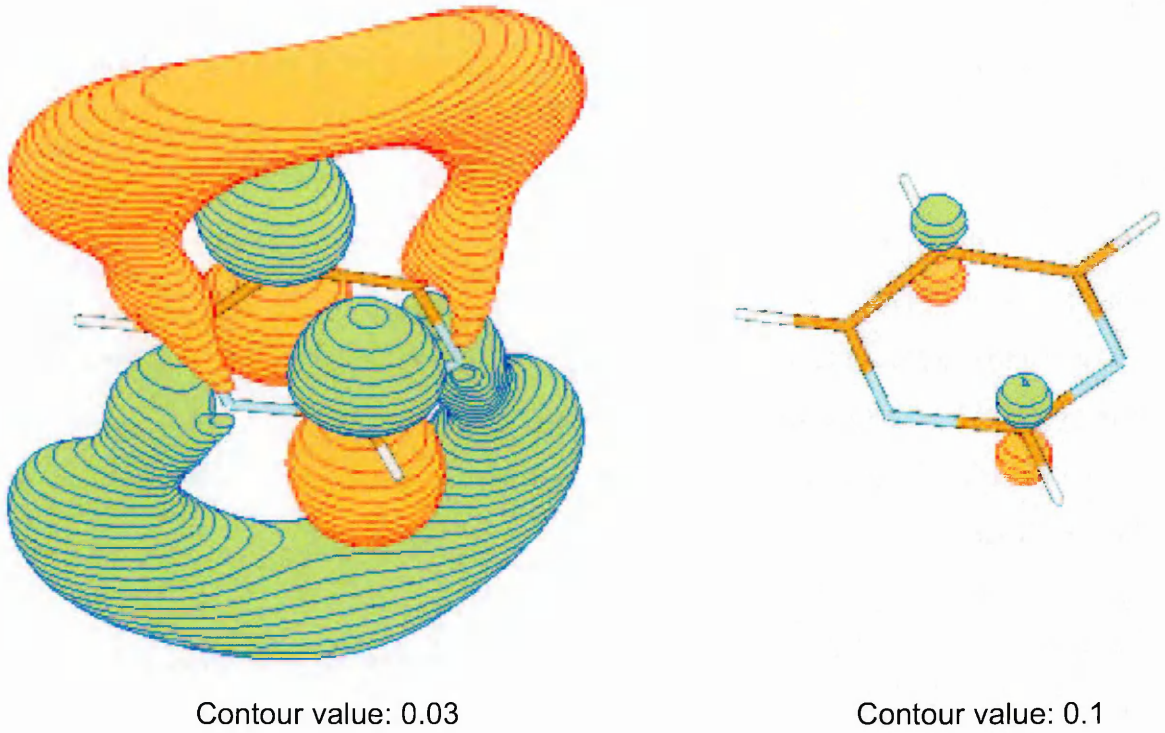

Figure 5.4: The third lowest-lying π^* virtual orbital of pyrimidine calculated at the HF level using the diffuse basis set. The shape of the orbital was obtained using MOLDEN [94] by calculating the isosurface of the electron density with contour value 0.03 (left) and 0.1 (right). The wireframe model of the molecule is shown as well. Blue - nitrogen atoms, orange - carbons, red - oxygens and white - hydrogen atoms.

of the two lowest-lying π^* orbitals do not change significantly. The third π^* orbital, shown on Figure 5.4, develops a large lobe above (and below) the plane of the molecule: some of the density located in the vicinity of the ring in the calculation using the compact basis set gets transferred further away from the plane of the molecule when the diffuse basis set is used. The orbital obtained using the compact basis set does not possess (even for lower contour values) the lobes seen for the orbital calculated using the diffuse basis set. Even though the shapes of this orbital calculated in the two basis sets are somewhat different, the main, delocalized, character of this orbital remains the same in both calculations.

The orbitals of pyrimidine, see again Figure 5.3, possess the C_{2v} symmetry: in addition to the plane of symmetry defined by the plane in which the molecule lies, another plane of symmetry passes in between the two nitrogens and through the two opposite carbons perpendicularly to the first plane. Addition of one or two oxygens to the molecule breaks the second symmetry. However, we can see from the shapes of the two oxo-pyrimidine's orbitals that the extra oxygen atom attached to the ring tends to perturb the original pyrimidine orbitals so that they retain an approximate plane of symmetry (perpendicular to the ring) defined by the oxygen-carbon bond. In other words, the extra oxygen atom acts as if trying

to preserve the symmetry of the corresponding pyrimidine orbitals. This effect is translated in 4-oxo pyrimidine into a "rotation" of the orbital density by $\pi/3$ radians clockwise when compared with the density of the corresponding orbitals of pyrimidine. In 2-oxo pyrimidine the perturbation of the shapes of the densities of the first two π^* orbitals when compared with pyrimidine is rather small, because in this case the pseudosymmetry plane is almost the same as the symmetry plane of pyrimidine.

In uracil the combined effect of the two oxygens attached to the ring results in the density of the first two π^* orbitals being localized mainly in the vicinity of the oxygen atoms and some of the carbons: the density located on the nitrogen atoms is very small when compared with pyrimidine.

Except for the additional density on the oxygens, the third π^* orbital in all four molecules seems to have a rather unperturbed, delocalized, character which is not significantly altered by the presence of the oxygen atoms. However, in the two oxo-pyrimidines we can again observe the approximate "symmetrization" effect of the oxygen atom on the density of this orbital. Apart from this, the most significant effect of the oxygen atoms on the third π^* orbital lies in removing the density located on one of the carbon atoms.

We can summarize our findings by saying that the densities of the two lowest-lying π^* orbitals in uracil and the two oxo-pyrimidines are significantly affected by the presence of the oxygen atoms, whereas the main property (delocalization) of the third π^* orbital is preserved in all molecules. These differences in the orbital densities when compared with the pyrimidine orbitals may partly explain the differences and similarities between the positions of the two lowest-lying π^* resonances in pyrimidine and the three oxygen containing pyrimidines.

5.3.2 CC calculations: an analysis of the Simplified model

In the previous chapter the CC calculations aimed to produce cross sections and determine parameters of resonances (obtained from the time-delays) for all diazines that would be accurate enough to be suitable for comparison with experiment. In this chapter the purpose of the CC calculations is rather different. We perform the CC calculations *only using the Simplified model.* Therefore the cross-sections derived from the results of the CC calculations presented in this chapter are less appropriate for comparison with the experiment.

However, as we showed in the previous chapters, the Simplified CC model still has considerable predictive power when it comes to finding and characterizing the resonances, while keeping the computational demand of the calculations reasonable. Consequently, as men-

tioned already at the beginning of this Chapter, the only purpose of performing the CC calculations using the Simplified model for uracil and the two oxo-pyrimidines was to find and characterize resonances formed in electron collisions with these targets and compare the results for these systems and with pyrimidine.

Before we describe the results of the CC calculations for the oxygen containing pyrimidines, it is important to describe in a greater detail the properties and limits of the Simplified CC model and how we expect our results would change (at least approximately) if the full CC model was used instead. In Section 3.6 we have already demonstrated the consistency of the Simplified and the full models in characterizing all resonances in the system. However, here we are more interested in quantitative differences in the calculated cross sections and resonances since we cannot determine more accurate data using the full CC model. In order to provide these estimates we choose pyrimidine as a model.

Figure 5.5 shows the comparison of the integral elastic and inelastic cross sections and time-delays calculated for pyrimidine using the full and the Simplified models (including partial waves up to $l = 4$). Generally, the integral elastic cross sections have a very similar magnitude in the region up to ≈ 8 eV. The larger cross section for the full model above 8 eV comes from larger contributions of the B_1 (around 8.5 eV) and the A_1 symmetry (around 10 eV). The larger B_1 contribution is caused by the broad GS resonance E4, characterized in Section 4.8.2. The peak lying around $\approx$ 10 eV in the elastic cross section for the full model corresponds to a very broad resonance found in the time-delay in the A_1 symmetry around the same energy. The same broad resonance lying above 10 eV also appears in the A_g symmetry for pyrazine and in the A_1 symmetry for pyridazine in the calculations using the full CC model. This resonance was not included in the list of resonances for the diazines (see Table 4.10) due to its appearance above 10 eV, which we take as an approximate value for the ionization threshold in our calculations. However, analyzing the branching ratios for this broad resonance for pyrimidine reveals that it has shape character *only*, i.e. this resonance forms in the same way as the two lowest-lying π^* resonances. Therefore, this resonance is associated with one of the virtual orbitals not occupied by the target electrons in the ground state of the molecule. Since our active space for the Simplified CC calculations does not include any virtual orbitals of σ^* character it is not surprising that the broad peak associated with this resonance is absent from the corresponding elastic cross section.

It was demonstrated in detail for pyrazine (see Section 3.6.2) that all resonances visible in the time-delay for the full model below $\approx$ 10 eV are also visible in the time-delay for the Simplified model. This is indeed also the case for pyrimidine, as evident from Figure 5.5. In

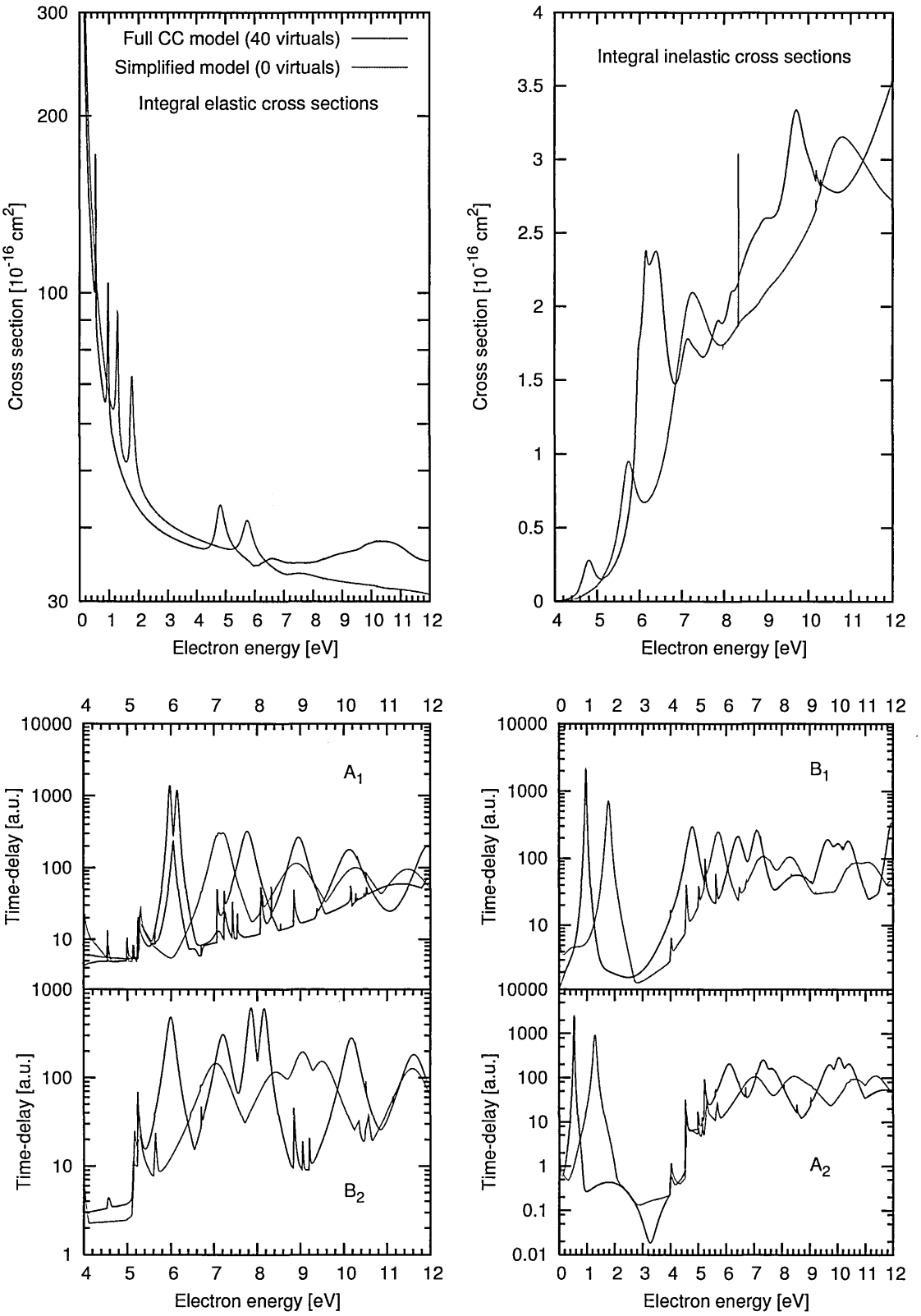

Figure 5.5: Comparison of scattering data for pyrimidine calculated using the full (40 virtual orbitals) and the Simplified (0 virtual orbitals) CC models and the compact basis set. The upper panels show the integral elastic (left panel) and inelastic (right panel) cross sections. No Born-correction has been added. The bottom panels show the time-delays for each of the scattering symmetries. The time-delay for the full CC model for A_1 symmetry includes the first and the second largest eigenvalues of the time-delay matrix to make the broad resonance around 11 eV more visible. Note the logarithmic scales in the upper left panel and in the bottom panels.

general, the higher-lying resonances in the full CC model which appear in the elastic cross sections tend to produce much larger peaks than the equivalent resonances in the elastic cross sections for the Simplified model.

The integral inelastic cross sections (see again Figure 5.5) for the two models also have a very similar magnitude and shape. The inelastic cross section for the Simplified model captures the main resonant features of the full model. As expected, the two Feshbach resonances in pyrimidine appear in both the Simplified and the full CC models and are visible as sharp spikes in the inelastic cross sections around 8.3 eV (the peak for the Simplified model hides the peak for the full model) and around 10.1 eV (where the resonances are visible as small peaks). The small spike around 8 eV visible in the cross section for the Simplified model (it also appears in the full CC model) comes from the A_2 symmetry contribution and might arise from an extremely narrow Feshbach resonance, but we have not been able to confirm this with confidence.

The resonances in the time-delay spectra for the Simplified model appear at energies from $\approx$ 1 eV to $\approx$ 1.5 eV higher than in the full CC model. The widths of the resonances appearing in the full and the Simplified model differ as well: the resonances become narrower in the full CC model. We now summarize our comparison of the scattering data calculated using the full and the Simplified CC models for pyrimidine in the following points. We assume that the conclusions are also valid for uracil and the two oxo-pyrimidines:

- For electron energies at least up to $\approx$ 8 eV the overall magnitudes of the integral elastic cross sections calculated using both CC models agree well. The inelastic cross sections for both models have very similar magnitudes in the whole energy range up to $\approx$ 12 eV.

- The integral inelastic cross sections calculated using the Simplified model capture the main features of the inelastic cross sections obtained from the full CC model.

- The higher-lying resonances appear as larger peaks in the elastic cross sections for the full model than in the elastic cross sections for the Simplified model.

- All resonances (with exception of the higher-lying σ^* shape resonances) found in the full CC model appear also in the Simplified model, but at energies from $\approx$ 1 eV to $\approx$ 1.5 higher and with larger widths. The relative energy order of the resonances in each of the scattering symmetries is the same in both CC models.

5.3.3 CC cross sections

Having understood the advantages and limitations of the Simplified model, we can now turn to a presentation and discussion of the scattering data obtained for uracil and the two oxo-pyrimidines. Figure 5.6 shows the integral elastic and inelastic cross sections for uracil and the two oxo-pyrimidines calculated using the Simplified CC model. For comparison, the Figure also contains the cross sections for pyrimidine obtained from calculations using the same model and the integral SEP cross sections, for all molecules, from Figure 5.2.

The relative magnitudes of the summed CC elastic cross sections correlate to the magnitudes of the dipole moments in the same way as the SEP ones. At 12 eV the summed integral cross sections for all four molecules attain approximately the same value. The A′ contribution to the elastic cross section is featureless for all molecules, perhaps with the exception of the isolated spikes corresponding to Feshbach resonances (in 4-oxo pyrimidine the Feshbach resonances appear only in the A″ symmetry). The A″ contribution, on the other hand, shows the structures corresponding to the three π^* shape resonances. For uracil and 4-oxo pyrimidine additional structures are visible in the A″ elastic cross sections above the third π^* resonance. These structures are due to resonances which will be further discussed in following sections. In accordance with the analysis performed in the previous section, we do not expect any σ^* shape resonances to appear in the Simplified CC calculations. However, as mentioned in Section 5.3.1, higher-lying σ^* shape resonances appear at energies below 10 eV in the SEP model for uracil and 4-oxo pyrimidine (and perhaps also in 2-oxo pyrimidine).

The SEP elastic cross sections, also shown in Figure 5.6, are similar in shape to the CC ones, but are always larger. We can see from Table 5.1 that the HF ground state dipole moments are always larger than the SA-CASSCF ones. Therefore, we ascribe the difference in magnitude between the SEP and the CC elastic cross sections to the larger dipole moments of the HF wavefunctions used in the SEP model.

The inelastic cross sections of the four targets differ significantly. Although they all have roughly a similar magnitude, the inelastic cross sections for uracil and the oxo-pyrimidines display more structure than the cross sections for pyrimidine. The cross sections for 2-oxo pyrimidine display narrow spikes due to Feshbach resonances. However, due to the scale and the number of points used for the energy grid, not all of the Feshbach resonances we found for this molecule are clearly visible in the cross sections. In all cases the other peaks (broader than the Feshbach resonances) in the integral inelastic cross sections originate in the A″ symmetry and, as we will see below, can be ascribed to resonances. The first (large)

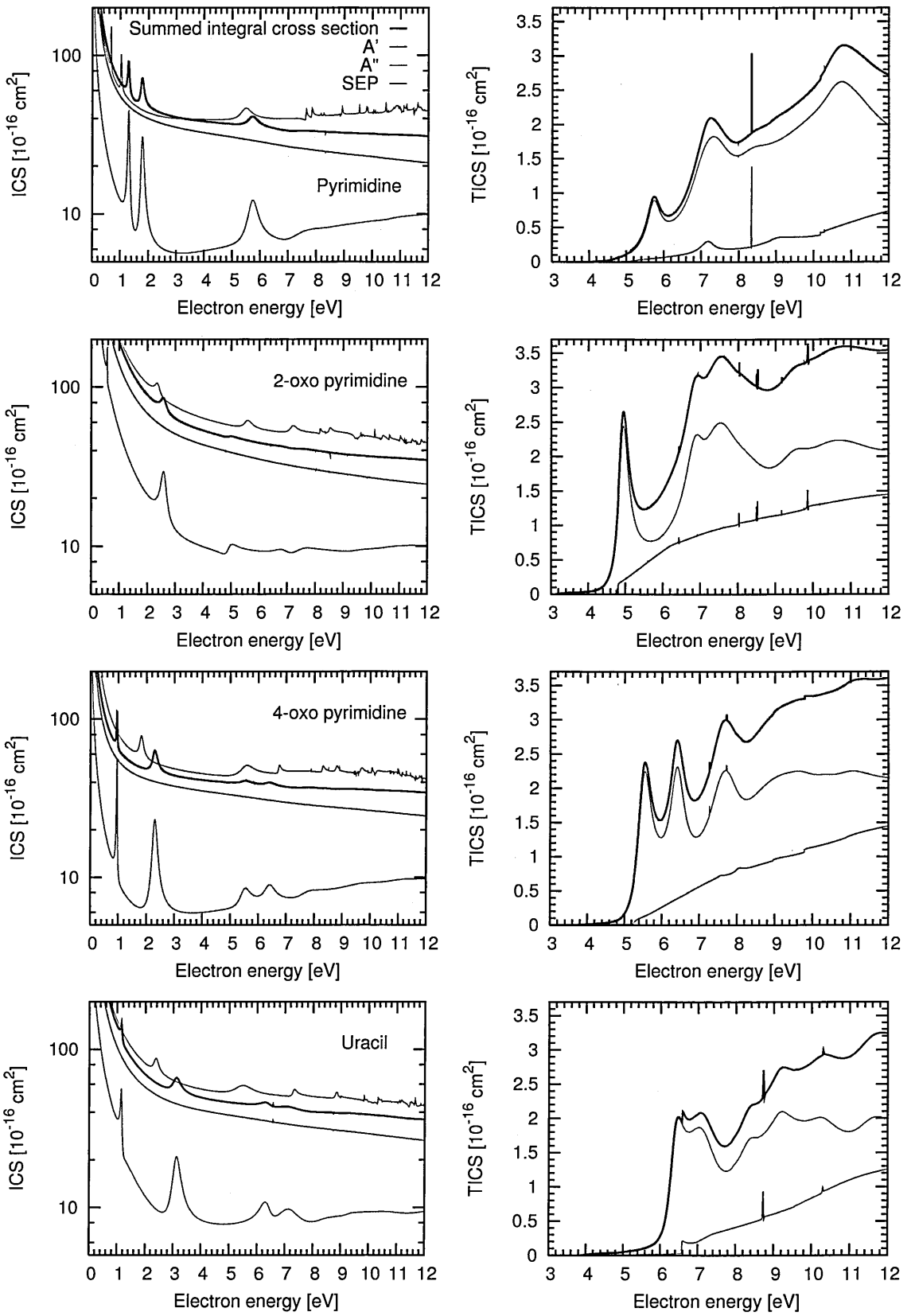

Figure 5.6: Integral elastic (left column) and inelastic (right column) cross sections for pyrimidine, 2-oxo pyrimidine, 4-oxo pyrimidine and uracil, calculated using the Simplified CC model and the compact basis set. Also shown are the integral elastic cross sections calculated at the SEP level. The ranges on the vertical axis for the elastic and the inelastic cross sections were kept the same for all molecules. The range on the vertical axis - note the logarithmic scale - for the elastic cross sections is [5:200] $\times 10^{-16}$cm^2. No Born correction has been added.

	Pyrimidine	2-oxo pyrimidine	4-oxo pyrimidine	Uracil
A′	7	7	7	5
A″	7	7	8	5

Table 5.5: Number of resonances lying below 10 eV in the A′ and A″ symmetries of pyrimdine, 2-oxo pyrimidine, 4-oxo pyrimidine and uracil as determined from the time-delay spectra calculated using the Simplified CC model and the compact basis set. Feshbach resonances have been excluded.

peak in each of the inelastic cross sections corresponds to the third mixed core-excited shape π^* resonance. Based on our experience with the diazines, we expect this peak to become significantly smaller in the calculations using the full CC model. However, the positions of the Feshbach resonances and their imprints in the cross sections should remain the same.

5.4 Resonances in oxo-pyrimidines and uracil and comparison with pyrimidine

Figure 5.7 shows the time-delays calculated for uracil, 2-oxo pyrimidine, 4-oxo pyrimidine and pyrimidine. It is immediately apparent from the number of peaks in the time-delay spectra that uracil and the two oxo-pyrimidines possess, like the diazines, a large number of resonances. In order to quantify this finding, we list in Table 5.5 the number of resonances for each target (in each symmetry) lying below 10 eV. It appears from the Table that the number of resonances in uracil is somewhat smaller than the number of resonances found in the other molecules, for which the numbers are very similar. However, uracil is the largest molecule studied in this work: it is entirely possible that the Simplified CC model represents the short range polarization/correlation effects on a poorer level than for the other molecules*. Consequently, the resonances in uracil might appear in our Simplified CC model at higher energies than they would have, had the short range effects been modelled at the same level of quality as in the other molecules.

It is worth pointing out that the number of resonances found by us in uracil surpasses the number of resonances found by Dora et al. These authors report only the three π^* shape resonances and three resonances of A′ symmetry, which they claim have Feshbach character. We discuss later that it is actually much more likely that these A′ resonances found by Dora et al. are CE* resonances (see Section 4.8.2).

We showed in Section 4.8.3 how the resonances found in the three diazines can be cor-

*This problem is closely related to the problem of size-extensivity studied in quantum chemistry, i.e. the fact that for two molecules of a different size, the same CAS-CI description of the electronic states lead to a "poorer" description of the excited states in the larger molecule when compared with the smaller molecule.

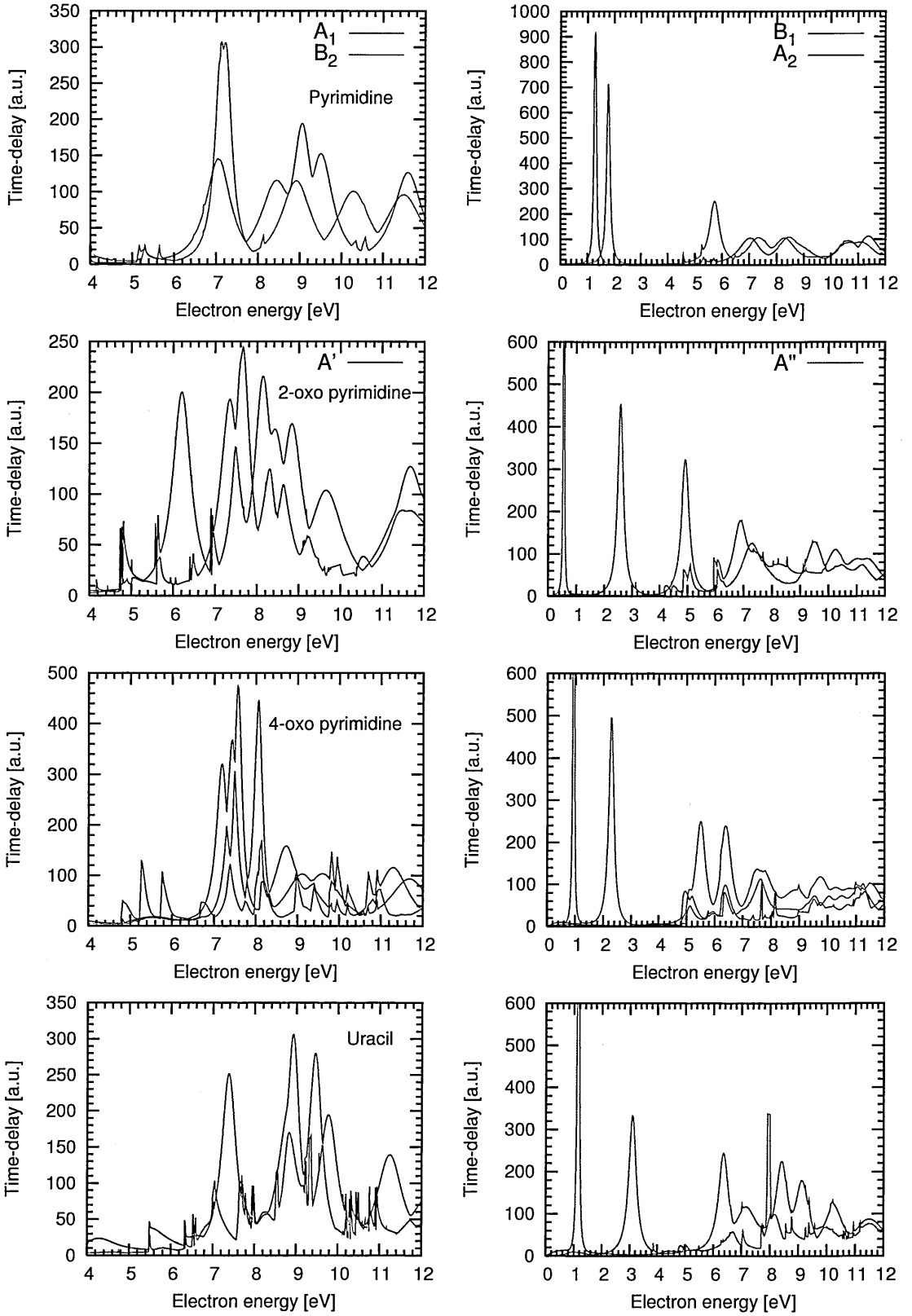

Figure 5.7: Time-delay spectra for pyrimidine, 2-oxo pyrimidine, 4-oxo pyrimidine and uracil, all calculated using the Simplified CC model and the compact basis set. The panels on the left show the A′ contributions (i.e. A_1 and B_2 symmetries for pyrimidine), while the panels on the right show the A″ ones (i.e. B_1 and A_2 for pyrimidine). The time-delay spectra for 2-oxo and 4-oxo pyrimidine and uracil include the *two* largest eigenvalues of the time-delay matrix: this is to aid visual identification of resonant peaks. The narrow asymmetric sharp peaks in the spectra correspond to threshold features. For clarity, peaks corresponding to Feshbach resonances have been removed from the spectra.

related one-to-one. However, it is not possible to do the same for the resonances found in pyrimidine, uracil and the two oxo-pyrimidines for the following reasons. We cannot base the comparison of the resonances on their parent states, because there is no trivial correlation between the electronic states of different molecules. We cannot use the energy order of, for example, the resonances found in the A′ symmetry for the two oxo-pyrimidines and the resonances appearing in the A′ symmetry ($A' = A_1 + B_2$) of pyrimidine either, because many of the resonances lie so close to each other that perturbations in the electron collision with the target molecule caused by the oxygen atoms attached to the pyrimidine ring might have changed their relative order. It also appears from our time-delay spectra for uracil and the two oxo-pyrimidines that the oxygen atoms attached to the ring cause the resonances to appear at rather different energies (and with different widths) in these three molecules. Consequently, we cannot rule out the possibility of swapping of the energy order of resonances which correlate with the ones found in pyrimidine.

We find consistently, in all molecules, an A″ resonance lying just above the third π^* resonance (i.e. a fourth π^* resonance), which appears in the elastic cross section. This resonance can be correlated easily with equivalent resonances appearing in all molecules studied in this work. Recently Dora et al. found a fourth π^* resonance with similar characteristics also in the purinic [62] and pyrimidinic [63] DNA bases. The results of our study now prove that this fourth π^* resonance originates in fact in the equivalent resonances in diazines.

Since we cannot correlate the resonances one-to-one across the three molecules and with the resonances found in pyrimidine, we now turn to the description of their character. For all resonances found below 10 eV in uracil and in the two oxo-pyrimidines we performed the analysis of the parent states using the branching ratios and the excited state elastic cross sections (see Section 3.6).

In Table 5.6 we list the approximate positions and the parent states of the resonances found in uracil and the two oxo-pyrimidines. In this case we did not perform fits to the time-delay spectra in order to determine accurate values for the positions and widths of these resonances: as explained in Section 5.3.2 we expect these parameters to change significantly when compared with the calculations using the full CC model. For all molecules we found higher-lying structures in the A″ elastic cross sections that are caused by CES resonances. However, these structures were relatively weak, as is typical for the Simplified CC model, and we found it difficult to decide which ones of the many higher-lying and closely-spaced A″ resonances are actually responsible for these structures. In uracil, we did not have this problem, since the identification of the type of the A″ resonances lying below 10 eV turned

Uracil				2-oxo pyrimidine				4-oxo pyrimidine			
Type	Pos.	Sym.	Parents	Type	Pos.	Sym.	Parents	Type	Pos.	Sym.	Parents
S	1.16	A″	g.s.	S	0.56	A″	g.s.	S	0.95	A″	g.s.
S	3.11	A″	g.s.	S	2.59	A″	g.s.	S	2.30	A″	g.s.
MCES	6.36	A″	g.s.,$1^3A'$	MCES	4.92	A″	g.s.,$1^3A'$	MCES	5.50	A″	g.s.,$1^3A'$
CES	7.14	A″	g.s.,$1^3A'$	CES	6.88	A″	g.s.,$1^3A'$,$2^3A'$	CES	6.39	A″	g.s.,$1^3A'$,$2^3A'$
CES	8.42	A″	g.s.,$2^3A'$,$2^1A'$	CES	7.29	A″	g.s.,$1^3A'$,$1^3A''$	CE	7.51	A″	$1^3A'$,$2^1A'$,$3^3A'$
CES	9.13	A″	g.s.,$2^1A'$,$2^3A'$	CE*	8.29	A″	$2^3A'$,$2^1A''$,$1^1A''$	CES	7.80	A″	g.s.,$2^3A'$,$1^3A'$
CE*	7.38	A′	$1^3A''$,$1^1A''$	CES	9.51	A″	g.s.,$4^3A''$,$1^1A''$	CE*	8.87	A″	$2^3A'$,$3^3A'$,$1^3A'$
CE*	8.74	A′	$1^1A''$,$4^1A''$,$4^3A''$	CE*	6.20	A′	$1^3A''$,$1^1A''$	CE*	9.74	A″	$3^3A'$,$4^3A'$,$2^1A'$
CE*	8.93	A′	$2^3A''$,$1^3A''$	CE*	7.34	A′	$2^3A''$	CE*	7.19	A′	$1^3A''$
CE*	9.46	A′	$2^1A''$,$1^1A''$	CE*	7.68	A′	$1^1A''$,$2^1A''$,$3^1A''$	CE*	7.43	A′	$1^1A''$
CE*	9.77	A′	$1^3A''$,$1^1A''$,$4^1A''$	CE*	8.14	A′	$2^1A''$,$1^3A''$	CE*	7.57	A′	$2^3A''$
				CE*	8.43	A′	$1^1A''$,$2^3A''$	CE*	8.06	A′	$2^1A''$
				CE*	8.84	A′	$2^3A''$,$3^3A''$,$2^1A''$	CE*	8.73	A′	$1^3A''$,$1^1A''$,$3^3A''$
				CE*	9.66	A′	$3^3A''$,$3^1A''$	CE*	9.12	A′	$2^3A''$
								CE*	9.60	A′	$3^3A''$,$3^1A''$

Table 5.6: Positions, symmetries and parent states of the shape and core excited resonances found in uracil, 2-oxo pyrimidine and 4-oxo pyrimidine for the CC scattering calculations using the compact basis set and the Simplified model. (The Feshbach resonances are listed in Table 5.7.) We use the abbreviations for the type of the resonances as defined in Section 4.8.2: shape (S), mixed core-excited shape (MCES), core-excited shape (CES) and 'inelastic' (CE*).

out to be easier. The time-delay analysis of the resonances in 2-oxo pyrimidine and 4-oxo pyrimidine did not resolve this problem since the branching ratios for the decay into the elastic channels were, not surprisingly, also quite small. Therefore, the assignment of CES character to some of the higher-lying resonances in these two molecules is tentative. These results show that the higher-lying CES resonances are either particularly sensitive to the treatment of the short-range correlation/polarization or some of the higher-lying orbitals (probably of a$''$ symmetry), not included in our CAS, are involved in their formation.

As in the case of diazines, the resonances found in uracil and in the two oxo-pyrimidines can be divided into two basic groups: the GS resonances and the CE* resonances. The former appear in the elastic cross section for the ground state of the target and the latter enhance cross sections for the target in an excited state. All resonances found (with exception of the Feshbach ones) in uracil and the two oxo-pyrimidines in the A$'$ symmetry are of the CE* type, while most of the resonances found in the A$''$ symmetry are of the GS type. An interesting insight into the nature of these resonances is gained comparing the symmetry properties of the parent states of the CE* resonances appearing in different symmetries and molecules. In the case of the CE* resonances appearing in the A$'$ symmetry, all main parent states have A$''$ symmetry, while the CE* resonances appearing in the A$''$ symmetry have main parent states of A$'$ symmetry. In fact the same is true for the parent states of the diazine CE* resonances (listed in Table 4.12): all main parent states of the CE* resonances appearing in A$''$ symmetry have A$'$ symmetry and vice-versa.

We found in Section 4.8.5 that the CE* resonances are core-excited shape. For pyrimidine, we analyzed in detail the A_1 (A$'$) CE* resonances using the SE-like model and found that these had the configurations of the type (parent state)$^N \otimes$ (virtual)^1, where the parent state was 1^1B_1 (i.e. a state of A$''$ symmetry) and the virtual orbitals were of b_1 symmetry (i.e. A$''$ symmetry). The two lowest-lying virtual orbitals of b_1 symmetry in pyrimidine are responsible for formation of two of the GS π^* resonances. Note that the A_1 CE* resonances of pyrimidine arise in A$'$ symmetry and they have a parent state with A$''$ symmetry. These resonances in pyrimidine are typical examples of the CE* resonances.

In the following we will *assume* that *all* of the CE* resonances found in diazines have the main configuration of the form (parent state)$^N \otimes$ (virtual)^1. As described above, *all* CE* resonances (of all molecules studied in this work) forming in $^2A'$ symmetry have main parent states of A$''$ symmetry and vice-versa. Consequently, using the assumption just described, the virtual orbitals responsible for formation of the CE* resonances should have A$''$ symmetry. This phenomenon might actually have a simple explanation linked to the three π^* shape

Pos.	Sym.	Parent
Uracil		
6.565	$^2A'$	$2^1A'$
8.728	$^2A'$	$4^1A'$
10.309	$^2A'$	$7^1A'$
10.758	$^2A'$	$8^1A'$
2-oxo pyrimidine		
4.753	$^2A'$	$2^3A'$
5.608	$^2A'$	$3^3A'$
6.435	$^2A'$	$3^1A'$
6.923	$^2A'$	$4^3A'$
7.622	$^2A'$	$5^3A'$
8.029	$^2A'$	$4^1A'$
8.495	$^2A'$	$5^1A'$
8.521	$^2A'$	$5^1A'$
9.166	$^2A'$	$6^1A'$
9.859	$^2A'$	$7^1A'$
4-oxo pyrimdine		
7.267	$^2A''$	$4^3A''$
7.717	$^2A''$	$4^1A''$

Table 5.7: Positions (in eV) and symmetries of the Feshbach resonances found in our CC scattering calculations using the compact basis set. Their most likely parent states as well as the resonance symmetry are listed. The positions were estimated from the corresponding peaks in the cross sections.

resonances.

The three low-lying π^* shape resonances are associated with virtual orbitals of A$''$ symmetry. We can speculate that it is these three π^* virtual orbitals that are responsible for formation of the CE* resonances. In the case of the CE* resonances the parent state is not the ground state, but an excited state. Consequently, in this picture of the CE* resonances, we can interpret them as the usual π^* shape resonances, but with the parent ground state replaced by an excited state.

In Table 5.7 we list the Feshbach resonances found for the three molecules. The resonances are visible as more or less pronounced sharp spikes in the inelastic cross sections. (They are less visible in the elastic ones, due to the scale of the figures). We can see that 2-oxo pyrimidine possesses the largest number of these resonances, followed by uracil, 4-oxo pyrimidine and pyrimidine. In the previous Chapter we found that the Feshbach resonances formed only in the dipolar diazines. Pyridazine supported a larger number of these resonances than pyrimidine which is in agreement with the larger dipole moment of this molecule. The same picture emerges here: 2-oxo pyrimidine (the molecule with the largest dipole moment) possesses the largest number of Feshbach resonances. Similarly to diazines,

most of the parent states of the Feshbach resonances found in uracil and 2-oxo pyrimidine have large dipole moments and large transition moments with the ground state. These findings provide further arguments for our hypothesis that most of the Feshbach resonances in pyrimidinic molecules are dipole-supported.

An exception to this rule are the Feshbach resonances in 2-oxo pyrimidine with triplet parent states and those in 4-oxo pyrimidine (which we discuss later). Since these Feshbach resonances in 2-oxo pyrimidine have triplet parent states dipole-mediated transition from the ground state to the parent excited state is spin-forbidden.

In sharp contrast with the Feshbach resonances in uracil, 2-oxo pyrimidine and the diazines are those found in 4-oxo pyrimidine. Surprisingly, these Feshbach resonances appear in A'' symmetry and their parents are the $4^1A''$ and $4^3A''$ states. (The eigenphase sums show clear steps by π just below the thresholds for the two excited states, hence the resonances are indeed Feshbach resonances and not threshold effects.) The $4^3A''$ parent state has a zero transition moment with the ground state, but it has an extremely large dipole moment: 7.27 D. The singlet state has a dipole moment of 2.00 D, but a non-negligible dipole transition moment with the ground state: 1.30 D.

Finally, we would like to correlate the Feshbach resonances found by us in uracil with the three A' Feshbach resonances found by Dora et al. at energies 6.17 eV, 7.62 eV and 8.12 eV with widths in the range $0.11 - 0.15$ eV. We did not find in our calculations any Feshbach resonances with these parameters and vice-versa: Dora et al. do not find the Feshbach resonances reported by us. The positions of Feshbach resonances are directly associated with the vertical excitation (VE) energies of their parents. Most importantly, Feshbach resonances typically lie fractions of eV below the energy corresponding to the VE energy of their parent state. Therefore, the positions of the Feshbach resonances are not significantly affected by differences in modelling short-range correlation/polarization. It follows that the fact that Dora et al. used the full CC model instead of the Simplified one, employed by us, should not significantly affect the positions of these resonances. Our calculations and those of Dora et al. use the same description of the excited states, i.e. the VE energies do not differ. Consequently, the Feshbach resonances should appear in both calculations at very similar energies and with a similar width, but that is clearly not the case.

In order to understand this discrepancy we ran a number of test calculations. Dora et al. placed the molecule in the xy plane. However, in our calculations we oriented the molecule in the yz plane with the dipole moment parallel to the z axis. Due to the limitations of the outer region part of the UKRmol code, the calculations of Dora et al. did not take fully into

account the dipole moment of the molecule, whereas our calculations did. We found that, indeed, in the calculations which placed the molecule in the xy plane no Feshbach resonances appear. Therefore, the reason why Dora et al. did not find the Feshbach resonances reported by us can be traced to the limitations of our code. However, this does not explain why we did not find the three A' resonances reported by Dora et al. The peculiar property of the A' resonances of Dora et al. is their width which is, from our experience with the pyrimidinic molecules, too large to correspond to genuine Feshbach resonances. On the basis of this evidence, we propose that the resonances found by Dora et al. in the A' symmetry do not correspond to Feshbach resonances, but rather to some of the CE* resonances found in our Simplified CC calculations at higher energies. Dora et al. used the eigenphase sums to characterize resonances. We found that some of the CE* resonances in diazines in the full CC models are clearly visible in the eigenphase sums. Consequently, it is entirely possible that Dora et al. mistook some of the narrower CE* resonances for Feshbach resonances.

5.5 Resonances in pyrimidinic molecules

In this section we summarize our findings on the resonances in pyrimidinic molecules and how to describe them using our models, and then compare them with other calculations. Finally, we propose links between some of the higher-lying resonances found by us and peaks in the dissociative electron attachment (DEA) spectra. Following the experience gained from our work, we can divide the resonances found in pyrimidinic molecules into the three basic groups:

- Resonances (excluding the Feshbach ones) enhancing the elastic cross section for the ground state (GS resonances),
- CE* resonances, which enhance the elastic cross sections for the excited states,
- Feshbach resonances (that also enhance the ground state elastic cross section).

The GS resonances can be further classified as shape, mixed core-excited shape and core-excited shape. It follows from the points above that we distinguish between the core-excited shape (CES) resonances and the CE* ones. However, it is important to state clearly that we *do not* deem the CE* resonances fundamentally different from the core-excited shape ones. *The CE* resonances are core-excited shape resonances*, but their phenomenological properties (i.e. how they appear in the calculated data) are quite different when compared

with the resonances that we label as simple core-excited shape. For this reason we separate the discussion of the CE* resonances from the GS resonances. In both cases (CES and CE* resonances), the potential responsible for formation of the resonance is associated with the potential of the parent(s) of the resonance, however we hypothesize that the difference between the CE* and CES resonances lies in the *mechanism of their formation*, i.e. in the dynamical process whereby the incoming electron gets attached to the molecule. We discuss this hypothesis further in Section 5.5.2 below.

5.5.1 GS resonances

We find, as expected [32], three low-lying π^* shape resonances for each of the molecules studied. The positions of the two lowest-lying resonances are in a good agreement with the experimental data. The third π^* mixed core-excited shape resonance always lies too high in energy for all of the molecules studied. All GS resonances found in the diazines appear in the scattering symmetries with π character. In uracil and 4-oxo pyrimidine we find additional broad σ^* shape resonance below 10 eV.

Apart from the low-lying shape resonances, we find several higher-lying GS resonances, that have not been characterized for diazines before. The nature of these resonances is still not entirely clear from the present calculations. In particular we cannot ascertain whether they actually possess mixed core-excited shape or simply CES character. This possibility was discussed in detail in Section 3.6.5. The core-excited shape resonances are responsible for the largest peaks in the total inelastic cross sections.

The measurements of the total anion yield for uracil [137, 40] show that the most significant structure at higher energies (> 4 eV) occurs in the energy range $\approx 5 - 7.5$ eV. An additional structure between $\approx 8 - 9$ eV appears in the experiment as well. It is reasonable to assume that these structures are associated with resonances of the GS type. Our CC calculations for uracil using the Simplified model find two π^* GS resonances which might, in the full CC calculations, fall close to or within the range of energies where the largest peaks in the DEA appear. These two resonances are responsible for large peaks in our calculated total inelastic cross sections and are also visible in the elastic cross sections. Our CC calculations for uracil find no GS resonances in the A' symmetry. However, our SEP calculations definitely show a broad structure around 7 eV in the A' symmetry and perhaps even a second structure around 9 eV. Both of these structures appear to have a resonant origin and their positions fall within the ranges of the large peaks in the DEA spectra of uracil. Therefore, we propose

that the two higher-lying π^* resonances (of $^2A''$ symmetry) and the two σ^* resonances (of $^2A'$ symmetry) in uracil are associated with the large peaks in the DEA spectra in the energy range $\approx 5 - 7.5$ eV.

It is more difficult to see from the results of our calculations whether the higher-lying ($\approx 8 - 9$ eV) structure in the DEA spectra of uracil can be correlated with some of the other core-excited shape resonances we find in this molecule. We find a GS resonance in A'' symmetry just above 10 eV, but the quality of representation of this resonance is questionable due to the simple nature of the CC calculations and the high energy of this resonance. More evidence on the position and character (GS or CE*) of this resonance would be provided by analyzing the results of the full CC model. However, we note that we have found in the full CC model a higher-lying A'' GS resonance close to the ionization threshold (i.e. around 10 eV) in all diazines and therefore it is possible that the A'' resonance in uracil correlates with these.

Our highest-level CC calculations for the diazines find two higher-lying π^* GS resonances in the energy region $\approx 5.7 - 6.4$. The recent experiments of Modelli et al. [35] showed the presence of a core-excited resonance in pyrimidine around 5.5 eV. Our calculations suggest that the structure seen in the experiment corresponds in fact to the two overlapping core-excited shape resonances in B_1 and A_2 symmetries found by us around 6 eV. These resonances in pyrimidine, and their equivalents in the other two diazines, have properties very similar to the two higher-lying π^* resonances found in uracil: they are visible in the elastic cross sections and are responsible for the largest peaks in the total inelastic cross sections. Clearly, these two sets of resonances are correlated and therefore the uracil resonances originate in the simpler diazine molecules. Unlike uracil, we find in the diazines one σ^* (shape) resonance above 10 eV (above the ionization threshold); we cannot confirm with confidence whether this resonance would appear in an experiment below the ionization threshold of these molecules.

The recent calculations of Dora et al. [63] on electron collisions with thymine and cytosine and the calculations of Wang et al. [64], who studied electron collisions with all DNA nucleobases, report higher-lying σ^* shape resonances in all of them (Wang et al.) or structures in the A' cross sections for thymine and cytosine (Dora et al.) which seem to have a resonant origin. It is very likely that at least some of these resonances correlate with the σ^* shape resonances found by us in uracil and 4-oxo pyrimidine. Winstead and McKoy [56] also find some evidence for the presence of a broad higher-lying (around 8.5 eV) resonance in their elastic calculations on electron collisions with uracil. Gianturco et al. [53, 54] found in uracil two shape resonances in the energy range $8.29 - 8.47$ eV with widths exceeding 1.5 eV.

All these results, combined with our results for the pyrimidinic molecules, provide strong evidence that higher-lying broad σ^* shape resonances are present in the nucleobases.

The calculations of Grandi et al. [55] find a higher-lying (around 9 eV) π^* shape resonance in uracil. These calculations were carried out using effective potentials which do not take into account the possible coupling of this resonance to the electronic excited states. Neglecting this type of coupling can shift a resonance to a much higher energy [33]. Therefore, we suggest that this resonance actually correlates with one of the higher-lying π^* resonances we find in uracil. Since the uracil π^* resonances can be traced back to the equivalent resonances in diazines, which appear around $\approx 5.7 - 6.4$ in our CC calculations using the full model, we propose that the accurate position of this uracil π^* resonance also falls within this range of energies.

In order to explain the low-energy DEA spectra of uracil, Scheer et al. [39, 40] invoked a low-lying (below 2 eV) σ^* shape resonance. To the best of our knowledge the elastic calculations of Winstead and McKoy [56] are the only ab-initio scattering calculations that have been able to find a σ^* resonance that could correspond to the resonance invoked by Scheer et al. We do not find any low-lying structure in the A′ symmetry of uracil (neither in any of the diazines) that could correspond to this resonance. In Section 4.8.6 we discussed the possible reasons for that.

5.5.2 CE* resonances

We found a large number of these resonances in all molecules studied. In diazines, 11 CE* resonances were found; a similar number was found in uracil and the two oxo-pyrimidines. The main property of these resonances is that they enhance the elastic cross sections for the excited states which are their parent states. However, a few of these resonances are clearly visible in the total inelastic cross sections for the ground state. The CE* resonances have the same underlying, core-excited shape, character as the CES resonances discussed above. However, the picture of the CE* resonances that emerges from our calculations shows that it matters very much for the formation of these resonances, whether the target state is *initially* in an excited state or not. This is in a sharp contrast with the phenomenology of the CES resonances: these form with a high probability in collisions in which the target is initially in the ground state and also in collisions in which the target is initially in an excited state. It is this significant difference in the phenomenology of the CES and the CE* resonances which called for a separate discussion of these two, despite the fact (emphasized again) that their

underlying, core-excited shape, character is the same.

We found that the CE* resonances appearing in A′ symmetries have main parent states of A″ symmetry and vice-versa. We have proposed an explanation of this correspondence based on the configurations of these resonances (see Section 5.4). This explanation seems to be in line with the findings presented in Section 4.8.5 which show explicitly that the CE* resonances are indeed core-excited shape.

None of these resonances were identified in any of the previous theoretical and experimental studies on pyrimidinic molecules. Direct experimental confirmation of the presence of these resonances in the pyrimidinic systems seems to be very unlikely: the excited states of these molecules decay rapidly through conical intersections making experiments with excited targets very difficult. The short lifetime of the excited states in the gas-phase probably makes the CE* resonances rather irrelevant for gas-phase electron-molecule collisions.

5.5.3 Feshbach resonances

The Feshbach resonances were found only in the dipolar molecules. It seems that most of these resonances are formed due to a large permanent ground state dipole moment of the target molecule and a large transition dipole moment between the ground state and the parent state of the resonance. The positions of these resonances are related to vertical excitation (VE) energies of the parent states. Since the calculated VE energies of the electronic states which support these resonances are much higher than their corresponding experimental values we expect the Feshbach resonances to appear in experiment, in some cases, even several electronvolts lower.

Most of the Feshbach resonances we found in the diazines, uracil and 2-oxo pyrimidine are dipole-supported and are found in symmetries with A′ character, but we find some which are not dipole-supported. Four lower-lying resonances in 2-oxo pyrimidine and all Feshbach resonances in 4-oxo pyrimidine are probably not dipole supported and a different mechanism is involved in their formation. Furthermore the ones found in 4-oxo pyrimidine appear in the A″ symmetry.

5.6 Summary

We performed elastic and inelastic scattering calculations for uracil, 2-oxo pyrimidine and 4-oxo pyrimidine at the SEP and the CC level.

In the case of uracil experimental data for the positions of the three low-lying π^* resonances was available allowing us to calibrate our SEP scattering models so as to obtain a fair agreement with the experimental positions. Data (both experimental and theoretical) on the electronic excited states of uracil were also available, hence we were able to compare some of the calculated VE energies with experiment and obtained a good agreement for the low-lying electronic states. For the two oxo-pyrimidines neither target data nor scattering data were available. Therefore, in order to construct the target and the scattering models we relied solely on the experience gained for the calculations performed for the diazines.

The positions of the π^* resonances for uracil obtained at the SEP level were in worse agreement with the experimental values when compared with the agreement reached for pyrimidine. The positions of the three π^* resonances in the two oxo-pyrimidines were similar to those in uracil. The third π^* resonance was in all three molecules found at a position similar to pyrimidine. We investigated the shapes of the π^* virtual orbitals responsible for trapping the scattering electron and found significant differences between the first two π^* orbitals of pyrimidine and the substituted pyrimidines: the addition of the extra oxygen(s) into the parent pyrimidine molecule changes them significantly. We conclude that the significant difference in the positions of the two π^* resonances in the substituted pyrimidines when compared with pyrimidine can be probably explained by the perturbed shapes of the underlying π^* orbitals. The third π^* orbital has a delocalized character in pyrimidine and a similar shape in the three substituted pyrimidines. This might be the reason why the third π^* resonance does not change its position significantly.

The SEP cross sections for the A$'$ symmetry show the presence of shape resonances above 7 eV in uracil and 4-oxo pyrimidine. It is not clear from the present results whether a shape resonance of A$'$ symmetry also appears in 2-oxo pyrimidine.

The CC calculations using the Simplified model revealed, as in the diazines, a large number of resonances in the substituted pyrimidines. We found a number of CE* resonances (mainly in the A$'$ symmetry) and also several higher-lying GS resonances in the A$''$ symmetry which have the ground state as one of their parent states. However, it is not straightforward to correlate these resonances one-to-one with those found in pyrimidine.

We found Feshbach resonances in all three molecules studied and conclude that most of them are dipole supported. However, the low-lying Feshbach resonances in 2-oxo pyrimidine and all Feshbach resonances in 4-oxo pyrimidine are probably not dipole supported. It is likely that a different mechanism is involved in their formation.

For all three molecules we calculated the total elastic and integral inelastic cross sections

using the Simplified CC model. In order to estimate the quality of these cross sections, we compared in detail those for pyrimidine calculated using the Simplified and the full CC models. We concluded that the cross sections calculated using the Simplified model provide a good estimate of the magnitude and shape of the elastic and inelastic cross sections. However, for electron energies above $\approx$ 8 eV, the Simplified model might give very inaccurate cross sections. This is probably caused by the absence of the σ^* orbitals in the active space: the σ^* orbitals describe the higher-lying resonances which lead to broad peaks in the cross sections.

The detailed comparison of the resonances found in all molecules studied in this work allows us to conclude that the oxygen atoms attached to the pyrimidine ring influence only the positions of the resonances (and their widths), but they do not lead to formation of resonances associated exclusively with the oxygen atoms. The number of resonances found in the oxygen-containing molecules is similar to pyrimidine. Consequently, the oxygen atoms do not suppress resonance formation.

Chapter 6

Conclusions

This work focused on studying collisions of low-energy electrons with pyrimidinic molecules using the *ab-initio* R-matrix method. We studied the diazine molecules (pyrazine, pyrimidine and pyridazine) and three substituted pyrimidines, which contained one oxygen atom (2-oxo pyrimidine, 4-oxo pyrimidine) and two oxygens (uracil). The main goal of this work was to investigate the formation of resonances in these systems. Throughought this thesis a special emphasis was placed on the inelastic scattering calculations which, at the time of writing, are still scarce for molecules of a size comparable with pyrimidine. The molecules studied can be thought of as models or precursors for the (more complex) pyrimidinic nucleobases of DNA. Therefore understanding the formation of resonances in the systems studied here contributes to the current understanding of resonance formation in the nucleobases. Studying the molecules which are derived from pyrimidine allowed us to elucidate the effect various structural perturbations have on the formation of resonances and on the elastic and inelastic cross sections. The work presented in this thesis can be placed within the wider range of studies trying to complement our understanding of the electron-induced damage to DNA.

- In all the systems studied, we found an unexpectedly large number of resonances, most of which had not been characterized before. Time-delay analysis was found to be an indispensable tool for identifying and characterizing resonances in our calculations. We showed that the traditional analysis based on the eigenphase sums does not necessarily reveal the presence of all resonances in the system and we explained the reasons why. Previous inelastic R-matrix calculations on uracil [59], the pyrimidinic [63] and the purinic nucleobases [62] did not use the time-delay approach and we deem it very likely that, as a result, they missed a large number of resonances in these systems. In fact, we showed explicitly that uracil possesses a much larger number of resonances

than reported by Dora et al. [59]. Generally, we strongly recommend the use of the time-delay method for the analysis of, especially, the results of calculations containing inelastic channels.

- Based on the appearance of resonances in the calculated data we assigned them into one of the three groups: GS (ground-state) resonances, CE* (core-excited shape) resonances or Feshbach resonances. The GS resonances, some of which were well known before, enhance the elastic cross sections for the ground state of the target. Resonances of this type were found predominantly in the A″ scattering symmetries with the only exception of the higher-lying σ^* shape resonances found in uracil, 4-oxo pyrimidine and possibly also in 2-oxo pyrimidine. We linked these resonances to some of those found by previous studies of pyrimidinic and purinic molecules and in particular to the structures in the gas-phase dissociative electron attachment (DEA) spectra. Surprisingly, the CE* resonances do not enhance the elastic cross sections for the ground state, although some of them enhance the total inelastic cross sections. We have confirmed that the CE* resonances enhance the elastic cross sections for the *excited* states. We have proposed an explanation for the formation of these resonances, but more work is still required before they are fully understood. Our work shows that these resonances are strongly associated with the electronically excited states of the target molecule. The Feshbach resonances were found only in the dipolar molecules and most of them are dipole-supported, caused by the large dipole moments of their parent states and the large dipole transition moments of the parents with the ground state.

- The diazine molecules are a good model for the pyrimidinic nucleobases. Considering the limitations of our calculations, it seems that all of the resonances present in uracil are also present in the diazines, albeit at different energies. However, the number and character (GS, CE* or Feshbach) of the resonances in uracil and in diazines are very similar. Our studies of electron collisions with the two oxo-pyrimidines and uracil allowed us to conclude that the oxygen atoms attached to the pyrimidine ring do not have a significant effect on the formation of resonances in these molecules. The oxygen atoms may affect the positions of the resonances (as shown for the lowest-lying ones) but do not lead to the formation of additional resonances associated *exclusively* with these atoms. Similarly, we have not found any evidence that the oxygen atoms prevent the formation of some resonances. We conclude that the resonances we found are associated with the ring structure of the pyrimidinic molecules.

The main conclusion of this work is that the picture of electron resonances in pyrimidinic molecules is much more complex than previously expected. This is mainly due to the large number of CE* resonances forming in these systems which have very different imprints in the cross sections compared to the GS resonances. More work is needed to elucidate the role these resonances might play in the DEA process and in turn in electron-induced damage of DNA. Since the CE* resonances are associated with (short-lived) electronically excited states gas-phase electron-molecule experiments which would confirm their formation are probably very difficult to perform, but it is important to elucidate whether the CE* resonances might play a role when the nucleobases are immersed in an environment resembling the conditions in a living cell.

Based on the experience gained from this thesis, we believe that future work should address the following issues:

1. Understanding the formation of the CE* resonances and their role in the DEA process.
2. Ensuring that larger R-matrix radii can be used in the calculations in order to be able to use diffuse target basis sets and describe, for example, Rydberg states.
3. Using larger CAS models to ensure better representation of the correlation/polarization effects.
4. Improving the description of the electronically excited states included in the inelastic scattering calculations.

For smaller systems, fullfiling points 2 and 3 implies success in 4, but this is not the case for the (large) molecules studied in this work. In the following paragraphs we discuss these points one by one.

Since the CE* resonances are strongly associated with the electronically excited states, it will be advantageous to study these resonances in smaller systems possessing fewer excited states where these can be represented at a higher level of quality than in bigger targets (like the pyrimidines). In order to understand better the formation of the CE* resonances an in depth analysis of the time-delay matrices calculated for each of the resonances could be useful. According to our hypothesis explaining the formation of the CE* resonances, the target needs to support at least one shape resonance for any CE* resonances to be present. Additionally, we hypothesize that electronically excited states supporting the CE* resonances should have charge densities similar to the ground electronic state. However, we cannot elucidate from the results of this work to what extent the formation of the CE* resonances is a phenomenon

common to many different molecules or whether it is a highly selective process specific to the molecules studied in this thesis.

The need for use of larger R-matrix radii in future calculations is given by the advantages a diffuse atomic basis set would bring. We have seen that the use of a diffuse basis can result in several improvements: the very low-energy behaviour (< 3 eV) of the cross sections for non-polar molecules (e.g. pyrazine) can be more accurately represented, Rydberg excited states can be described more accurately and, finally, we discussed the possibility that the low-lying σ^* resonance in uracil may only be described by calculations using a diffuse atomic basis set. Large R-matrix radii require the use of diffuse (Gaussian) continuum orbitals which in turn cause numerical linear dependencies with the orbitals of the target. A possible remedy to this problem would be to replace, or augment, the Gaussian basis set with a different set of functions that would allow us to use larger R-matrix radii without sacrificing the quality of representation of the continuum. The use of basis functions with a compact support (e.g. B-splines) might be one way of achieving this goal and we are currently exploring this approach, which seems very promising.

A significant drawback of our calculations is that we cannot construct accurate scattering models for molecules for which prior scattering experimental data are not available. This is due to the fact that we need to use $N+1$ configurations in which the scattering electron occupies a virtual orbital. Unfortunately, we cannot determine the number of virtual orbitals used (and the appropriateness of the basis set to represent these orbitals) without comparing the calculated data with experiment. Most importantly, our scattering models are *not convergent* with respect to the number of virtuals included. For smaller molecules (e.g. water) models which do not use virtual orbitals for the description of the $N+1$ system have been shown to provide accurate scattering data; they do not suffer from the lack of convergence. This is not the case for larger molecules (like the ones studied in this thesis), for which the configurations using virtual orbitals are essential to accurately describe the correlation/polarization effects. One way to mitigate this problem may be to use CC scattering models which employ a much larger CAS, but no virtual orbitals. In principle, larger CAS models should lead to a better representation of the correlation/polarization effects and also of the electronically excited states. We expect that as the size of the CAS is increased, the scattering model will provide increasingly more accurate results, while keeping the calculation reasonably well balanced. In this way *convergence* of the scattering model can be achieved even for large molecules. However, as explained below, we have reasons to believe that for large molecules the size of the CAS models required to achieve accurate results is huge. Therefore, it remains to be

seen whether this approach is computationally feasible. We conclude by mentioning that we found it easier to represent the correlation/polarization effects in elastic collisions using the (simple) SEP model. However, these calculations suffer from appearance of pseudoresonances at energies above the first vertical excitation (VE) threshold and cannot be used to obtain information on the inelastic processes.

Finally, a very challenging problem for the future is to improve on the quality of representation of the electronically excited states included in our CC calculations. In particular, it is important that VE energies of these states are accurate: ideally within fractions of eV when compared with experiment. Most of the states included in our CC calculations have VE energies larger (even by several eV in some cases) than the experimental ones. Based on the experience gained from this work, we are convinced that merely increasing the size of the CAS, used for the description of the electronic states, is not going to resolve this issue (see Section 4.9 for details). We deem it unlikely that a *purely variational* approach based on the CASSCF method is going to lead to significant improvements in the quality of representation of the target states. Perturbative corrections (e.g. CASPT2) need to be included in the target description to obtain accurate VE energies and to keep the computational requirements realistic. However, if the perturbational corrections are introduced for the target description they must, for reasons associated with balance, be used also for the $N+1$ *scattering* wavefunctions. Unfortunately, defining the form of the perturbative corrections for the $N+1$ wavefunctions that would be consistent with the corrections for the target wavefunctions is a difficult problem. On the other hand, the benefits associated with successfully resolving this issue are huge. If successful, this approach will lead not only to a much better description of the target states, but also to a vastly improved description of the correlation/polarization effects in the scattering calculations, while keeping the size of the CAS within the limits of current computers.

Bibliography

[1] P. W. Atkins and R.S. Friedman. *Molecular Quantum Mechanics.* Oxford University Press, USA, 5th edition, December 2010. [cited at p. vii, 54]

[2] United Nations Scientific Committee on the Effects of Atomic Radiation. *Sources and effects of ionizing radiation.* United Nations, New York, 2010. [cited at p. 3]

[3] I. Baccarelli, I. Bald, F. A. Gianturco, E. Illenberger, and J. Kopyra. Electron-induced damage of DNA and its components: Experiments and theoretical models. *Phys. Rep.*, 508(1-2):1–44, November 2011. [cited at p. 3, 12, 14]

[4] E. J. Hall and A. J. Giaccia. *Radiobiology for the radiologist.* Lippincott Williams & Wilkins, 2006. [cited at p. 3, 5]

[5] L. Sanche. Low energy electron-driven damage in biomolecules. *Eur. Phys. J. D.*, 35(2):367–390, 2005. [cited at p. 4, 5, 12]

[6] V. Cobut, Y. Frongillo, J. P. Patau, T. Goulet, M. J. Fraser, and J. P. Jay-Gerin. Monte carlo simulation of fast electron and proton tracks in liquid water - I. physical and physicochemical aspects. *Radiation Physics and Chemistry*, 51(3):229–243, March 1998. [cited at p. 5]

[7] M.A. Huels, I. Hahndorf, E. Illenberger, and L. Sanche. Resonant dissociation of DNA bases by subionization electrons. *J. Chem. Phys.*, 108(4):1309–1312, January 1998. [cited at p. 5]

[8] B. Boudaïffa, P. Cloutier, D. Hunting, M. A. Huels, and L. Sanche. Resonant formation of DNA strand breaks by low-energy (3 to 20 eV) electrons. *Science*, 287(5458):1658–1660, March 2000. [cited at p. 5, 6]

[9] R. Panajotovic, F. Martin, P. Cloutier, D. Hunting, and L. Sanche. Effective cross sections for production of single-strand breaks in plasmid DNA by 0.1 to 4.7 eV electrons. *Radiation Research*, 165(4):452459, April 2006. [cited at p. 6]

[10] L. Sanche. Low energy electron damage to DNA. In M. K. Shukla and J. Leszczynski, editors, *Radiation Induced Molecular Phenomena in Nucleic Acids*, volume 5 of *Challenges and Advances in Computational Chemistry and Physics*, pages 531–575. Springer Netherlands, 2008. [cited at p. 5, 12]

[11] S. Denifl, T. D. Märk, and P. Scheier. The role of secondary electrons in radiation damage. In G. García and M. C. Fuss, editors, *Radiation Damage in Biomolecular Systems*, Biological and Medical Physics, Biomedical Engineering, pages 45–58. Springer Netherlands, 2012. [cited at p. 5, 12]

[12] M. D. Barry and P. ONeill. A sting in the tail of electron tracks. *Science*, 287(5458):1603–1604, March 2000. [cited at p. 7]

[13] P. G. Burke. *R-Matrix Theory of Atomic Collisions*, volume 61 of *Springer Series on Atomic, Optical, and Plasma Physics*. Springer, 1st edition, 2011. [cited at p. 6, 11]

[14] J. Tennyson. Electron-molecule collision calculations using the R-matrix method. *Phys. Rep.*, 491:29–76, 2010. [cited at p. 7, 11, 17, 28, 32]

[15] G. J. Schulz. Resonances in electron impact on diatomic molecules. *Rev. Mod. Phys.*, 45(3):423, 1973. [cited at p. 8]

[16] H. Hotop, M. Rul, and I.I. Fabrikant. Resonance and threshold phenomena in low-energy electron collisions with molecules and clusters. *Phys. Scr.*, 110:22–31, 2004. [cited at p. 8, 13]

[17] C. Winstead and V. McKoy. Electron-Biomolecule collision studies using the Schwinger multichannel method. In G. García and M. C. Fuss, editors, *Radiation Damage in Biomolecular Systems*, Biological and Medical Physics, Biomedical Engineering, pages 87–113. Springer Netherlands, 2012. [cited at p. 9, 12, 16]

[18] J.R. Taylor. *Scattering theory: The quantum theory on nonrelativistic collisions*. Wiley, 1972. [cited at p. 10, 26, 52, 58, 227]

[19] B. I. Schneider. Role of the Born-Oppenheimer approximation in the vibrational excitation of molecules by electrons. *Phys. Rev. A*, 14(5):1923, November 1976. [cited at p. 10]

[20] J. Simons. How do Low-Energy (0.1-2 eV) electrons cause DNA-Strand breaks? *Accounts of Chemical Research*, 39(10):772–779, October 2006. [cited at p. 10, 12, 13]

[21] R. Barrios, P. Skurski, and J. Simons. Mechanism for damage to DNA by Low-Energy electrons. *J. Phys. Chem. B*, 106(33):7991–7994, 2002. [cited at p. 10, 13]

[22] C. Winstead and V. McKoy. Parallel computational studies of electron-molecule collisions. *Computer Phys. Comm.*, 128:386 – 398, 2000. [cited at p. 11, 12]

[23] K. Takatsuka and V. McKoy. Variational scattering theory using a functional of fractional form. I. General theory. *Phys. Rev. A*, 23(5):2352–2358, May 1981. [cited at p. 11]

[24] T.N. Resigno, C.W. McCurdy, A.E. Orel, and B.H. Lengsfield III. The complex kohn variational method. In W M Huo and F A Gianturco, editors, *Computational Methods for Electron Molecule Collisions*, pages 1–44. Plenum Press, New York, 1995. [cited at p. 11]

[25] N. Sanna, I. Baccarelli, and G. Morelli. SCELib3.0: the new revision of SCELib, the parallel computational library of molecular properties in the Single Center Approach. *Comput. Phys. Commun.*, 180(12):2544–2549, December 2009. [cited at p. 11]

[26] S. Tonzani. FERM3D: a finite element R-matrix electron molecule scattering code. *Computer Phys. Comm.*, 176(2):146–156, January 2007. [cited at p. 11]

[27] C. Winstead and V. McKoy. Resonant interactions of slow electrons with DNA constituents. *Radiation Physics and Chemistry*, 77(10-12):1258–1264, October 2008. [cited at p. 12, 15]

[28] I. Baccarelli, F. Sebastianelli, F.A. Gianturco, and N. Sanna. Modelling dissociative dynamics of biosystems after metastable electron attachment: the sugar backbones. *Eur. Phys. J. D.*, 51(1):131–136, January 2009. [cited at p. 12]

[29] L. Bryjko, A. Dora, T. Mourik, and J. Tennyson. Resonances in electron collisions with small biomolecules using the R-matrix method. In G. García and M. C. Fuss, editors, *Radiation Damage in Biomolecular Systems*, Biological and Medical Physics, Biomedical Engineering, pages 115–126. Springer Netherlands, 2012. [cited at p. 12, 16]

[30] K. Aflatooni, G.A. Gallup, and P.D. Burrow. Electron attachment energies of the DNA bases. *J. Phys. Chem. A*, 102(31):6205–6207, July 1998. [cited at p. 12, 163, 169, 172]

[31] A.M. Scheer, K. Aflatooni, G.A. Gallup, and P.D. Burrow. Bond breaking and temporary anion states in uracil and halouracils: Implications for the DNA bases. *Phys. Rev. Lett.*, 92(6), February 2004. [cited at p. 12, 163]

[32] I. Nenner and G. J. Schulz. Temporary negative ions and electron affinities of benzene and N-heterocyclic molecules: pyridine, pyridazine, pyrimidine, pyrazine, and s-triazine. *J. Chem. Phys.*, 62:1747, 1975. [cited at p. 12, 16, 62, 63, 65, 77, 90, 113, 131, 138, 169, 172, 173, 190]

[33] C. Winstead and V. McKoy. Low-energy electron scattering by pyrazine. *Phys. Rev. A*, 76:012712, 2007. [cited at p. 12, 15, 63, 66, 77, 84, 86, 90, 97, 142, 148, 192]

[34] P. Palihawadana, J.P. Sullivan, M.J. Brunger, C. Winstead, V. McKoy, G. García, F. Blanco, and S.J. Buckman. Low-energy elastic electron interactions with pyrimidine. *Phys. Rev. A*, 84:062702, 2011. [cited at p. 12, 63, 64, 107, 111, 112, 113, 114, 116, 137]

[35] A. Modelli, P. Bolognesi, and L. Avaldi. Temporary anion states of pyrimidine and halopyrimidines. *J. Phys. Chem. A*, 115(39):10775–10782, 2011. [cited at p. 12, 63, 154, 191]

[36] H. Abdoul-Carime, S. Gohlke, and E. Illenberger. Site-Specific dissociation of DNA bases by slow electrons at early stages of irradiation. *Phys. Rev. Lett.*, 92(16):168103, April 2004. [cited at p. 12]

[37] S. Ptasinska, S. Denifl, B. Mroz, M. Probst, V. Grill, E. Illenberger, P. Scheier, and T.D. Mark. Bond selective dissociative electron attachment to thymine. *J. Chem. Phys.*, 123(12), September 2005. [cited at p. 12]

[38] P.D. Burrow, G.A. Gallup, A.M. Scheer, S. Denifl, S. Ptasinska, T. Mark, and P. Scheier. Vibrational feshbach resonances in uracil and thymine. *J. Chem. Phys.*, 124(12), March 2006. [cited at p. 13]

[39] A. Scheer, K. Aflatooni, G. Gallup, and P. Burrow. Bond breaking and temporary anion states in uracil and halouracils: Implications for the DNA bases. *Phys. Rev. Lett.*, 92:068102, 2004. [cited at p. 13, 155, 192]

[40] A.M. Scheer, C. Silvernail, J.A. Belot, K. Aflatooni, G.A. Gallup, and P.D. Burrow. Dissociative electron attachment to uracil deuterated at the N1 and N3 positions. *Chem. Phys. Lett.*, 411(1-3):46–50, August 2005. [cited at p. 13, 155, 163, 190, 192]

[41] T. Skalický, C. Chollet, N. Pasquier, and M. Allan. Properties of the π^* and σ^* states of the chlorobenzene anion determined by electron impact spectroscopy. *Phys. Chem. Chem. Phys.*, 4(15):3583–3590, 2002. [cited at p. 13]

[42] K. Aflatooni, G. A. Gallup, and P. D. Burrow. Dissociative electron attachment in nonplanar chlorocarbons with π^*/σ^*-coupled molecular orbitals. *J. Chem. Phys.*, 132(9):094306, 2010. [cited at p. 13]

[43] S. Ptasinska, S. Denifl, P. Scheier, E. Illenberger, and T.D. Mark. Bond- and site-selective loss of H atoms from nucleobases by very-low-energy electrons (3 eV). *Angewandte Chemie International Edition*, 44(42):6941–6943, 2005. [cited at p. 13, 14]

[44] Yi Zheng, P. Cloutier, D. J. Hunting, J. R. Wagner, and L. Sanche. Glycosidic bond cleavage of thymidine by Low-Energy electrons. *J. Am. Chem. Soc.*, 126(4):1002–1003, 2004. [cited at p. 13]

[45] Yi Zheng, P. Cloutier, D. J. Hunting, L. Sanche, and J. R. Wagner. Chemical basis of DNA Sugar-Phosphate cleavage by Low-Energy electrons. *J. Am. Chem. Soc.*, 127(47):16592–16598, 2005. [cited at p. 13]

[46] Yi Zheng, P. Cloutier, D. J Hunting, J. R. Wagner, and L. Sanche. Phosphodiester and N-glycosidic bond cleavage in DNA induced by 4-15 eV electrons. *J. Chem. Phys.*, 124(6):064710–064710–9, February 2006. [cited at p. 13]

[47] S. Denifl, S. Ptasinska, G. Hanel, B. Gstir, M. Probst, P. Scheier, and T. D. Mark. Electron attachment to gas-phase uracil. *J. Chem. Phys.*, 120(14):6557–6565, April 2004. [cited at p. 14, 15, 163]

[48] S. Ptasinska, S. Denifl, P. Scheier, and T.D. Mark. Inelastic electron interaction (attachment/ionization) with deoxyribose. *J. Chem. Phys.*, 120(18):8505–8511, May 2004. [cited at p. 14]

[49] I. Bald, J. Kopyra, and E. Illenberger. Selective excision of C5 from D-Ribose in the gas phase by Low-Energy electrons (0-1 eV): Implications for the mechanism of DNA damage. *Angewandte Chemie International Edition*, 45(29):4851–4855, July 2006. [cited at p. 14]

[50] C. König, J. Kopyra, I. Bald, and E. Illenberger. Dissociative electron attachment to phosphoric acid esters: The direct mechanism for single strand breaks in DNA. *Phys. Rev. Lett.*, 97(1):018105, July 2006. [cited at p. 14]

[51] J. Horáček, M. Čížek, and W. Domcke. Generalization of the nonlocal resonance model for low-energy electron collisions with hydrogen halides: the variable threshold exponent. *Theoretical Chemistry Accounts: Theory, Computation, and Modeling Theoretica Chimica Acta)*, 100(1):31–35, November 1998. [cited at p. 14]

[52] G. A. Gallup and I. I. Fabrikant. Vibrational feshbach resonances in dissociative electron attachment to uracil. *Phys. Rev. A*, 83(1):012706, January 2011. [cited at p. 15]

[53] F. A. Gianturco and R. R. Lucchese. Radiation damage of biosystems mediated by secondary electrons: Resonant precursors for uracil molecules. *J. Chem. Phys.*, 120:7446–7455, 2004. [cited at p. 15, 63, 163, 191]

[54] F. A. Gianturco, F. Sebastianelli, R. R. Lucchese, I. Baccarelli, and N. Sanna. Ring-breaking electron attachment to uracil: Following bond dissociations via evolving resonances. *J. Chem. Phys.*, 128:1714302–8, 2008. [cited at p. 15, 63, 163, 191]

[55] A. Grandi, F. A. Gianturco, and N. Sanna. H^- desorption from uracil via metastable electron capture. *Phys. Rev. Lett.*, 93:048103, 2004. [cited at p. 15, 63, 148, 154, 163, 192]

[56] C. Winstead and V. McKoy. Low-energy electron collisions with gas-phase uracil. *J. Chem. Phys.*, 125:174304–8, 2006. [cited at p. 15, 63, 154, 155, 163, 191, 192]

[57] S. Tonzani and C.H. Greene. Low-energy electron scattering from DNA and RNA bases: Shape resonances and radiation damage. *J. Chem. Phys.*, 124(5):054312, 2006. [cited at p. 15]

[58] S. Yalunin and S. B. Leble. Multiple-scattering and electron-uracil collisions at low energies. *Eur. Phys. J. Special Topics*, 144:115–122, 2007. [cited at p. 15, 63, 163]

[59] A. Dora, J. Tennyson, L. Bryjko, and Tanja van Mourik. R-matrix calculation of low-energy electron collisions with uracil. *J. Chem. Phys.*, 130:164307, 2009. [cited at p. 15, 52, 66, 67, 71, 131, 154, 155, 157, 162, 163, 197, 198]

[60] C. Winstead and V. McKoy. Resonant channel coupling in electron scattering by pyrazine. *Phys. Rev. Lett.*, 98:113201, 2007. [cited at p. 15, 63, 97]

[61] C. Winstead and V. McKoy. Interaction of low-energy electrons with the purine bases, nucleosides, and nucleotides of DNA. *J. Chem. Phys.*, 125(24), December 2006. [cited at p. 16]

[62] Amar Dora, Lilianna Bryjko, Tanja van Mourik, and Jonathan Tennyson. Low-energy electron scattering with the purine bases of DNA/RNA using the R-matrix method. *J. Chem. Phys.*, 136(2):024324, 2012. [cited at p. 16, 155, 157, 184, 197]

[63] A. Dora, L. Bryjko, T. van Mourik, and J. Tennyson. R-matrix study of elastic and inelastic electron collisions with cytosine and thymine. *J. Phys. B: At. Mol. Opt. Phys.*, 45(17):175203, September 2012. [cited at p. 16, 157, 184, 191, 197]

[64] Yong-Feng Wang and Shan Xi Tian. Shape resonance states of the low-energy electron attachments to DNA base tautomers. *Phys. Chem. Chem. Phys.*, 13(13):6169, 2011. [cited at p. 16, 154, 191]

[65] C. Winstead and V. McKoy. Low-energy electron scattering by deoxyribose and related molecules. *J. Chem. Phys.*, 125(7):074302–074302–6, August 2006. [cited at p. 16]

[66] I. Baccarelli, F. Sebastianelli, F. A. Gianturco, and N. Sanna. Modelling dissociative dynamics of biosystems after metastable electron attachment: the sugar backbones. *Eur. Phys. J. D.*, 51(1):131–136, January 2009. [cited at p. 16]

[67] R.F. da Costa, M.H.F. Bettega, M.T. do N. Varella, and M.A.P. Lima. Electron collisions with α-D-glucose and β-D-glucose monomers. *J. Chem. Phys.*, 132(12):124309–124309–7, March 2010. [cited at p. 16]

[68] S. Tonzani and C.H. Greene. Radiation damage to DNA: electron scattering from the backbone subunits. *J. Chem. Phys.*, 125(9):094504–094504–7, September 2006. [cited at p. 16]

[69] C.S. Trevisan, A.E. Orel, and T.N. Rescigno. Elastic scattering of low-energy electrons by tetrahydrofuran. *J. Phys. B: At. Mol. Opt. Phys.*, 39(12):L255–L260, June 2006. [cited at p. 16]

[70] D. Bouchiha, J.D. Gorfinkiel, L.G. Caron, and L. Sanche. Low-energy electron collisions with tetrahydrofuran. *J. Phys. B: At. Mol. Opt. Phys.*, 39(4):975–986, February 2006. [cited at p. 16]

[71] C. Winstead, V. McKoy, and S. Sanchez. Interaction of low-energy electrons with the pyrimidine bases and nucleosides of DNA. *J. Chem. Phys.*, 127:085105, 2007. [cited at p. 16, 64]

[72] J.M. Carr, P. Galiatsatos, J. Gorfinkiel, A. Harvey, M. Lysaght, D. Madden, Z. Mašín, M. Plummer, J. Tennyson, and H. Varambhia. UKRmol: a low-energy electron- and positron-molecule scattering suite. *Eur. Phys. J. D.*, 66:1–11, 2012. [cited at p. 17, 32, 55, 56, 59]

[73] H. Friedrich. *Theoretical Atomic Physics.* Birkhäuser, 2006. [cited at p. 24, 26, 41, 42, 219]

[74] P. G. Burke, A. Hibbert, and W. D. Robb. Electron scattering by complex atoms. *J. Phys. B: At. Mol. Opt. Phys.*, 4(2):153–161, 1971. [cited at p. 28]

[75] C. Bloch. Une formulation unifiée de la théorie des réactions nucléaires. *Nucl. Phys.*, 4(4):503–528, 1957. [cited at p. 29]

[76] T. Helgaker, P. Jørgensen, and J. Olsen. *Molecular Electronic-Structure Theory.* John Willey & Sons, England, 2000. [cited at p. 34, 158]

[77] K. L. Baluja, P. G. Burke, and L. A. Morgan. R-matrix propagation program for solving coupled second-order differential equations. *Comput. Phys. Commun.*, 27(3):299–307, September 1982. [cited at p. 39]

[78] M. Gailitis. New forms of asymptotic expansions for wavefunctions of charged-particle scattering. *J. Phys. B: At. Mol. Opt. Phys.*, 9(5):843–854, 1976. [cited at p. 41, 42]

[79] A. U. Hazi. Behavior of the eigenphase sum near a resonance. *Phys. Rev. A*, 19:920–922, 1979. [cited at p. 42]

[80] I. Baccarelli, F. Sebastianelli, F. A. Gianturco, and N. Sanna. Modelling dissociative dynamics of biosystems after metastable electron attachment: the sugar backbones. *Eur. Phys. J. D.*, 51(1):131–136, January 2009. [cited at p. 42, 144]

[81] I. Shimamura, E. Brändas C.A. Nicolaides, and J.R. Sabin. Chapter 4 - Quasi-Bound states of electronic and positronic Few-Body systems: Analysis of multichannel scattering information. In *Advances in Quantum Chemistry*, volume 63, pages 165–245. Academic Press, 2012. [cited at p. 42, 43]

[82] F.T. Smith. Lifetime matrix in collision theory. *Phys. Rev.*, 118(1):349–356, April 1960. [cited at p. 43]

[83] A. Szabó and N.S. Ostlund. *Modern quantum chemistry: introduction to advanced electronic structure theory.* Courier Dover Publications, 1996. [cited at p. 45]

[84] P.G. Szalay, T. Müller, G. Gidofalvi, H. Lischka, and R. Shepard. Multiconfiguration self-consistent field and multireference configuration interaction methods and applications. *Chem. Rev.*, 112(1):108–181, January 2012. [cited at p. 46]

[85] B.O. Roos. The complete active space Self-Consistent field method and its applications in electronic structure calculations. In *Adv. Chem. Phys.*, volume 69, pages 399–445. John Wiley & Sons, Inc., Hoboken, NJ, USA, 1987. [cited at p. 46, 48]

[86] Christopher J. Cramer. *Essentials of computational chemistry: theories and models.* John Wiley and Sons, 2004. [cited at p. 47, 48]

[87] N.F. Mott and H.S.W. Massey. *The Theory of atomic collisions.* Oxford University Press, 3rd edition, 1965. [cited at p. 50]

[88] J. Tennyson. R-matrix calculation of rydberg states of CO. *J. Phys. B: At. Mol. Opt. Phys.*, 29:6185–6201, 1996. [cited at p. 52]

[89] J.D. Gorfinkiel and J. Tennyson. Electron impact ionization of small molecules at intermediate energies: the molecular R-matrix with pseudostates method. *J. Phys. B: At. Mol. Opt. Phys.*, 38(11):1607–1622, June 2005. [cited at p. 54]

[90] R. D. Johnson III Editor. NIST Standard Reference Database Number 101, August 2011. [cited at p. 54, 55, 64]

[91] A. Faure, J. D. Gorfinkiel, L. A. Morgan, and J. Tennyson. GTOBAS: fitting continuum functions with gaussian-type orbitals. *Comput. Phys. Commun.*, 144:224–241, 2002. [cited at p. 57, 71]

[92] N. Sanna and F. A. Gianturco. Differential cross sections for electron/positron scattering for polyatomic molecules. *Comput. Phys. Commun.*, 114:142–167, 1998. [cited at p. 58, 132, 229, 230, 231]

[93] Shih-I Chu and A. Dalgarno. Rotational excitation of CH^+ by electron impact. *Phys. Rev. A*, 10(3):788–792, 1974. [cited at p. 58, 133, 147, 234]

[94] G. Schaftenaar and J.H. Noordik. Molden: a pre- and post-processing program for molecular and electronic structures. *J. Comput.-Aided Mol. Design*, 14:123–134, 2000. [cited at p. 59, 174, 175]

[95] Z. Mašín and J. D. Gorfinkiel. Elastic and inelastic low-energy electron collisions with pyrazine. *J. Chem. Phys.*, 135(14):144308, 2011. [cited at p. 61]

[96] Z. Mašín and Jimena D. Gorfinkiel. Shape and core excited resonances in electron collisions with diazines. *J. Chem. Phys.*, 137(20):204312–204312–14, November 2012. [cited at p. 61, 107, 113]

[97] J. B. Maljković, A. R. Milosavljević, F. Blanco, D. Šević, G. García, and B. P. Marinković. Absolute differential cross sections for elastic scattering of electrons from pyrimidine. *Phys. Rev. A*, 79:052706, 2009. [cited at p. 63]

[98] D.B. Jones, S.M. Bellm, P. Limo-Vieira, and M.J. Brunger. Low-energy electron scattering from pyrimidine: Similarities and differences with benzene. *Chem. Phys. Lett.*, 535(0):30–34, May 2012. [cited at p. 63]

[99] D. B. Jones, S. M. Bellm, F. Blanco, M. Fuss, G. Garca, P. Limo-Vieira, and M. J. Brunger. Differential cross sections for the electron impact excitation of pyrimidine. *J. Chem. Phys.*, 137(7):074304–074304–8, August 2012. [cited at p. 63]

[100] P. L. Levesque, M. Michaud, and L. Sanche. Absolute vibrational and electronic cross sections for low-energy electron (2–12 eV) scattering from condensed pyrimidine. *J. Chem. Phys.*, 122(9):094701, 2005. [cited at p. 63, 118, 119, 120, 121]

[101] S. Tonzani and C. H. Greene. Low-energy electron scattering from DNA and RNA bases: Shape resonances and radiation damage. *J. Chem. Phys.*, 124:054312, 2006. [cited at p. 64, 163]

[102] A Zecca, L Chiari, G García, F Blanco, E Trainotti, and M J Brunger. Total cross sections for positron and electron scattering from pyrimidine. *J. Phys. B: At. Mol. Opt. Phys.*, 43:215204, 2010. [cited at p. 64]

[103] T.D. Scarborough, D.B. Foote, and C. J. G. J. Uiterwaal. Ultrafast resonance-enhanced multiphoton ionization in the azabenzenes: Pyridine, pyridazine, pyrimidine, and pyrazine. *J. Chem. Phys.*, 136(5):054309–054309–6, February 2012. [cited at p. 64]

[104] I. C. Walker and M. H. Palmer. The electronic states of the azines. IV. Pyrazine, studied by VUV absorption, near-threshold electron energy-loss spectroscopy and ab initio multi-reference configuration interaction calculations. *Chem. Phys.*, 153:169–187, 1991. [cited at p. 64, 65, 127]

[105] M.H. Palmer, I.C. Walker, M.F. Guest, and A. Hopkirk. The electronic states of the azines. III. pyrimidine, studied by VUV absorption, near-threshold electron energy-loss spectroscopy and ab initio multi-reference configuration calculations. *Chem. Phys.*, 147(1):19–33, October 1990. [cited at p. 64, 65, 108, 115, 117, 127, 129]

[106] M.H. Palmer and I.C. Walker. The electronic states of the azines. V. pyridazine, studied by VUV absorption, near threshold electron energy-loss spectroscopy and ab-initio multireference configuration-interaction calculations. *Chem. Phys.*, 157(1-2):187–200, November 1991. [cited at p. 64, 65, 123, 124, 125, 127, 129]

[107] G. L. Blackman, R. D. Brown, and F. R. Burden. Microwave spectrum, dipole moment, and nuclear quadrupole coupling constants of pyrimidine. *J. Mol. Spectrosc.*, 35(3):444–&, 1970. [cited at p. 64, 108, 127]

[108] W. Werner, H. Dreizler, and H.D. Rudolph. Zum mikrowellenspektrum des pyridazins. *Zeitschrift fur naturforschung part A*, A 22(4):531–&, 1967. [cited at p. 64, 124, 127]

[109] K. K. Innes, I. G. Ross, and W. R. Moomaw. Electronic states of azabenzenes and azanaphthalenes: A revised and extended critical review. *J. Mol. Spect.*, 132:492–544, 1988. [cited at p. 65, 66, 125, 129]

[110] M. Oku, Yu Hou, Xi Xing, B. Reed, H. Xu, C. Chang, Cheuk-Yiu Ng, K. Nishizawa, K. Ohshimo, and T. Suzuki. 3s rydberg and cationic states of pyrazine studied by photoelectron spectroscopy. *J. Phys. Chem. A*, 112(11):2293–2310, March 2008. [cited at p. 65, 68]

[111] C.F. Dion and E.R. Bernstein. On the low-lying rydberg states of azabenzenes. *J. Chem. Phys.*, 103(12):4907–4913, September 1995. [cited at p. 65]

[112] Yoshiteru Matsumoto, Sang Kyu Kim, and Toshinori Suzuki. Femtosecond photoelectron imaging of pyridazine: S_1 lifetime and $(3s(n^{-1}),3p(n^{-1}))$ Rydberg state energetics. *J. Chem. Phys.*, 119(1):300, 2003. [cited at p. 65]

[113] F. Ferreira da Silva, D. Almeida, G. Martins, A. R. Milosavljevic, B. P. Marinkovic, S. V. Hoffmann, N. J. Mason, Y. Nunes, G. García, and P. Limão Vieira. The electronic states of pyrimidine studied by VUV photoabsorption and electron energy-loss spectroscopy. *Phys. Chem. Chem. Phys.*, 12(25):6717–6731, 2010. [cited at p. 65, 108, 109, 117, 121, 129]

[114] M. Stener, P. Decleva, D. M. P. Holland, and D. A. Shaw. A study of the valence shell electronic states of pyrimidine and pyrazine by photoabsorption spectroscopy and time-dependent density functional theory calculations. *J. Phys. B: At. Mol. Opt. Phys.*, 44(7):075203, 2011. [cited at p. 65, 66, 108, 109, 115, 117, 119, 120, 121, 128, 129, 130, 159]

[115] G. Fischer, Z.-L. Cai, J. R. Reimers, and P. Wormell. Singlet and triplet valence excited states of pyrimidine. *J. Phys. Chem. A*, 107(17):3093–3106, may 2003. [cited at p. 65, 108, 109, 115, 117, 122, 129, 144]

[116] R. J. Suffolk. The photoelectron spectra of the perfluorodiazines. *J. Electron Spectrosc. Relat. Phenom.*, 3:53, 1974. [cited at p. 65]

[117] N. S. Hush and A. S. Cheung. Ionization potentials and donor properties of nucleic acid bases and related compounds. *Chem. Phys. Lett.*, 34(1):11 – 13, 1975. [cited at p. 65, 164]

[118] B. O. Roos, K. Andersson, and M. P. Fülscher. Towards an accurate molecular orbital theory for excited states: the benzene molecule. *Chem. Phys. Lett.*, 192(1):5–13, April 1992. [cited at p. 65]

[119] M. P. Fülscher, K. Andersson, and B. O. Roos. Toward an accurate molecular orbital theory for excited states: the azabenzenes. *J. Phys. Chem.*, 96:9204–9212, 1992. [cited at p. 65, 66]

[120] P. Weber and J. Reimers. Ab initio and density functional calculations of the energies of the singlet and triplet valence excited states of pyrazine. *J. Phys. Chem. A*, 103:9821–9829, 1999. [cited at p. 65, 66, 67, 68, 129, 158]

[121] M. Schreiber, M. R. Silva-Junior, S. P. A. Sauer, and W. Thiel. Benchmarks for electronically excited states: CASPT2, CC2, CCSD, and CC3. *J. Chem. Phys.*, 128(13):134110–25, April 2008. [cited at p. 65, 108, 123, 128, 158, 164, 235]

[122] C. Woywod, A. Papp, G. Halsz, and A. Vibk. Theoretical investigation of the electronic spectrum of pyrazine. *Th. Chim. Acta*, 125:521–533, 2010. [cited at p. 65, 68]

[123] Y. Li, J. Wan, and X. Xu. Theoretical study of the vertical excited states of benzene, pyrimidine, and pyrazine by the symmetry adapted cluster-configuration interaction method. *J. Comp. Chem.*, 28:1658–1667, 2007. [cited at p. 65, 68, 129]

[124] H.-J. Werner, P. J. Knowles, R. Lindh, F. R. Manby, M. Schütz, and et al. *MOLPRO, version 2009.1, a package of ab initio programs.*, 2009. [cited at p. 67, 108]

[125] C. W. Bauschlicher. The construction of modified virtual orbitals (MVO's) which are suited for configuration interaction calculations. *J. Chem. Phys.*, 72:880, 1980. [cited at p. 67]

[126] D. Bouchiha, J. D. Gorfinkiel, L. G. Caron, and L. Sanche. Low-energy electron collisions with tetrahydrofuran. *J. Phys. B: At. Mol. Opt. Phys.*, 39:975–986, 2006. [cited at p. 71]

[127] M. Tarana and J. Tennyson. Polarization effects in electron collisions with Li_2: application of the molecular R-matrix method with pseudostates. *J. Phys. B: At. Mol. Opt. Phys.*, 41:205204, 2008. [cited at p. 71, 75]

[128] J. D. Gorfinkiel and J. Tennyson. Electron-H_3^+ collisions at intermediate energies. *J. Phys. B: At. Mol. Opt. Phys.*, 37:L343, 2004. [cited at p. 72]

[129] P. Palihawadana, J. P. Sullivan, S. J. Buckman, and M. J. Brunger. Electron scattering from pyrazine: Elastic differential and integral cross sections. *J. Chem. Phys.*, 137(20):204307–204307–7, November 2012. [cited at p. 83, 84]

[130] Z. Mašín, J. D. Gorfinkiel, D. B. Jones, S. M. Bellm, and M. J. Brunger. Elastic and inelastic cross sections for low-energy electron collisions with pyrimidine. *J. Chem. Phys.*, 136(14):144310–144310–10, April 2012. [cited at p. 107, 115]

[131] Y. J. Li, J. Wan, and X. Xu. Theoretical study of the vertical excited states of benzene, pyrimidine, and pyrazine by the symmetry adapted cluster-configuration interaction method. *J. Comput. Chem.*, 28(10):1658–1667, 2007. [cited at p. 115, 117]

[132] Marcel Nooijen. Similarity transformed equation of motion coupled-cluster study of excited states of selected azabenzenes. *Spectrochim. Acta A*, 55:539–559, 1999. [cited at p. 115]

[133] M. J. Brunger and S. J. Buckman. Electron-molecule scattering cross-sections. I. Experimental techniques and data for diatomic molecules. *Phys. Rep.*, 357:215–458, 2002. [cited at p. 116]

[134] Y. Itikawa. Vibrational excitation of polyatomic molecules by electron collisions. *J. Phys. B: At. Mol. Opt. Phys.*, 37(3):R1–R24, 2004. [cited at p. 116]

[135] M. Ohno and W. Domcke. Theory of resonance and threshold effects in the electronic excitation of molecules by electron impact. *Phys. Rev. A*, 28(6):3315–3327, December 1983. [cited at p. 152]

[136] S. Feil, K. Gluch, S. Matt-Leubner, P. Scheier, J. Limtrakul, M. Probst, H. Deutsch, K. Becker, A. Stamatovic, and T.D. Mark. Partial cross sections for positive and negative ion formation following electron impact on uracil. *J. Phys. B: At. Mol. Opt. Phys.*, 37(15):3013–3020, August 2004. [cited at p. 163]

[137] K. Aflatooni, A.M. Scheer, and P.D. Burrow. Dissociative electron attachment in uracil: Total anion yield. *Chem. Phys. Lett.*, 408(46):426–428, June 2005. [cited at p. 163, 190]

[138] I. Chernyshova, J. Kontros, P. Markush, and O. Shpenik. Excitation of lowest electronic states of the uracil molecule by slow electrons. *Optics and Spectroscopy*, 113(1):5–8, 2012. [cited at p. 163, 164, 167]

[139] R. Sanchez, B. M. Giuliano, S. Melandri, L. B. Favero, and W. Caminati. Gas-phase tautomeric equilibrium of 4-hydroxypyrimidine with its ketonic forms: a free jet millimeterwave spectroscopy study. *J. Am. Chem. Soc.*, 129(19):6287–6290, May 2007. [cited at p. 164, 165]

[140] B. M. Giuliano, V. Feyer, K. C. Prince, M. Coreno, L. Evangelisti, S. Melandri, and W. Caminati. Tautomerism in 4-hydroxypyrimidine, s-methyl-2-thiouracil, and 2-thiouracil. *J. Phys. Chem. A*, 114(48):12725–12730, December 2010. [cited at p. 164]

[141] L. Lapinski, M. J. Nowak, A. Leś, and L. Adamowicz. Comparison of ab initio HF/6-31G**, HF/6-31++G** and MP2/6-31G** calculated infrared spectra of 4(3H)-pyrimidinone and 4-hydroxypyrimidine with matrix isolation spectra. *Vibrational Spectroscopy*, 8(3):331–342, March 1995. [cited at p. 164]

[142] G. Lamanna. Abinitio study of the tautomeric equilibria of hydroxydiazines in the vapor-phase. 2. 4-hydroxypyrimidine. *Theochem-Journal of Molecular Structure*, 37(1-2):83–87, June 1987. [cited at p. 164]

[143] M. Moreno and W. H. Miller. On the tautomerization reaction 2-pyridone - 2-hydroxypyridine: an ab initio study. *Chem. Phys. Lett.*, 171(56):475–479, August 1990. [cited at p. 164]

[144] L. Lapinski, R. Czerminski, M.J. Nowak, and J. Fulara. Ab initio, CNDO/2 and matrix isolation studies of 2-hydroxypyrimidine infrared absorption spectra. *J. Mol. Struct.*, 220(0):147–167, April 1990. [cited at p. 164]

[145] A. Leś and L. Adamowicz. The correlated molecular electrostatic potential and electric field of 2 (1H)-pyrimidone and 2-hydroxypyrimidine. *Chem. Phys.*, 153(3):409–414, June 1991. [cited at p. 164]

[146] L. D. Hatherley, R. D. Brown, P. D. Godfrey, A. P. Pierlot, W. Caminati, D. Damiani, S. Melandri, and L. B. Favero. Gas-phase tautomeric equilibrium of 2-pyridinone and 2-hydroxypyridine by microwave spectroscopy. *J. Phys. Chem.*, 97(1):46–51, January 1993. [cited at p. 164]

[147] S. Mata, V. Cortijo, W. Caminati, J. L. Alonso, M. E. Sanz, J. C. Loez, and S. Blanco. Tautomerism and microsolvation in 2-hydroxypyridine/2-pyridone. *J. Phys. Chem. A*, 114(43):11393–11398, November 2010. [cited at p. 164]

[148] K. Sakota, S. Tokuhara, and H. Sekiya. Dispersed fluorescence spectroscopy of 2-hydroxypyridine and its cyclically hydrogen-bonded water clusters in the gas phase: An examination of occurrence of excited-state proton transfer. *Chem. Phys. Lett.*, 448(46):159–163, November 2007. [cited at p. 164]

[149] M. R. Nimlos, D. F. Kelley, and E. R. Bernstein. Spectroscopy, structure, and proton dynamics of 2-hydroxypyridine and its clusters with water and ammonia. *J. Phys. Chem.*, 93(2):643–651, January 1989. [cited at p. 164]

[150] M. R. Silva-Junior, M. Schreiber, S. P. A. Sauer, and W. Thiel. Benchmarks of electronically excited states: Basis set effects on CASPT2 results. *J. Chem. Phys.*, 133(17), November 2010. [cited at p. 164, 165, 166, 167]

[151] E. Epifanovsky, K. Kowalski, P.D. Fan, M. Valiev, S. Matsika, and A.I. Krylov. On the electronically excited states of uracil. *J. Phys. Chem. A*, 112(40):9983–9992, October 2008. [cited at p. 164, 166, 167]

[152] T. Fleig, S. Knecht, and C. Hättig. Quantum-chemical investigation of the structures and electronic spectra of the nucleic acid bases at the coupled cluster CC2 level. *J. Phys. Chem. A*, 111(25):5482–5491, June 2007. [cited at p. 164]

[153] J. D. Petke, G. M. Maggiora, and R. E. Christoffersen. Ab initio configuration interaction and random phase approximation calculations of the excited singlet and triplet states of uracil and cytosine. *J. Phys. Chem.*, 96(17):6992–7001, 1992. [cited at p. 164, 166]

[154] J. Lorentzon, M. P. Fuelscher, and B. O. Roos. Theoretical study of the electronic spectra of uracil and thymine. *J. Am. Chem. Soc.*, 117(36):9265–9273, September 1995. [cited at p. 164, 166]

[155] N. A. Oyler and L. Adamowicz. Electron attachment to uracil: theoretical ab initio study. *J. Phys. Chem.*, 97(42):11122–11123, October 1993. [cited at p. 166]

[156] R. D. Brown, P. D. Godfrey, D. McNaughton, and A. P. Pierlot. Microwave spectrum of uracil. *J. Am. Chem. Soc.*, 110(7):2329–2330, March 1988. [cited at p. 166]

[157] L. B. Clark, G. G. Peschel, and I. Tinoco. Vapor spectra and heats of vaporization of some purine and pyrimidine bases1. *J. Phys. Chem.*, 69(10):3615–3618, October 1965. [cited at p. 167]

[158] H. H. H. Homeier and E. O. Steinborn. Some properties of the coupling coefficients of real spherical harmonics and their relation to gaunt coefficients. *J. Molec. Struct.*, 368:31–37, September 1996. [cited at p. 221]

[159] S. Altshuler. Theory of low-energy electron scattering by polar molecules. *Phys. Rev.*, 107(1):114, July 1957. [cited at p. 228]

[160] Y. Itikawa. Electron scattering by polar molecules. *Phys. Rep.*, 46(4):117–164, October 1978. [cited at p. 228]

[161] Y. Itikawa. Electron scattering from polar molecules: Frame transformation and the Born closure approximation. *Physics Essays*, 13(3):344–349, September 2000. [cited at p. 232]

Appendices

Appendix A

Potentials for the radial Close-Coupling equations

In this section we derive the expression for the coupling potentials (2.62):

$$V_{ij}(r) = \sum_{\lambda=0}^{\infty} a_{ij\lambda} r^{-\lambda-1}, \; i,j = 1,\ldots,n, \; r \geq a. \tag{A.1}$$

These potentials are defined in Section 2.3.2 using the formula (2.61):

$$V_{ij}(r) = \left(\Phi_i \mathcal{Y}_{l_i,m_i}(\hat{\mathbf{x}}_{N+1}) \middle| \sum_{p=1}^{N} \frac{1}{r_{p(N+1)}} - \sum_{k=1}^{Nuclei} \frac{Z_k}{\rho_{k(N+1)}} \middle| \Phi_j \mathcal{Y}_{l_j,m_j}(\hat{\mathbf{x}}_{N+1}) \right). \tag{A.2}$$

The derivation is based on the well known expansion of the Coulomb potential into Legendre polynomials [73]:

$$\frac{1}{r_{ij}} = \frac{1}{|\mathbf{r_i} - \mathbf{r_j}|} = \sum_{\lambda=0}^{\infty} \frac{{r_j}^{\lambda}}{r_i^{\lambda+1}} P_\lambda(\cos\theta), \; r_j < r_i, \tag{A.3}$$

where θ is the angle between the vectors $\mathbf{r_i}$ and $\mathbf{r_j}$, $(\cos\theta = \hat{\mathbf{r}}_i.\hat{\mathbf{r}}_j)$. We have assumed that $r_j < r_i$. In the outer region the distance of the scattering electron from the origin is always greater than that of the target molecules' electrons: $r_{N+1} > r_i$, $i = 1,\ldots,N$ and the molecule's nuclei (see Figure 2.1). Therefore in the expressions below, the radial distance of the scattering electron will always be in the denominator.

Using the Legendre expansion (A.3), we can calculate the contribution to the potentials

$V_{ij}(r)$ of the first term in (A.2):

$$\left(\Phi_i \mathcal{Y}_{l_i,m_i}(\hat{\mathbf{x}}_{N+1}) \Big| \sum_{p=1}^{N} \frac{1}{r_{p(N+1)}} \Big| \Phi_j \mathcal{Y}_{l_j,m_j}(\hat{\mathbf{x}}_{N+1})\right) = \tag{A.4}$$

$$= \sum_{\lambda=0}^{\infty} \frac{1}{r^{\lambda+1}} \sum_{p=1}^{N} \left(\Phi_i \mathcal{Y}_{l_i,m_i}(\hat{\mathbf{x}}_{N+1}) \big| P_\lambda(\hat{\mathbf{x}}_{N+1}.\hat{\mathbf{x}}_p) r_p^\lambda \big| \Phi_j \mathcal{Y}_{l_j,m_j}(\hat{\mathbf{x}}_{N+1})\right). \tag{A.5}$$

Utilizing the addition theorem of real spherical harmonics:

$$P_l(\hat{\mathbf{x}}_i.\hat{\mathbf{x}}_j) = \frac{4\pi}{2l+1} \sum_{m=-l}^{l} \mathcal{Y}_{lm}(\hat{\mathbf{x}}_i) \mathcal{Y}_{lm}(\hat{\mathbf{x}}_j), \tag{A.6}$$

we can carry out separately, in the preceding equation, the integrations over the coordinates of the target molecule's electrons and the angular coordinates of the scattering electron and obtain:

$$\sum_{\lambda=0}^{\infty} \frac{1}{r^{\lambda+1}} \sum_{p=1}^{N} \left(\Phi_i \mathcal{Y}_{l_i,m_i}(\hat{\mathbf{x}}_{N+1}) \big| P_\lambda(\hat{\mathbf{x}}_{N+1}.\hat{\mathbf{x}}_p) r_p^\lambda \big| \Phi_j \mathcal{Y}_{l_j,m_j}(\hat{\mathbf{x}}_{N+1})\right) = \tag{A.7}$$

$$= \sum_{\lambda=0}^{\infty} \sum_{m=-\lambda}^{\lambda} \frac{4\pi}{2\lambda+1} \frac{T_{ij}^{\lambda m}}{r^{\lambda+1}} \langle \mathcal{Y}_{l_i,m_i} | \mathcal{Y}_{\lambda,m} | \mathcal{Y}_{l_j,m_j} \rangle, \tag{A.8}$$

where the elements of the matrix $\mathbf{T}^{\lambda m}$ are given by the formula:

$$T_{ij}^{\lambda m} = \sum_{p=1}^{N} \langle \Phi_i | \mathcal{Y}_{\lambda,m}(\hat{\mathbf{x}}_p) r_p^\lambda | \Phi_j \rangle. \tag{A.9}$$

The second term in (A.2) is calculated similarly:

$$\left(\Phi_i \mathcal{Y}_{l_i,m_i}(\hat{\mathbf{x}}_{N+1}) \Big| - \sum_{k=1}^{Nuclei} \frac{Z_k}{\rho_{k(N+1)}} \Big| \Phi_j \mathcal{Y}_{l_j,m_j}(\hat{\mathbf{x}}_{N+1})\right) = \tag{A.10}$$

$$= -\sum_{\lambda=0}^{\infty} \frac{1}{r^{\lambda+1}} \sum_{k=1}^{Nuclei} \left(\Phi_i \mathcal{Y}_{l_i,m_i}(\hat{\mathbf{x}}_{N+1}) \Big| Z_k P_\lambda(\hat{\mathbf{x}}_{N+1}.\hat{\mathbf{R}}_k) R_k^\lambda \Big| \Phi_j \mathcal{Y}_{l_j,m_j}(\hat{\mathbf{x}}_{N+1})\right) = \tag{A.11}$$

$$= -\langle \Phi_i | \Phi_j \rangle \sum_{\lambda=0}^{\infty} \sum_{m=-\lambda}^{\lambda} \frac{4\pi}{2\lambda+1} \frac{1}{r^{\lambda+1}} \langle \mathcal{Y}_{l_i,m_i} | \mathcal{Y}_{\lambda,m} | \mathcal{Y}_{l_j,m_j} \rangle \sum_{k=1}^{Nuclei} Z_k \mathcal{Y}_{\lambda,m}(\hat{\mathbf{R}}_k) R_k^\lambda. \tag{A.12}$$

Collecting the two terms which we just evaluated (equations (A.8) and (A.12)) we get the

final expression for the coupling potentials $V_{ij}(r)$:

$$V_{ij}(r) = \sum_{\lambda=0}^{\infty} \frac{1}{r^{\lambda+1}} \times$$
$$\times \underbrace{\sum_{m=-\lambda}^{\lambda} \langle \mathcal{Y}_{l_i,m_i} | \mathcal{Y}_{\lambda,m} | \mathcal{Y}_{l_j,m_j} \rangle \underbrace{\frac{4\pi}{2\lambda+1} \left(T_{ij}^{\lambda m} - \langle \Phi_i | \Phi_j \rangle \sum_{k=1}^{Nuclei} Z_k \mathcal{Y}_{\lambda,m}(\hat{\mathbf{R}}_k) R_k^{\lambda} \right)}_{Q_{ij}^{\lambda m}}}_{a_{ij\lambda}}, \quad \text{(A.13)}$$

which conicides with (A.1). The coefficients $Q_{ij}^{\lambda m}$ are the spherical multipole transition moments of the electronic states of the target molecule. Finally, the term $\langle \mathcal{Y}_{l_i,m_i} | \mathcal{Y}_{\lambda,m} | \mathcal{Y}_{l_j,m_j} \rangle$ is an integral over three real spherical harmonics, which can be calculated using the formula [158]:

$$\langle \mathcal{Y}_{l_i,m_i} | \mathcal{Y}_{\lambda,m} | \mathcal{Y}_{l_j,m_j} \rangle = \sum_{m_2,m_3} \left[U_{l_i,m_2+m_3}^{m_i} \right]^* U_{\lambda,m_2}^{m} U_{l_j,m_3}^{m_j} \left(l_i, m_2 + m_3 | \lambda, m_2 || l_j, m_4 \right), \quad \text{(A.14)}$$

where the last term on the right hand side is the usual Clebsch-Gordan coefficient. The unitary matrix $\mathbf{U}$ provides the mapping between the complex and the real spherical harmonics and its form is:

$$U_{lm}^{\mu} = \delta_{m0}\delta_{\mu 0} + \frac{1}{\sqrt{2}} [\theta(\mu)\delta_{m\mu} + \theta(-\mu)(+\imath)(-1)^m \delta_{m\mu} + \theta(-\mu)(-\imath)\delta_{m-\mu} + \quad \text{(A.15)}$$
$$+ \theta(\mu)(-1)^m \delta_{m-\mu}],$$

with

$$\theta(m) = \begin{cases} 1 & \text{, for } m > 0, \\ 0 & \text{, for } m \leq 0. \end{cases} \quad \text{(A.16)}$$

The sum over λ in (A.13) formally extends to infinity, but in practice this sum is always finite, because of the finite number of the spherical harmonics included in the calculation and the triangular inequality for addition of the spherical harmonics:

$$\lambda = l_i + l_j, l_i + l_j - 1, \ldots, |l_i - l_j|. \quad \text{(A.17)}$$

Let l_M be the largest angular momentum of the scattering electron included in the calculation. We can see that the coupling coefficients $a_{ij\lambda}$ which can be nonzero correspond only to the

following values of λ:

$$\lambda = 0, 1, \ldots, 2l_M. \tag{A.18}$$

Appendix B

Short-range and long-range electron-molecule interactions

The purpose of this Appendix is to explain how some basic properties of the electron-molecule interaction translate into ab-initio models of electron-molecule collisions. In particular, we discuss the partial wave expansion of the wavefunction describing the scattering electron and its relation to the short and long-range contributions to the electron-molecule interaction. We also describe in detail some properties of electron scattering from polar target molecules and the use of the Born approximation, which is very important for these systems.

The interaction of the scattering electron with a molecule is a complex process which, due to electron correlation, cannot be reduced to a potential scattering problem. However, there are some elementary aspects of the collision which can be understood even from the simplest of approximations, which treats it as a potential scattering problem. We discuss this approach below. Generally, the electron-molecule interaction arises from contributions of various effects, which have short-range and long-range character. In this work we regard as short range those effects that can be approximately described by a potential with the asymptotic behaviour $\approx r^{-2-\epsilon}$, where $\epsilon > 0$. It follows that the long range effects asymptotically behave as $\approx r^{-2+\epsilon}$ with $\epsilon \geq 0$. Below we specify these two types of interactions in more detail:

- short-range interactions can be completely neglected beyond a certain distance from the center of mass of the molecule. Typically, this "cut-off radius" is not larger than a few diameters of the molecule. Electron exchange and the attractive force on the incoming electron due to the polarization of the target molecule are typical examples of such interactions.

- long-range interactions cannot be neglected even at large distances from the molecule. In this work we have encountered only one, albeit very important, example of this type of interaction: the dipolar interaction. This interaction occurs in collisions of electrons with molecules with a permanent dipole moment. Another type of long-range interaction is the Coulomb interaction, present in collisions with a charged molecule. However, since all the targets studied in this thesis are neutral, we do not discuss the Coulomb interaction here.

We can obtain a simple qualitative picture of the electron-molecule collision by modelling it as the incoming electron scattering from a spherically symmetric potential, approximately representing the electron-molecule interactions. This potential is constructed as a superposition of short-range and the long-range interaction potentials. In order to solve the potential scattering problem, one usually invokes the partial wave expansion of the scattering wavefunction and solves the scattering problem in each angular momentum channel separately (see Section 2.2). The total cross section is then obtained by summing the cross sections calculated separately for each partial wave.

The R-matrix method as described in detail in Section 2.3, also makes use of the partial-wave expansion (see Section 2.3.2). Therefore the discussion of the potential scattering picture of the electron-molecule collision below is relevant also for our ab-initio scattering calculations. For reasons which will be explained later, it is difficult to include in our ab-initio calculations a large number of partial waves of the scattering electron. It is therefore important to estimate the minimum number of partial waves required to obtain converged cross sections. It will be shown below that this number depends strongly on the character of the electron-molecule interaction (i.e. if it has a long-range component or not).

B.1 Short-range interactions

For neutral, non-polar molecules (e.g. pyrazine) the only significant interactions affecting the collision are the short-range interactions. In this case the number of partial waves of the scattering electron (for low-energy collisions) which need to be included in the calculation is usually small (up to $l = 4$). In order to understand this fact we reduce the full complexity of electron collision with a neutral non-polar molecule to a simplified picture of electron

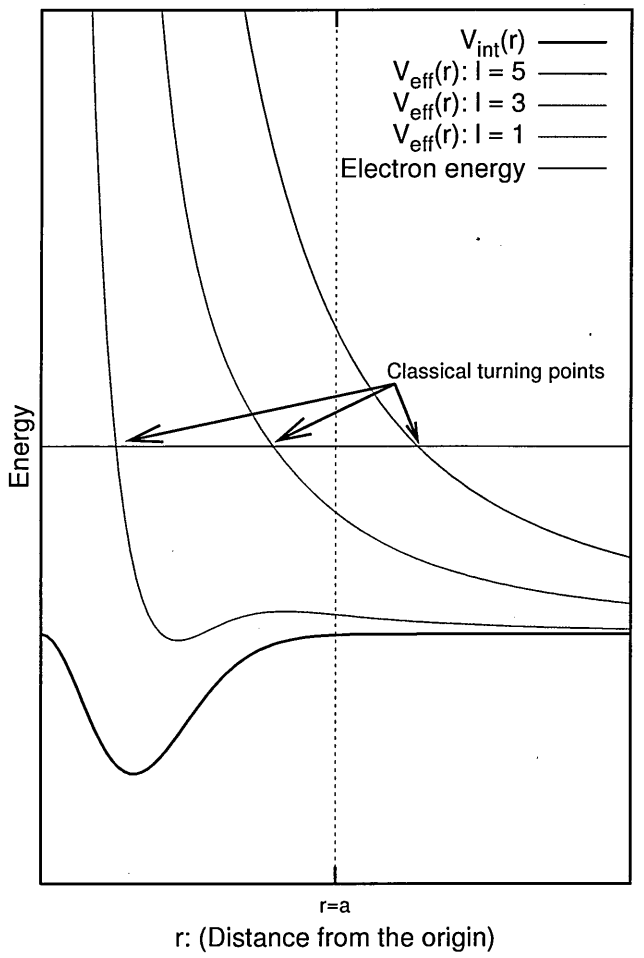

Figure B.1: A simplified, potential scattering, picture of electron-molecule collision. The approximate short-range interaction potential $V_{int}(r)$ is shown together with the effective potentials $V_{eff}(r) = V_{int}(r) + \frac{l(l+1)}{2r^2}$ for scattering in selected partial waves: $l = 1, 3, 5$. The effective potential for s-wave ($l = 0$) scattering is equivalent to $V_{int}(r)$. The vertical dashed line delimits the range of the short-range interaction (i.e. $V_{int} \approx 0$ for $r > a$). The pink line shows the energy of the incoming electron. The arrows mark the positions of the classical turning points for each of the effective potential curves shown.

scattering from a static *short-range* spherically symmetric potential $V_{int}(r)$:

$$V_{int}(r) = 0, \; r \geq a, \tag{B.1}$$

$$V_{int}(r) = V(r), \; r < a. \tag{B.2}$$

Figure B.1 shows (qualitatively) effective potential curves for scattering in partial waves for different angular momenta of the scattering electron. The vertical line $r = a$ denotes the range of the short-range potential. The horizontal line represents the energy of the scattering electron. In the following it will be important to keep in mind that we are interested in *low-energy* collisions only. The most important feature of the potential curves for $l \neq 0$ is their strong increasing character towards $r \to 0$. This is caused by the angular momentum barrier of the $\frac{l(l+1)}{2r^2}$ potential. We can see that the potential curve for $l = 0$ (i.e. that of $V_{int}(r)$) does not exhibit any classical turning points. * Consequently, the wavefunction in this channel

*The classical turning point is defined as the radial distance r_0 for which the following holds:

$$E = V_{int}(r_0) + \frac{l(l+1)}{2r_0^2}, \tag{B.3}$$

where E is the energy of the scattering electron.

is going to extend over the whole radial range and will be very sensitive to the details of the short-range interaction (potential). For partial waves with $l = 1$ the classical turning point appears within the range of the short-range potential. As we increase the angular momentum of the scattering electron, the turning point moves further away from $r = 0$ towards larger values of r. For the partial wave $l = 5$ the classical turning point is located at $r > a$, i.e. beyond the range of the short-range potential. Consequently, the wavefunction in this channel will differ only slightly from the wavefunction of the free electron. (The scattering wavefunction decays exponentially in the region to the left of the classical turning point and therefore will be only negligibly affected by the interaction potential $V_{int}(r)$). For partial waves with even larger l, we can completely neglect the effect of the electron-molecule interaction on the scattering electron. We have thus demonstrated that for neutral non-polar molecules, the partial wave expansion of the wavefunction of the scattering electron converges very rapidly.

B.2 Long-range interactions and the Born correction

Having understood the effects of short-range electron-molecule interactions on the number of partial waves to be included in the calculation, we can now explain how the *long-range* dipolar interaction affects the number of partial waves that are needed. In this case we can write our simple electron-molecule interaction potential as a superposition of the short-range interaction and the long-range dipolar interaction. The potential of electron in the field of a point dipole has the form:

$$V_{dip}(r, \theta) = \frac{-\mu \cos\theta}{r^2}, \tag{B.4}$$

where μ is the dipole moment (in a.u.) of the target molecule, θ is defined by the direction of the incoming electron with respect to the dipole and r is the distance from the center of coordinates. Clearly, this potential does not possess a sharp cut-off point and decreases with the distance in the same way ($\sim r^{-2}$) as the potential associated with the angular momentum barrier of the scattering electron. Consequently, we cannot clearly delimit the range of the electron-molecule interaction with respect to the angular momentum barrier: the long-range dipolar interaction prevents us from doing so. Therefore, it is advisable to include in the calculation as many partial waves as possible to account for the fact that the dipolar interaction affects scattering in *all* partial waves.

However, in R-matrix calculations, it is customary to include partial waves up to $l = 4$ or

$l = 5$ only. The inclusion of higher partial waves increases the computational requirements and causes further problems. First of all, the number of integrals needed for construction of the Hamiltonian matrix depends on the number of partial waves of the continuum electron included in the calculation. (The number of the integrals needed scales as n^4, where n is the number of one-electron basis functions for both the target electrons and the scattering electron). Therefore, including partial waves with high values of l causes a rapid increase in the compute time. Secondly, the basis functions of the continuum need to be orthogonalized to all target molecular orbitals and among themselves (see Section 2.7). It follows that as the number of the continuum basis functions increases it becomes more and more difficult to perform the orthogonalization leading to the deletion of more and more continuum basis functions with obvious consequences for the quality of representation of the continuum wavefunction. These problems are particularly pronounced for calculations using a diffuse target atomic basis set: in this case the orthogonalization step is especially difficult due to the possible similarities between some of the diffuse target orbitals and the (naturally) diffuse continuum functions.

We can see that including in the *ab-initio* calculations a large number of partial waves is complicated. Therefore, in order to fully account for the dipolar interaction, we resort to approximate methods for calculating the contributions of the partial waves corresponding to higher angular momenta. For this task the first Born approximation [18] is sufficient. This means that the we can apply a Born correction for calculation of the cross sections: the contributions of the partial waves with small angular momenta are calculated ab-initio and those with large angular momenta using the Born approximation.

The Born approximation is very accurate for the large angular momenta, which are not significantly affected by the short-range effects arising for example from the polarization of the target molecule. The contributions from the partial waves corresponding to the small angular momenta have to be calculated using accurate methods. However, in the intermediate range of values of angular momentum, the effects of the short-range interactions on the partial waves may not be negligible. This is due to the nonspherical nature of the dipolar interaction, evident from equation (B.4), which causes strong coupling of partial waves with different angular momentum (for a given l the partial waves coupled are $l+1$, l and $l-1$). In this way the effects associated with the short-range part of the electron-molecule interaction (described by the partial waves with small l) can be propagated into partial waves with larger l. Consequently, it is advisable to include in the ab-initio calculation for a polar target molecule as many partial waves as possible in order represent as accurately as possible the

effects associated with the intermediate values of angular momentum.

The long-range character of the dipolar interaction is responsible not only for the large number of scattered partial waves required, but also for the divergence of the *fixed-nuclei* cross sections. It is trivial to calculate the scattering amplitude and the differential cross section (DCS) for electron scattering from a fixed dipole using the first Born approximation [159]:

$$\frac{d\sigma}{d\Omega} = |f_{\mathbf{p}\to\mathbf{p}'}(\theta)|^2, \tag{B.5}$$

$$f_{\mathbf{p}\to\mathbf{p}'}(\theta) = \imath\frac{2\mu\cos\gamma}{q}, \tag{B.6}$$

$$q^2 = 2p^2(1-\cos\theta) \tag{B.7}$$

where μ is the dipole moment of the molecule, p is the momentum of the electron, q is the momentum transfer, θ the scattering angle and γ is the angle between the orientation of the dipole and the vector of the momentum transfer. We can see from the formulas above that as $\theta \to 0$ the DCS diverges to infinity. Consequently, the integral cross section diverges as well. In fact the divergence of the DCS is a property common for all *fixed-nuclei* calculations (i.e. not only within the first Born approximation) for dipolar molecules.

In order to remove the divergent behaviour of the dipolar scattering cross section it is necessary to include molecular rotations into the model. Generally, this approach leads to a set of close-coupling equations. If we model the molecule as a rigid rotor and use again the first Born approximation, we obtain the following formula for the scattering amplitude [160]:

$$f^B_{j_0,\mathbf{p}\to j,\mathbf{p}_j}(\theta) = \frac{4\mu^2}{3}\frac{p_j}{p}\frac{j}{2j_0+1}\frac{1}{q^2}\delta_{j,j_0\pm1}, \tag{B.8}$$

$$q^2 = p^2 + p_j^2 - 2pp_j\cos\theta, \tag{B.9}$$

where j_0 and j are, respectively, the initial and final rotational states of the molecule. Similarly, p_j is the momentum of the outgoing electron in the channel corresponding to the final rotational state. The selection rule $\delta_{j,j0\pm1}$ can be shown to originate from the simple $\cos\theta$ angular dependence of the dipole potential. Clearly, the selection rule now implies a *finite* Born cross section for all scattering angles. Specifically, the selection rule $\Delta J = 1$ applied to scattering from the ground rotational state implies that the Born correction needs to be calculated only for the rotational transition $0 \to 1$: the first Born correction is zero for transitions to any higher rotational states. The reason why the divergent behaviour of the Born correction has disappeared is that the molecular rotations effectively average out the prob-

lematic asymptotic behaviour of the fixed point-dipole potential. Finally, we remark that the Born correction is generally valid only in cases for which the dipole moment is not too large, so that the dipolar interaction can be treated, correctly, only as a perturbation.

B.2.1 Implementation of the Born-correction for the elastic cross sections

We use the program POLYDCS [92] to calculate Born-corrected elastic differential and integral cross sections. This program calculates the total (differential or integral) *electronically elastic* cross sections in the Born approximation, adds to them the partial cross section calculated *ab-initio* for partial waves up to l_{max} and then subtracts partial cross sections for $l \leq l_{max}$ determined within the Born approximation. However, before we describe how the Born correction is implemented in the POLYDCS program we need to describe first the procedure for calculation of the DCS from the *fixed-nuclei* **K**-matrices.

In the following we provide only the equations necessary to understand the principles of the calculation of the DCS. The full derivation of these equations can be found in [92]. If we neglect the rotational state of the target molecule then the DCS for elastic electron scattering from the molecule into a solid angle $d\Omega$ is defined using the following formula:

$$\frac{d\sigma}{d\Omega} = \frac{1}{8\pi^2}\int |f_{SF}(\mathbf{k}.\mathbf{r};\alpha,\beta,\gamma)|^2 d\Omega_M, \tag{B.10}$$

where α, β, γ are the three Euler angles specifying the orientation of the molecule in the space-fixed (SF) frame of reference, $f_{SF}(\mathbf{k}.\mathbf{r};\alpha,\beta,\gamma)$ is the space-fixed scattering amplitude for an electron incoming with momentum $\mathbf{k}$ and scattering into the direction $\mathbf{r}$ and $d\Omega_M$ indicates integration over the three Euler angles. In other words the DCS is obtained averaging the squared modulus of the scattering amplitude f_{SF} over all molecular orientations with respect to the fixed directions of the vectors $\mathbf{k}$ and $\mathbf{r}$.

The ab-initio calculations, which we use to provide an accurate description of the scattering process for the partial waves $l \leq l_{max}$, are carried out in the body-fixed (BF) frame of reference and hence provide the scattering amplitude f_{BF} for the body-fixed frame of reference. The connection between f_{BF} and the elements of the **S**-matrix, determined ab-initio[†], is given by the equation:

$$f_{BF}(\mathbf{k}.\mathbf{r}) = \frac{2\pi}{\imath k}\sum_{lhl'h'p\mu} X^{p\mu}_{lh}(\hat{\mathbf{k}}) X^{p\mu}_{l'h'}(\hat{\mathbf{r}}) \imath^{l-l'} (S^{p\mu}_{lh,l'h'} - \delta_{ll'}\delta_{hh'}), \tag{B.11}$$

[†]Our ab-initio calculations determine the **K**-matrix rather than the **S**-matrix, but both approaches are equivalent and all equations in this Section can be rewritten using the **K**-matrix.

where $X_{lh}^{p\mu}$ are symmetry-adapted functions which belong to the μ-th component of the p-th irreducible representation, with h distinguishing between different basis with the same set of $|p\mu l\rangle$ indices. These functions can be expressed as finite linear combinations of real spherical harmonics. The terms in brackets on the right hand side are in fact elements of the **T**-matrix.

Connecting f_{BF} with its space-fixed equivalent (f_{SF}) is a matter of rotating the functions $X_{l'h'}^{p\mu}(\hat{\mathbf{r}})$ and $X_{lh}^{p\mu}(\hat{\mathbf{k}})$ using the frame-transformation between the BF and the SF frames of reference (see [92] for the equations). Following this transformation we obtain the expression for the space-fixed scattering amplitude using the **S**-matrix (or **T**-matrix) obtained from the body-fixed (ab-initio) calculations:

$$f_{SF}(\mathbf{k}.\mathbf{r}';\alpha,\beta,\gamma) = \sum_{lhml'h'm'\lambda p\mu} \frac{\sqrt{\pi(2l+1)}}{\imath k} \imath^{l-l'} \bar{b}_{lhm}^{p\mu} \bar{b}_{l'h'm'}^{p\mu} Y_{l'}^{\lambda}(\hat{\mathbf{r}}') \times \\ \times \mathcal{D}(\alpha,\beta,\gamma)_{\lambda m}^{l'} \mathcal{D}(\alpha,\beta,\gamma)_{0m}^{l} (S_{lh,l'h'}^{p\mu} - \delta_{ll'}\delta_{hh'}), \tag{B.12}$$

where $\mathcal{D}(\alpha,\beta,\gamma)_{\cdots}^{\cdots}$ are elements of the rotational matrices corresponding to the angles α,β,γ and the b-coefficients are defined in [92]. Inserting expression (B.12) into the equation (B.10) and performing the angular integration leads to the final expression for the DCS:

$$\frac{d\sigma}{d\Omega} = \sum_{L=0}^{L_{max}} A_L P_L(\cos\theta), \tag{B.13}$$

where θ is the scattering angle. $P_L(\cos\theta)$ is the Legendre polynomial and the coefficients A_L are given by a complicated expression depending on the elements of the **T**-matrix and the Clebsh-Gordan coefficients. For our purposes the exact form of the A_L coefficients is not important. All A_L coefficients for $L \geq 2l_{max}+1$, where l_{max} is the largest angular momentum included in the ab-initio calculations, are identically zero, i.e. $L_{max} = 2l_{max}+1$.

The integral cross section can be obtained from the DCS (B.13) easily utilizing the orthogonality of the Legendre polynomials:

$$\sigma_I = \int \frac{d\sigma}{d\Omega} d\Omega = \sum_{L=0}^{L_{max}} A_L \int P_L(\cos\theta)\sin(\theta) d\theta d\phi = 4\pi A_0. \tag{B.14}$$

So far we have not taken into account the rotational motion of the target molecule. In order to calculate the DCS for the rotational elastic or inelastic process we need to start with the scattering amplitude $\langle j|f_{SF}(\mathbf{k}.\mathbf{r}';\alpha,\beta,\gamma)|j_0\rangle$, where $|j_0\rangle$ and $|j\rangle$ are the initial and the final rotational states of the molecule, i.e. the amplitude entering equation (B.10) is averaged over the function corresponding to the product (overlap) of the two rotational functions. This

approach is accurate for incident electron energies which are not extremely small (in the mili-eV regime) so that the rotational motion of the molecule can be regarded as much slower than the collision time. Consequently, it is a good approximation to regard the target molecule as a rigid rotor. It can be shown then that the DCS for rotational excitation has the following form which is similar to equation (B.13):

$$\frac{d\sigma_{j_0,\mathbf{p}\to j,\mathbf{p}_j}}{d\Omega} = \frac{p_j}{p}\sum_{L=0}^{L_{max}} A'_L P_L(\cos\theta), \tag{B.15}$$

where $\mathbf{p}_j$ and $\mathbf{p}$ are the electron momenta after and before the collision respectively. The coefficients A'_L now depend on the initial and final rotational states of the molecule. As in the previous case $L_{max} = 2l_{max} + 1$. Whether the molecule is a spherical top, symmetric top or asymmetric top determines the rotational states of the molecule (and their energies) and in turn determines the coefficients A'_L, whose precise form for each of these models can be found in [92]. The approach just described is used in the POLYDCS program to determine the rotationally inelastic DCS for a neutral non-polar molecule.

For collisions with polar molecules the Born correction needs to be included. As we saw at the end of the previous section (see equation (B.8)), the only rotational transition which is dipole allowed is that for $\Delta J = 1$ and it is therefore the DCS for this process that needs to include the Born correction. For the transitions for which $\Delta J = 1$ the DCS is calculated using the expression:

$$\frac{d\sigma_{j_0,\mathbf{p}\to j,\mathbf{p}_j}}{d\Omega} = |f^B_{j_0,\mathbf{p}\to j,\mathbf{p}_j}(\cos\theta)|^2 + \sum_{L=0}^{L_{max}} (A'_L - A^B_L) P_L(\cos\theta), \tag{B.16}$$

which is called the Born closure approximation. In this equation $f^B_{j_0,\mathbf{p}\to j,\mathbf{p}_j}(\cos\theta)$ stands for the scattering amplitude for electron collisions with the *rotating dipole* calculated using the first Born approximation. The coefficients A'_L are obtained in the same way as above. Similarly to equation (B.13) the DCS corresponding to the amplitude (B.6), calculated in the first Born approximation for electron collisions with the *fixed* dipole, can be expressed as

$$\frac{d\sigma_{j_0,\mathbf{p}\to j,\mathbf{p}_j}}{d\Omega} = \sum_{L=0}^{\infty} A^B_L P_L(\cos\theta). \tag{B.17}$$

This expression defines the coefficients A^B_L which are used in equation (B.16). The Born closure approximation (B.16) can be justified by noting that the difference $A'_L - A^B_L$ mostly comes from the short-range part of the interaction. The long-range contribution (i.e. the

dipole one) can be reliably evaluated with the first Born approximation for the rotating dipole, which does not result in divergent cross sections. The use of the fixed-dipole approximation, for the calculation of the A_L^B coefficients, is conceptually equivalent to using the fixed-nuclei approximation in the ab-initio calculations and hence taking the difference $A'_L - A_L^B$ of the two coefficients guarantees the consistency of this approach. By choosing a large enough value of L_{max} in (B.16) we obtain a converged DCS.

The choice of the value of L_{max} is crucial to obtain an accurate DCS [161]. There is no one-to-one correspondence between L and the electron angular momentum in the equation (B.17). In fact, each of the coefficients A_L contains terms which have the form of interference between **T**-matrix elements corresponding to different angular momenta l. The elements with higher l values can be replaced with the Born ones, but the ones with small values of l cannot. Consequently, it is these interference terms which do not get cancelled with the corresponding terms in A_L^B. Nevertheless, as L increases, the contribution of the interference terms relatively decreases and therefore the difference $A'_L - A_L^B$ gets smaller: we achieve convergence for a large enough value of L_{max}. If L_{max} is chosen too small the interference behaviour prevails and the resulting DCS may show an oscillatory behaviour or can even contain negative values.

The magnitude of the dipole moment of the molecule governs the minimum value of the angular momentum for which the Born approximation is appropriate, i.e. for a given value of the angular momentum the Born approximation is not equally accurate for molecules with a small or a large dipole moment. Consequently, the total magnitude of the interference terms which do not get cancelled in (B.17) will usually be larger the larger the dipole moment of the molecule is. Even for large values of L_{max} this might lead to the appearance of the oscillatory behaviour, or negative values, in the resulting the DCS. This unphysical behaviour is an artifact of the method chosen for the calculation of the Born correction and can be observed in the DCS calculated for pyrimidine in Figure 4.1 (10 eV and 15 eV), as the small oscillations in the calculations using the cc-pVDZ basis set, and in the DCS for pyridazine in Figure 4.9 for 10 eV.

An alternative approach [161], based on Born-correcting the *scattering amplitude*, rather than the DCS, removes the problem associated with the negative values in the cross section, because the DCS is defined as a squared modulus of the scattering amplitude. Hence the correction calculated in this way is guaranteed to be always positive.

The POLYDCS program uses the elastic part of the **K**-matrix (calculated using the R-matrix suite in our case) to generate the DCS. The **K**-matrix has dimension equal to the

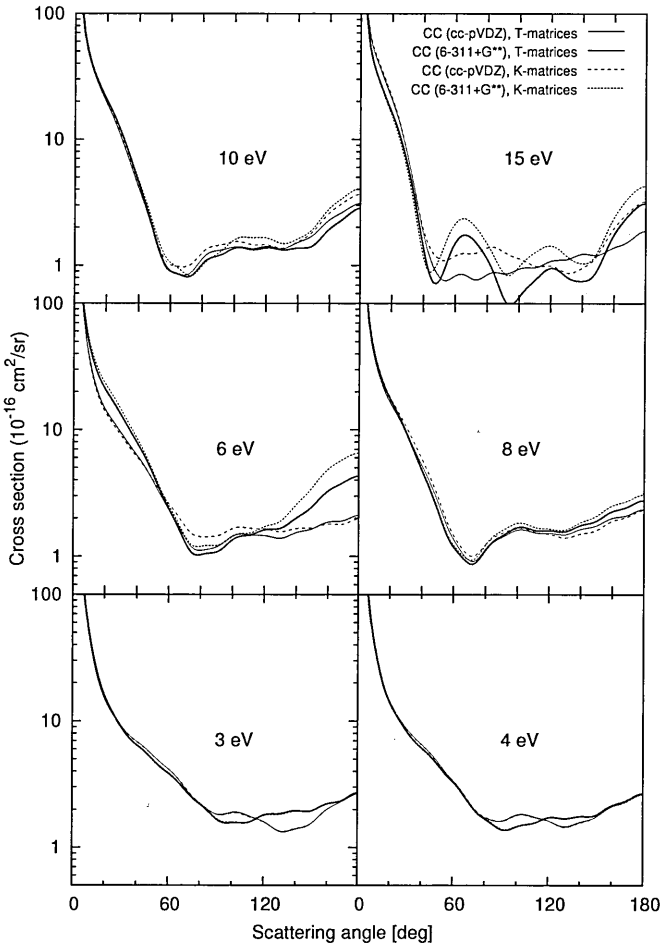

Figure B.2: Comparison of the Born corrected elastic DCS for pyrimidine obtained from the CC calculations using POLYDCS and **K**-matrices and **T**-matrices on input. See Section 4.2 for details of the ab-initio calculations.

number of open channels for a given electron energy. In the case of the CC calculations the **K**-matrix has a larger dimension above the first excited threshold than below, due to the additional channels linked to the electronically excited states. In order to calculate the DCS we extract only the submatrix of the full **K**-matrix corresponding to the elastic channels. This approach neglects couplings of the elastic channels to the inelastic ones and therefore is only an approximation. Clearly, this approximation will become less accurate with increasing electron energy, that is, as more inelastic channels become open and especially for energies where strong coupling to the inelastic channels is present. In order to quantify this effect we have modified POLYDCS to accept on input **T**-matrices instead of **K**-matrices and compared the resulting DCS calculated using both methods. The use of **T**-matrices has the advantage that its elements are directly related to the scattering amplitude (see equation (B.11) and the comments below) and therefore no truncation of the ab-initio results takes place. We have found (see Figure B.2) that at energies above the first excitation threshold the approach using **K**-matrices indeed introduces non-negligible errors into the calculated elastic DCS. Therefore all our DCS have been calculated using the modified version of POLYDCS that accepts **T**-matrices on input.

B.2.2 Implementation of the Born-correction for the inelastic cross sections

In order to correct the integral electronically *inelastic* cross sections we follow the approach of Chu and Dalgarno [93]. The Born-correction needs to be calculated for the dipole-allowed electronic excitation cross sections. The method of Chu and Dalgarno which applies the Born-correction to the integral cross sections is in principle similar to the one explained above for the elastic collisions. The rotational motion of the molecule is taken into account by modelling it as a rigid rotor and assuming that the molecule is linear. In order to calculate the Born-correction for a particular excitation cross section, the dipole transition moment for transition from the ground state to the given excited state is used. The full Born correction is calculated and the Born contributions from the partial waves included in the ab-initio calculation are subtracted. The Born correction for the inelastic cross sections is typically very small compared to the size of the cross section calculated ab-initio using a small number partial waves.

Qualitatively, we can understand the origin of the small magnitude of the inelastic Born correction by realizing that the process of electronic excitation involves rearrangement of the electronic density of the target molecule and scattering of the incident electron in an arbitrary direction. In contrast to this is the process of elastic scattering in which it is only the scattering electron whose trajectory gets deflected (the ground state density of the target molecule remains intact). As we explained above, due to the long-range nature of the dipolar interaction, this process takes place even for large angular momenta of the scattering electron. However, the process of electronic excitation is not a small perturbation of the electronic density which can be easily triggered by the electron passing far away from the molecule. Furthermore, electronic excitation involves deposition of a certain amount of energy of the scattering electron in the target molecule. Therefore the electronic excitation is more likely to occur if the scattering electron gets in the vicinity of the target molecule's electron cloud. As we saw above, this event is very unlikely to happen for electrons with large angular momenta. Hence the Born correction for the inelastic cross sections is rather small.

Appendix C

Optimized geometries of 2-oxo pyrimidine and 4-oxo pyrimidine

In this Appendix we list the geometries of 2-oxo pyrimidine and 4-oxo pyrimidine used in our calculations. These geometries were optimized using the MP2 theory and the cc-pVDZ basis set. For comparison we also include here the geometry of uracil used by us and optimized by Schreiber et al. [121] using the MP2 theory and the 6-31G* basis set. The molecules and the numbering of the atoms are shown in Figure C.1. All three molecules were assumed to be planar during the optimization step. Table C.1 contains all bond-lengths and angles required to fully specify the geometries.

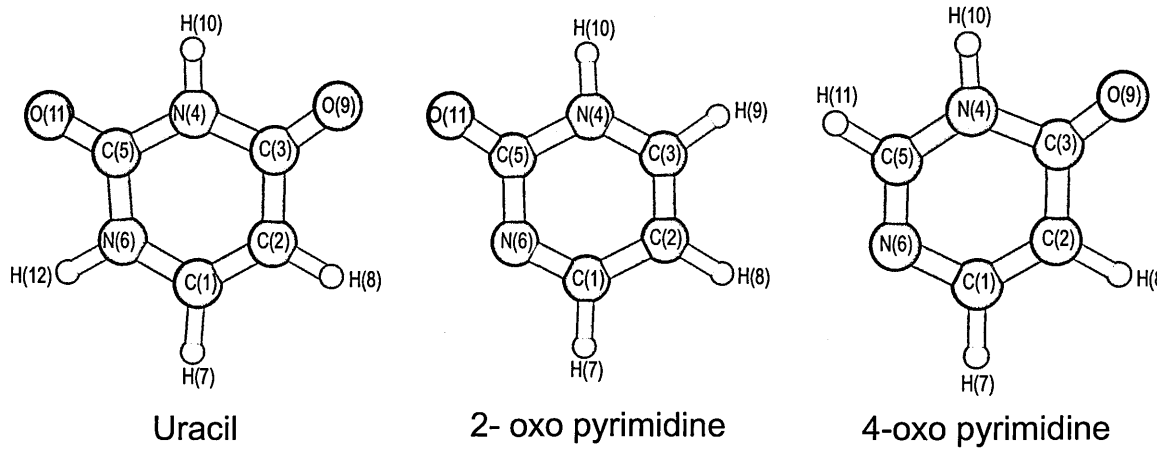

Figure C.1: Balls and sticks models of uracil, 2-oxo pyrimidine and 4-oxo pyrimidine and the numbering of the atoms used in Table C.1.

2-oxo pyrimidine				4-oxo pyrimidine				Uracil			
Bond	Bond length	Angle	Bond angle	Bond	Bond length	Angle	Bond angle	Bond	Bond length	Angle	Bond angle
1-2	2.70594	1-2-3	115.92520	1-2	2.59587	1-2-3	120.84501	1-2	2.55449	1-2-3	119.91470
1-6	2.48860	1-2-8	122.28544	1-6	2.61733	1-2-8	121.45844	1-6	2.60169	1-2-8	121.68051
1-7	2.07828	1-6-5	118.68325	1-7	2.07046	1-6-5	114.37659	1-7	2.05087	1-6-5	123.86945
2-3	2.59484	2-1-6	125.99858	2-3	2.75365	2-1-6	124.95071	2-3	2.75354	2-1-6	121.74822
2-8	2.06020	2-1-7	118.59523	2-8	2.06512	2-1-7	120.08855	2-8	2.04451	2-1-7	122.85460
3-4	2.56972	2-3-4	118.69700	3-4	2.67696	2-3-4	110.45457	3-4	2.66047	2-3-4	113.22008
3-9	2.06733	2-3-9	124.37563	3-9	2.31566	2-3-9	128.49475	3-9	2.31950	2-3-9	126.23428
4-5	2.68171	3-2-8	121.78935	4-5	2.57756	3-2-8	117.69654	4-5	2.61791	3-2-8	118.40477
4-10	1.92427	3-4-5	124.96742	4-10	1.92745	3-4-5	124.69278	4-10	1.92194	3-4-5	128.81890
5-6	2.65101	3-4-10	120.59810	5-6	2.47404	3-4-10	115.36924	5-6	2.62629	3-4-10	115.86708
5-11	2.30484	4-3-9	116.92736	5-11	2.07163	4-3-9	121.05066	5-11	2.31274	4-3-9	120.54563
		4-5-6	115.72853			4-5-6	124.68031	6-12	1.91438	4-5-6	112.42862
		4-5-11	119.65307			4-5-11	115.74881			4-5-11	124.36838
		5-4-10	114.43447			5-4-10	119.93796			5-4-10	115.31401
		6-1-7	115.40618			6-1-7	114.96073			6-1-7	115.39716
		6-5-11	124.61839			6-5-11	119.57086			6-5-11	123.20299
										1-6-12	121.23208
										5-6-12	114.89846

Table C.1: Bond lengths (in a.u.) and bond angles (in degrees) specifying the planar geometries of 2-oxo pyrimidine, 4-oxo pyrimidine and uracil. The numbering of the atoms forming the bonds and angles corresponds to the numbering in Figure C.1.

List of Figures

List of Tables